

Microseismic Monitoring and Geomechanical Modelling of CO₂ Storage in Subsurface Reservoirs

by

James P. Verdon

A thesis submitted to the University of Bristol in accordance with the requirements
for award of degree of Doctor of Philosophy in the Faculty of Science.

Department of Earth Science

University of Bristol

September 2010

Supervisor:

Professor J-M. Kendall

It has been the consideration of our wonderful atmosphere in its various relations to human life, and to all life, which has compelled me to this cry for the children and for outraged humanity. Let everything give way to this. Vote for no one who says 'It can't be done'. Vote only for those who declare 'It shall be done'.

Alfred Russel Wallace,
Man's Place in the Universe, 1903

ABSTRACT

Capture of CO₂ produced at fossil-fuel burning power stations, and its subsequent storage in deep geological formations (Carbon Capture and Storage, CCS) has the potential to become an important tool in mankind's struggle to reduce climate-changing CO₂ emissions while ensuring that the world's energy needs are met. In order for CCS to become socially acceptable and economically viable, the risks of CO₂ leakage must be quantified and minimised. We must be able to model how CO₂ will flow through the subsurface, and we must be able to monitor this flow. We must also be able to model the effects of CO₂ injection on the rocks in and around a reservoir, and we must develop monitoring methods to track these effects in the field. These requirements generate a number of scientific and engineering questions on which this thesis focuses.

In 2000, a CCS component was added to EnCana's enhanced oil recovery operations at the Weyburn oil field, Saskatchewan Province, Canada. This project has provided a testing ground for many modelling and monitoring techniques, including passive seismic monitoring. The first aim of this thesis is to analyse the microseismic data recorded at Weyburn to see what microseismic events can tell us about geomechanical deformation induced by injection. The second part of the thesis aims to model geomechanical deformation using finite element techniques. The final part of the thesis links the two techniques by showing how microseismic observations can be used as a tool to help calibrate geomechanical models, and also how stress changes predicted by geomechanical modelling can help interpret microseismic data in terms of storage security.

A downhole microseismic monitoring array was installed at Weyburn in 2003, and CO₂ injection was initiated in a nearby well in 2004. CO₂ injection induced approximately 100 events during the first year, and approximately 40 in the following 3 years. Events are located in two clusters associated with nearby production wells. Events are located at reservoir depths and in the overburden as well. Event locations - around production wells and in the overburden - are difficult to interpret within a conventional framework for injection-induced seismicity, where locations are expected to form a cloud around the injection well.

Microseismic events provide excellent S-wave sources to image seismic anisotropy in reservoirs using shear-wave splitting (SWS). As part of this thesis I have developed an approach using rock physics to invert SWS measurements for the presence of aligned fractures sets. Using the Weyburn data, I find two sets of aligned fractures that strike to the NW and NE, matching fracture sets previously identified in core samples and borehole image logs from Weyburn.

The use of microseismic data at Weyburn has highlighted how little we know about the microseismic and geomechanical response to CO₂ injection in comparison to other commonly injected fluids such as water. To address this uncertainty I analyse microseismic data from a set of hydraulic fracture stimulations into a reservoir that use both water and CO₂ as the injection fluids. I make a direct comparison of microseismicity generated by the two fluids, finding that the rates and magnitudes of microseismicity during CO₂ and water injection are very similar. SWS measurements are also unable to distinguish between the fracturing induced by the different injection fluids suggesting that there is no reason to expect lower rates of microseismicity or geomechanical deformation during CO₂ injection.

Microseismic activity is an observable manifestation of geomechanical deformation induced by injection. As the pore pressure is increased in a reservoir, effective compressive stress is reduced, causing it to expand. I use a recently developed coupled fluid-flow/geomechanical modelling technique to model this injection-induced deformation. I develop a series of simple, representative models to study how the stress path induced by injection is modulated by the geometry of the reservoir and the material properties of both the reservoir and surrounding non-pay rocks. I find that small reservoirs that are softer than the surrounding rocks are most prone to stress arching effects, while flat extensive reservoirs that are stiffer than surrounding rocks tend to experience only the hydrostatic effective stress decrease induced by pore pressure increase. By computing the changes in deviatoric stress induced by injection, I am able to analyse which types of reservoir will be most prone to brittle failure (fracturing) and where this failure is most likely to occur. I find that small reservoirs are most prone to fracturing - in small soft reservoirs the overburden is most likely to fracture above the injection well, in small stiff reservoirs fracturing is most likely to occur in the reservoir.

Changes in the applied stress field will change the seismic properties of rocks in and around the reservoir. Therefore in theory it should be possible to image geomechanical deformation using seismic methods. To do so, a rock physics model is needed to map modelled stress changes into changes in seismic velocities. I have developed a model that uses a microstructural effective medium approach to map triaxial stress changes into anisotropic changes in P and S wave velocity. I have calibrated this model with over 200 sets of stress-dependent ultrasonic velocity data, measured on core samples, taken from the literature. I use this model to show that the differences in stress path caused by differing reservoir geometries and material properties may well generate resolvable variations in the 4-D seismic response of a CO₂ injection site. These responses have the potential to be used as a diagnostic in imaging geomechanical deformation, and thereby be used to contribute a greater understanding of the risk of CO₂ leakage due to fracturing.

I have developed a workflow to construct geomechanical models, make seismic and microseismic predictions, and thereby to make comparisons with geophysical observations. In the final part of this thesis I apply this workflow to the Weyburn field. I construct a representative geomechanical model to simulate production from the reservoir, followed by CO₂ injection for storage and EOR. The modelled rock mechanical properties are based on measurements made on core samples from Weyburn. I use the modelled stress changes to make microseismic and seismic anisotropy predictions, finding a poor match between predicted microseismic zones and where microseismicity has been observed at Weyburn, and a poor match between predicted and observed seismic anisotropy. However, I develop a second model that takes into account the softening effect that vugs and fractures will have on the stiffness of the reservoir that will not be included if core sample measurements are used without modification. This new model provides a much better match for both microseismicity and seismic anisotropy. The model indicates that microseismicity observed in the overburden at Weyburn does not represent fluid migration through the caprock but stress transfer through the rock frame. This approach shows how geophysical observations can be used to help calibrate and thereby improve the accuracy of a geomechanical model, providing a greater understanding of the risks that geomechanical deformation can pose to the secure storage of CO₂.

AUTHOR'S DECLARATION

I declare that the work in this thesis was carried out in accordance with the requirements of the University's Regulations and Code of Practice for Research Degree Programmes and that it has not been submitted for any other academic award. Except where indicated by specific reference in the text, the work is the result of the candidate's own independent research performed at the University of Bristol, Department of Earth Sciences, between September 2006 and September 2010. Work done in collaboration with, or with the assistance of, others, is indicated as such. Any views expressed in the thesis are those of the author and not necessarily those of the University.

James P. Verdon

Date: September 2010

CHAPTER 0. AUTHOR'S DECLARATION

ACKNOWLEDGMENTS

There are many things for which an aspiring Ph.D student should be grateful, including: assistance with technical and scientific issues; the acquisition of interesting datasets; seemingly endless supplies of money to attend conferences; top-quality BBQs; and most importantly the encouragement and motivation to keep going throughout the three (and a bit) years required. I have been very fortunate that in Mike Kendall I have had a supervisor who has provided all of the above throughout my time at Bristol, and to him goes my first and largest thank you.

I am also extremely grateful to Doug Angus, with whom I worked closely on the geomechanical and rock physics aspects of this project. Not only did he teach me the joys of FORTRAN 77, but he has done much to help turn some of my ideas and models into workable codes, and spent many hours sourcing ultrasonic data with which to calibrate my rock physics models.

Most of the funding during my Ph.D came from UKERC, and I am grateful to them for providing this money. Towards the end of this project I received some extra funding from the Petroleum Technology Research Center of Canada.

Much of the geomechanical work in this thesis was done under the umbrella of the IPEGG project, and I wish to thank the project leader, Quentin Fisher, as well as all those who have worked on IPEGG, especially Jose Segura and Sergei Skachkov at Leeds University, and Tony Crook and Martin Dutko at Rockfield Software, Swansea. I also thank the project sponsors: BP, Statoil, ENI and BG for funding the IPEGG research

I would like to thank Pinnacle Technologies Ltd for providing the hydraulic fracturing data used in Chapter 4. In particular I would like to thank Shawn Maxwell for setting this opportunity up, and Natalia Verkhovtseva for showing me around Pinnacle's in-house software. Shawn also did some of the initial work in locating and describing the microseismic data from Weyburn. Also from Canada, I am grateful to Don White of the Canadian Geological Survey for providing the microseismic data from the Weyburn project, and for acting as my liaison with those working at Weyburn. I would also like to thank all the reviewers who provided feedback on my journal articles: many of their comments have fed back into this thesis.

I would like to thank Andrew Curtis, from Edinburgh University, and Fiona Whitaker from Bristol, for acting as my examiners. I would also like to thank my Ph.D committee, George Helffrich and Alison Rust for their helpful reviews of my work, and also James Wookey for all his helpful shear-wave splitting codes, and most notably for providing (and troubleshooting) the SHEBA routines. I would like to thank all those that have worked with me in the Bristol Geophysics Group during my time here - Glenn Jones (titis aye), James Hammond, Kit Chambers, Ricky Ramalho, Jenny Caddick, Ian 'WGGW' Bastow, 'scruffy' Dave Thompson, Othman Al-Harrasi, Andreas 'Dr Sausage' Wüstefeld, Andy Nowacki, and Jenny Di Leo - for their assistance, advice and friendship. It has been a pleasure to work with you all.

Finally I would like to thank my parents for funding, and inspiring, so much of my education over the last 26 years.

CHAPTER 0. ACKNOWLEDGMENTS

TABLE OF CONTENTS

Abstract	V
Author's Declaration	VII
Acknowledgments	IX
Preface	XV
1 Introduction	1
1.1 The motivation for geologic CO ₂ storage	1
1.2 CCS overview	2
1.2.1 Storage mechanisms	3
1.2.2 Unmineable coal seams	3
1.2.3 Depleted hydrocarbon reservoirs	4
1.2.4 Saline aquifers	5
1.3 Thesis Overview	5
1.3.1 Geomechanical Deformation	6
1.3.2 Microseismic monitoring	6
1.3.3 Thesis outline	7
2 The Weyburn CO₂ injection project	9
2.1 Introduction to Weyburn	9
2.2 Weyburn geological setting	10
2.2.1 History of the Weyburn field	12
2.3 Microseismic monitoring at Weyburn	14
2.3.1 System setup	14
2.4 Event timing and locations	15
2.4.1 Phase IB	15
2.4.2 Phase II	20
2.5 Discussion	22
2.6 Summary	25
3 Inverting shear-wave splitting measurements for fracture properties	27
3.1 Introduction	27
3.2 Inversion method	28
3.2.1 Model building using rock physics	28
3.2.2 Inversion for rock physics properties	35
3.3 Synthetic testing of inversion method	38
3.3.1 Sensitivity of δ and γ	38

TABLE OF CONTENTS

3.4	SWS measurements at Weyburn	41
3.4.1	Method	41
3.4.2	Splitting results for Weyburn	43
3.4.3	Phase IB	45
3.4.4	Modelling two fracture sets	47
3.4.5	Phase II	47
3.5	Discussion	50
3.6	Summary	53
4	A comparison of microseismic monitoring of fracture stimulation due to water versus CO₂ injection	55
4.1	Introduction	55
4.1.1	Field background and description	55
4.2	Event locations	56
4.2.1	Water injection	57
4.2.2	CO ₂ injection	60
4.3	Event magnitudes	61
4.4	Shear wave splitting	64
4.4.1	Splitting measurements	64
4.5	Initial S-wave polarisation	66
4.5.1	Modelling the effects of θ_S on splitting analysis	69
4.5.2	θ_S and ψ in the data	71
4.6	Interpretation of shear wave splitting results	72
4.6.1	Synthetic tests	72
4.6.2	Interpretation of datasets	78
4.7	Discussion	81
4.8	Summary	82
5	Geomechanical simulation of CO₂ injection	83
5.1	Introduction	83
5.2	Effective stress and stress path parameters	83
5.2.1	Mean and differential stress	84
5.2.2	Mohr circles	84
5.2.3	Stress path parameters	85
5.3	Numerical modelling	86
5.3.1	Fluid-flow simulation	87
5.3.2	Geomechanical modelling	87
5.3.3	Coupling of fluid-flow and geomechanical simulations	88
5.3.4	Workflow	90
5.3.5	Simple representative models	90

5.4	Results	93
5.4.1	Stress arching	96
5.4.2	Fracture potential	98
5.4.3	Shallower reservoirs	100
5.5	Surface uplift	100
5.6	Summary	104
6	Generating anisotropic seismic models based on geomechanical simulation	105
6.1	Introduction	105
6.2	Stress-sensitive rock physics models	105
6.2.1	3rd-order nonlinear elasticity	106
6.3	A micro-structural model for nonlinear elasticity	108
6.3.1	Theoretical background	108
6.3.2	Inversion for scalar cracks	110
6.3.3	Joint inversion for α and β	111
6.3.4	Effects of stress on crack density	119
6.3.5	Results	120
6.3.6	Anisotropy	120
6.3.7	Coring and damage	123
6.4	Calibration with literature data	126
6.5	Comparison of rock physics models	130
6.6	Summary	134
7	Forward modelling of seismic properties	135
7.1	Introduction	135
7.2	<i>SeisModel</i> [©] workflow	135
7.2.1	Input of results and parameters	135
7.2.2	Initialisation	136
7.2.3	Stress dependence	138
7.2.4	Fractures	138
7.2.5	Fluid substitution	139
7.2.6	<i>SeisModel</i> [©] Output	139
7.3	Results from simple geomechanical models	139
7.3.1	Overburden travel time-shifts	139
7.3.2	Shear wave splitting	141
7.4	Summary	145
8	Linking geomechanical modelling and microseismic observations at Weyburn	147
8.1	Introduction	147
8.2	Model description	147
8.2.1	Fluid flow simulation	149

TABLE OF CONTENTS

8.2.2	Geomechanical model	149
8.2.3	Material properties	151
8.2.4	Rock physics properties	151
8.3	Results	153
8.3.1	Stress evolution and failure	153
8.3.2	Seismic Properties	155
8.4	A softer reservoir?	159
8.4.1	Heterogeneity	164
8.5	Discussion	164
8.6	Summary	167
9	Conclusions	169
9.1	Novel Contributions	173
9.2	Future Work	174
	References	177
A	List of Symbols	187
B	In Support of Carbon Capture and Storage	189

PREFACE

‘Research is not an end in itself: to communicate results, methodologies and theories is so fundamental that publishing has become an integral part of the research process. Global human progress is intrinsically linked not only to the advancement of knowledge but also to the diffusion of knowledge. The dissemination of recently-acquired knowledge among stakeholders is also crucial to attract interest and, let’s face it, funding. Likewise, academic researchers have a responsibility towards their sponsors and funding bodies to show the results of their research activities and their contribution to the advancement of the particular topics they are working on. The publication of new scientific findings is based on a peer-review process so others may comment on our work and positively contribute to the quality of the publications. As it happens, for better or worse, publication is often considered a metric of performance. Thus it is useful nowadays, when starting a research project, to set up a publication strategy. Furthermore, the writing and submission of scientific papers is a valuable skill and an integral part of academic training.’

R. Ramalho, 2010

I have written a number of peer-reviewed journal articles and expanded abstracts during the course of my Ph.D. Often, theses that have produced a number of publications are written in the form of an introduction and conclusion bolted onto the front and back of the publications printed verbatim. However, I feel that this format often produces unnecessary repetition, and spoils the flow of a thesis as a coherent document. Additionally, the brevity required in many journals (particularly industry focused ones) means that a thesis is often a good place to expand at length on interesting details that might only be touched on briefly in an academic paper. Therefore I have not followed this format. The first chapters of this thesis introduce the datasets on which I have worked, while the latter chapters sequentially outline a workflow that can be followed to interpret the data. In the final research chapter I apply this workflow to the Weyburn data already introduced. As such, the typical format where each chapter equals one paper is not appropriate. The papers and expanded abstracts that have followed from this research are listed below, and elements of them can be found throughout the thesis. I recommend that the busier reader consult these papers for an overview before turning to this thesis for a fuller account of my research.

Journal Articles

1. **J.P. Verdon** & J-M. Kendall, 2011. Detection of multiple fracture sets using observations of shear-wave splitting in microseismic data. *Geophysical Prospecting*, *accepted*.
2. D.J. White, M. Meadows, S. Cole, A. Ramirez, Y. Hao, S. Carle, A. Duxbury, C. Samson, J-M. Kendall, **J.P. Verdon**, B. Dietker, T. Urbancic, J. Johnson & I. Morozov, 2011. *Geophysical*

- monitoring of the Weyburn CO₂ flood: Results during 10 years of injection. *Energy Procedia*, *accepted*.
3. **J.P. Verdon**, J-M. Kendall & S.C. Maxwell, 2010. A comparison of passive seismic monitoring of fracture stimulation due to water versus CO₂ injection. *Geophysics*, 75(3), MA1-MA7.
 4. **J.P. Verdon**, D.J. White, J-M. Kendall, D. Angus, Q. Fisher & T. Urbancic, 2010. Passive seismic monitoring of carbon dioxide storage at Weyburn. *The Leading Edge*, 29(2), 936-942.
 5. A. Wüstefeld, O. Al-Harrasi, **J.P. Verdon**, J. Wookey & J-M. Kendall, 2010. A strategy for automated analysis of passive microseismic data to study seismic anisotropy and fracture characteristics. *Geophysical Prospecting*, 58(5), 755-773.
 6. **J.P. Verdon** & J-M. Kendall, 2009. Imaging fractures and sedimentary fabrics using shear wave splitting measurements made on passive seismic data. *Geophysical Journal International*, 179(2), 1245-1254.
 7. D.A. Angus, **J.P. Verdon**, Q.J. Fisher & J-M. Kendall, 2009. Exploring trends in microcrack properties of sedimentary rocks: An audit of dry core velocity-stress measurements. *Geophysics*, 74(5), E193-E203.
 8. **J.P. Verdon**, D.A. Angus, J-M. Kendall & S.A. Hall, 2008. The effects of microstructure and nonlinear stress on anisotropic seismic velocities. *Geophysics*, 73(4), D41-D51.

Expanded Abstracts

1. **J.P. Verdon**, J-M. Kendall, 2011. Detection of multiple fracture sets using observations of shear-wave splitting in microseismic data. 3rd EAGE Passive Seismic Monitoring Workshop, Athens.
2. **J.P. Verdon**, X. Campman, 2010. The feasibility of imaging the CO₂ plume at CO2SINK using 4D seismics. 72nd EAGE Annual Meeting, Expanded Abstracts, P205.
3. **J.P. Verdon**, D.J. White, J.M. Kendall, D.A. Angus, Q.J. Fisher, T. Urbancic, 2010. Passive seismic monitoring of CO₂ storage at Weyburn. 72nd EAGE Annual Meeting, Expanded Abstracts, K011.
4. **J.P. Verdon**, X. Campman, 2010. A study of the feasibility of imaging CO₂ injection at the CO2SINK project using seismic techniques. 2nd EAGE CO₂ Geological Storage Workshop, Berlin.
5. **J.P. Verdon**, J.M. Kendall, D.J. White, D.A. Angus, Q.J. Fisher, T. Urbancic, 2010. Passive seismic monitoring and geomechanical modelling of CO₂ injection at Weyburn. 2nd EAGE CO₂ Geological Storage Workshop, Berlin.

6. D. Angus, J-M. Kendall, **J.P. Verdon**, Q. Fisher, J. Segura, M. Dutko, 2010. Evaluating seismic attributes of reservoirs using coupled fluid-flow and geomechanical simulation. 44th U.S. Rock Mechanics Symposium.
7. **J.P. Verdon**, J-M. Kendall, 2009. Constraining fracture geometry from shear-wave splitting of passive seismic data. 71st EAGE Annual Meeting, Expanded Abstracts, P164.
8. **J.P. Verdon**, S.C. Maxwell, J-M. Kendall, 2009. A comparison of passive seismic monitoring of fracture stimulation due to water versus CO₂ injection. 71st EAGE Annual Meeting, Expanded Abstracts, P107.
9. A. Wüstefeld, O. Al-Harrasi, **J.P. Verdon**, J-M. Kendall, 2009. Towards fully automated fracture characterisation in microseismic datasets using shear wave splitting. I-GET Final Conference.
10. J-M. Kendall, O. Al-Harrasi, **J.P. Verdon**, A. Wuestefeld, A. Al-Anboori, 2009. Fracture characterisation using estimates of shear wave splitting from microseismic data. EAGE Passive Seismic Monitoring Workshop, Cyprus.
11. **J.P. Verdon**, D.A. Angus, J-M. Kendall, J. Segura, S. Skachkov, Q.J. Fisher, 2008. The effects of geomechanical deformation on seismic monitoring of CO₂ sequestration. SEG Expanded Abstracts, **27**, 2869-2873.
12. **J.P. Verdon**, D.A. Angus, J-M. Kendall, J. Segura, S. Skachkov, Q.J. Fisher, 2008. The effects of geomechanical deformation on seismic monitoring of CO₂ sequestration. 1st EAGE CO₂ Geological Storage Workshop, Budapest.
13. D.A. Angus, **J.P. Verdon**, J-M. Kendall, Q.J. Fisher, J. Segura, S. Skachkov, M. Dutko, A.J.L. Crook, 2008. Influence of fault transmissibility on seismic attributes based on coupled fluid-flow and geomechanical simulation. SEG Expanded Abstracts, **27**, 1600-1604.
14. D.A. Angus, **J.P. Verdon**, J-M. Kendall, 2007. Modelling frequency dependent waveform effects in fractured and porous media with a narrow-angle one-way elastic wave propagator. 3rd International Workshop on Frequency Dependent Geophysics, Edinburgh.
15. D.A. Angus, J-M. Kendall, Q.J. Fisher, M. Dutko, A.J.L. Crook, S.A. Hall, **J.P. Verdon**, 2007. Linking coupled fluid-flow and geomechanical models with rock physics derived elastic models for reservoir seismic forward modelling applications. 69th EAGE Annual Meeting, Expanded Abstracts, D006.

A technology push approach, based on large-scale research and technology deployment programmes and new breakthrough technologies, is needed to achieve deeper GHG cuts in the long run (2050 and beyond).

*Global Environmental Outlook 4
United Nations Environment Programme*

1.1 The motivation for geologic CO₂ storage

In 1903, A.R. Wallace (Charles Darwin's co-discoverer of evolution) identified that the coal smog and pollution produced by large industrialised cities represented a grave threat to the health of the inhabitants. On the inside cover of this thesis I have reprinted his exhortation for political leadership to do something about it. Our response as a society was such that, 100 years later, air pollution is no longer a major problem in most modern cities (although it remains a problem in less developed nations lacking the technology to deal with it). His exhortation is still equally relevant today, however, because humanity now faces a new threat, still related to the burning of coal which Wallace railed against over a century ago. This threat is not limited to the inhabitants of one smoggy city, but could well affect all life, human and not, on the planet. While we have been able to dramatically reduce the emission of sulphur dioxide, nitrous oxide and particulate matter that caused so many problems in 19th Century London, coal fired power plants emit to the atmosphere essentially as much CO₂ per tonne of coal burned as they did in Wallace's time.

Now the scale is magnified because there are many more people around the world depending on coal power than 100 years ago. Furthermore, according to the latest climate predictions, we must find a solution to the CO₂ problem far faster than we managed to deal with the air pollution issues of 100 years ago. Clearly, dealing with the rapidly rising atmospheric CO₂ concentrations caused by anthropogenic emissions presents one of the greatest challenges of the 21st century. We must act now, and we must act decisively, in order to bring our CO₂ emissions under control. Wallace was right 100 years ago, and he is still right today.

Mankind's burning of fossil fuels produces globally approximately 30×10^9 tonnes of CO₂ per year (Holloway, 2001). Under a 'business-as-usual' scenario, the International Energy Agency (IEA) estimates that by 2050 this rate will have risen to 60×10^9 tonnes/yr. If atmospheric CO₂ levels are to stay below 500ppm (the value deemed acceptable by the Intergovernmental Panel on Climate Change (IPCC)), then emissions must be reduced to 14×10^9 tonnes/yr by 2050, a four-fold reduction from the 'business-as-usual' scenario. Figure 1.1 shows how the IEA anticipates such reductions will be achieved. It is clear that efficiency improvements, renewable energy and nuclear power must all play their part in meeting emissions targets.

The largest increases in CO₂ emissions in the next 40 years will come from developing countries, in particular India and China. These countries are already becoming the largest outright CO₂ emitters

in the world (though still much lower in per capita terms). This is due to their rapid urbanisation and industrialisation, and the huge need for energy this generates. At present, most of these energy needs are met with coal, which is cheap, highly abundant and geopolitically secure. With both countries putting economic development and increases in living standards ahead of climate change concerns, it is likely that this scenario will persist. Hence, if we are to avoid increases in atmospheric CO_2 concentrations from burning this coal, we must find ways to store the resulting CO_2 in domains of our planet other than the atmosphere. Porous rocks deep underground provide a potential storage space. This is why the IEA estimates that by 2050 20% of our emissions reductions will have come through carbon capture and storage (CCS), while the IPCC predict that 15-55% of our emissions reductions will come through CCS.

For further discussion on the motivation for deploying CCS on a large scale, please see Appendix B. CCS is not universally popular amongst environmental protection agencies and NGOs. It is seen as being tainted by the mistrusted fingers of oil and power generation companies, and as an excuse to continue business as usual. It should not be seen as such - without CCS it will be very difficult to achieve the emissions reductions required by the IPCC.

1.2 CCS overview

At present there are four major sites where CO_2 is being stored in large volumes, as well as numerous smaller scale pilot and EOR sites. Figure 1.2 shows the largest currently operational CO_2 storage sites by annual mass of CO_2 stored. Figure 1.3 shows a cartoon depicting the main processes needed during CO_2 storage. CO_2 is captured at large point source emitters such as power stations and large

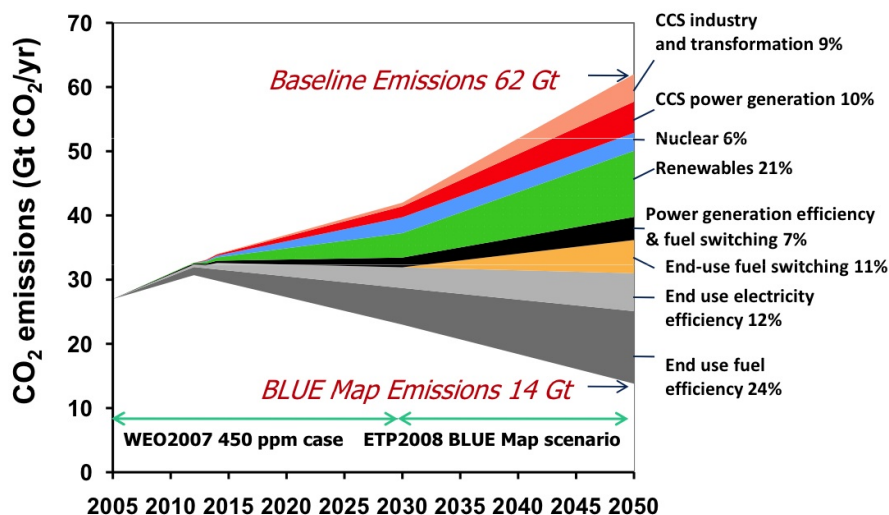


Figure 1.1: Estimates of how CO_2 emissions will be reduced from the business as usual scenario by 2050. Taken from the IEA Energy Technology Perspectives (2008).

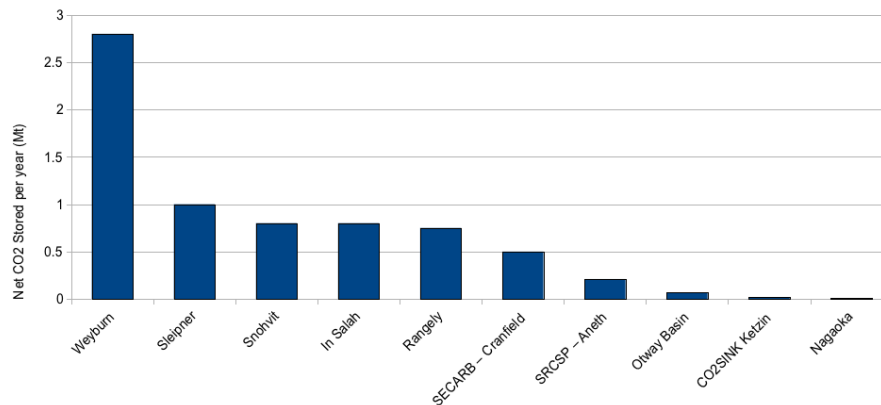


Figure 1.2: CCS sites by annual storage volume (as of 2009). Data provided by the IEA Greenhouse Gas Program. Many smaller CO₂ injection sites are not included on this plot.

industrial complexes and pumped via pipelines to the storage area. Storage can be achieved in saline aquifers, depleted oil reservoirs and unmineable coal seams.

1.2.1 Storage mechanisms

CO₂ is injected at pressures over 8MPa, where it exists as a supercritical fluid with a density of $\sim 700\text{kg/m}^3$, which is less dense than most formation brines and oils. Buoyancy forces will therefore drive the injected CO₂ upwards until it meets an impermeable layer capable of preventing further fluid migration. Once trapped, the CO₂ will exist as a free phase ‘bubble’ below the caprock. This is known as stratigraphic trapping, and it is estimated that, during the early stages of injection most of the injected CO₂ will be trapped in this manner (Johnson et al., 2001).

Free phase CO₂ will slowly dissolve into any residual fluids present in the reservoir. Dissolution of CO₂ increases the density of brine, so buoyancy forces will force such fluids down, reducing the risk of leakage. This is known as hydrodynamic trapping, and Johnson et al. (2001) estimates that up to 15% of injected CO₂ may be stored in this manner.

Free phase CO₂ and CO₂ enriched brines will be in chemical disequilibrium with the rocks of the reservoir, and so chemical reactions will occur between them. This may result in both dissolution and/or precipitation reactions. If minerals containing carbonate are precipitated, this will represent the optimum storage scenario, as the precipitated minerals will be immobile, so there is no risk of leakage. However, the reaction rates for such processes are very slow, so on decadal timescales only a very small amount (<1%) of injected CO₂ will be stored in this manner (Johnson et al., 2001).

1.2.2 Unmineable coal seams

Although generally imagined to be a solid fuel, coal does contain some porosity in the form of fracture networks and micropores (Holloway, 2001). This space is usually filled with methane created during

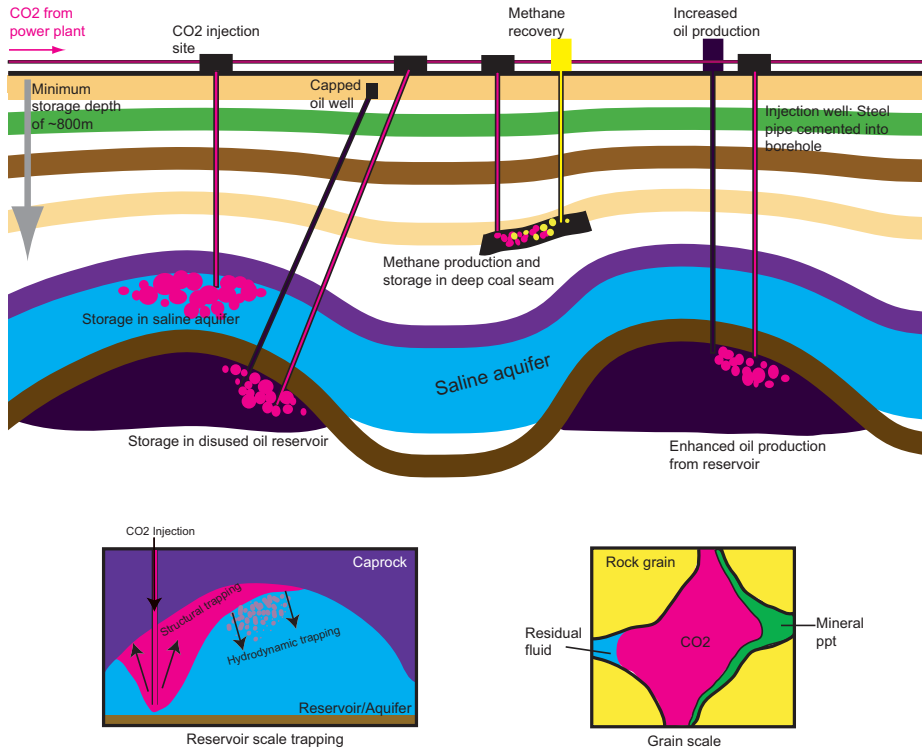


Figure 1.3: Cartoon showing the main processes needed during CO_2 storage. CO_2 is pumped from a power plant and can be injected into unmineable coal seams, saline aquifers or mature oil-fields. The buoyant CO_2 can be trapped stratigraphically, or it may dissolve and be stored hydrodynamically. It may also react with rock grains and residual fluids, and be stored as a mineral precipitate.

the heating of organic matter that makes the coal. This methane is adsorbed onto the surface of the coal by electromagnetic forces. However, CO_2 has a greater affinity for coal than methane, so introduction of CO_2 in such a system would result in the production of methane and adsorption of CO_2 . This is an attractive proposition, as the economic costs of injecting CO_2 would be offset by commercial methane production. However, the storage volumes available in such coal seams are not very large, and so are unlikely to play any significant role in global carbon storage operations. As such, I will not consider them further here.

1.2.3 Depleted hydrocarbon reservoirs

As hydrocarbon reservoirs are produced, pore pressure decreases and the hydrocarbons are gradually replaced by formation fluids (usually brine). As production continues, it has been common reservoir engineering practise since the 1960s to inject fluids into the reservoir to maintain elevated pore pressures, preventing subsidence and increasing production. Usually brine is used as the injected fluid, but on some occasions CO_2 has been used. As a result, some of the expertise and technology needed

for CO₂ to be injected into depleted hydrocarbon reservoirs is already in place. By changing the injection and/or production schemes in such situations, it will be possible to increase hydrocarbon output while ensuring that the injected CO₂ is stored underground. This is currently being conducted at In Salah in Algeria, and at the IEA GHG Weyburn-Midale CCS/EOR project, which will be discussed at length in this thesis.

Current estimates suggest that there is significant storage space available in such reservoirs, and the advantages of using such reservoirs are threefold: the economic benefits of increased oil production may offset some of the storage costs; depleted oil reservoirs will have been well mapped, so potential storage volumes will be known, and much of the infrastructure required will be present already. However, there are concerns that abandoned production wells could provide a pathway for CO₂ escape, so these must be sealed effectively, and that production activity may have damaged the caprock through fracturing. Despite these disadvantages, it is likely that most storage operations will initially focus on these targets, before moving on to saline aquifers when larger storage volumes are required.

1.2.4 Saline aquifers

Injected CO₂ is a buoyant fluid, so it will be trapped in porous reservoirs that are overlain by impermeable layers. Such stratigraphic arrangements abound in most sedimentary basins. These rocks are only occasionally filled with hydrocarbons - usually they remain filled with brine. These saline aquifers represent by far the largest volumes of storage available. Torvanger et al. (2004) estimate that there is storage potential for 8×10^{11} tonnes of CO₂ in saline aquifers in the North Sea, representing hundreds of years of European emissions. However, saline aquifers have no economic value, so are not usually well mapped. As such, estimating possible storage volumes and guaranteeing storage security will be more difficult. Storage in saline aquifers is currently being demonstrated at Sleipner and Snøhvit in the North Sea.

1.3 Thesis Overview

If CCS is to have a positive environmental impact then the injected CO₂ must be stored in the subsurface for as long as it takes for anthropogenic output rates to drop to acceptable levels and for the carbon cycle to have recovered and stabilised (Holloway, 2001). This constraint requires that CO₂ be stored for timescales of the order of 10^4 or even 10^5 years. To meet this requirement we must ensure that it is not possible for injected CO₂ to migrate large distances either vertically or horizontally away from the target reservoir. This compels us to answer several fundamental scientific questions for CCS to become economically and politically acceptable: can we develop models that can predict both how injected CO₂ will migrate through the subsurface and the effects on the subsurface of the CO₂, and can we monitor CO₂ migration in the subsurface using geophysical (and geochemical) methods? Finally, can we link model predictions to field observations to ensure that modelled behaviour matches the actual behaviour? Consideration of these fundamental research questions will strengthen the scientific foundations for CO₂ storage, and form the focus of this thesis.

1.3.1 Geomechanical Deformation

Injection of CO₂ will increase the pore pressure in the target reservoir. This will decrease the effective stress, leading to expansion of the reservoir rocks. This expansion will also lead to deformation of the rocks in the overburden. The extent of this geomechanical deformation will be controlled by the material properties of the reservoir and overburden and the magnitude of the pressure increase caused by CO₂ injection. Deformation of the overburden can cause a problem for storage integrity if fractures and faults are created or reactivated, providing a pathway for fluid migration beyond the target aquifer. Therefore, to guarantee security of storage, site operators must be able to demonstrate that geomechanical deformation will not be of sufficient magnitude to damage the caprock. Operators must also ensure that CO₂ injection will not induce earthquakes on any nearby faults.

Though well developed and routinely applied in tunnelling and mining industries, the use of geomechanics in the hydrocarbon industry is relatively recent. An important development was the coupling of fluid effects within a reservoir with geomechanical models (e.g., Dean et al., 2003). Minkoff et al. (2004) apply coupled fluid-flow/geomechanical simulations to show how hydrocarbon production can reduce pressure inside a reservoir, resulting in compaction and surface subsidence. With double coupling between a reservoir flow model and a geomechanical model, we can compute not only the effects of pressure changes on deformation, but also the effects of deformation on fluid flow via porosity and permeability changes, providing a more accurate solution.

Geomechanical models (like any model) need to be benchmarked and groundtruthed with field observations. Without these observations there can be no way to determine which models are successful and likely to provide accurate predictions going forward, and which are not. We must therefore seek geophysical monitoring methods that can be used to groundtruth geomechanical models. Possible links include controlled-source seismic monitoring, ground-surface deformation, and microseismic activity.

1.3.2 Microseismic monitoring

A number of recent studies have demonstrated the potential that microseismic monitoring has for reservoir characterisation. Many of the techniques used to analyse the recorded data are derived from global earthquake seismology. Accurate location of events can reveal clustering on discrete surfaces, indicating the presence of active faults (e.g., Jones and Stewart, 1997; De Meersman et al., 2006). The focal mechanism of an event can be determined by analysis of the polarisation of arriving waves. This can be used to evaluate the orientation of the stresses that have generated an event (e.g., Rutledge et al., 2004).

However, while event location techniques are becoming increasingly accurate, the interpretation of microseismic events, except during hydraulic fracture jobs, is still challenging. When events are located around a high pressure injection well it is relatively simple to show that the events represent the growth of fractures from this well. However, when events are distributed around a reservoir, and even in the overburden, and the injection wells are not at high pressures, it is harder to work out what microseismic activity signifies. This is where the link to geomechanical models must be crucial,

as microseismicity must surely be viewed as a manifestation of wider geomechanical deformation in and around a reservoir.

Furthermore, because the waves from events in the reservoir recorded on downhole geophones have travelled through only reservoir and caprock materials, wave propagation effects such as anisotropy can be directly attributed to these materials. Teanby et al. (2004a) show how analysis of shear wave splitting (SWS) can be performed on recorded microseismic events. By considering the magnitude of splitting and the orientation of the faster S-wave it is possible to identify the orientation and number density of fracture sets that act as flow paths within the reservoir, as well as image stress-induced anisotropy. Both stress changes and the presence of faults and fractures can significantly influence the security of CO₂ storage, and so the possibility of detecting them using microseismic monitoring will be of great use to a reservoir engineer. Furthermore, microseismic recording arrays, once installed, cost little to maintain and operate. As such, they will provide a more cost effective method of monitoring storage security over the long term, especially after injection has ceased and the field has been shut in.

1.3.3 Thesis outline

I will begin this thesis by introducing the Weyburn reservoir, currently the largest CO₂ storage site in the world. It is also the first CCS site to deploy microseismic monitoring, and in Chapter 2 I will discuss the results of this monitoring program, showing microseismic event locations and how they correlate with injection and production activities. In Chapter 3 I develop a novel approach to invert shear-wave splitting measurements for fracture properties. I use synthetic models to show the sensitivity of SWS analysis to the range of ray coverage available, before using the technique to image the fractures at Weyburn.

One of the key observations made at Weyburn is a very low rate of microseismic activity. This has led to the suggestion that CO₂ may have an inherently lower seismic deformation efficiency than other fluids such as oil or water. If CO₂ injection and/or migration does not generate microseismicity then this has obvious implications for the feasibility of microseismic monitoring for CCS. To evaluate this issue, in Chapter 4 I discuss a second microseismic dataset where both CO₂ and water have been injected into the same reservoir (a different North American oil-field). This allows me to make a direct comparison of the microseismic response to injection of the two fluids, and to discuss whether the abundant experience of water injection found in the oil industry will be applicable to CO₂ injection.

In Chapter 5 I outline the geomechanical modelling tools that were developed as part of the Integrated Petroleum Engineering, Geomechanics and Geophysics (IPEGG) research consortium. This consortium has developed a method to couple industry-standard fluid-flow simulations (such as Eclipse, MORE, VIP or MoReS) with a finite element geomechanical solver (ELFEN). I develop some simple numerical models to demonstrate the sensitivity of injection-induced stress changes to reservoir geometry and material properties. By examining the stress evolution, and in particular the development of differential stresses, I can determine which geometries and material properties are most prone to fracturing as a result of injection, and where fracturing is likely to occur.

In Chapter 6 I develop a microstructural model to map changes in stress predicted by geomechanical models into changes in elastic stiffness (from which seismic velocities can be computed). This model is fully anisotropic and includes the nonlinear response of velocity to stress changes. I have calibrated this model with over 200 stress-velocity measurements from the literature. In Chapter 7 I demonstrate this approach by forward modelling the changes in P-wave travel time and shear wave anisotropy from the simple models developed in Chapter 5, with the intention of seeing whether different styles of geomechanical deformation can be differentiated using seismic observations.

Through Chapters 5 to 7 I have outlined a workflow to go from the development of a geomechanical model to the prediction of changes to seismic properties caused by deformation. In Chapter 8 I bring this workflow together and demonstrate it in its entirety by developing geomechanical models of the Weyburn reservoir. By comparing predicted microseismic event locations with observations made in Chapter 2, and splitting predictions with measurements made in Chapter 3, the geomechanical models can be groundtruthed, and the most appropriate models selected. These geomechanical models aid the understanding of the microseismic observations made in Chapters 2 and 3. They help to show that the injection of CO₂ at Weyburn can be understood, and that there is little risk of leakage.

Finally, in Chapter 9 I present the main conclusions of this project, highlighting the significant contributions made towards the improved understanding of geological storage of CO₂, and I also make recommendations for future work.

Canada is an interesting place, the rest of the world thinks so, even if Canadians don't.

Terence M. Green

2.1 Introduction to Weyburn

A major issue concerning CCS is the lack of field demonstration. Plausible theories have been developed to cover most aspects of this process. However, there are at present only 4 major operational examples where CO₂ is injected for the purposes of storage: Statoil's Sleipner and Snøhvit sites in the North Sea, BP's In Salah Field (Algeria), and Weyburn. These pilot scale projects are intended to be used as experiments where ideas and theories relating to CO₂ storage can be tested, and where principles of best practise can be developed for future application to larger projects. Other projects likely to become operational in the near future are at the Gorgon Field (West Australia), and Shell's QUEST (Alberta) and Barendrecht (Netherlands) projects. The EU has mandated that 12 CCS demonstration projects come online by 2015.

The Weyburn oil-field, located in central Canada, was selected as the location for a major research project into CCS by the Canadian Petroleum Technology Research Center (PTRC) in collaboration with the field operators EnCana (now Cenovus) and the International Energy Agency (IEA). The aim was to develop a field scale demonstration of CCS in order to verify the ability of an oil-field to store CO₂. The knowledge thus gained would be used as a guide for best practise when implementing CCS projects worldwide (Wilson et al., 2004). In July 2000 a storage component was added to EnCana's Enhanced Oil Recovery (EOR) operation at the Weyburn-Midale Field. CO₂ has been injected through an increasing number of patterns since 2000, and the current rate of injection is ~3 million tonnes/yr. It is anticipated that 50 million tonnes will be stored during the life-of-field (LOF). This is equivalent to the emissions from 400 000 (gas-guzzling American) cars per year. The CO₂ is delivered to Weyburn through a pipeline from a coal gasification plant in Beulah, North Dakota. The primary form of monitoring is 4-D controlled source reflection seismology. The changes in the reflection amplitude of the reservoir layer have been used to image the spread of CO₂ plumes from the injection wells (White, 2008).

As part of the monitoring component of the project, geophones were installed in a disused borehole near to an injection site, with the aim of assessing the use of microseismic techniques for monitoring CO₂ injection. In this chapter I outline the geological setting and history of Weyburn, before focusing on the microseismic events recorded. The events have been located by contractors (ESG) and I discuss them here in relation to changes in injection and production in nearby wells.

2.2 Weyburn geological setting

The Weyburn field is situated in the Williston depositional basin, Saskatchewan, central Canada (Figure 2.1). The basin contains shallow marine sediments deposited from the Cambrian through to the Mesozoic. Figure 2.2 shows some of the major stratigraphic divisions identified in the basin. The Weyburn reservoir is found in the Charles Formation at depths of 1300-1500m. These rocks were formed in a peritidal regression-transgression sequence, depositing carbonates during high-stands and evaporitic dolomites during low-stands.

The Weyburn reservoir is situated in the Midale carbonate cycle. The reservoir is usually split into two parts, a lower limestone layer, the Vuggy, and an upper dolostone layer, the Marly. The Vuggy is so named because it contains vugs, or pore cavities larger than the grain size (as opposed to normal pores, which are usually smaller than the grains). The Vuggy is usually split into two components - the shoal and intershoal members. Table 2.1 lists the lithological properties of the rocks that make up the Weyburn reservoir. The seal for this reservoir group is the overlying Midale Evaporite. This was formed during the last phase of regression during deposition of the Midale strata. It consists of low permeability nodular and laminated anhydrite of 2-10m thickness. This bed forms a band of low-permeability caprock across much of Saskatchewan (Wilson et al., 2004). A second important seal is the Mesozoic Lower Watrous member, which lies unconformably on the Carboniferous beds. This member is of mixed lithology, but is generally siliclastic, and forms an impermeable layer due to its



Figure 2.1: Geographic location of the Weyburn field taken from Wilson et al. (2004). The field is set in the Williston sedimentary basin, which stretches across much of the north of the USA and central Canada.

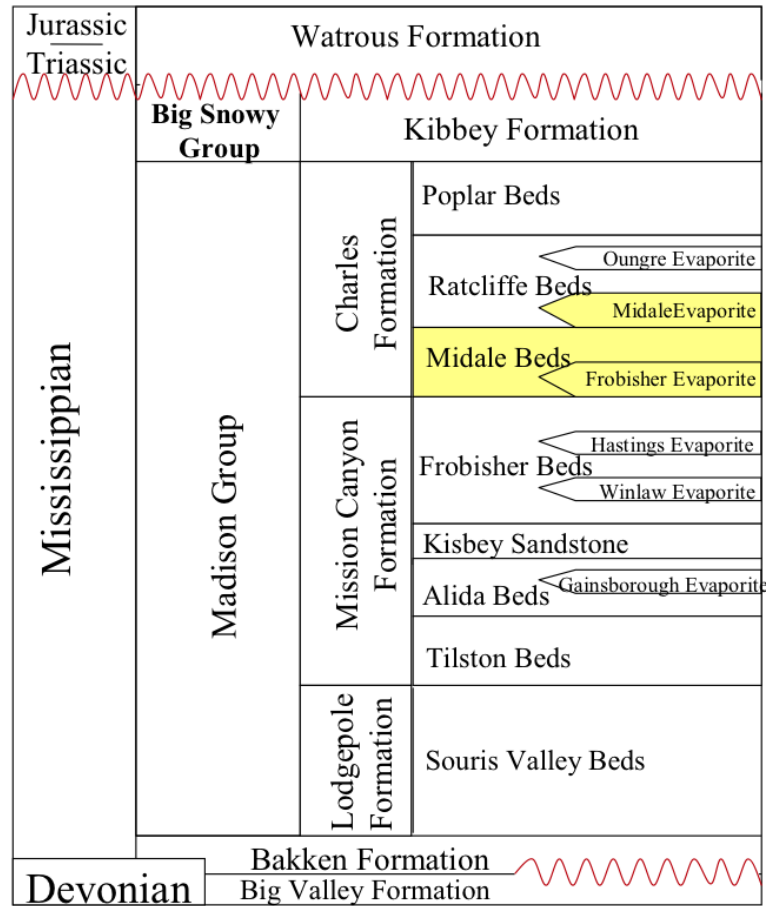


Figure 2.2: Major stratigraphic groups in the Williston Basin taken from Pendrigh (2004). The Weyburn reservoir is of Carboniferous age, set in the Charles Formation, which makes up part of the Madison Group.

	<i>Vuggy Shoal</i>	<i>Vuggy Intershoal</i>	<i>Marly</i>
Lithology	Coarse grained carbonate sand	Muddy carbonate	Microsugrosic dolomite
Permeability range	10-500mD	0.1-25mD	1-100mD
Avg permeability	50mD	3mD	10mD
Porosity range	0.12-0.2	0.03-0.12	0.16-0.38
Avg porosity	0.15	0.1	0.26
Thickness	10-22m	10-22m	6-10m
Sedimentary facies	Marine lagoonal carbonate shoal	Low energy lagoonal intershoal	Low energy marine

Table 2.1: Lithological properties of the rocks of the Weyburn reservoir. Taken from Wilson et al. (2004).

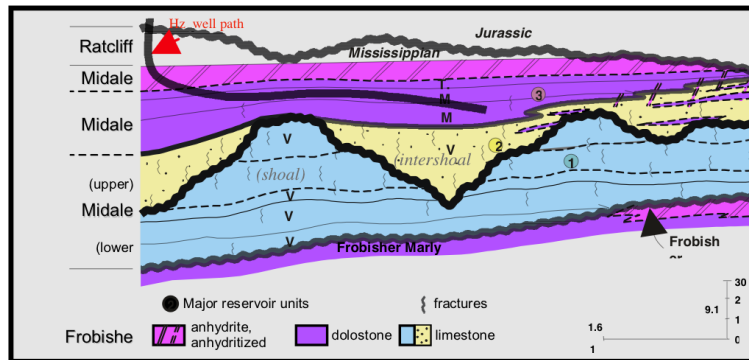


Figure 2.3: Schematic cross section of the Weyburn reservoir taken from Wilson et al. (2004). The Weyburn reservoir is split into the lower intershoal and shoal Vuggy (V) and upper Marly (M) units. The primary seal is the Midale anhydrite, while an important secondary seal is the unconformably overlying Watrous member of Jurassic age.

clay content and diagenetic infilling of pores. Figure 2.3 shows a schematic diagram of the reservoir arrangement.

2.2.1 History of the Weyburn field

It is estimated that the Weyburn reservoir initially held approximately 1.4 billion barrels of oil. Production at Weyburn began in 1954, continuing until 1964, when waterflood was initiated to increase production. Production peaked after the waterflood at 46000 barrels/day, and has been decreasing since. In 1991 drilling of horizontal wells was initiated to increase production, targeting in particular the less permeable Marly layer. It is estimated that prior to CO₂ injection, 25% of the original oil in place had been recovered. In 2000, injection of CO₂ was initiated, with the intention of increasing oil production in the 19 patterns of Phase IA. The CO₂ is sourced from a coal gasification plant in North Dakota, and is transported through a pipeline to the field. CO₂ is injected in horizontal wells while water continues to be injected through vertical wells. Following the success of Phase IA, CO₂ injection has been initiated in further patterns, Phase IB and Phase II, as well as the adjacent Midale Field. CO₂ is injected at a rate of between 74-588 tonnes per day per well. Enhanced oil recovery associated with the CO₂ injection currently accounts for 5000 barrels of the 20000 barrels per day total production at Weyburn. It is estimated that the EOR operations will increase production by 130 million barrels (10% of the original oil in place) and prolong the life of the field by 25 years.

When the Weyburn Field was discovered, pore pressure was estimated to be 14 MPa. During production, this dropped to between 2 and 6 MPa. During waterflood, pressures increased to between 8 and 19 MPa. Pressures in the Phase IA area are between 12.5 - 18MPa (Brown, 2002), with maximum anticipated pore pressure during injection of 23-25MPa.

A range of techniques have been deployed to monitor the initial CO₂ flood in Phase IA, including 4-D controlled source seismics, wellhead pressure sampling, cross well and vertical seismic profiling,

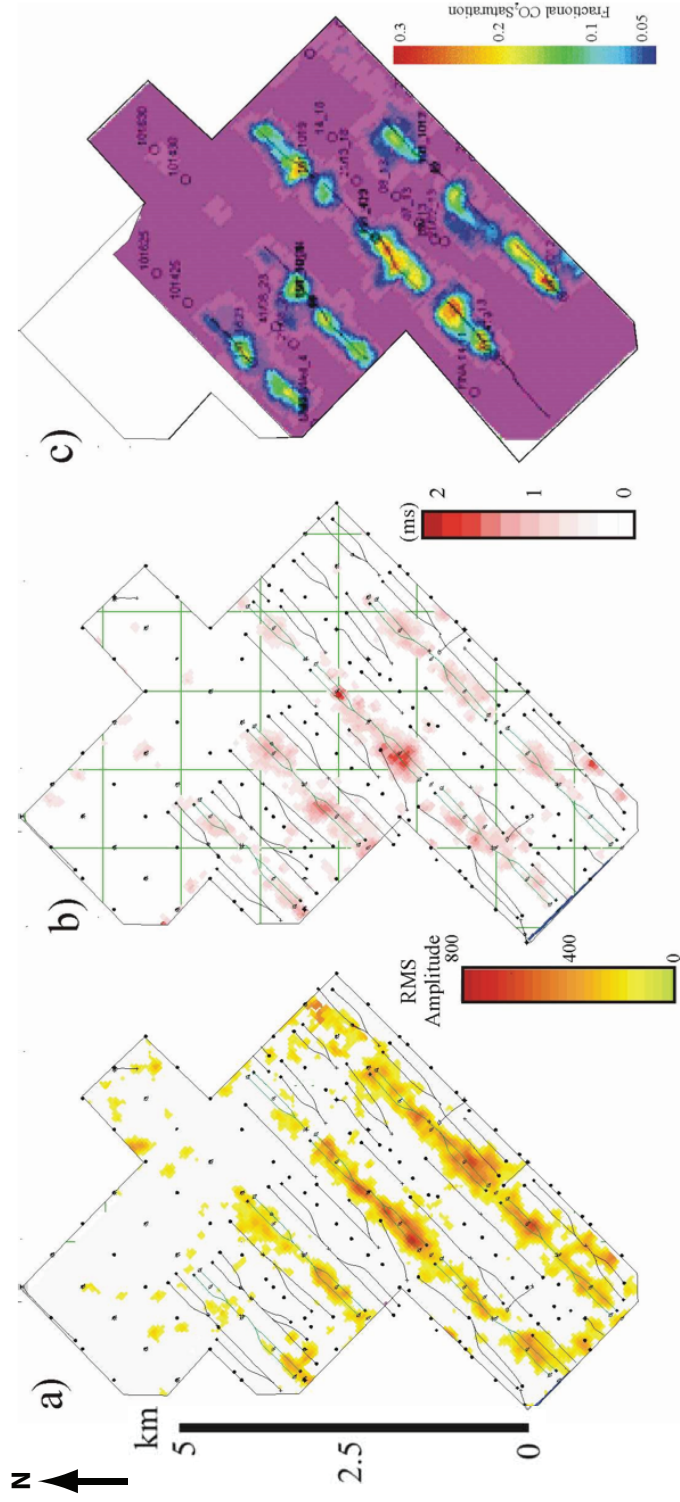


Figure 2.4: Results from the 2002 4-D controlled source seismic survey at Weyburn taken from Wilson et al. (2004). (a) shows the changes in reflection amplitude at the top of the reservoir, while (b) shows the travel time-shift through the reservoir. In (c), I show the results of a reservoir simulation for the distribution of the CO₂ plumes. The seismic survey clearly images the CO₂ plumes around the horizontal injection wells.

geochemical analysis and soil gas sampling (Wilson et al., 2004). However, microseismic monitoring was not used at this stage. The 4-D seismic monitoring has been the most successful in imaging CO₂ saturation (White, 2009), where travel time-shifts in the reservoir and reflection amplitude increases at the top of the reservoir are used to image zones of CO₂ saturation (Figure 2.4). In Phase IA the 4-D seismics show the CO₂ plumes migrating out from the horizontal injection wells.

In 2003, downhole microseismic monitoring was initiated with a new CO₂ injection site. This stage, named Phase IB and located to the southeast of Phase IA, is the only place at Weyburn so far to use microseismic monitoring. The injection, production and monitoring wells of Phase IB are shown in Figure 2.5.

2.3 Microseismic monitoring at Weyburn

Microseismic monitoring seeks to detect the seismic emissions produced by fracturing and fault reactivation around the reservoir. This technique was developed in the early 1990s, and has been used increasingly since then. The magnitudes of such events are such that they cannot usually be detected at the surface, so geophones are placed in boreholes near to the reservoir. When seismic energy is detected at the geophones, event location algorithms are used to locate the source of these emissions, indicating a point in the rock mass that has undergone brittle failure. Seismic energy can also be generated by other subsurface phenomena such as fluid motion through pipes and conduits (e.g., Balmforth et al., 2005), although these processes are not thought to be occurring at Weyburn. It is anticipated that CO₂ injection at Weyburn will alter the pore pressure and stress fields at Weyburn enough to generate failure. By tracking the event locations, the operators hope to track the regions of failure, and thereby the stress changes, and also to assess whether the fracturing presents a risk to the security of storage.

2.3.1 System setup

Phase IB has a vertical well (121/06-08) injecting CO₂ at a rate of between 50 - 250 MSCM/day (100-500 tonnes/day). To the northwest and to the southeast are horizontal producing wells (191/11-08, 192/09-06 and 191/10-08), all running NE-SW. Wells 191/11-08 and 192/09-06 were both in production before the array was installed, while well 191/10-08 was drilled in July 2005, 18 months after CO₂ injection had begun. The injection well was completed in November 2003, with water injection beginning on December 15th. CO₂ injection began on the 21st January. In August 2003 an 8-level, 3-component geophone string was installed in a disused vertical production well (101/06-08) about 50m to the east of the injection well. The sensors were sited at the depths given in Table 2.2. The top of the reservoir in this area is at a depth of 1430m. Surface orientation shots were fired on August 15th, confirming that the geophones had been installed with one component vertical, and the orientations of the horizontal components were calculated from these shots. Apart for some short periods where the system locked up, recording on this system was continuous until November 2004.

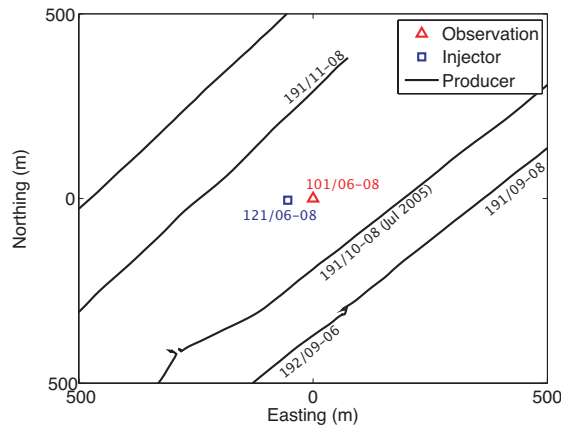


Figure 2.5: Map view of the microseismic setup at Weyburn. The vertical injection and monitoring wells are located within 50m of each other. To the NE and the SW are horizontal oil production wells. Well 191/10-08 began production in July 2005, after Phase IB but before Phase II.

<i>Sensor</i>	<i>Depth</i>	<i>Sensor</i>	<i>Depth</i>
1	1356.5m	5	1256.5m
2	1331.5m	6	1231.5m
3	1306.5m	7	1206.5m
4	1281.5m	8	1181.5m

Table 2.2: Geophone depths for Weyburn Phase IB.

In October 2005 a new recording system was connected to the installed geophones and recording was re-initiated for Phase II. Recording during Phase II has been continuous up to September 2009.

2.4 Event timing and locations

The rates of seismicity, the fluid injection rates in well 121/06-08 and periods when the geophones were not recording are plotted in Figure 2.6, which shows monthly event rates. Examples of daily event rates can be seen in Figures 2.11 and 2.12. Events are clustered temporally, as most days have no events, but sometimes as many as 7 events will occur in the space of a few hours. Although some seismicity is recorded during the initial stages of Phase II, there are no events at all for over 2 years from 2006.

2.4.1 Phase IB

In order to compute locations, a 1-D velocity model was computed using a dipole sonic velocity log from a nearby well. Event locations were provided by ESG, having been computed using P-wave particle motion for arrival azimuth and P- and S-wave ray tracing through this velocity model for

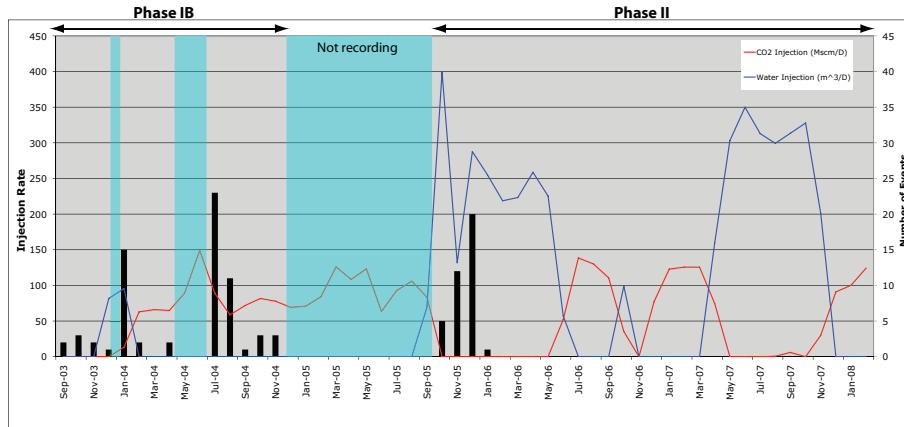


Figure 2.6: CO₂ (red) and water (blue) injection rates through well 121/06-08, as well as the rate of reliably located microseismic events (bars). The array was installed in August 2003. The periods when the geophones were not recording are marked in light blue.

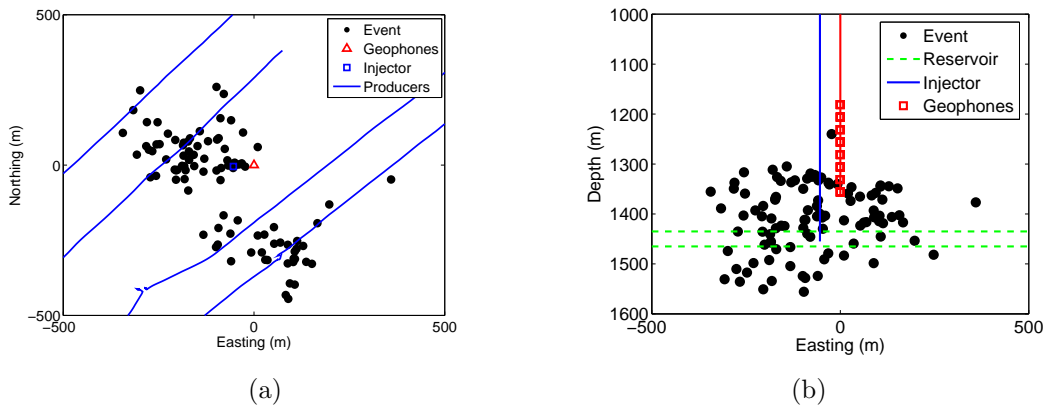


Figure 2.7: Map (a) and East-West cross-section (b) views of Phase IB events. This plot shows all events located by ESG, including completion related activity and events that I deem unreliable in Section 2.4.1. The horizontal oil production wells, the vertical injection well, the observation well, and the reservoir interval are all marked.

event depth and radial distance. The events are characterised by a low dominant frequency (15-80Hz) and poor signal-to-noise ratio. As such, the quality of event location is not good, and the errors associated with location are in some cases as large as 100m. As systematic event location errors were not provided by ESG, I am unable to plot error bars on the location plots. Furthermore, a sensitivity analysis of the velocity model, where velocities were varied by $\pm 250\text{ms}^{-1}$ resulted in location changes of up to 75m (Verdon et al., 2010c). The event locations for all events located by the ESG automated picking algorithm are shown in Figure 2.7.

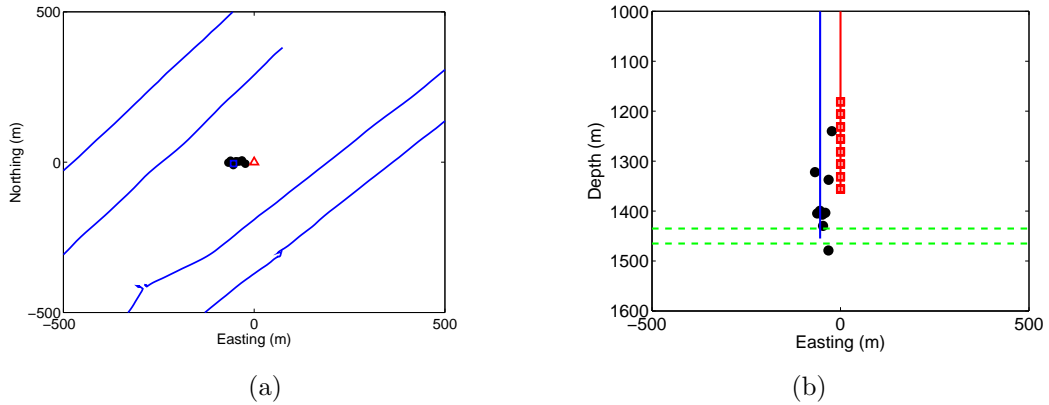


Figure 2.8: Map (a) and EW cross-section (b) views of seismic emissions detected during drilling and completion activities in injection well 121/06-08. The events are all located near the injection well, marked on (b) in blue. Wells are marked as per Figure 2.7.

<i>Month</i>	<i>No. of ESG 'events'</i>	<i>Locatable microseisms</i>	<i>Notes</i>
Aug-Sep 2003	6	2	Including 3 calibration shots
Oct 03	6	3	
Nov 03	15	2	Most of these 'events' were drilling noise and completion of the injection well
Dec 03	2	1	Recording array was shut down for 2 weeks during December 2003
Jan 04	15	15	All 15 events occur at the onset of injection
Feb 04	4	2	Two 'events' are from perforation shots in distant wells
Mar 04	15	0	These events cannot be reliably identified as microseismic events
Apr 04	2	2	
May 04			Array was not recording during May 2004
Jun 04			Array was not recording during June 2004
Jul 04	23	23	This period has an increased CO ₂ injection rate
Aug 04	11	11	
Sep 04	1	1	
Oct 04	3	3	
Nov 04	3	3	The Phase IB recording stage ended November 2004

Table 2.3: Microseismic activity rates during Phase IB. I have listed the total number of 'events' listed by ESG, some of which are produced by completion and drilling activities, or whose waveforms are not indicative of microseismic events (see Section 2.4.1). Therefore I have also listed the events that are genuine, reliably located microseismic events.

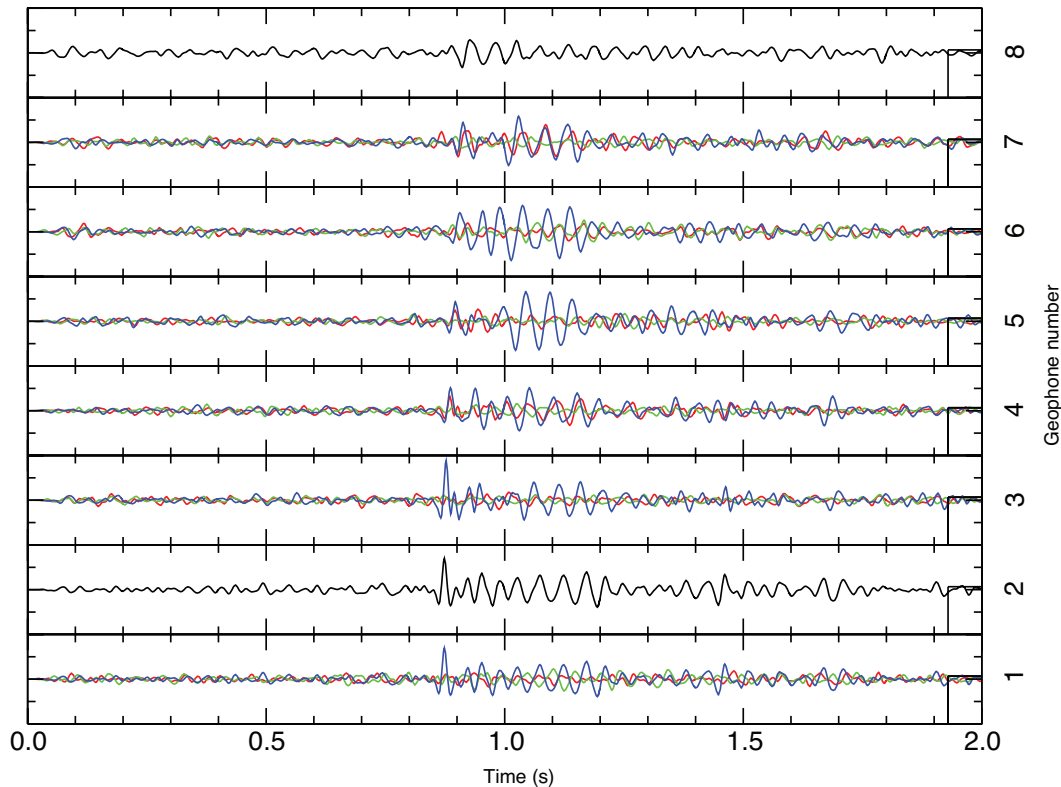


Figure 2.9: A typical ‘event’ from March 2004, recorded on all 8 geophones listed in Table 2.2, on X (red), Y (blue) and Z (green) components. Note that the maximum energy is always recorded on the Y component, regardless of the sensor orientation, which varies across the array. Hence the waves can not be reliably identified as coming from a microseismic event.

Table 2.3 lists the rates of seismic activity during Phase IB. During November 2003 much of the activity is related to drilling and completion activities that were being conducted in the injection well 121/06-08. These events are shown in Figure 2.8, and are all found to be located near the site of the injection well. As these events are not associated with deformation of the reservoir, they are discounted from the subsequent analysis.

I also note at this point the work of J-P. Deflandre (IFP Report No 58257, 2004), who has re-analysed the locations performed by ESG. He finds that some of the events identified as reliable by ESG may not correspond to microseismic activity. In particular, for the events identified during March 2004, there is no clear P-S succession, and, as Figure 2.9 shows, the maximum energy is always recorded on the Y component, regardless of sensor orientation (which varies across the array). This suggests that a vibration of the sensor array or borehole casing is the cause, and that this is not a recording of a microseismic event. What may have caused such a vibration is unclear. I regard these events as unreliable, and they are also discounted from the subsequent analysis.

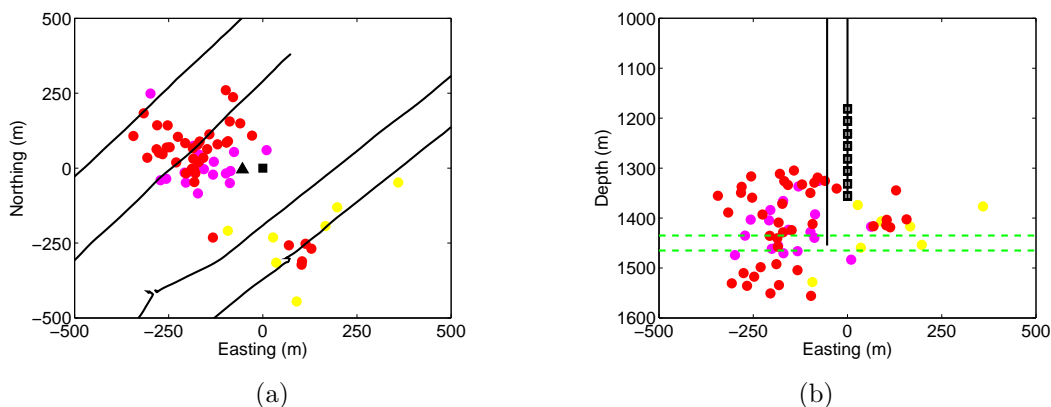


Figure 2.10: Map (a) and EW cross-section (b) views of reliably located Phase IB microseismic events. Wells are marked as per Figure 2.7. The events are colour-coded by time of occurrence: yellow = pre-injection (Aug - Dec 2003), magenta = initial injection period (Jan - Apr 2004), red = during elevated injection rate period (Jul - Nov 2004). The events are found near the producing wells to the NW and SE.

Having removed the events that are associated with drilling and completion activities, and those that cannot be reliably identifiable as microseismic events, I am left with 68 microseismic events for the period August 2003 to November 2004. This is a very low rate of seismicity in comparison to the 100s or even 1000s of events recorded per month at other producing carbonate reservoirs such as Ekofisk, Valhall (North Sea) and Yibal (Oman) (Dyer et al., 1999; Jones et al., 2010; Al-Harrasi et al., 2010). Figure 2.10 shows the locations for the remaining events that are reliably identified. The events can be divided into 2 clusters, one to the northwest of the injection well towards production well 191/11-08, and one to the southeast of the injection well, around production well 192/09-06.

The first cluster of events is located to the southeast of the injection well, around the horizontal production well 192/09-06. These events are all located in and just above the reservoir. These events occur throughout the monitoring period, including the period before injection. Comparison with production data for well 192/09-06 (Figure 2.11) indicates that the timing of the events correlates with periods where production is temporarily stopped. It is likely that these events are being generated by pressure increases around the well that result from the temporary cessation of pumping. Therefore these events are probably not directly related to CO₂ injection.

The second cluster of events is located between the injection well and the horizontal production well 191/11-08 to the NW. The first of these events occur on January 21st, coincident with the initiation of CO₂ injection. Microseismicity occurs at the onset of injection, and also appears to be correlated with periods of increased injection (Figure 2.12), although unfortunately the recording system was locked out during the period with maximum injection rate. The event locations mark a cloud of microseismicity which centres on the production well. Some events are located between the production and injection wells, while some events are located to the NW of the production well.

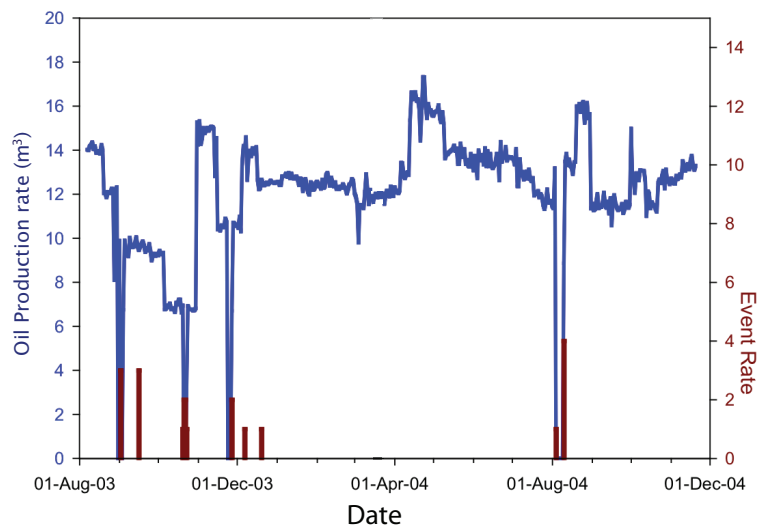


Figure 2.11: Comparison of production rates from well 192/09-06 with the rate of microseismicity in the nearby SE cluster. Microseismic activity occurs when production is temporarily stopped. Based on *Weyburn Microseismic Progress Report, ESG, Canada, April 2004*.

The majority of events are located above the reservoir, although some events are located within the reservoir interval, and some are located below it.

A histogram of event depths during Phase IB is plotted in Figure 2.13. Many events appear to be located above the reservoir. Although the large depth errors mean that some of these could actually be located within the reservoir interval, it is clear that at least some activity must be occurring in the overburden. This is an interesting observation, and without geomechanical modelling it is not clear whether this could represent fluid migration or merely stress transfer into the overburden.

The event magnitudes are plotted in Figure 2.14 as a function of distance. Event magnitudes range between -3 to -1. Event magnitudes of -2 are still detectable even at a distance of over 400m. Small events are still detectable at large distances, which suggests that the small number of events recorded is not an artifact of high noise levels. Figure 2.14 suggests that surface arrays would have limited use for microseismic monitoring under these conditions. The largest events recorded have magnitudes less than -1.0, and many are smaller than -2.0. Dense surface arrays would be required to detect such events, and their detectability would be strongly influenced by surface noise and the nature of event focal mechanisms.

2.4.2 Phase II

Recording for Phase II runs from October 2005 to the present. Although there are data recorded on the geophones, the majority of these represent near surface noise or electrical spikes. Only 39 have been reliably identified as microseismic events, occurring in two temporal clusters, with 18 events at the end of October 2005 and 21 in mid-January 2006. The Phase II events were located by ESG

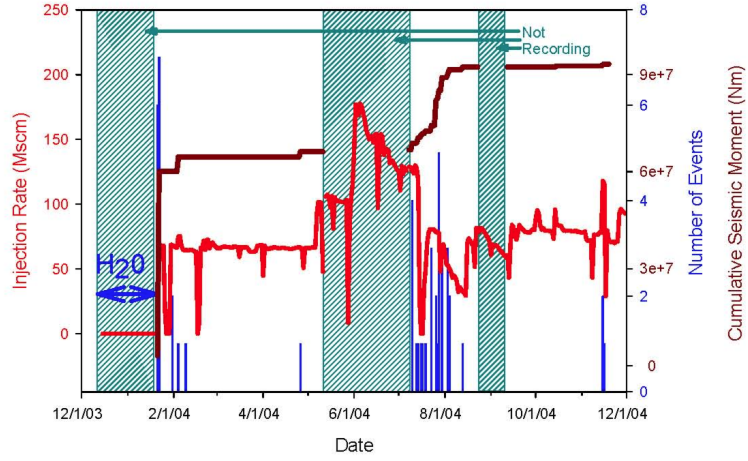


Figure 2.12: Comparison of CO₂ injection rate with microseismicity rate in the nearby NW cluster. Based on Verdon et al. (2010c).

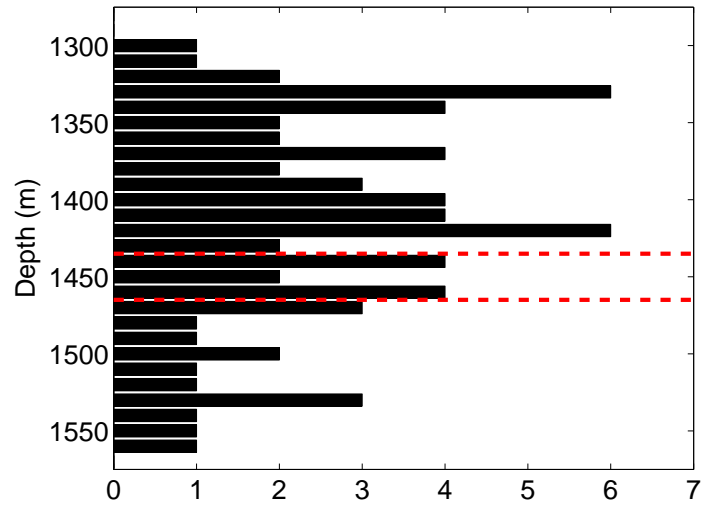


Figure 2.13: Histogram of event depths for reliably located microseismic events detected during Phase IB. The reservoir interval is marked. Many events are located above the reservoir.

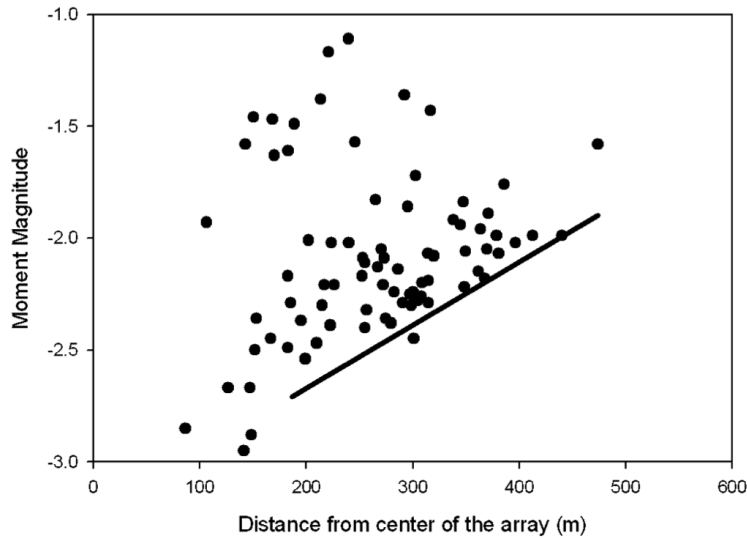


Figure 2.14: Event magnitudes at Weyburn plotted as a function of distance from the array. Based on Verdon et al. (2010c). The line marks the limit of detectability as a function of distance from the array.

using the same method and velocity model as described for Phase IB above. The event locations as computed by ESG are plotted in Figure 2.15.

The October 2005 events are located close to the observation well at a range of depths, from 900 to 1500m, but usually above reservoir depth. The mechanism causing these events is as yet unidentified. The majority of the January events cluster to the southeast of the observation well at reservoir depths. The field operator has attributed these events to completion activities in a nearby borehole. As such, only the 18 October 2005 events are microseisms, and of these only a minority occur in or close to the reservoir. Over 3 years of recording this represents a remarkably low rate of seismicity, continuing the trend already noted in Phase IB. Gaining an understanding of why activity is so low may well be more informative than the locations of the few events that are available.

2.5 Discussion

The temporal clustering of microseismic events is episodic (Figure 2.6), which raises the question of what causes these discrete episodes of localised deformation. If the events with a low dominant frequency are interpreted as fluid movement, why are they seen only occasionally when fluid movement is occurring continuously? Focal mechanism analysis can provide information here. For example fluid movement would perhaps generate non-double-couple mechanisms. Double-couple mechanisms describe rock failure in a pure shear mode, where there is no volume change during failure. Where volume change occurs, perhaps induced by fluid filling a new fracture and propping it open, then the focal mechanism would indicate not only shear failure but volume increase as well. Focal mechanism

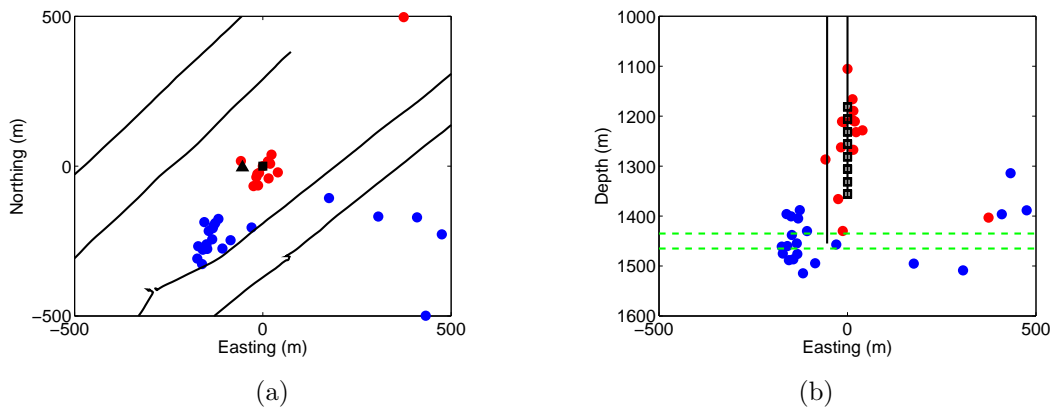


Figure 2.15: Map view (a) and EW cross section (b) of microseismic events recorded during Phase II. Events are broken up into two clusters occurring in October 2005 (red) and January 2006 (blue). The majority of the January 2006 events are located within one cluster to the SE. Wells are marked as per Figure 2.7.

analysis could also image the triaxial stress tensor in the reservoir. This would provide important information for guiding injection strategies and groundtruthing geomechanical models. However, focal mechanism analysis cannot be done with a single well array as at Weyburn.

Another important point is whether or not microseismicity above the reservoir indicates top-seal failure and the migration of CO_2 into the overburden. Stress arching effects, where loading of the reservoir transfers stress into the overburden, can also lead to failure in the overburden and sideburden, without any fluid leaving the reservoir. To determine whether or not deformation results in increased fault permeability it is necessary to consider the rheology of the rock with respect to the stresses at the time of faulting. This underscores the importance of having a good understanding of the potential geomechanical behaviour of the storage site - it is likely that fluid migration or a pore-pressure connection into the overburden will be documented by a different spatial and temporal pattern in seismicity from those associated with stress arching effects.

A key question is should CCS operations always/sometimes/never employ microseismic monitoring, and how should this decision be made? Downhole monitoring is now a commonly used tool for monitoring hydraulic fracture stimulation. It presents a low cost option for long term CCS monitoring. Ideally, such monitoring would record little seismicity, suggesting that the CO_2 plume moves aseismically through the reservoir, inducing no significant rock failure, as seems to be the case at Weyburn. In total, over the entire Phase IB and Phase II microseismic monitoring experiment, only 86 reliably identifiable microseismic events were recorded in 5 years. However, the lack of data has meant that the microseismic monitoring at Weyburn has provided little information about the reservoir stress state and injection induced pressure fronts. Microseismic monitoring can be viewed as an early warning system, where large swarms of events in unexpected locations could be used to indicate that there is a risk of leakage. Paradoxically then, we should be placing geophones in the ground in the hope

that they detect nothing. Other monitoring techniques deployed at Weyburn, such as soil gas flux monitoring and shallow aquifer sampling, are similar in the way that detection of nothing represents a success.

Should the lack of microseismicity seen at Weyburn always be expected for CO₂ injection scenarios? It has been suggested that, as it has a lower compressibility, CO₂ will have an inherently lower seismic deformation efficiency than other common injection fluids such as water. Seismic deformation efficiency describes the ratio between the energy used in pumping a fluid into the formation and the total seismic energy recorded on the geophones (e.g., Maxwell et al., 2008). If this is the case, then microseismic monitoring is less likely to be useful for CCS activities. Alternatively, there may be geomechanical explanations for the lack of microseismic activity at Weyburn. In the following chapter I will discuss shear wave splitting measurements made on the Weyburn microseismic data, developing a novel approach to invert splitting measurements for fracture properties. I will then switch my focus from the microseismic data and instead seek to explain the lack of it. To do this I will consider another microseismic dataset from a different CO₂ injection site, and construct representative geomechanical models that approximate the Weyburn reservoir.

2.6 Summary

- CO₂ storage and enhanced oil recovery has been ongoing at Weyburn since 2000. A downhole geophone array was installed in 2003 to monitor microseismicity in one pattern.
- The array has detected microseismicity, and events have been located by ESG using automated location algorithms.
- I have manually sorted the events between those that can be reliably identified as microseismic events, those that are due to operator activities (perf-shots, drilling, etc.), and have discarded those that where a clear P- and S-wave succession cannot be identified.
- 86 microseismic events have been located over 5 years of monitoring. This represents a low rate of microseismicity relative to many producing carbonate fields.
- Events during Phase IB can be divided into in 2 clusters, near the production wells to the NW and SE. Rates of seismicity can be correlated with activities in these wells.
- Although depth errors are large, events do appear to be located in the overburden. Without geomechanical modelling it is not clear whether this represents fluid migration from the reservoir, or merely failure induced by stress transfer into the overburden.
- The low rates of microseismicity, combined with only one array, means that it has not been possible to image the triaxial stress state in the reservoir, nor to track pressure or fluid migration fronts.

Images / split the truth / in fractions.

Denise Levertov

3.1 Introduction

Seismic anisotropy refers to the situation where the velocity of a seismic wave is dependent on its direction of propagation and/or polarisation. Seismic anisotropy in sedimentary rocks can have many causes, which act at many length-scales. These mechanisms include mineral alignment (e.g., Valcke et al., 2006), alignment of grain-scale fabrics (e.g., Hall et al., 2008), which can be distorted by non-hydrostatic stresses (e.g., Zatsepin and Crampin, 1997; Verdon et al., 2008), larger scale sedimentary layering (e.g., Backus, 1962) and the presence of aligned fracture sets (e.g., Hudson, 1981). In hydrocarbon settings, the most common anisotropic mechanisms are horizontally aligned sedimentary layers, and horizontally aligned mineral and grain-scale fabrics. Such an anisotropic system will have a vertical axis of symmetry, and is referred to as Vertical Transverse Isotropy (VTI). A second source of anisotropy is often introduced with vertically aligned fracture sets. Such an anisotropic system will have a horizontal axis of symmetry, and is referred to as Horizontal Transverse Isotropy (HTI). The combination of such VTI and HTI mechanisms leads to anisotropic systems with orthorhombic or lower symmetry systems. The presence of fractures has a significant impact on permeability and fracture alignment leads to anisotropic permeability. The detection of seismic anisotropy has the potential to image aligned fracture sets, and so can be a useful tool to help guide CCS injection strategies.

Shear wave splitting (SWS) is probably the least ambiguous indicator of seismic anisotropy. As a shear wave enters an anisotropic region it is split into two orthogonally polarised waves, one of which will travel faster than the other. The polarisation of the fast wave (ψ), and the time-lag (δt) between the arrival of the fast and slow waves, characterises the splitting along a raypath. The splitting along many raypaths characterises the overall anisotropy symmetry system. Usually, δt is normalised by the path length to give the percentage difference in S-wave velocities, δV_S .

SWS is used as a matter of course in global seismological studies (e.g., Kendall et al., 2006) to identify such features as fractures (e.g., Crampin, 1991; Boness and Zoback, 2006), melt inclusion alignment (e.g., Blackman and Kendall, 1997; Kendall et al., 2005), alignment of crystals caused by mantle flow (e.g., Blackman et al., 1993; Rumpker et al., 1999; Barruol and Hoffmann, 1999), and the nature of the Earth's solid inner core (Wookey and Helffrich, 2008). SWS has even been suggested as a tool for predicting the occurrence of earthquakes (Crampin et al., 2008). Despite these successes, SWS is rarely used to detect seismic anisotropy in reservoir settings.

In hydrocarbon settings, the shear waves used to measure SWS can come from two very different sources: the first being controlled source multicomponent reflection seismics, the second being mi-

cross-seismic events in and around the reservoir caused by stress changes and recorded on geophones located in boreholes. In reflection surveys seismic waves travel subvertically. When interpreting the splitting in such situations, ψ is assumed to represent the orientation of a fracture set, with increasing δV_S representing an increase in fracturing. However, this method of interpretation is limited in its validity to situations where the shear waves have propagated subvertically. This is rarely the case when measuring SWS from microseismic events recorded on downhole geophones. Interpretation of SWS then becomes far less intuitive (Verdon et al., 2009).

From both rock physics theory and observation (see Crampin and Peacock, 2008, for a review) it is known that ψ and δV_S are highly dependent on the direction of ray propagation with respect to a fracture set. Additionally, other subsurface structures such as sedimentary fabrics can contribute to the overall anisotropy. I argue that any interpretation of SWS from non-vertically propagating shear waves must be guided by elastic models that consider the range of plausible anisotropy mechanisms in a reservoir setting.

In this chapter, I outline an inversion approach that selects the best fit fracture geometries and sedimentary fabrics to match SWS observations using rock physics modelling. Previous attempts to invert splitting measurements include Horne and MacBeth (1994), Teanby et al. (2004a) and Rial et al. (2005). I note that synthetic tests can provide insight into any inversion technique. The checkerboard test used in seismic velocity tomography is probably the best example of this. Synthetic tests constrain what can and cannot be imaged given the real data available, and can highlight which parameters are the most significant. By developing synthetic examples for the inversion technique I show that the success of a SWS inversion is highly dependent on the range of arrival azimuths and inclinations that are available. It is possible, using such techniques, to determine in advance which structures are detectable with SWS, and which are not. It is also possible to identify potential trade-offs between parameters that can affect the accuracy of such inversions. This will be useful not only in assessing the reliability of SWS interpretations, but also potentially in advance when selecting geophone locations for microseismic monitoring in order to maximise what can be imaged using SWS.

Having demonstrated the inversion technique, I use the semi-automated splitting algorithm of Teanby et al. (2004b) to measure the SWS that has taken place at Weyburn. I invert these measurements to image the fracture sets in the Weyburn reservoir. As the Weyburn reservoir is a low-permeability carbonate system, these fractures are crucial in controlling the flow of injected CO_2 . Therefore, their detection using SWS measurements on microseismic events demonstrates the usefulness of microseismic monitoring in CCS scenarios.

3.2 Inversion method

3.2.1 Model building using rock physics

In order to model SWS caused by fractures and sedimentary fabrics, I need to construct realistic rock physics models. As I wish to model splitting of S-waves travelling in any direction, I must have a model that computes the full $3 \times 3 \times 3 \times 3$ stiffness tensor \mathbf{C} (or its inverse, compliance $\mathbf{S} = \mathbf{C}^{-1}$). I use

the additional compliance approach of Schoenberg and Sayers (1995), where the compliance of the fractures, $\Delta\mathbf{S}$, is added to the rock frame compliance, \mathbf{S}^r , to give the overall compliance,

$$\mathbf{S} = \mathbf{S}^r + \Delta\mathbf{S}. \quad (3.1)$$

Symmetry arguments reduce the number of independent terms in the $3 \times 3 \times 3 \times 3$ stiffness tensor from 81 to 21 components. To simplify notation, the Voigt system can be used to contract \mathbf{C} into a 6×6 matrix, where the i, j and k, l subscripts of the $3 \times 3 \times 3 \times 3$ tensor are mapped to m and n following the convention

$$\begin{array}{c|cccccc} ij \text{ or } kl & 11 & 22 & 33 & 23 = 32 & 13 = 31 & 12 = 21 \\ \downarrow & \downarrow & \downarrow & \downarrow & \downarrow & \downarrow & \downarrow \\ m \text{ or } n & 1 & 2 & 3 & 4 & 5 & 6 \end{array} \quad (3.2)$$

The rock frame compliance \mathbf{S}^r can be anisotropic if horizontal layering is present. Based on previous estimates of sedimentary fabric anisotropy in siliclastic rocks (Kendall et al., 2007) I consider the rock fabric to have VTI symmetry. For such a system, the frame compliance tensor (in Voigt notation) is given by

$$\mathbf{S}^r = \begin{pmatrix} C_{11}^r & (C_{11}^r - 2C_{66}^r) & C_{13}^r & 0 & 0 & 0 \\ (C_{11}^r - 2C_{66}^r) & C_{11}^r & C_{13}^r & 0 & 0 & 0 \\ C_{13}^r & C_{13}^r & C_{33}^r & 0 & 0 & 0 \\ 0 & 0 & 0 & C_{44}^r & 0 & 0 \\ 0 & 0 & 0 & 0 & C_{44}^r & 0 \\ 0 & 0 & 0 & 0 & 0 & C_{66}^r \end{pmatrix}^{-1}. \quad (3.3)$$

The strength of the shear wave anisotropy caused by the VTI system is given by Thomsen's (1986) γ and δ parameters, defined as

$$\gamma = \frac{C_{66}^r - C_{44}^r}{2C_{44}^r} \quad (3.4)$$

and

$$\delta = \frac{(C_{13}^r + C_{44}^r)^2 - (C_{33}^r - C_{44}^r)^2}{2C_{33}^r(C_{33}^r - C_{44}^r)}. \quad (3.5)$$

The additional compliance introduced by a set of vertical, aligned fractures in a VTI medium with normals parallel to the x_1 axis ($\mathbf{n} = [1, 0, 0]$) is given by Grechka (2007) as

$$\Delta\mathbf{S} = \begin{pmatrix} B_N & 0 & 0 & 0 & 0 & 0 \\ 0 & 0 & 0 & 0 & 0 & 0 \\ 0 & 0 & 0 & 0 & 0 & 0 \\ 0 & 0 & 0 & 0 & 0 & 0 \\ 0 & 0 & 0 & 0 & B_{Tv} & 0 \\ 0 & 0 & 0 & 0 & 0 & B_{Th} \end{pmatrix}. \quad (3.6)$$

B_N is the normal compliance of the fracture, and B_{Th} and B_{Tv} are the shear compliances in the vertical and horizontal planes. Having computed the stiffness tensor for fractures aligned in the $x_2:x_3$ plane I rotate this tensor to give the stiffness tensor for fractures with the desired strike. B_{Th} and

B_{Tv} will only differ when significant VTI anisotropy is present. Furthermore, I believe that they will only differ when the mechanism causing VTI anisotropy acts at a smaller length-scale than the vertical fractures (e.g., horizontally aligned anisotropic minerals). If the VTI anisotropy is induced by horizontally aligned fractures or by larger scale sedimentary layers (e.g., Backus, 1962) then it is not clear that B_{Th} and B_{Tv} should be allowed to differ.

It is possible to calculate the fracture normal and tangential compliance as a function of fracture density, aspect ratio and fill by assuming an idealised fracture geometry (e.g., penny-shaped or elliptical). Several such methods are available in the literature (e.g., Hudson, 1981; Hudson et al., 1996), and well summarised by Hall and Kendall (2000).

Fractures and fluids

A key difference between fracture models in the literature is how they treat the fluids that fill the fractures. Reservoirs will be saturated with gas, brine or oil (or a multiphase mixture), and these fluids will also saturate the fractures. The presence of fluid in a fracture will have a significant effect on the fracture compliance, and hence the overall rock stiffness tensor.

The compliance of a flat, low aspect ratio crack will be far greater than a spherical pore. As a result, the incidence of a pressure wave will compress a fracture far more than a pore, leading to non-uniform compression of the saturating fluid and the development of pressure gradients between fluids in the pores and fractures. The fluid will attempt to flow to equalise these gradients, however it will be restricted by the permeability of the rock matrix and its own viscosity. The extent to which this pressure gradient equalisation can occur is crucial for determining the fracture compliance. This phenomenon is known as squirt-flow, and can be best demonstrated by considering an idealised system of aligned penny-shaped fractures that can either be fully connected to a system of spherical pores, partially connected to them, or totally isolated from the porosity (Figure 3.1).

Isolated fractures

Early effective medium models such as Hudson (1981) and Tandon and Weng (1984) consider there to be no fluid connection between fractures. An incident P-wave travelling normal to the fracture faces must compress both the fracture faces and the fluid within it. Because the fluid has some stiffness the overall compliance of the fracture is decreased. The normal and tangential compliance, B_N and B_T , of a set of isolated, fluid-filled fractures is given by Hudson (1981) as

$$\begin{aligned} B_N &= \frac{4}{3} \left(\frac{\xi}{\mu^r} \right) \left(\frac{\lambda^r + 2\mu^r}{\lambda^r + \mu^r} \right) \frac{1}{1 + K}, \\ B_T &= \frac{16}{3} \left(\frac{\xi}{\mu^r} \right) \left(\frac{\lambda^r + 2\mu^r}{3\lambda^r + 4\mu^r} \right) \frac{1}{1 + M}, \end{aligned} \quad (3.7)$$

where

$$\begin{aligned} K &= \frac{K_{fl} (\lambda^r + 2\mu^r)}{\pi a \mu^r (\lambda^r + \mu^r)}, \\ M &= \frac{4\mu_{fl} (\lambda^r + 2\mu^r)}{\pi a \mu^r (3\lambda^r + 4\mu^r)}. \end{aligned} \quad (3.8)$$

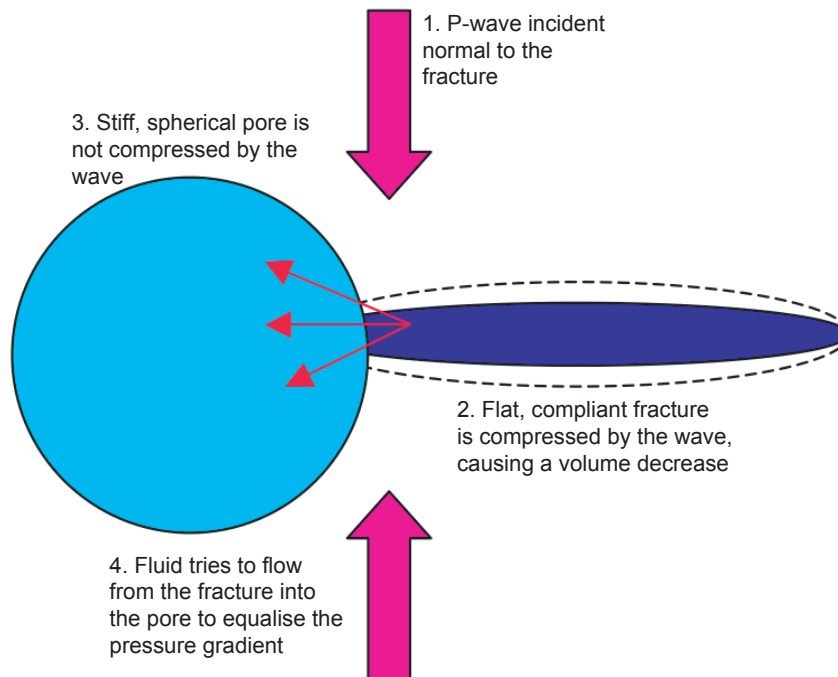


Figure 3.1: Schematic cartoon showing how squirt-flow occurs in fractured rocks. As a compressive wave travels through this system, the volume change of the compliant fracture is larger than that of the stiff pore. As a result, fluid will try to flow from the fracture into the pore-space. The extent to which this can occur will control the effective compliance of the fracture, and is determined by the permeability of the rock and the viscosity of the fluid.

λ^r and μ^r are the Lamé parameters of the rock matrix along the axis of deformation in question (i.e., when computing B_N and B_{Th} , $\mu^r = C_{66}^r$ and $\lambda^r + 2\mu^r = C_{11}^r$, but when computing B_{Tv} , $\mu^r = C_{44}^r$ and $\lambda^r + 2\mu^r = C_{33}^r$). K_{fl} and μ_{fl} are the bulk and shear moduli of the fluid (usually, $\mu_{fl} = 0$), and ξ and a are the scalar density and average aspect ratio of the fracture set. The fracture density is a non-dimensional term given by the number of fractures in a volume and their average radius, $\xi = Nr^3/V$.

For the assumption of isolated fractures made by Hudson (1981) to be valid, either the pore space and fractures must be hydraulically isolated (this is unrealistic for reservoir rocks), or the frequency of the propagating wave must be high enough that there is no time for the pressure gradient to be equalised. Thus, theories which consider fractures to be hydraulically isolated must be considered as applicable only at high (generally ultrasonic) frequencies (though without violating the condition that wavelength is much larger than inclusion size) or where the fluid bulk modulus is ~ 0 . If fluid flow between fractures can occur, this theory becomes inaccurate. This inaccuracy has been demonstrated in experimental tests by Rathore et al. (1994).

Fully connected fractures

An alternative approach is to consider the low frequency limit (Hudson et al., 2001). In this limit, there will be enough time for the pressure gradient to be completely equalised between fractures and pores. In this limit I treat the fractures as being drained. The widely known formulations of Gassmann (1951) can then be used to compute the effects of fluid saturation on the overall system. The Gassmann equations have been generalised for anisotropic rocks by Brown and Korrington (1975), who find that the fluid saturated compliance is given by

$$S_{ijkl}^{sat} = S_{ijkl}^d - \frac{(S_{ij\alpha\alpha}^d - S_{ij\alpha\alpha}^m)(S_{kl\alpha\alpha}^d - S_{kl\alpha\alpha}^m)}{\left(\frac{1}{K^d} - \frac{1}{K^m}\right) + \Phi\left(\frac{1}{K_{fl}} - \frac{1}{K^m}\right)} \quad (3.9)$$

where S_{ijkl}^m and K^m are the compliance tensor (in uncontracted $3 \times 3 \times 3 \times 3$ form) and bulk modulus of the minerals making up the rock, S_{ijkl}^d and K^d are the compliance tensor and bulk modulus of the dry rock frame, and Φ is the porosity.

Restricted fluid flow

I have now described the two endmembers, high and low frequency, that correspond to a fully connected pore space and an isolated pore space. To model between the low and high frequency endmembers then frequency dependence must be factored into the calculations. Hudson et al. (1996) present an extension to the Hudson (1981) model which can account for flow between fractures and equant porosity. As discussed previously, fluid flow will affect the normal compliance of the fracture, so a correction is made to the Hudson (1981) term for B_N , such that K is now

$$K = \frac{K_{fl}}{\pi a \mu^r} \frac{(\lambda^r + 2\mu^r)}{(\lambda^r + \mu^r)} \frac{1}{1 + (3(1-i)J/2c)} \quad (3.10)$$

where

$$J^2 = \frac{K_{fl}\Phi\kappa}{2\eta\omega}. \quad (3.11)$$

κ is the permeability of the rock, η is fluid viscosity, ω is the frequency of the incident wave, and c is the average fracture aperture. Note that, because strain parallel to a fracture does not cause a volume change, the tangential compliance of the fracture is not affected by fluid flow, and does not need to be modified.

K can now be considered in terms of two parameters, a fluid incompressibility factor P_i and an equant porosity factor P_{ep} (Pointer et al., 2000), such that

$$K = \left(\frac{P_i}{\pi} \frac{\lambda^r + 2\mu^r}{\lambda^r + \mu^r}\right) \left(1 + \frac{3(1-i)}{2\sqrt{P_{ep}}}\right)^{-1} \quad (3.12)$$

where

$$\begin{aligned} P_i &= \frac{1}{a} \frac{K_{fl}}{\mu^r}, \\ P_{ep} = \left(\frac{c}{J}\right)^2 &= \frac{2\omega\eta_{fl}}{\Phi K_{fl}\kappa} c^2. \end{aligned} \quad (3.13)$$

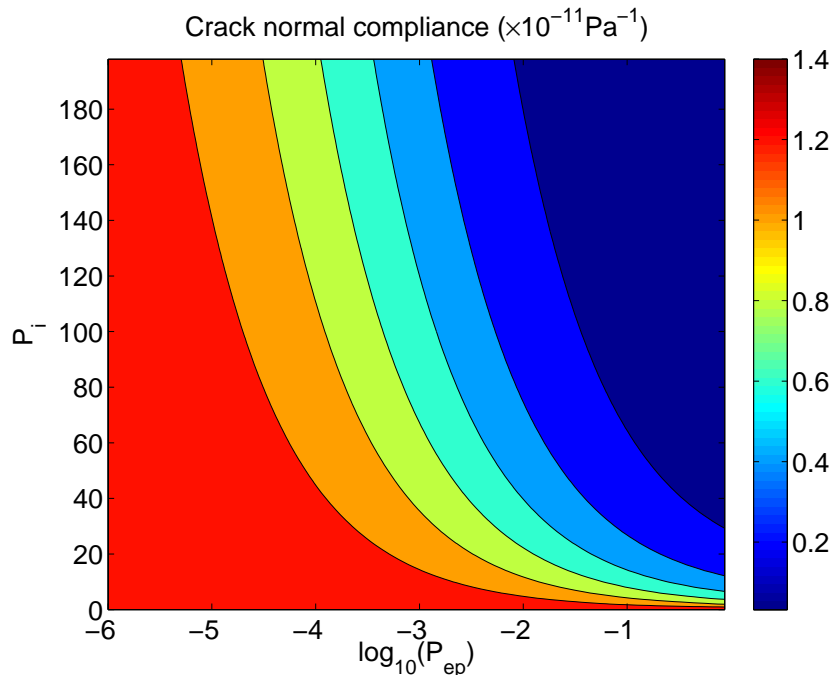


Figure 3.2: Fracture normal compliance B_N for a set of aligned fractures connected by equant porosity, given as a function of P_i and P_{ep} , computed using equations 3.7, 3.8, 3.12 and 3.13. The high and low frequency endmembers for this system have compliances $3.2 \times 10^{-13} \text{Pa}^{-1}$ and $1.4 \times 10^{-11} \text{Pa}^{-1}$ respectively, corresponding to the extremes of the contours.

The effects of P_i and P_{ep} on fracture normal compliance B_N are shown in Figure 3.2. The invariant parameters used to compute this plot are $\mu^r = 16 \text{GPa}$, $\lambda^r = 8 \text{GPa}$, and a fracture density of 0.1. The main control on P_i is the fluid bulk modulus K_{fl} . When $P_i \rightarrow 0$, the fluid has insufficient stiffness to have any effect on fracture compliance, regardless of whether flow can occur or not. Hence the compliance is always equivalent to the low frequency case, with a large compliance. Where fluid has significant stiffness ($P_i \neq 0$), whether or not fluid can flow (given by P_{ep}) becomes significant. Where P_{ep} is low (corresponding to low frequency or high permeability), $K \rightarrow 0$ and B_N is equivalent to that of the ‘Gassmann’ endmember, where fluids can flow and pressure is equalised throughout the pore space, leading to a larger compliance. Where P_{ep} is high (corresponding to high frequency or low permeability), $J \rightarrow 0$ and B_N is equivalent to that given by Hudson (1981), where the fractures are isolated and no fluid flow can occur, leading to a very low compliance.

Experimental testing of fluid flow models

In order to test these models empirically, *a priori* knowledge of the fracture geometry is required. However, in naturally occurring rocks, these parameters are generally unknown (usually, we wish to determine them using an effective medium theory). Rathore et al. (1994) constructed a synthetic rock using a mixture of sand and epoxy, in which were embedded numerous metal discs with common ge-

<i>Parameter</i>	<i>Value</i>
Frequency (ω)	100kHz
Fluid viscosity (η)	1×10^{-3} Pa.s
Fracture aperture (c)	2×10^{-5} m
Fracture aspect ratio (a)	0.0036
Fracture density (ξ)	0.1
Porosity (ϕ)	0.3460
Fluid bulk modulus (K_{fl})	2.16GPa
Rock shear modulus (μ^r)	12.7GPa
Rock bulk modulus (K^r)	16.6GPa
P_i	50
P_{ep}	3×10^{-4}

Table 3.1: Physical properties of the synthetic fractured rock created by Rathore et al. (1994), used to test the influence of fractures on ultrasonic velocities.

ometry and orientation. These were subsequently dissolved from the matrix using a chemical leachate, leaving the resultant voids to represent a network of fractures whose geometries were known *a priori*. The seismic velocities of these samples were then measured in the lab at ultrasonic frequencies when both dry and water saturated. Their results provide a benchmark against which the above models can be tested.

Table 3.1 lists the relevant parameters for the brine saturated synthetic sandstone constructed by Rathore et al. (1994). Rathore et al. did not compute κ , so I use the estimate given by Hudson et al. (2001) as $\kappa = 300mD$. Using these values, $P_{ep} \approx 3 \times 10^{-4}$ and $P_i \approx 50$. Therefore I expect fluid flow to occur and pressure gradients to be fully equalised. As a result, Hudson’s (1981) model, which assumes that fractures are hydraulically isolated, will not be appropriate. Figure 3.3 shows Rathore et al. (1994)’s experimental results along with the modelled values for P- and S-wave velocity assuming isolated fractures in (a) and using frequency dependence in (b). I note in Figure 3.3(a) the P-wave velocity from the experimental results does not match the predictions from Hudson’s 1981 isolated fracture model, of a $\cos(4\zeta)$ periodicity, where ζ is the incidence angle between the aligned fracture faces and the ultrasonic waves. In contrast, Figure 3.3(b) compares experimental velocities with those predicted from Hudson’s 1996 fluid exchange model, which does account for frequency-dependent flow. It is clear that the fit is far superior, with a $\cos(2\zeta)$ periodicity. This testing demonstrates the sensitivity of rock physics modelling to the extent of fluid flow, and highlights the need when interpreting data for awareness of the likely extent of fluid flow through estimation of P_i and P_{ep} and use of an appropriate model.

For seismic waves passing through reservoir rocks, ω is small ($10 < \omega < 250$) and κ is likely to be high. Table 3.2 shows values for the relevant parameters for a generic reservoir example with CO₂ and brine filled fractures, and the resultant values of P_{ep} . It can be seen that P_{ep} for both cases

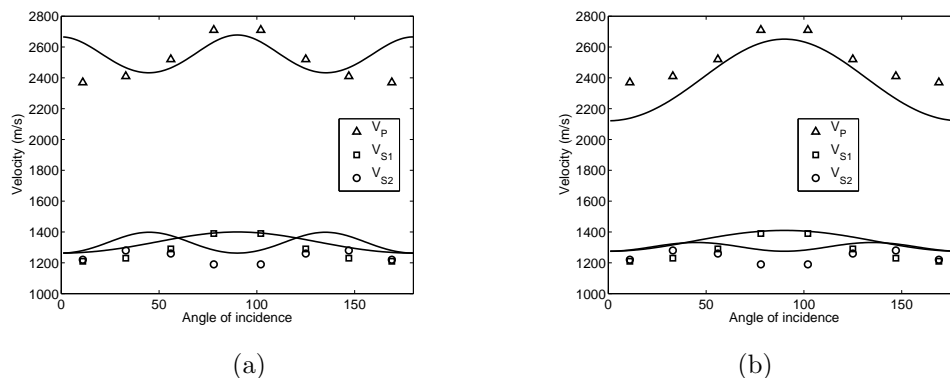


Figure 3.3: Experimental observations (symbols) from Rathore et al. (1994) for ultrasonic P- and S-wave velocities as a function of incidence angle with a synthetic aligned fracture set, and theoretical predictions (lines) from: (a) Hudson (1981), where fractures are isolated and (b) Hudson et al. (1996), where fluid can flow between fractures and equant porosity. The 1996 model (b) produces far more representative results.

is low, meaning that the fracture normal compliance can be reasonably approximated by using the low frequency endmember case. This is important because fracture compliance will be independent of fluid compressibility. As a result, SWS orientations and magnitudes will be independent of the fluid present in the fractures. For the subsequent models, I use the low frequency approximations to Hudson et al. (1996) given by Pointer et al. (2000), where the fracture compliance is a function only of fracture density (ξ) and fracture strike (α). Along with the strength of the VTI fabric given by γ and δ , these are the 4 free parameters that I use to invert SWS measurements. Effectively, I derive an orthorhombic symmetry, and it is worth noting that *a priori* knowledge of the exact cause of the anisotropy is not required. For example, the VTI component could be caused by fractures, minerals or microcracks, all of which can show a horizontal preferred alignment.

3.2.2 Inversion for rock physics properties

In order to find the best fit rock physics model, I perform a grid search over the free parameters (ξ , α , γ and δ), computing the elastic stiffness tensor in each case. Using ray theory the slowness surface, and hence the speeds and polarisations for propagation in any direction of all three body waves (P, fast and slow S), can be computed by solving the Christoffel equation,

$$(C_{ijkl}p_j p_k - \rho \delta_{il})g_l = 0, \quad (3.14)$$

where p_i is the i -th component of slowness, g_l is the l -th component of polarisation, and ρ is the rock density. A non-trivial solution for the polarisation g_l requires

$$\det |a_{ijkl}n_j n_k - v_n^2 \delta_{il}| = 0, \quad (3.15)$$

<i>Parameter</i>	<i>Brine</i>	<i>CO₂</i>
Frequency (ω)	100Hz	100Hz
Fluid viscosity (η)	1×10^{-3} Pa.s	1×10^{-4} Pa.s
Fracture aperture (c)	5×10^{-4} m	5×10^{-4} m
Fracture aspect ratio (a)	0.0005	0.0005
Porosity (ϕ)	0.2	0.2
Fluid bulk modulus (K_{fl})	3GPa	0.1GPa
Permeability (κ)	50mD	50mD
Rock shear modulus (μ^r)	12GPa	12GPa
P_i	500	16.7
P_{ep}	1.6×10^{-6}	5×10^{-6}

Table 3.2: Generic values of P_{ep} for brine and CO₂ filled fractures, and the parameters used to calculate them

where a_{ijkl} is the elastic tensor normalised by ρ , n_i is the wave normal, $p_i v_n$, and v_n is the n -th phase velocity. I use the Christoffel equation to compute ψ and δV_S for each S-wave arrival azimuth (θ) and inclination (ϕ) that is present in the observed dataset. The modelled ψ and δV_S values are compared with the observed values, and the RMS misfit computed. Note that in all cases, ψ refers to the fast wave polarisation in ray-frame coordinates, there is no rotation into geographical or other coordinate systems as is often done when interpreting SWS. Also, I assume that in all cases splitting does occur, and that there are no null results caused by coincidence of a symmetry axis with the initial S-wave polarisation (e.g., Wüstefeld and Bokelmann, 2007). This is because I have not systematically identified null results in the data from Weyburn. Furthermore, the inclusion of null result information would require extra parameters, in the form of initial S-wave polarisations, to be included in the inversion algorithm.

I compute the misfit between ψ and between δV_S separately, and normalise both by their minimum values, before summing them to give the overall misfit. Conceptually, there is no reason why this sum could not be weighted such that fitting either δV_S or ψ was given priority in the inversion (for instance, if one was more accurately known than the other), however, I have no reason to treat them differently here. The outcome of this process is that a misfit surface is defined throughout the 4-parameter space. This surface describes how well constrained a result is. Where many different models provide a reasonable fit to the data, the misfit minima will be broad and shallow. Where there is a well constrained best-fit model, the misfit surface will show a clearly defined minimum. I conduct an F-test (see, for e.g., Silver and Chan, 1991, in appendix) to numerically delineate this constraint. The workflow for this process is outlined in Figure 3.4. I anticipate that with sufficient data (i.e., a sufficient range of S-wave arrival angles), models will be well constrained. When arrival ranges are limited, results may be poorly constrained, with multiple models able to fit the data.

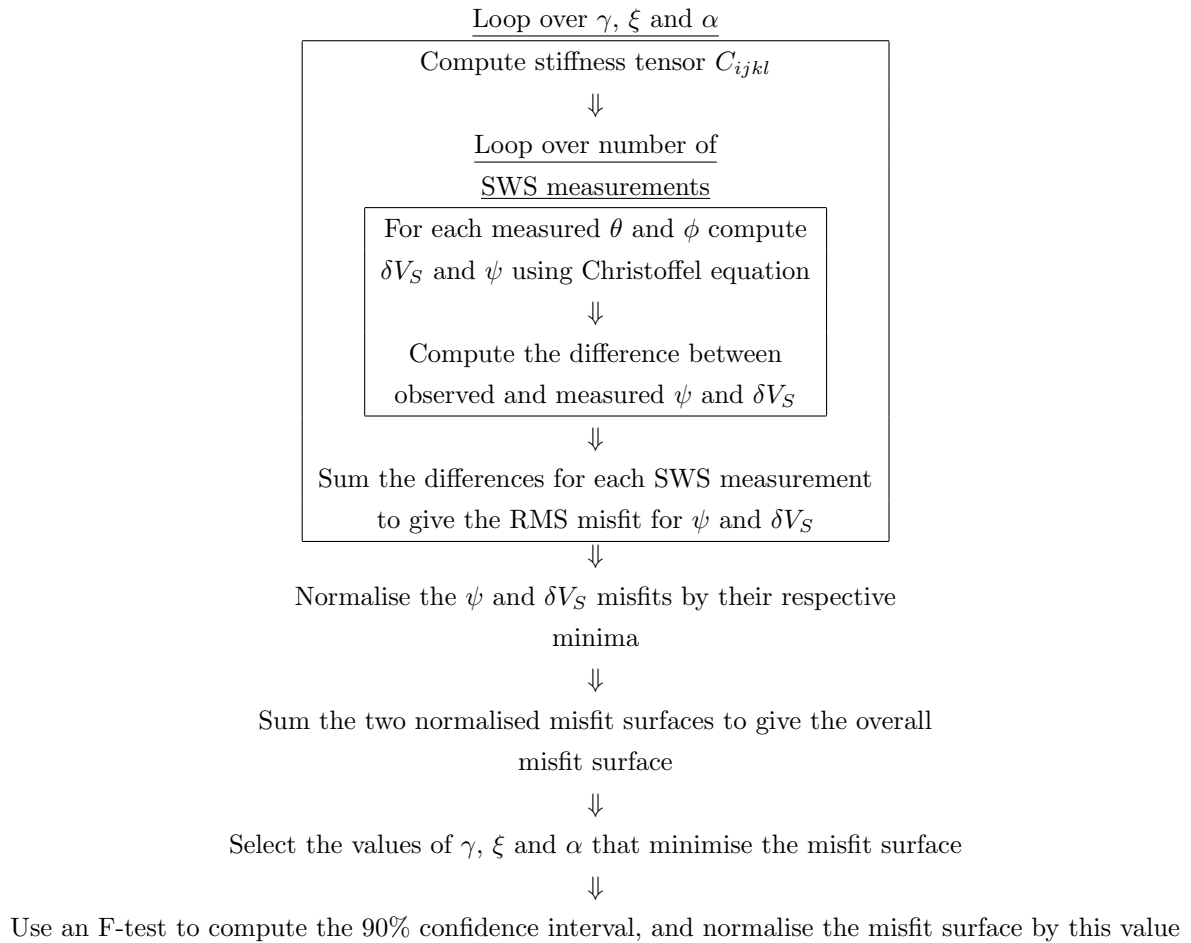


Figure 3.4: Workflow for inverting for rock physics parameters from SWS measurements.

An assumption implicit in this approach is that all the rock mass through which the shear waves have travelled has similar physical properties. If there is significant spatial variation in the anisotropic system along a single - or between different - raypaths then this approach may break down. Tomographic techniques are being developed that invert for spatial variations in anisotropy (e.g., Abt and Fischer, 2008; Wookey, 2010). However these tend to run into under-determination problems, where the number of free parameters available (the spatial distribution of each area with differing anisotropy, as well as the anisotropic parameters for each area) serve only to introduce trade-offs and non-uniqueness to the solutions. Where no significant variations in anisotropic system are anticipated this approach has the advantage of ease of application and much reduced computational requirements - the tomographic approach of Wookey (2010) requires a cluster to perform the computations! In practise, I anticipate that for real cases where significant spatial variation exists our approach would fail to find significant minima. This could be used as an indication that spatial variations are present, and that tomographic techniques are necessary.

3.3 Synthetic testing of inversion method

Before applying this technique to a real dataset I develop synthetic examples to demonstrate and understand the inversion process better. The first step is the construction of an initial elastic model using the rock physics model outlined above. A range of plausible raypath arrival azimuths and inclinations are chosen. For each case described here, 130 synthetic data points are produced, using a grid of 13×10 (azimuth \times inclination) points, the limits of this grid being defined specifically for each case. The splitting parameters ψ and δV_S for each raypath are calculated using the Christoffel equation. I add noise to the data by assuming a random error distribution between $\pm 10^\circ$ for ψ and $\pm 0.5\%$ for δV_S , which are typical error ranges for real splitting data (e.g., Al-Harrasi et al., 2010). Because there will also be uncertainty regarding the event location, and therefore the angle of wave propagation through the rock, I also add noise of $\pm 10^\circ$ to the inclinations and azimuths of the synthetic data - this is done after the splitting operators have been computed.

This then represents the ‘observed’ dataset, which I use to invert for the initial model parameters. The proximity of the initial parameters used to construct the elastic model and those found by the inversion will indicate the linearity of the objective function around the point of interest. The extent of the confidence interval within the misfit space will show how unique a solution is. Where well constrained, unique solutions can be found, this implies a well posed problem, with features that are resolvable with the data available. Where a wide misfit minimum, or multiple solutions that fit the data are found, this implies an under-determined problem, and that the data are not sufficient to resolve the structures present.

3.3.1 Sensitivity of δ and γ

My first use of synthetic data is to test the sensitivity of the inversion to γ and δ . These parameters control the strength of a VTI fabric, so I anticipate that they will be highly sensitive to the angle of ray propagation with respect to this structure, i.e., the angle of inclination. I perform 3 inversions, with subhorizontal ($0-30^\circ$), subvertical ($60-90^\circ$) and oblique ($30-60^\circ$) arrivals. In each case there is a full range of arrival azimuths from $0-180^\circ$, and the initial elastic model has $\gamma=0.04$, $\delta=0.1$, $\xi=0.04$ and $\alpha=120^\circ$. In Figures 3.5 - 3.7 I plot the RMS misfit contours as a function of γ , δ and α , at the best fit value of ξ .

The first thing that I note from Figures 3.5 - 3.7 is the apparent linearity of the solutions. For every parameter, for every set of arrival angles, the rock physics parameters found by the synthetic inversion matches the initial parameters used to create the model. Furthermore, in almost every case, excepting γ and δ for subvertical arrivals, the misfit surface describes an ellipse around the best fit model, with no alternative best fit model. The equations used to generate the inversion are complex and nonlinear. However, it appears that, around the regions of interest they can be approximated by a linear relationship.

However, the misfit surfaces surrounding the best fit models are not circular, showing instead a high degree of ellipticity in some cases, implying that there are differences in how well constrained

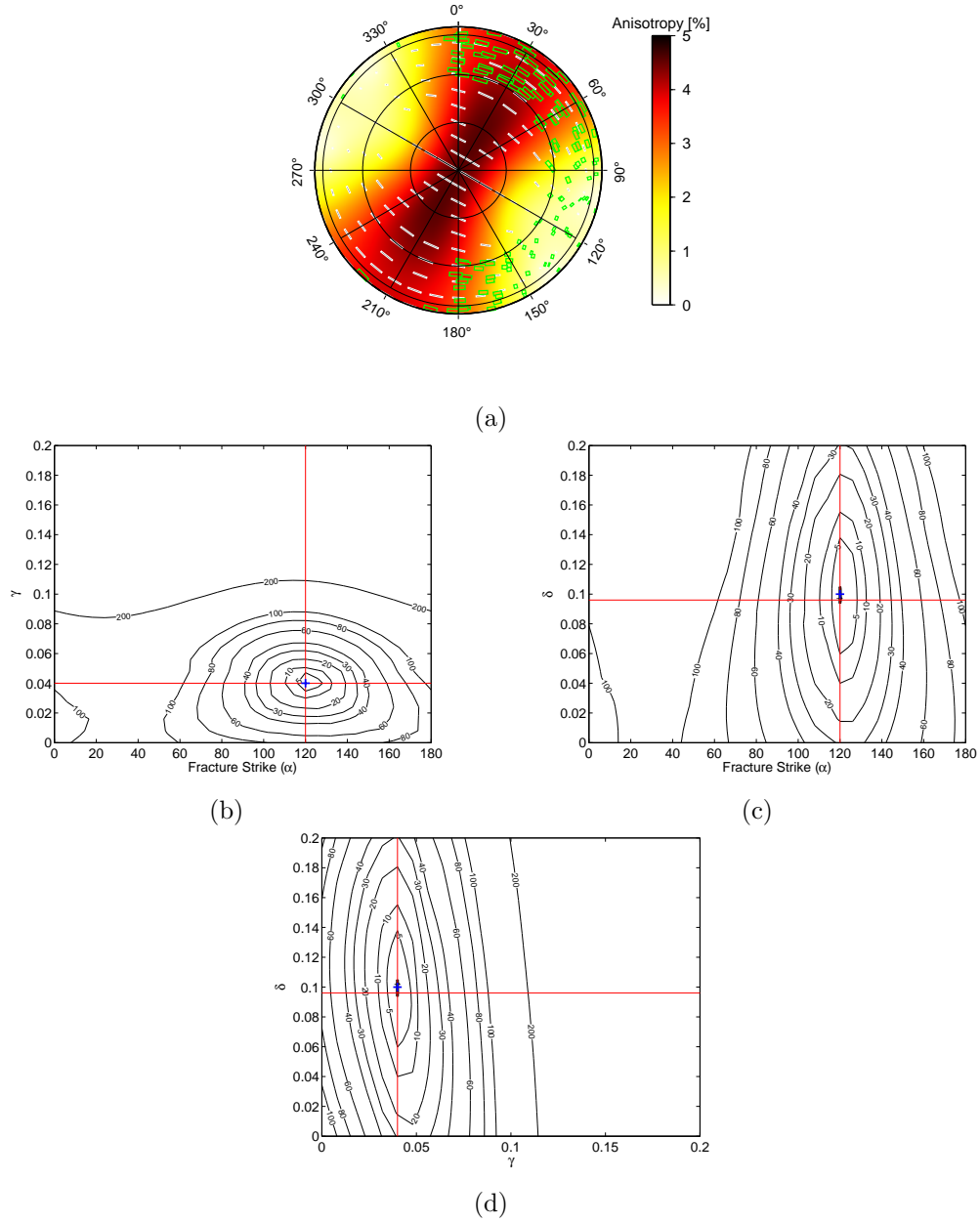


Figure 3.5: Inversion results for the first synthetic example, with subhorizontal arrivals. In (a) I plot an upper hemisphere projection of the synthetically generated dataset (coloured ticks with green outline). The position of the ticks mark the arrival azimuths and inclinations of the S-waves. The orientation of the ticks mark ψ , while the length of the ticks, and the colour, give δV_S . Also plotted, with thin ticks and coloured contours, is the modelled splitting using the best fit model parameters. Panels (b - d) show the RMS misfit between data and model, as a function of fracture strike (α), γ and δ . The blue crosses mark the initial values used to generate the synthetic data ($\gamma=0.04$, $\delta=0.1$, $\alpha=120^\circ$ and $\xi=0.04$) and the red lines indicate the inversion results. The misfit contours are normalised such that 1 is the 90% confidence limit. The ellipticity of the 90% confidence interval indicates how well constrained the parameters are in relation to each other. In this case, γ and α are well constrained, while δ is not.

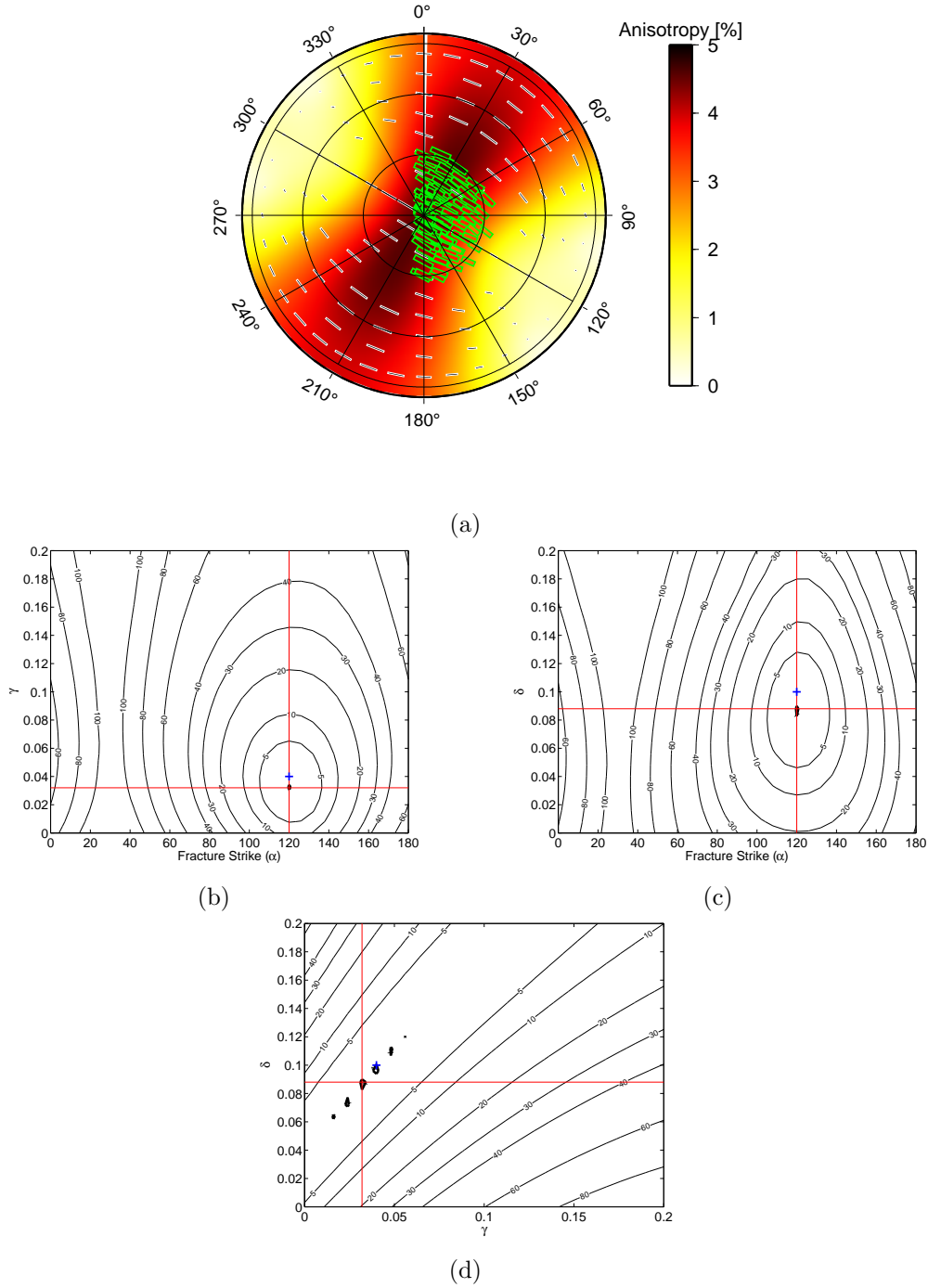


Figure 3.6: Inversion results for the second synthetic example, with subvertical arrivals, in the same format as Figure 3.5. The initial elastic model is also the same. In this case, there is a trade-off between γ and δ , meaning that neither is well constrained.

the different parameters are. In the case with subhorizontal arrivals (Figure 3.5). Fracture strike and γ are well constrained. However, from the elongation of the misfit contours along the δ axis, I infer that this parameter is not as well constrained. This is because splitting of subhorizontal shear waves is not significantly affected by the size of δ , and therefore it does not have an influence on the inversion.

For the case with subvertical arrivals (Figure 3.6), there is a trade-off in the inversion between δ and γ , meaning that neither is well constrained. Essentially, for a set of splitting measurements on subvertical S-waves, any modelled value of γ , with the appropriate value of δ , can produce splitting patterns that match well with the actual splitting.

For the case with obliquely arriving waves (Figure 3.7) there is still some trade-off between γ and δ , though both are better constrained than with the subvertical arrivals. In all the examples the fracture strike and density are both well imaged. This is because I use a full range of arrival azimuths from 0 - 180°. Much as horizontal fabrics are most sensitive to the range of arrival inclinations, vertical fabrics (such as fractures) will be most sensitive to the range of azimuths available. As can be seen in Chapter 4, constraints on fracture strike and density will be dependent on the azimuthal range of S-wave arrivals.

This section does not intend to cover every possible source-receiver geometry, these will obviously be specific to the problem being investigated. However, I have outlined how synthetic modelling can guide the interpretation of SWS results, and highlight what real data is likely to identify, and what it cannot. This capacity may well be of use to field engineers when selecting sites to place geophones because geophones sites can be selected to maximise the structures that SWS can constrain. In subsequent sections I will construct further synthetic models that are appropriate to the actual problems being investigated. However, before I do so I will first discuss the SWS measurements made at Weyburn.

3.4 SWS measurements at Weyburn

3.4.1 Method

In order to analyse SWS, the seismograms must first be rotated into the ray frame coordinates. I do this using the P-wave particle motion orientation to indicate the direction of ray propagation, using the *prostate* algorithm described by Al-Anboori (2006). Where the P-wave has not been picked, or where this does not produce a satisfactory rotation, the events are rotated using the azimuth of the located event from the receivers and the inclination assuming a straight source-receiver path.

If SWS has occurred, the S-wave particle motion will be elliptical. However, a rotation of the components by ψ and a time-shift of δt will remove the effects of splitting and leave the particle motion linearised. I use the methodology of Silver and Chan (1991), performing a grid search over ψ and δt to find values that best linearise S-wave particle motion (indicated by a minimised second eigenvalue of the covariance matrix). To ensure a stable and reliable result, the analysis is conducted over a range of windows centred on the S-wave arrivals. This ensures that the result is not dependent on S-wave picking accuracy. 100 picked windows are automatically generated on which to perform the

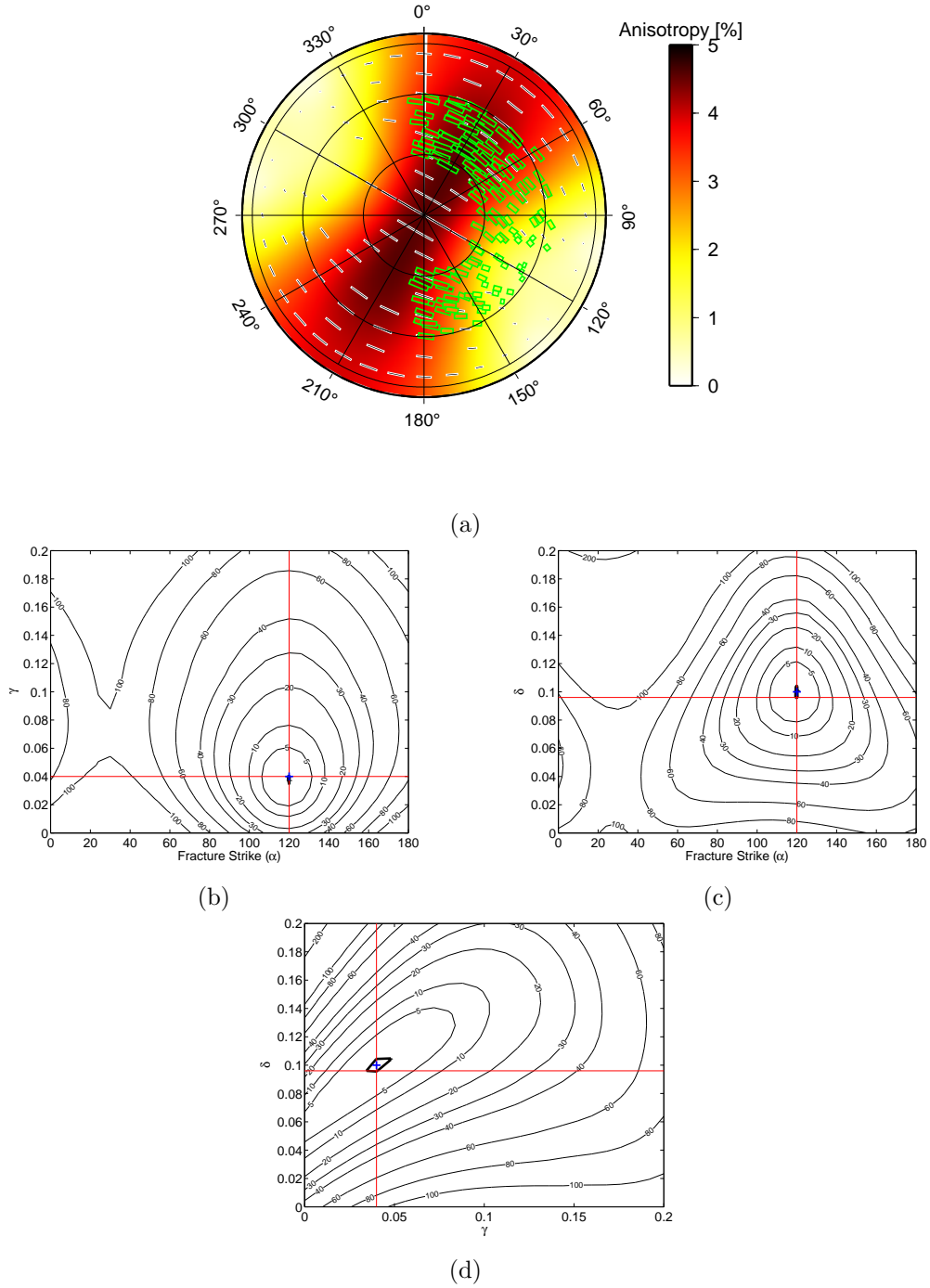


Figure 3.7: Inversion results for the third synthetic example, with oblique arrivals, in the same format as Figure 3.5. The initial elastic model is still the same. There is still some trade-off between γ and δ , but both are better constrained than in Figure 3.6.

eigenvalue minimisation analysis. Cluster analysis is performed to choose the best cluster of results, from which the best result is selected. To conduct the analysis I use the SHEar-wave Birefringence Analysis (SHEBA) algorithm developed by Teanby et al. (2004b).

Figure 3.8 shows the results for an example event from the dataset. In panel (a), the seismograms are rotated into the ray frame. There should be no P-wave energy on the Sv and Sh components. Panel (b) shows the S-wave components rotated into radial and transverse components with respect to the initial source polarisation, both before and after the splitting correction. After correction, the transverse component should be minimised. Panel (c) shows the S-wave particle motion before and after correction, and the fast and slow waveforms before and after correction. The particle motion should be linearised after the splitting correction, and the fast and slow waveforms should be similar. Panel (d) shows a contour plot of the energy on the transverse component after correction as a function of ψ and δt stacked for each of the 100 picked splitting analysis windows. An F-test is used to normalise this surface such that a value of 1 represents the 95% confidence interval. The cluster analysis is also displayed to the right of this panel. The upper cluster analysis panel shows the results (ψ and δV_S) of the splitting measurement for each of the splitting analysis windows. The lower cluster analysis panel maps the results for each window in ψ - δV_S space, highlighting the clusters identified by SHEBA.

Teanby et al. (2004b) provide a number of requirements that must be fulfilled if a splitting result is to be deemed reliable:

- Well defined S-wave and successful rotation, with all the P-wave energy on the ‘c’ component ((quasi-)parallel to the raypath), and S-wave energy on the ‘a’ and ‘b’ components (perpendicular to ‘c’).
- Energy minimised on the transverse component after correction.
- Linear S-wave particle motion after correction.
- Good match between fast and slow waveforms.
- Unique solution, with a well defined and small error ellipse.

If a splitting measurement fulfils all of the above criteria then it is graded class A. Should it fulfil all but one of the above requirements it is graded class B. If it fails to satisfy two or more of these criteria, it is classed as C and considered to be unreliable.

3.4.2 Splitting results for Weyburn

Of the 688 possible splitting measurements (86 events \times 8 receivers) only 72 provided class A and B results. This is a very low success rate for SWS analysis (compare with, for e.g., Al-Harrasi et al., 2010). There are two probable reasons for this. Firstly, the data generally has a very poor signal-to-noise ratio. Secondly, many of the events are located close to the array ($<400\text{m}$), and have a low dominant frequency ($<50\text{Hz}$). As such, the P and S phases have travelled an insufficient distance to

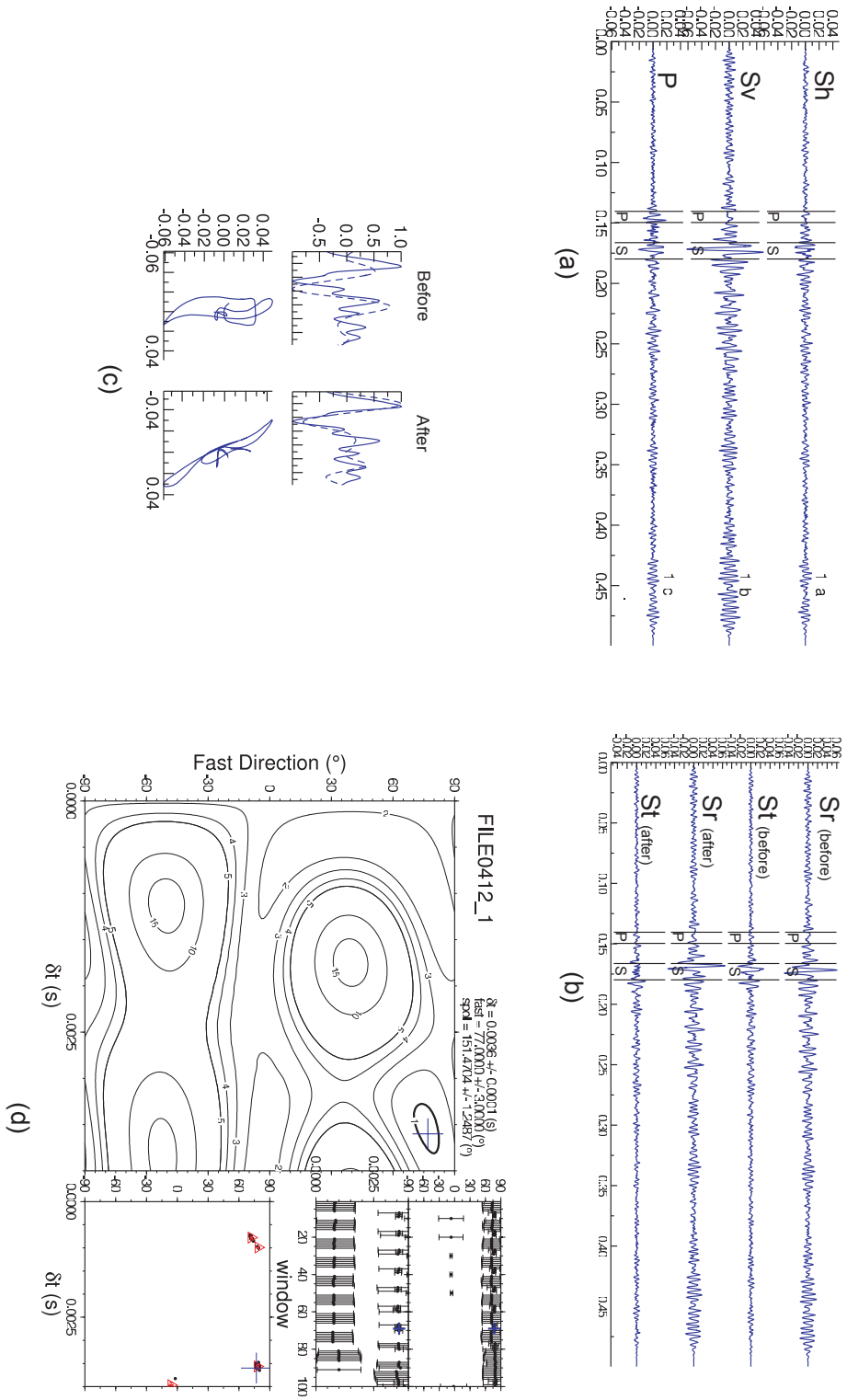


Figure 3.8: An example of SWS analysis. (a) shows the input seismograms rotated into the ray frame. (b) shows the radial and transverse components both before and after correction. A good correction will minimise the energy on the Sr component. (c) shows the fast and slow waveforms, and S-wave particle motion. A good correction will linearise particle motion and leave the fast and slow waveforms looking similar. (d) shows the error surface and cluster analysis. A good result will have one clearly defined error minimum.

	ξ^1	α^1	ξ^2	α^2	γ	δ
Inversion for 1 fracture set	0.14	138°	NA	NA	0.03	0.0
Inversion for 2 fracture sets	0.3	150°	0.21	42°	NA	NA
From Brown (2002)	1.0 - 1.6 m ⁻¹	148°	2.3 - 3.8 m ⁻¹	40°	NA	NA

Table 3.3: Results for the inversion of Weyburn SWS measurements assuming 1 and then 2 fracture sets are present. I also give the results of core and borehole analysis at Weyburn provided by Brown (2002). The fracture densities in this study are given by Hudson (1981)’s non-dimensional fracture density term, but in Brown (2002) they are written as the number of fractures per meter of rock.

separate fully. The presence of P-wave coda arriving coincident with the S-wave will contaminate the SWS analysis, leading to unreliable results. Although it is common practise to include only the class A results in analysis, the lack of good quality events means that I include class A and B events in the subsequent discussions.

The events recorded during Phase IB are located at reservoir depths, and occur between December 2003 and July 2004. The events recorded during Phase II occur above the reservoir during October 2005. Given their differing temporal and spatial distributions, I will analyse the Phase IB and II results separately.

3.4.3 Phase IB

I invert the 30 successful SWS measurements from Phase IB, assuming a VTI fabric and one set of fractures. The results are plotted in Figure 3.9 and the best fit results are listed in Table 3.3. The inversion suggests that there is little VTI, and images a fracture set striking at 138° (NW-SE) with a density $\xi=0.14$. When we consider the RMS misfit surface in Figure 3.9, the 90% confidence interval is large, suggesting that the inversion has not found a particularly well constrained result.

Core analysis and borehole image logs at Weyburn have imaged the presence of aligned fracture sets in the Weyburn reservoir (Bunge, 2000; Brown, 2002). Two of the fracture sets identified by these studies are listed in Table 3.3. These sets have strikes of 40° and 148°, with the set at 40° being the more pervasive. However, our SWS inversion has identified the apparently weaker set at 138°. One reason for this may be the geometry of the arrivals available to conduct the inversion. My initial interpretation was that perhaps although the NE-SW set had a greater fracture density when unstressed core samples were considered, stress evolution during production has kept this set closed at depth, while opening the NW-SE set, making it more ‘visible’ to the shear waves.

An alternative explanation for why the supposedly stronger NE-SW fracture set is not imaged can be provided by synthetic models. To test this possibility I generated an elastic model containing two vertical fracture sets aligned orthogonally with strikes NW-SE and NE-SW, as observed from Weyburn cores. I assign a higher fracture density to the NE-SW set, as is believed to be the case at Weyburn. I then perform a synthetic inversion using the range of arrivals observed in the real

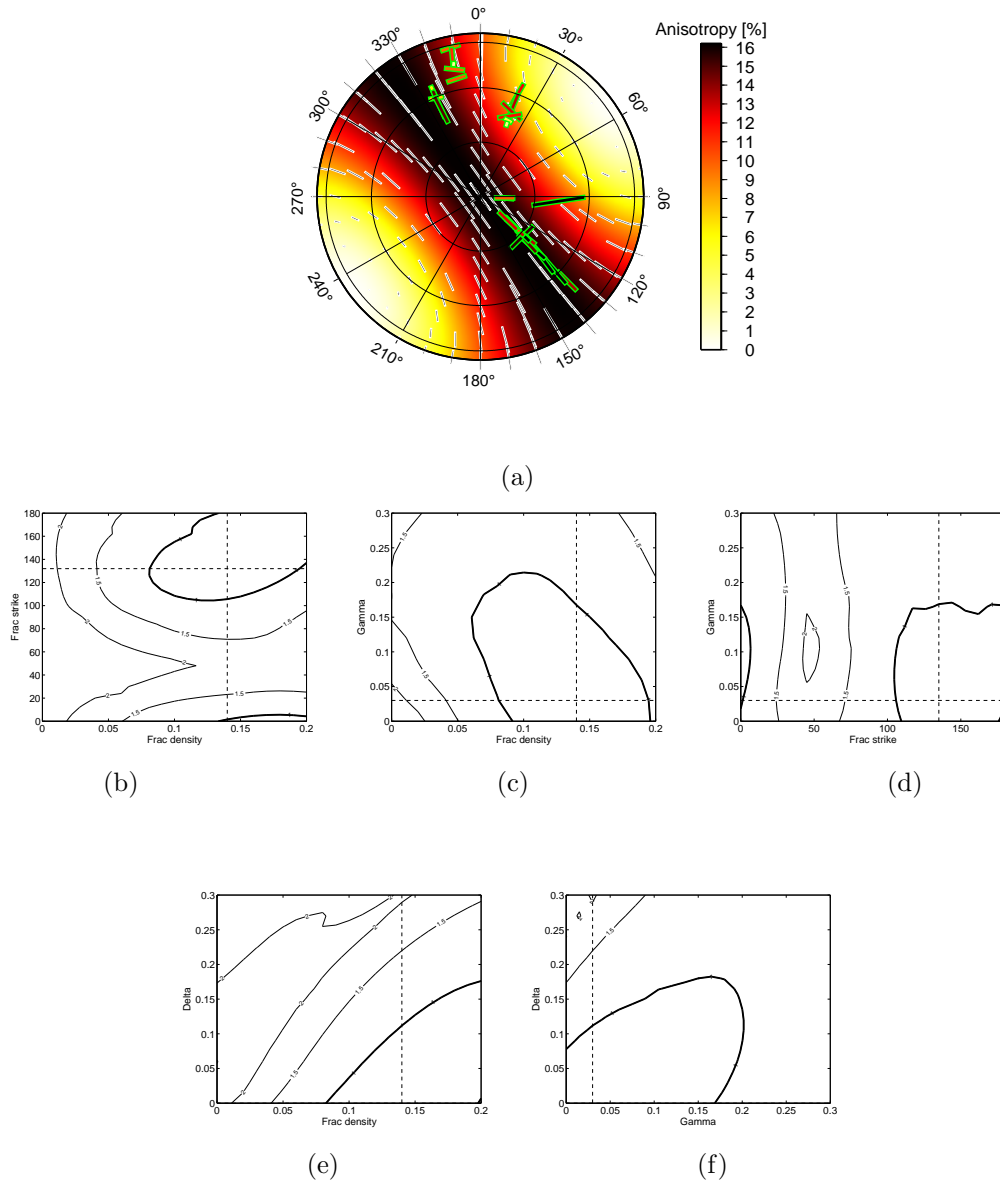


Figure 3.9: Splitting inversion results for Phase IB, assuming one fracture set is present. Panel (a) shows the observed and modelled SWS in the same format as Figure 3.5a. In (b)-(f) I show the normalised misfit contours as a function of ξ , α , γ and δ . The 90% confidence limit is marked in bold, and the dotted lines mark the best fit values. The inversion images the strike and density of a fracture set, and suggests that there is little VTI fabric.

dataset. The results are plotted in Figure 3.10. Although the NE-SW set has a higher density, it is the NW-SE set, at $\sim 140^\circ$, that is imaged by the synthetic inversion, just as it is with the real data. The explanation for this observation is that most of the events have arrived with azimuths close to NW or SE. As a result, they are travelling subparallel to the NW-SE set, and close to the normal of the NE-SW set. When shear waves travel parallel to the normals of a fracture set they are not split by them. Hence, although in reality the NE-SW set has a higher density, it is at the wrong orientation to be imaged by the arrivals available, and so the inversion images the NW-SE set.

This demonstrates how synthetic inversions can significantly enhance the interpretation of splitting results. This example also demonstrates how important the range of arrival angles available can be in determining what SWS can and cannot image. I conclude that while the splitting appears to image the secondary fracture set, this does not necessarily imply that the NE-SW set is not also open, only that I do not have the ray coverage to image it.

3.4.4 Modelling two fracture sets

An alternative approach to inverting the splitting results is to assume that two fracture sets are present, and to attempt to find the strikes and densities of both. To simplify the inversion I neglect the effects of any sedimentary fabric, as this was found to be small by the initial inversion (Figure 3.9). I list the inversion results in Table 3.3, and plot the results in Figure 3.11. The inversion finds fractures striking at 42° and 150° , providing a good match with the fracture sets identified in core samples and borehole image logs. When I examine the misfit surfaces, I note that the best fit fracture densities trade off against each other (Figure 3.11b) - this is because the two fracture set orientations are close to orthogonal. Bakulin et al. (2002) and Grechka and Tsvankin (2003) have shown that the same stiffness tensor, \mathbf{C} , and therefore the same SWS patterns, can be produced by a range of fracture densities, so long as the fractures are close to orthogonal. This means that the absolute value of fracture density for the two sets is not uniquely resolvable. However, I can determine the relative strength of each set: in Figure 3.11b the 90% confidence interval shows that the best fit fracture density for the set at 150° must be larger than the density of the set at 42° . This is in disagreement with the core sample work, which finds that the set at 40° has a higher density. However, there may well be geomechanical reasons for this disagreement, with injection activities altering the stress conditions to preferentially open the set at 150° (which runs perpendicular to the horizontal well trajectories at Weyburn). This will be discussed further in Chapter 8. I note now that because the splitting occurs over the whole of the raypath, which includes the overburden, as the receivers are placed above the reservoir, it is impossible to determine whether the fractures modelled are located in the reservoir, overburden or both.

3.4.5 Phase II

I also perform the inversion technique on SWS measurements from Phase II. The results are plotted in Figure 3.12. The 90% confidence intervals are very large, as the inversion does not appear to find a reliable interpretation for subsurface structure. There are a number of possible reasons for this failure.

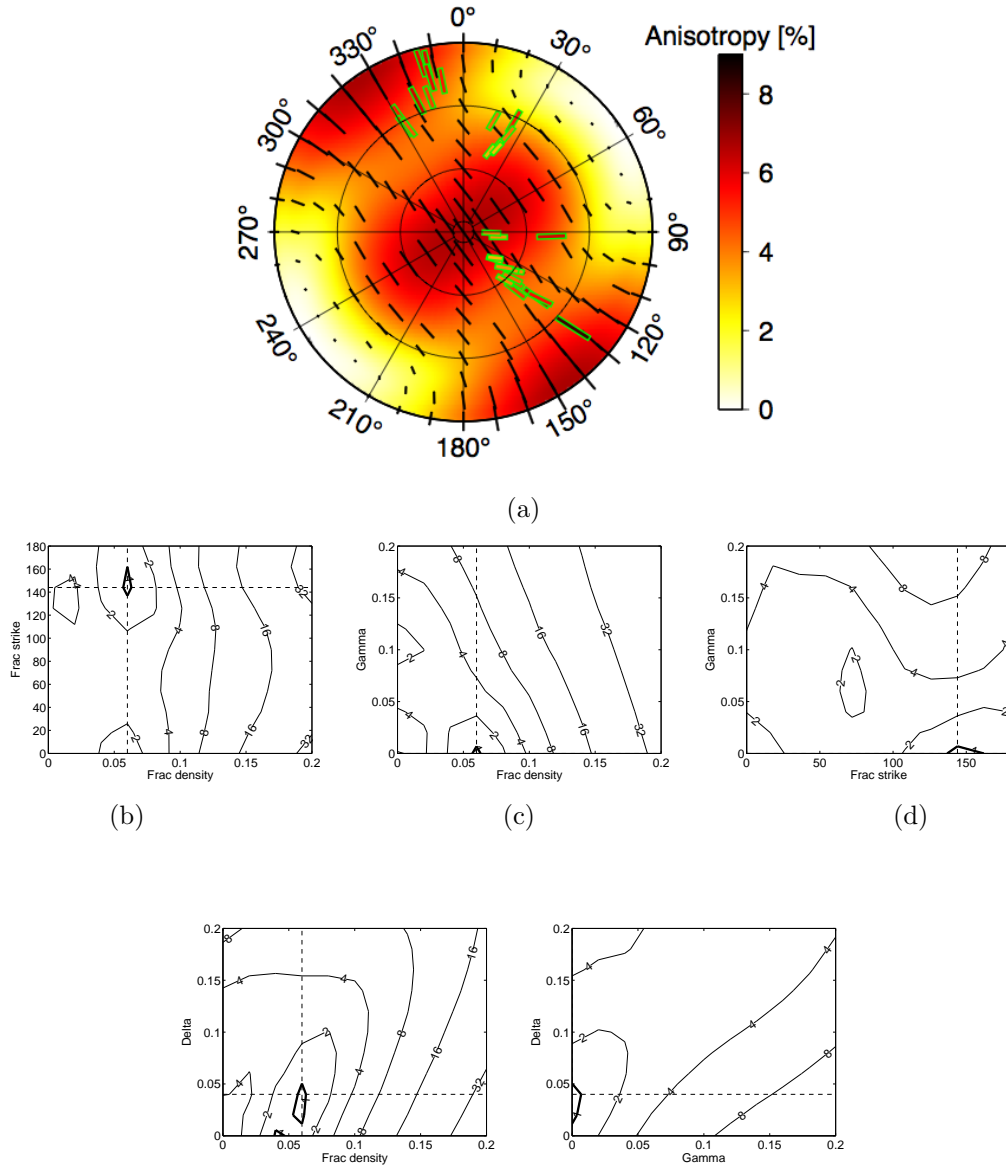


Figure 3.10: Synthetic inversion results for Phase IB. The initial model is constructed using two fracture sets, with the NE-SW set having a higher density. However, the inversion result images the fracture set that strikes to the NW-SE. In (b)-(f) I show the normalised misfit contours as a function of ξ , α , γ and δ . The inversion finds the fractures striking to the NW.

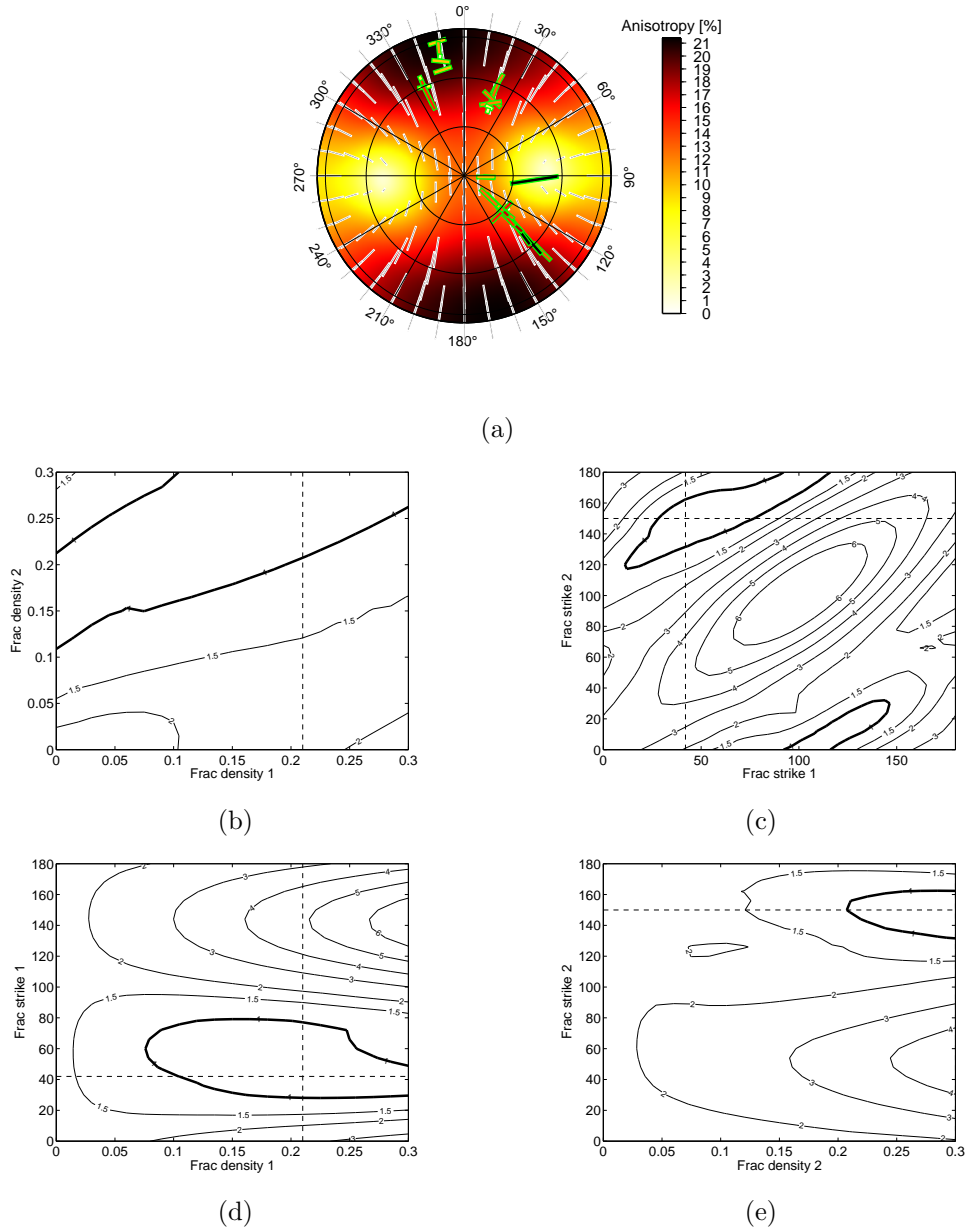


Figure 3.11: Inversion results for Phase IB assuming two vertical fracture sets are present. In (a) I plot the observed and modelled SWS. Panel (b) shows the misfit surface as a function of the fracture densities, and (c) shows the misfit surface as a function of the fracture strikes. The inversion finds two fracture sets with strikes of 150° and 42° . The fracture densities are poorly constrained because they trade off against each other, but the 2nd set, with a strike of 150° , is always the more dominant. Panels (d) and (e) show the misfit as a function of the fracture densities and strikes of each set - it is clear that the best fit results require two fracture sets with different orientations.

If the subsurface structure being illuminated by the Phase II results is too complicated to be modelled by one set of HTI fractures and a VTI fabric then the inversion may fail. Another possibility is that the Phase II arrivals come from many different locations and travel through different layers, and so are illuminating different zones of the subsurface that have differing properties. A final possibility is that, in lumping together A and B class measurements in order to increase the number of results to an amount worth interpreting I have included too many unreliable SWS measurements and there are not enough A class measurements to conduct the inversion using these alone.

The inversion procedure has now been successfully applied to a number of settings, including: the Yibal oil field, Oman (Al-Harrasi et al., 2010); the Valhall oil field, North Sea (Wüstefeld et al., 2010a); Weyburn during Phase IB (this chapter and Verdon et al., 2010b,c); the hydraulic fracture stimulation presented in Chapter 4 (Verdon et al., 2009, 2010a); a hydraulic fracture stimulation in the Cotton Valley field, Texas (A. Wüstefeld et al., *in prep.*, 2010); and during block-collapse mining at Northparkes mine, Australia (Wüstefeld et al., 2010b). This method has also demonstrated the potential to image multiple fracture sets (Verdon and Kendall, 2010). The wide ranging successful application of this approach suggests that the approximations made in the rock physics model are suitable for characterising fractures in many different settings. Therefore, I do not think that it is an excessive complexity of the fracture system that has caused the inversion to fail. It is far more likely to be a combination of the other two reasons given, that the splitting results are of poor quality and that the arrivals may have imaged portions of the subsurface that differ excessively.

3.5 Discussion

When interpreting SWS caused by fractures, it is commonly assumed that the fast direction rotated into geographical coordinates corresponds to the strike of the major fracture strike and/or the maximum horizontal principle stress orientation, and that an increase in δV_S corresponds to an increase in fracture density. However, in reality, this may be an oversimplification. The presence of fractures, sedimentary layering and other structures all combine to give the overall elasticity of a rock. The respective contributions must all be understood before SWS can be interpreted with confidence. For instance, with the Phase IB data the principal fracture set is not imaged, while the secondary set is. This is because most of the waves have travelled normal to the principal fracture set, and so are not split by them. This highlights the need to consider all the potential contributions to anisotropy when interpreting SWS. It also demonstrates how detailed modelling can be used to infer fracture properties despite an unfavourable source-receiver geometry.

As mentioned above, I invert for an orthorhombic symmetry assuming either a single set of vertical fractures and a horizontal sedimentary fabric, or two sets of vertical fractures. Furthermore, the model I use to estimate the fracture compliance is quite simple. These assumptions were made in order to reduce the number of free parameters and therefore simplify the inversion, while being appropriate for the reservoir analysed. They are not necessary conditions. I could certainly conceive of situations where additional fracture sets, dipping fractures or dipping sedimentary structures, or more

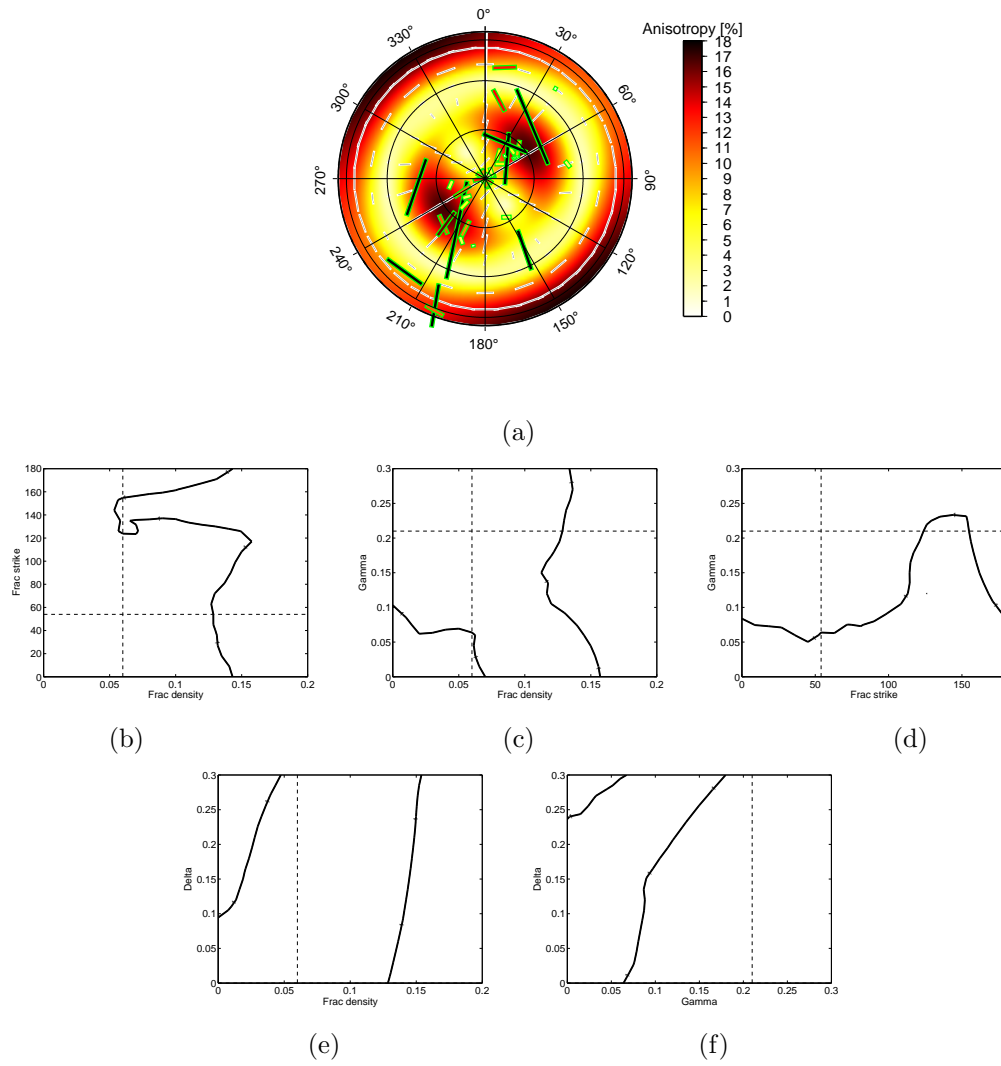


Figure 3.12: Inversion results for Phase II assuming 1 fracture set is present. The inversion fails to find a suitable minimum misfit, implying that no stable result is possible.

complex fracture models, might be preferred, particularly if there was *a priori* evidence to suggest their existence in a reservoir. This would increase the number of free parameters and therefore increase the complexity (and computational requirements) of the inversion. However, this may be appropriate under certain circumstances.

3.6 Summary

- I have developed a novel approach for inverting SWS measurements for fracture properties. I have also developed a method to generate synthetic SWS data in order to test the resolution of inversion results.
- Synthetic inversions show the sensitivity of the various parameters in the inversion to the range of shear wave arrival angles available. In particular, γ cannot be resolved for subvertical arrivals, while δ is poorly constrained for both subvertical and subhorizontal (but not oblique) arrivals.
- I have made SWS measurements on the Weyburn microseismic events using a semi-automated algorithm. The data quality is poor and few successful results are found.
- Using one fracture set to invert the SWS data, Phase IB images a fracture set striking at 138° . Though this does match with one of the fracture sets observed in core samples, it is not believed to be the principal set, which is NE-SW in core samples.
- A synthetic model shows that the range of S-wave arrivals make it easier to image the NW-SE striking set, even if the NE-SW set is stronger. This may be why the NE-SW set is not picked up in the real data.
- An alternative approach is to invert for two fracture sets. In this case, the Phase IB data image two fracture sets striking at 150° and 42° , closely matching the fractures observed in core sample work. However, the inversion finds the set at 150° is the strongest, which is not the principal set in core and borehole work. We may have to seek a geomechanical explanation for why this set has been opened.
- Inversions for the Phase II data failed to find a stable result. It is possible that the quality of the SWS measurements were not good enough, or that, as the arriving waves have sampled very different regions of the subsurface, that there is too much variation in anisotropic symmetry system type, strength and orientation.
- Beyond this thesis, the inversion method I developed has now been successfully applied by several authors to a range of oil field, hydraulic fracture stimulation and block mining scenarios.

A COMPARISON OF MICROSEISMIC MONITORING OF FRACTURE STIMULATION DUE TO WATER VERSUS CO₂ INJECTION

Don't force it, get a bigger hammer.

Arthur Bloch

4.1 Introduction

I have observed a very low rate of seismicity at Weyburn. A key question to ask is whether this is always to be expected for CCS scenarios? It is not clear that CO₂ injection should induce the same rates, patterns and magnitudes of seismicity as water injection. The lower density of CO₂ in comparison to the oil and/or water in a formation may lead to density-driven stress changes, causing different patterns of seismicity (e.g., Sminchak et al., 2002). Supercritical CO₂ has a bulk modulus at least an order of magnitude smaller than water, and it has been suggested that, as it has a higher compressibility, CO₂ represents a ‘softer hammer’ than other injection fluids, and as such will have an inherently lower seismic deformation efficiency. Furthermore, depending on the fluid initially present in the pore space, there may be relative permeability differences between the two fluids. This would influence the injectivity, and therefore presumably the amount of fracturing induced. As a result, there is still significant uncertainty as to the amount of fracturing and seismicity to expect when injecting CO₂.

The dataset presented in this chapter comes from a hydraulic fracture job. As such, it does not directly represent a sequestration scenario such as Weyburn. However, in many ways it can be viewed as representing a ‘worst-case’ scenario, where the injection of CO₂ has led to significant fracturing of the reservoir (albeit deliberately so in this case). I wish to make a direct empirical comparison between water and CO₂ injection. To make the comparison as fair as possible, both fluids have been injected at similar rates, with similar injection pressures, into similar units within the same reservoir. Both stages have been monitored on the same downhole geophone array. I aim to use this dataset to image the orientation and extent of the fracturing, and to use both event magnitudes and shear wave splitting analysis to place bounds on the density of fracturing caused by fluid injection. This will allow me to consider the seismic efficiency of CO₂ in comparison to other fluids.

4.1.1 Field background and description

In a producing North American oil-field a hydraulic fracture job was performed in order to create and improve pathways for fluid migration and to stimulate production. Owing to confidentiality agreements information about the geology and history of this field is limited. The reservoir is thick and contains potential barriers to vertical flow. Therefore, in order to ensure fracturing throughout

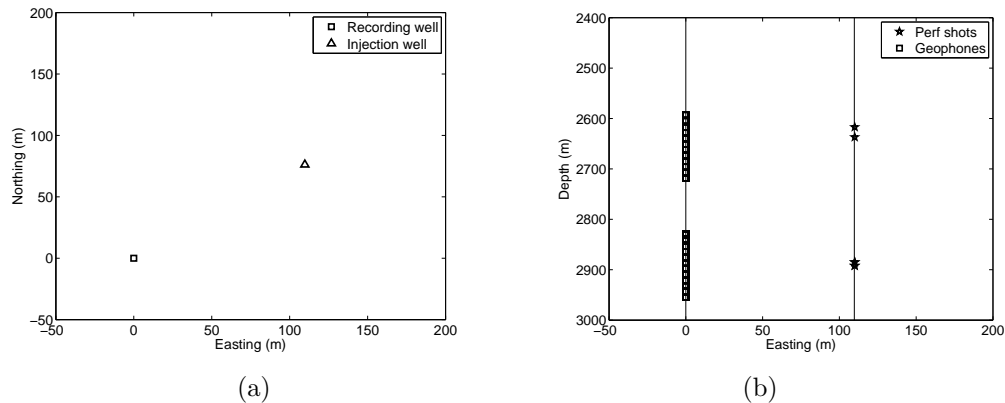


Figure 4.1: Map view (a) and cross-section (b) plots showing the injection depths and recording geophones for both stages of fracturing. The upper shots and receivers in (b) are for the CO₂ injection stage, the lower shots and receivers are the water stage.

the reservoir thickness, nine stages of fracturing were conducted from one vertical well through the reservoir, beginning at the base of the reservoir and moving upwards. For the first seven stages a water-based gel (referred to as water hereafter for brevity) was used as the injected fluid. However, supercritical CO₂ was used for the final two stages. The motivation for this was to test the effectiveness of hydraulic fracturing with different fluids. I have available data from one water injection stage and one CO₂ injection stage conducted a month later. No significant lithological differences have been identified between the two fracture depths, so any differences in seismicity observed can be attributed to the different injection fluids. In order to monitor the fracturing, 12 3-component geophones spaced at 12m intervals were installed in a vertical well a short distance from the injection well. For each stage, the receivers were moved such that the majority of the waves recorded have travelled subhorizontally through the reservoir. The locations of the injection depths and recording geophones for the two stages are plotted in Figure 4.1.

4.2 Event locations

In order to locate the microseismic events, a 1-D P-wave velocity model was generated using sonic log information. An S-wave velocity model was initially computed based on constant V_P/V_S ratios, but where small manual adjustments were found to improve location errors modifications were made. The final velocity model used is shown in Figure 4.2.

I performed the initial analysis and event locations using Pinnacle Technology’s in-house microseismic analysis software, SeisPT[©]. Events were considered as reliable when orthogonally polarised P and S-waves could be identified arriving in a consistent manner across at least two geophones in the array. Of the hundreds of potential triggers recorded by the automated triggering mechanism, approximately 50-100 for each stage were found to be reliable microseismic events. For these events, I manually picked P- and S-wave arrivals. Event locations were computed using P-wave polarisation

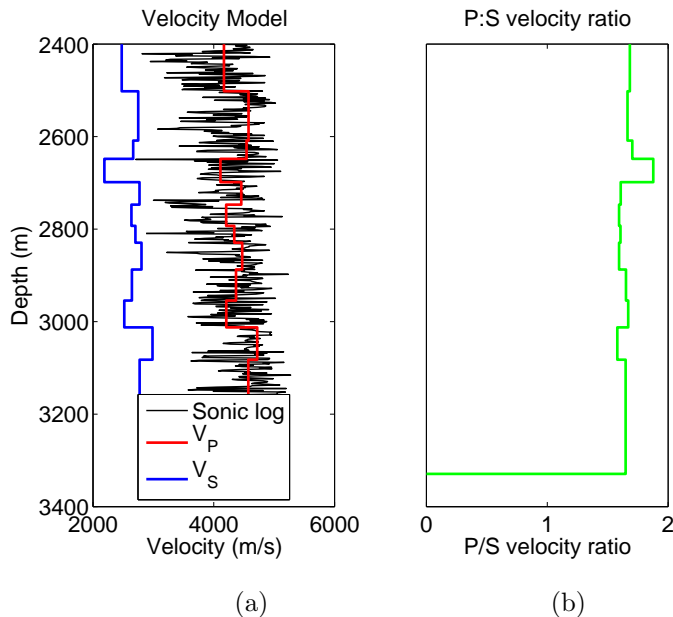


Figure 4.2: Velocity model showing sonic log measurements, P- and S- wave approximations (a), and, in (b), the P:S ratio.

(or, where P-wave polarisation was unreliable, S-wave polarisation) for azimuth, and P/S travel time differences for distance. Arrival time-shifts across the geophone array were combined with ray-tracing through the velocity model to compute event elevation. SeisPT[©] provides automated quality control by assessing both the coherency of takeoff azimuths across the geophone array and the agreement between observed moveout across the array and that modelled by ray tracing. Combining these tests with the signal/pre-event noise ratio allows SeisPT[©] to assign a confidence number for each event, with 5 being extremely reliable and 0 for totally unreliable (Zimmer et al., 2007). The event magnitudes and the location errors were also computed automatically by SeisPT[©]. The error bars shown in the subsequent figures represent the 1σ errors computed from the variation in P-wave particle motion across the array and residuals between predicted and picked travel times. These errors are low. However, they do not take into account potential errors in the velocity model used to compute event locations (e.g., Eisner et al., 2009). These may be introduced in a number of ways - anisotropy (which we know to be present from shear wave splitting observations), lateral heterogeneity, and in upscaling sonic logs to seismic velocities. The errors introduced by having a simplified velocity model (i.e., 1-D, isotropic) are much harder to quantify, so the errors plotted here must be considered a lower bound for the actual errors.

4.2.1 Water injection

The water injection stage was initiated by perforation shots that penetrated the well at depths between 2885 and 2892m. Water was then injected into the reservoir at high pressures. Immediately after

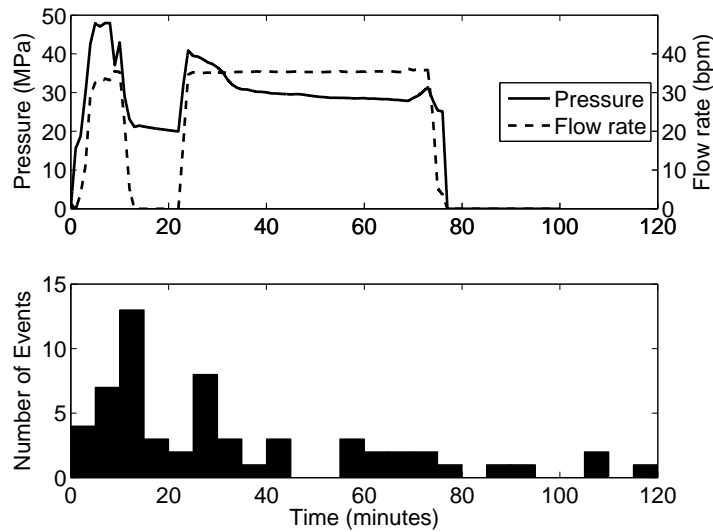


Figure 4.3: The upper panel shows the injection pressures (at surface) and flow rates during water injection. The lower panel shows the rate of microseismicity.

injection, microseismic activity was recorded, which continued for the duration of the injection and a short while after. Figure 4.3 shows in detail the flow rates and injection pressures (at the surface) during injection, and the rate of microseismic activity. In total, 65 events were reliably identified and located.

Figure 4.4 shows the locations for events recorded during water injection. The location errors are generally low - indeed the radial errors are not visible to be seen beyond the dots marking event location. The events form a trend extending NW-SE at 120° from the injection well. In cross-section, the events are highly restricted in vertical extent, occurring only at the depth of the perforation. For all of the events, the moveout across the array, as shown in Figure 4.5, is such that the first arrivals are near the centre of the array (geophone 4), with moveout (delayed arrival times) both above and below this first arrival. This indicates that the waves have arrived sub-horizontally from an event at reservoir level. The containment of microseismicity to a narrow band at the injection depth may indicate containment of the elevated pressures caused by injection to a narrow band in the reservoir. However, without further knowledge of the geology of the reservoir, it is difficult to comment on why this might be the case.

The observation of events extending in a linear fashion from the injection well almost certainly represents the growth of fractures with a NW-SE orientation. Assuming that the maximum principal stress is subvertical, I deduce that the minimum principal stress is horizontal trending NE-SW. From the lateral extent of microseismic activity I observe the fractures extending at least 125m to the NW and 80m to the SE of the injection well, a total distance of 205m.

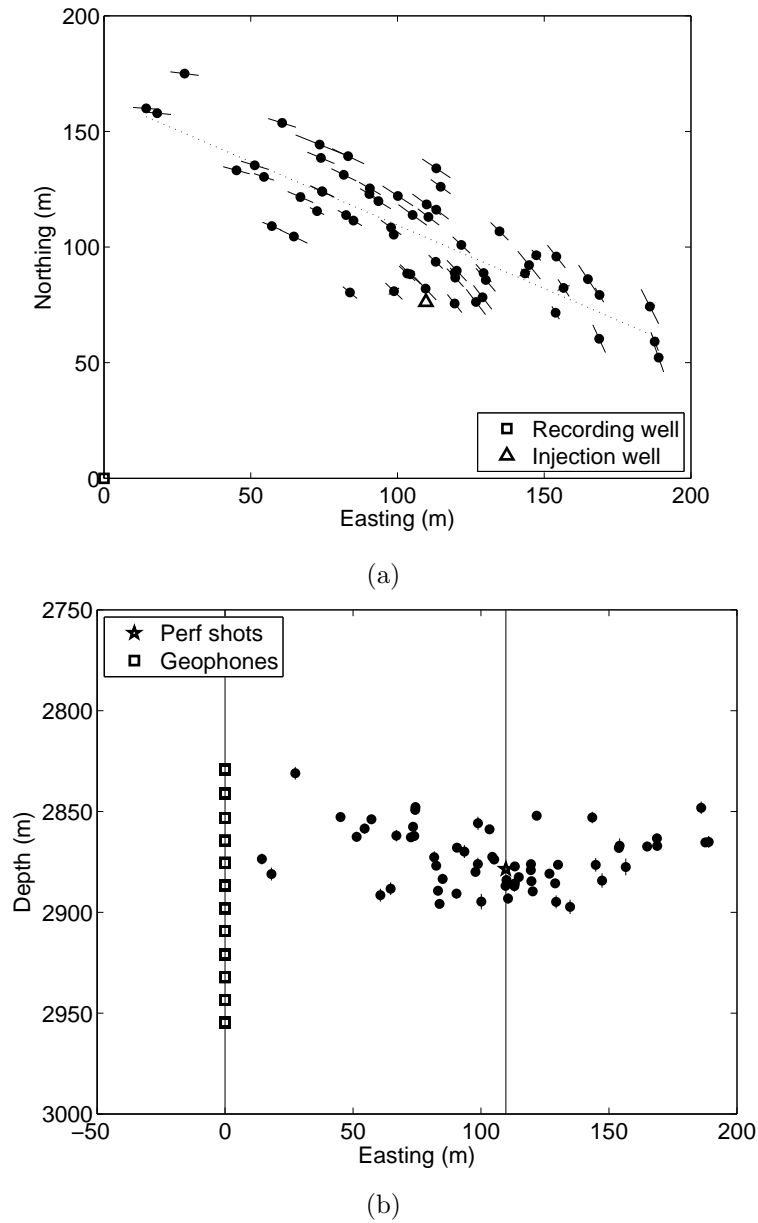


Figure 4.4: Map (a) and cross-section (b) views of event locations during water injection. The location of the recording well is at (0,0), and the injection well is shown. Error bars represent those calculated automatically by SeisPT[©]. The events appear to fall along a trend at 120°, and occur at depths close to the injection depth.

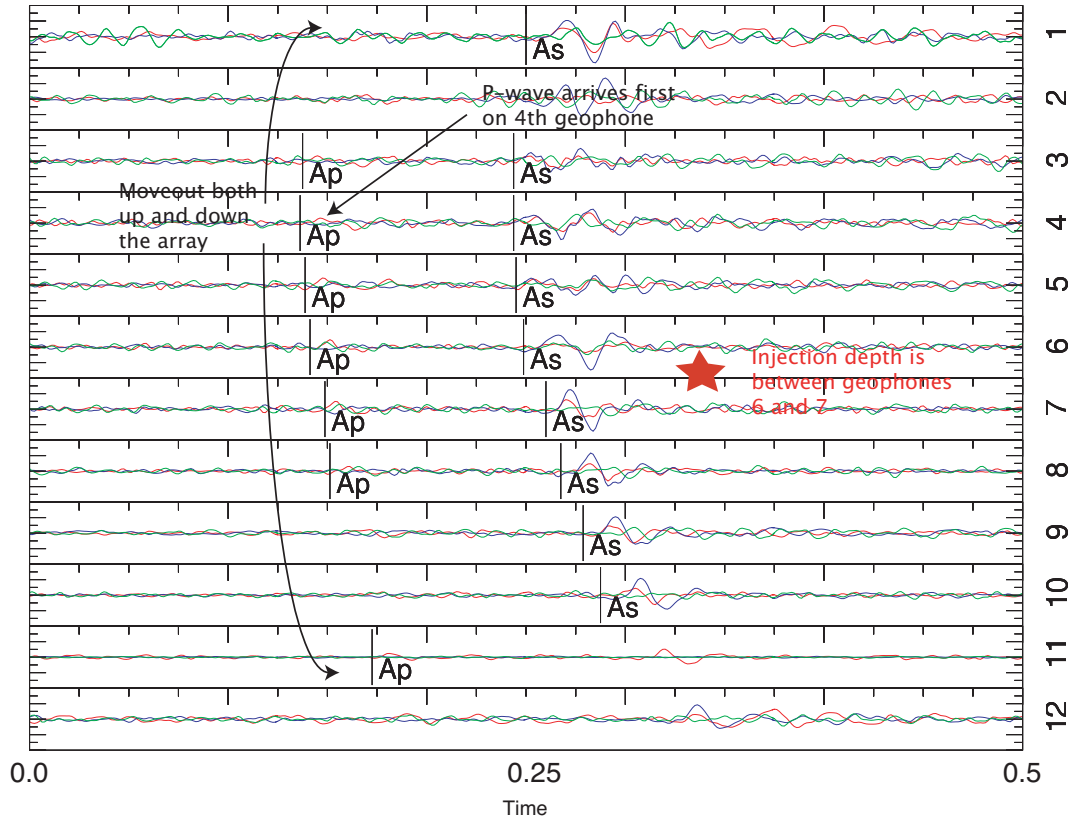


Figure 4.5: Moveout for a typical event during water injection. P and S-wave picks are marked. The energy arrives first near the centre of the array, and moveout is similar both above and below. This indicates that the energy is travelling sub-horizontally from an event at a similar elevation to the injection depth.

4.2.2 CO₂ injection

CO₂ injection was initiated a month after the water injection stage. The injection well was perforated between 2617-2637m, and supercritical CO₂ was used as the injected fluid. Again, microseismic activity was recorded for the duration of injection. The injection rates and pressures are plotted in Figure 4.6 along with the microseismicity rate.

Figure 4.8 shows the event locations during CO₂ injection. In map view the locations show a similar pattern to the water injection events, extending to the NW and SE of the injection well at $\sim 120^\circ$, imaging the formation of vertical fractures with this strike. However, the events migrate upwards to depths of 2530m, 100m above the injection depth during CO₂ injection. This increased range of event depths during CO₂ injection can be seen more clearly in Figure 4.7, which shows a histogram of event depths relative to the injection point.

I confirm that these events are accurately located by considering the moveout for some of the events recorded near the end of CO₂ injection (see Figure 4.9). It can be seen that energy arrives first

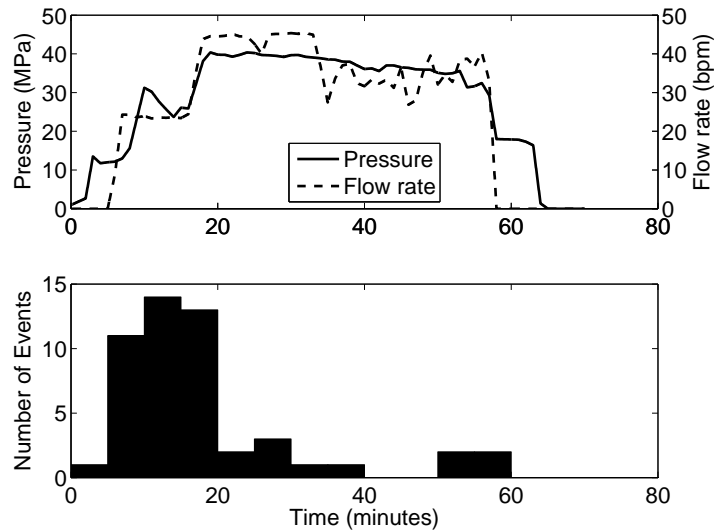


Figure 4.6: The upper panel shows the surface injection pressures and flow rates during CO₂ injection. The lower panel plots the rate of microseismicity.

on the upper receivers, with consistent moveout down the array, indicating that the event really is located above the shallowest receiver in the array. It is certainly possible that this increased vertical extent is a result of the increased buoyancy and mobility of CO₂ in comparison to water. However, without more detailed knowledge of the reservoir it is not possible to rule out the presence of higher permeability pathways (such as pre-existing fractures) or stress barriers at this depth that could also generate this observation. The events during CO₂ injection extend 65m to the NW and 50m to the SE, a total of 115m, which is slightly less than that observed for water injection.

The injection pressures and rates are similar for both stages, as are the rates of microseismicity. In total 50 events were recorded during 63 minutes of CO₂ injection (or 1.26 minutes per event), in comparison with 65 during water injection (at 1.2 minutes per event). Furthermore, the maximum rates of seismicity in Figures 4.3 and 4.6 are similar, with at most 13 events in 5 minutes during water injection and 14 events in 5 minutes during CO₂ injection.

4.3 Event magnitudes

In order to compare the intensity of fracturing caused by injection of the two different fluids, I compare the magnitudes of events recorded during the two stages. The magnitudes are computed automatically by SeisPT[®]. Figure 4.10 plots the injection pressures and event magnitudes during both stages - the scales in both plots are equal. I note that event magnitudes are similar for both stages, with the majority of events having magnitudes between -3.6 and -3.2. For both stages there is a good correlation between injection pressures and event magnitudes. Note, for example, the drop in

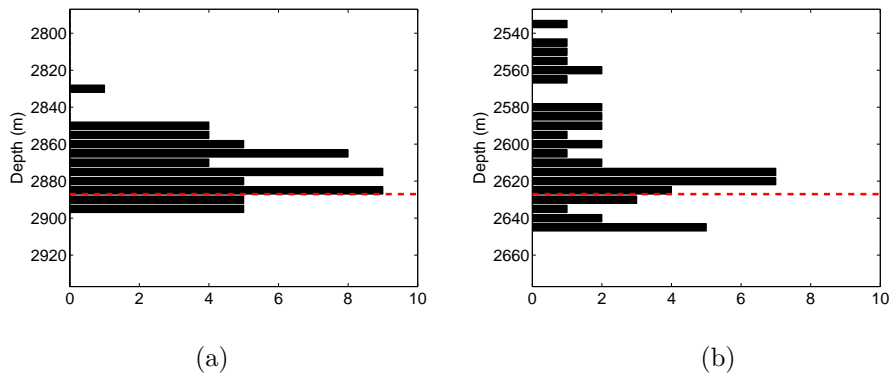


Figure 4.7: Histograms of event depths during (a) water injection and (b) CO₂ injection. The injection depths are marked by the dotted red line. There is a greater spread in event depths during CO₂ injection.

injection pressures between 16 and 22 minutes during water injection correlates with a drop in event magnitudes. During CO₂ injection, the initial stepped increase in injection pressures matches the stepped increase in event magnitudes.

This correlation between injection pressures and event magnitudes can be tested more directly by computing the correlation coefficients between magnitude and the injection pressure at the time the event occurs. The statistical significance of the correlations is computed using a t-test, with the null hypothesis that there is no correlation. I consider the water and CO₂ cases separately. If the magnitudes *are* independent of fluid properties, then combining the datasets should not decrease the correlation. Therefore I also compute correlation for all the data points together. The correlation coefficients and statistical significance of correlation are given in Table 4.1.

In Figure 4.11 I plot the event magnitudes as a function of the injection pressure. The best linear fit lines are shown for water and CO₂ separately and for the overall dataset. The data are quite scattered, and the correlation coefficients are not particularly high. Nevertheless, during water injection, and for the combined data, the correlation is significant at the 99% level. The correlation coefficient for CO₂ injection is poorer, and lacks good statistical significance. From Figure 4.11 it appears that the events during CO₂ injection have slightly higher magnitudes than during water injection at the same pressures. Although no exact relationship should be inferred from this data, we suggest that larger event magnitudes should be expected during periods of higher injection pressures, regardless of the compressibility of the injection fluid.

Above I have noted some differences between water and CO₂ injection. I also note that there is a greater temporal spread of events during water injection, while the majority of events during CO₂ injection occur during the first 25 minutes. However, the most striking observation is the similarity of the response from the two fluids. The injection rates and pressures used during both stages are similar, and the result is that event magnitudes and rates of seismicity are also similar. There is certainly no evidence to suggest that CO₂ - the softer hammer - has induced less seismicity than water.

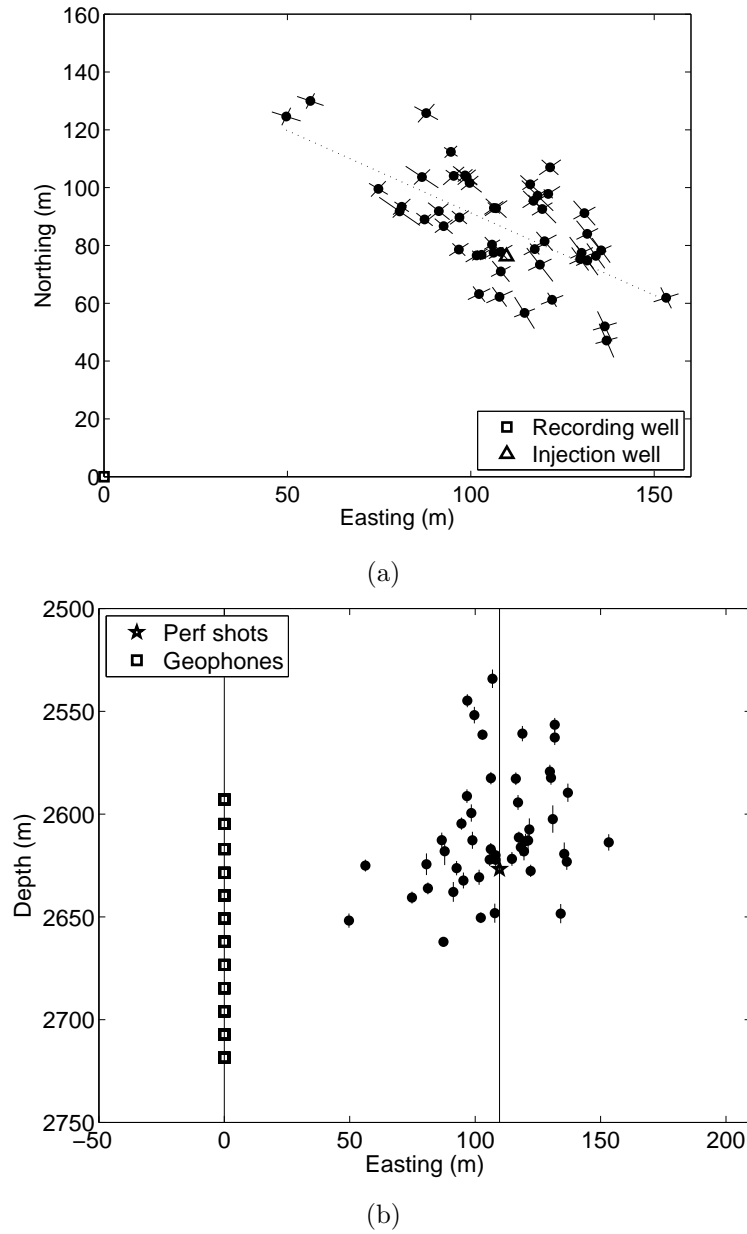


Figure 4.8: Map (a) and cross-section (b) views of event locations during CO₂ injection. The location of the recording well is at (0,0), and the injection well is shown. Error bars represent those calculated automatically by SeisPT[®]. The events fall along a trend at 120°, and some events occur at depths well above the injection depth.

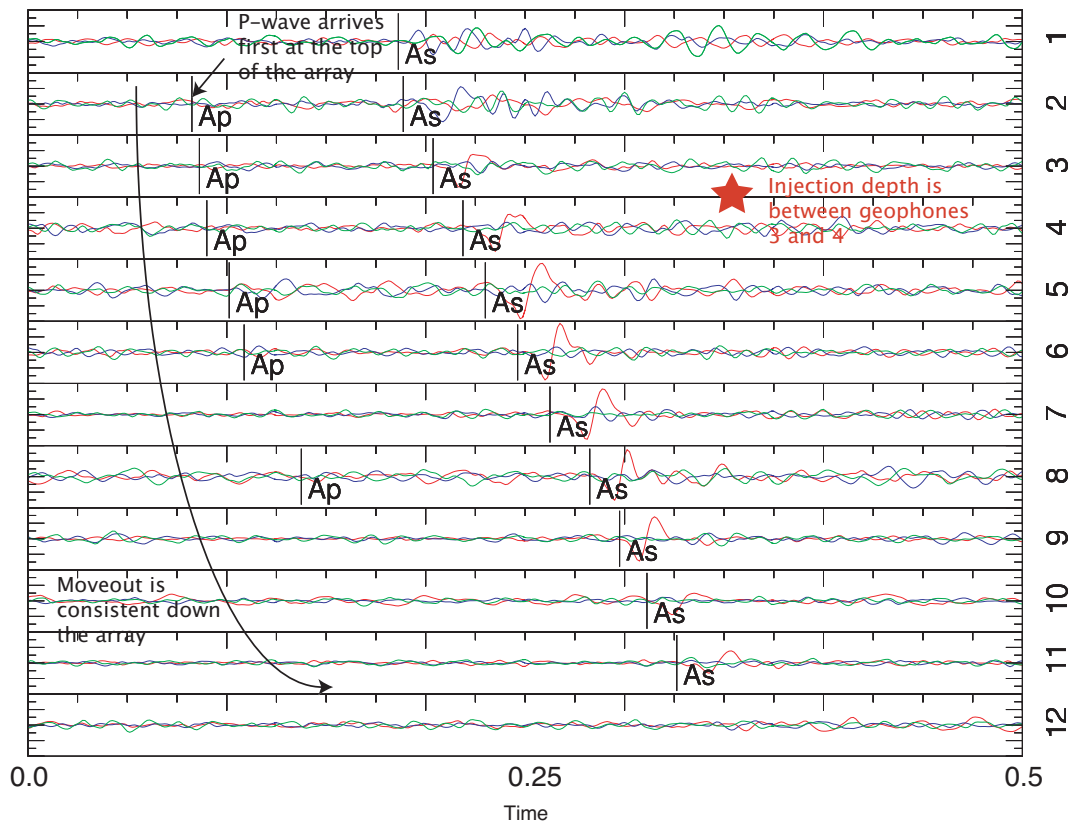


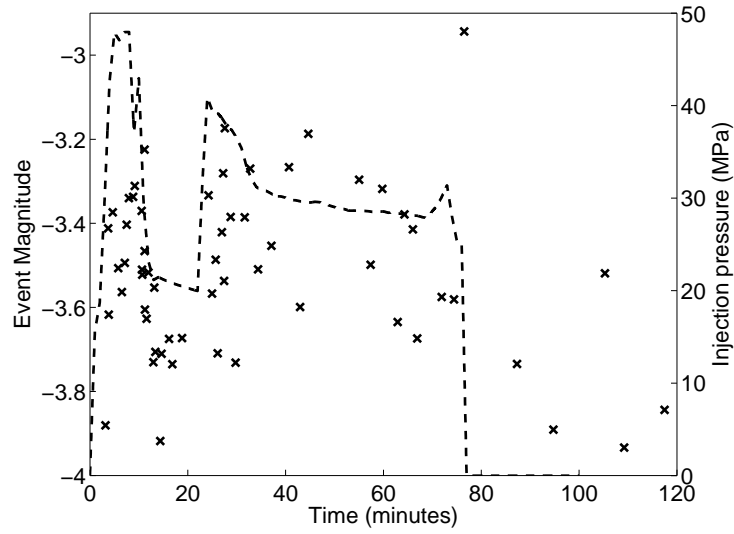
Figure 4.9: P- and S-wave moveout for an event during CO₂ injection located well above the injection depth and recording array. The energy arrives first near the top of the array, with consistent moveout going down. This indicates that the energy is arriving from an event above the array, and well above the injection depth.

4.4 Shear wave splitting

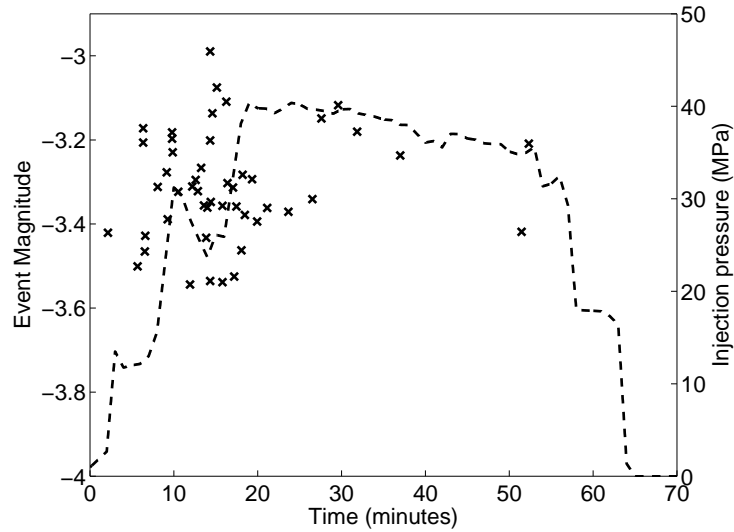
An alternative method to estimate the degree of fracturing is, as discussed in Chapter 3, to use shear wave splitting. As with the Weyburn microseismic data, for both stages I use the semi-automated approach of Teanby et al. (2004b) to compute the fast direction polarisations and time-lags. I invert these measurements for fracture distributions using the inversion technique outlined in Chapter 3 and Verdon et al. (2009).

4.4.1 Splitting measurements

Of the 780 potential SWS measurements (65 events \times 12 receivers) during water injection, 45 provided class A results as defined by Teanby et al. (2004b). This distribution of result quality is to be expected for a typical microseismic dataset (e.g., Al-Anboori, 2006). Figure 4.12 shows a cylindrical projection (Liu et al., 1989) of the splitting results as a function of arrival azimuth (θ) and inclination (ϕ). The



(a)



(b)

Figure 4.10: Surface injection pressures (dotted line) and event magnitudes (crosses) through time for water (a) and CO_2 (b) injection. There appears to be correlation between event magnitudes and injection pressures during both stages. Injection pressures and event magnitudes are similar for both stages, although events are distributed more evenly during water injection.

orientation of the ticks represents the fast direction, with horizontal ticks indicating that ψ is parallel to the S_H axis, while the size of the ticks indicates the magnitude of δV_S . Most of the arrivals recorded during Stage 4 have propagated subhorizontally through the reservoir. As such, ψ will represent a

<i>Fluid</i>	<i>R</i>	<i>P</i>
Water	0.422	99.9%
CO ₂	0.124	60.0%
Combined	0.260	99.3%

Table 4.1: Correlation coefficients (R) and statistical significance of correlation (P) for event magnitudes versus both injection pressure. We consider the data for both fluids separately, and the overall dataset combined.

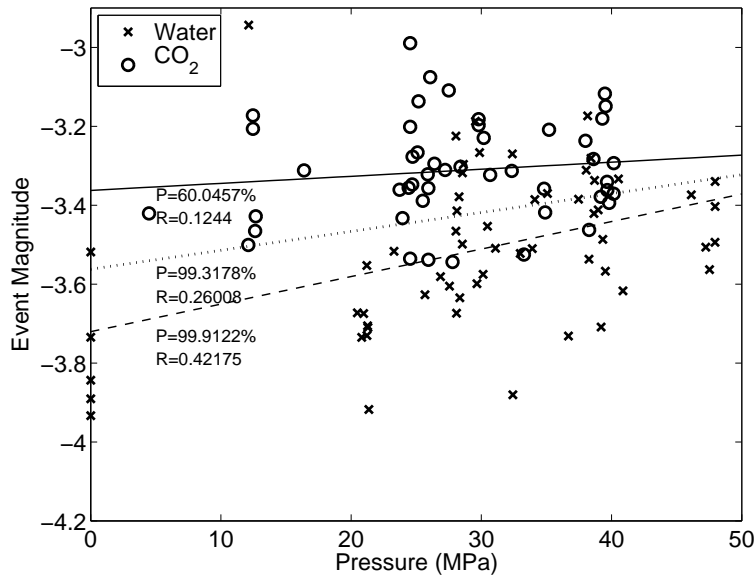


Figure 4.11: Event magnitudes as a function of the pressure at the time that the event occurs. The events during water injection are marked by 'x', during CO₂ by 'o'. The best-fit lines (dashed=water, solid=CO₂, dotted=combined), correlation coefficients, and statistical significances are all marked.

dip. From Figure 4.12, it appears that the majority of results have ψ orientated horizontally. This is confirmed in Figure 4.13, which shows a histogram of ψ orientations.

Of the 600 potential splitting measurements (50 events \times 12 receivers) available during CO₂ injection, 47 provided class A results. The SWS results are plotted in Figure 4.14, with a histogram of ψ orientations in Figure 4.15. As during water injection, the majority of results have ψ orientated subhorizontally.

4.5 Initial S-wave polarisation

It appears that the majority of events recorded during both stages have ψ orientated subhorizontally. From engineering work done in the reservoir (S.C. Maxwell, *pers. comm.*, 2008), it is believed that the

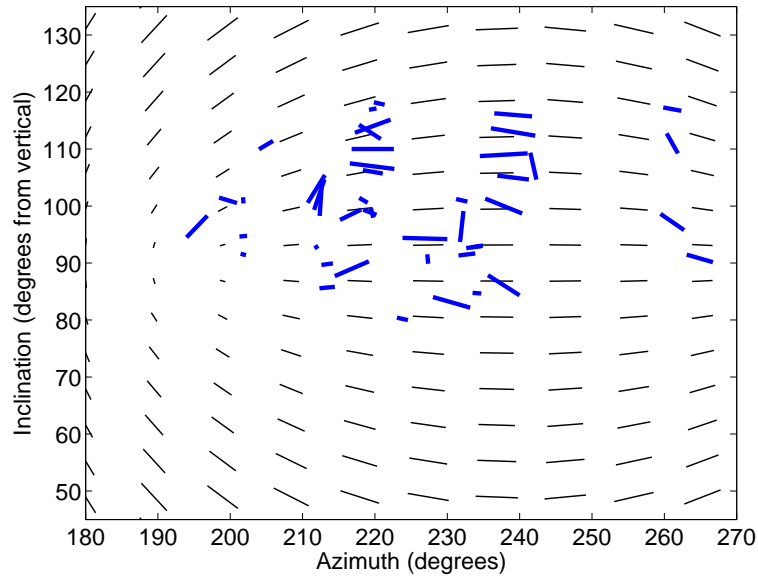


Figure 4.12: Cylindrical projections of splitting measurements (blue) for water injection. The x- and y-axes give the arrival angles of the S-waves used to measure splitting. The tick orientations indicate ψ - a vertical tick indicates that ψ is parallel to the qS_V axis, a horizontal tick indicates that ψ is parallel to S_H . Tick lengths represent δV_S . Also plotted (black) are the results for the models that best fit the data.

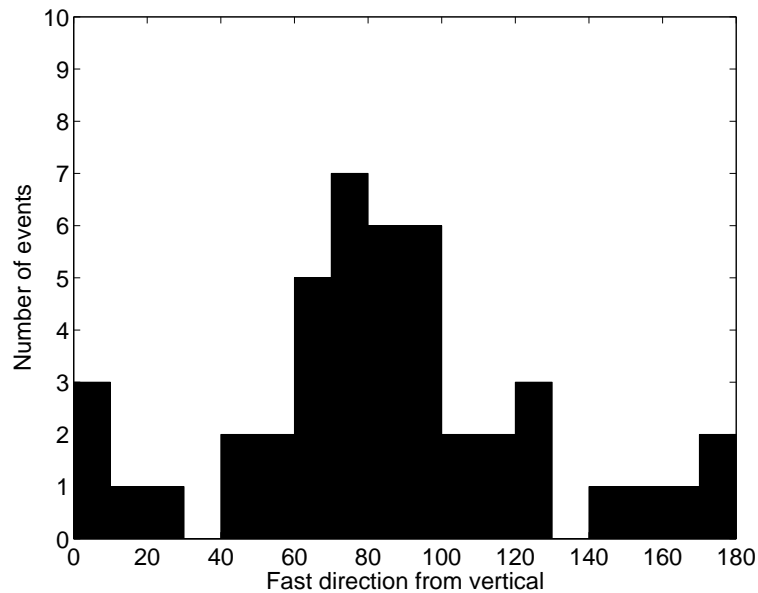


Figure 4.13: Histogram showing ψ (in degrees from qS_V) for the SWS results during water injection.

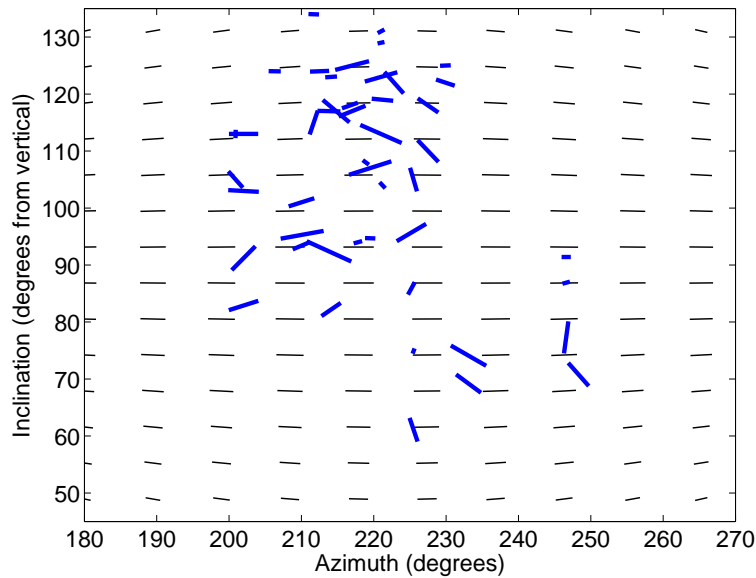


Figure 4.14: Horizontal projection of splitting orientations and magnitudes during CO₂ injection, in the same format as Figure 4.12.

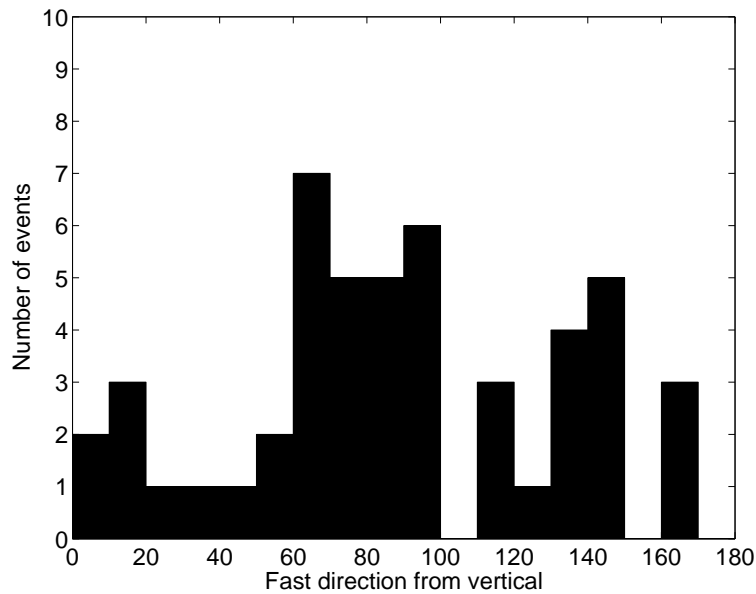


Figure 4.15: Histogram showing ψ (in degrees from qS_V) for the SWS results during CO₂ injection.

deformational regime in this field is strike slip. As such, for S-waves travelling subhorizontally from a strike slip event, the orientation of the initial S-wave polarisation, θ_S , will be subhorizontal. θ_S is computed by SHEBA as part of the SWS analysis, and the results are plotted as histograms in Figure 4.16. During water injection θ_S appears mainly to be orientated subhorizontally, consistent with the

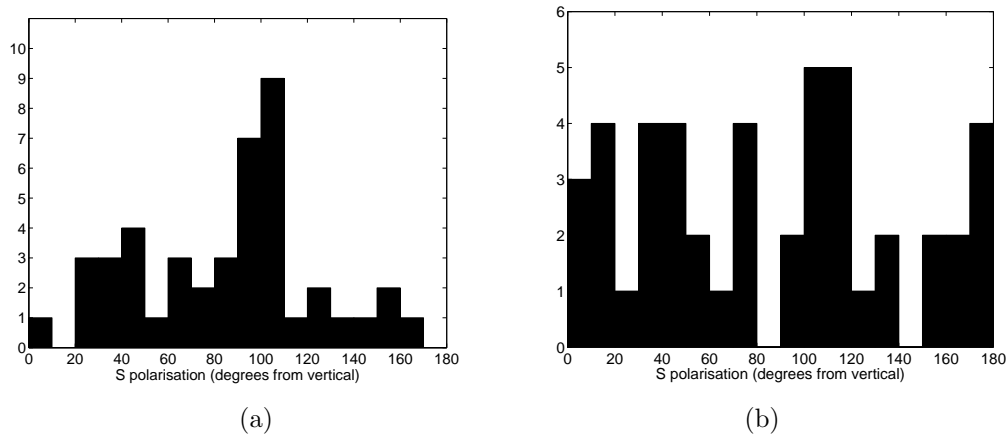


Figure 4.16: Histograms of initial S-wave polarisation for the successful splitting results during water (a) and CO₂ injection (b). The modal polarisation during water injection is subhorizontal, suggesting a strike-slip failure mechanism. The polarisations during CO₂ injection are much more scattered.

above inferences, while during CO₂ injection the data has significantly more scatter, but shows the same trend. This raises a potential problem in that ψ and θ_S are apparently very close (i.e., both are horizontal). In theory, if ψ and θ_S are identical, then splitting will not occur and null results will be produced by the splitting analysis (Wüstefeld and Bokermann, 2007; Wüstefeld et al., 2010a). In reality, with real data that contain noise, if ψ and θ_S are close then the SWS analysis may produce unreliable results.

4.5.1 Modelling the effects of θ_S on splitting analysis

In order to investigate this issue I developed synthetic tests to assess how close θ_S and ψ can get before the results become unreliable. I assess the reliability of the SWS measurement while varying 3 parameters: the difference between θ_S and ψ ; the signal/noise ratio; and the time-lag between the fast and slow S waves, considered here as a non-dimensional parameter by multiplying by the dominant wave frequency.

<i>Time-lag</i> δt	<i>Non-dimensional time-lag</i> δt^N ($=\delta t \times \omega$)
0.5s	0.075
1.0s	0.15
2.0s	0.30
3.0s	0.45

Table 4.2: Time-lags and equivalent non-dimensional time-lags for synthetic modelling of the effects of θ_S on SWS analysis.

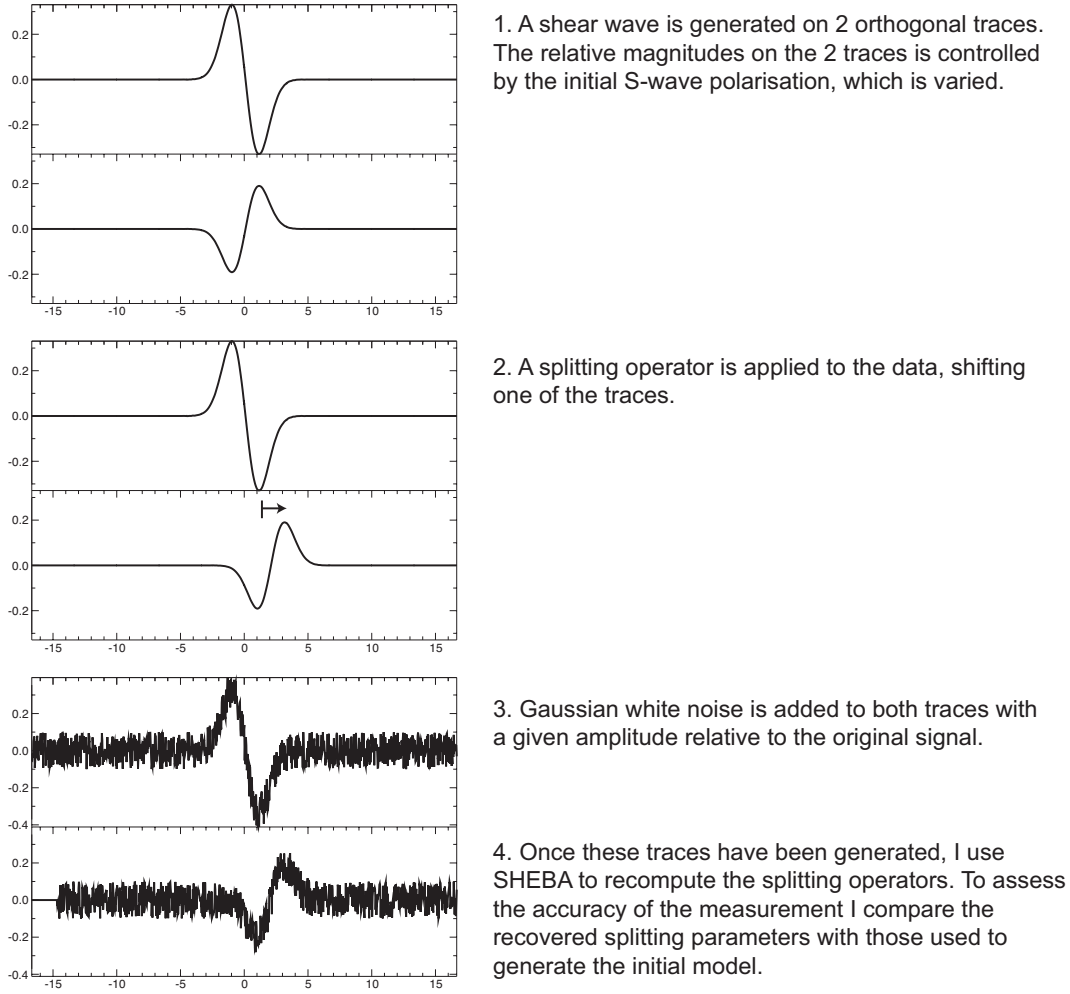


Figure 4.17: Workflow for generating synthetic splitting results to test the effects of θ_S on SWS analysis.

I generated synthetic waveforms with a given θ_S (varying between $90-130^\circ$), and a frequency of 0.15Hz, before applying a splitting operator with ψ of 90° and δt of between 0.5-3.0 seconds. The splitting operator rotates the waveform to provide a fast and a slow component, and delays the waveform parallel to the slow axis by δt . The time-lags used are given in Table 4.2, along with the corresponding non-dimensional equivalents δt^N . I add Gaussian white noise to the waveforms with a given amplitude relative to the initial unsplit waveform amplitude of between 0-0.3. The workflow for this process is outlined in Figure 4.17.

Having generated these synthetic waveforms, I use SHEBA to regenerate the initial splitting operators ψ and δt . These can then be compared with the initial input splitting operators to assess how accurate the splitting measurement has been. I find that the measurement of ψ is almost always accurate except when ψ and θ_S are exactly equal. Figure 4.18 shows the accuracy of the measurement

of δt as a function of the difference between ψ and θ_S , the signal/noise ratio and δt . From this figure I note that the measurement of δt is not always accurate. When $\delta t^N=0.075$ the boundary between accurate and inaccurate δt measurement appears to follow a linear relationship between $(\psi - \theta_S)$ and $(\text{signal-to-noise})^{-1}$. When δt^N is increased to 0.15 or above, the limit for accurate measurement of δt appears to be where $(\psi - \theta_S) \geq 10 - 15^\circ$, excepting where there is a very low signal-to-noise ratio. This result is in agreement with the more in depth analysis on this issue conducted by Wüstefeld and Bokelmann (2007).

This analysis used a Gaussian white noise distribution, which may not be the most appropriate way to add noise. A method to analyse this issue in greater depth would be to use the noise as it is found in the pre-first-arrival traces, which will be of a more correlated nature. Such a noise distribution might start to interfere with the signal at higher signal:noise ratios. However, using such a distribution, while it might affect the signal:noise ratios at which small $\psi - \theta_S$ values become an issue, it would not affect the limit at which small $\psi - \theta_S$ becomes an issue for accurate measurement (i.e. the $\pm 10^\circ$ limit identified here).

4.5.2 θ_S and ψ in the data

The average splitting magnitude in the real data is approximately 2ms, and the dominant frequencies are $\approx 150\text{Hz}$. Hence, δt^N is approximately 0.3. At this limit (Figure 4.18c), the splitting measurements will be reliable so long as the difference between θ_S and ψ is greater than 10° (the same applies when θ_S is close to the slow direction, 90° away from ψ).

The difference between ψ and θ_S for the data is plotted in Figure 4.19. I note at this point that the selection of class A events was made before the modelling work was undertaken, and so did not explicitly take into account the difference between θ_S and ψ in the selection of reliable splitting results. The sole selection criteria were those discussed in Teanby et al. (2004b). The overall pattern is for θ_S and ψ to be similar (i.e., as expected, both are sub-horizontal). I would expect that, in reality, the overall majority of recorded events would have θ_S and ψ very similar. However, I note that no reliable events are found when θ_S and ψ are within 10° of each other. These events have been rejected not explicitly because θ_S and ψ are within 10° , but because they do not fulfil the criteria of Teanby et al. (2004b). However, it is evident that, as anticipated from the synthetic analysis, almost no reliable results are found when θ_S and ψ are within 10° (or $80-100^\circ$). None are found in the water injection data, 2 are found in the CO_2 injection data, so 2 out of 92 measurements fall within this 10° limit. This serves as a verification of the conclusions presented above regarding unreliable results when θ_S and ψ are similar, and demonstrates that the selection criteria outlined by Teanby et al. (2004b) are effective in removing unreliable splitting measurements. An example of a typical null event rejected during the analysis is shown in Figure 4.20. I conclude that, although the polarisation of the initial S-waves and the fast splitting direction do appear to be similar, the splitting measurements that we use are still reliable.

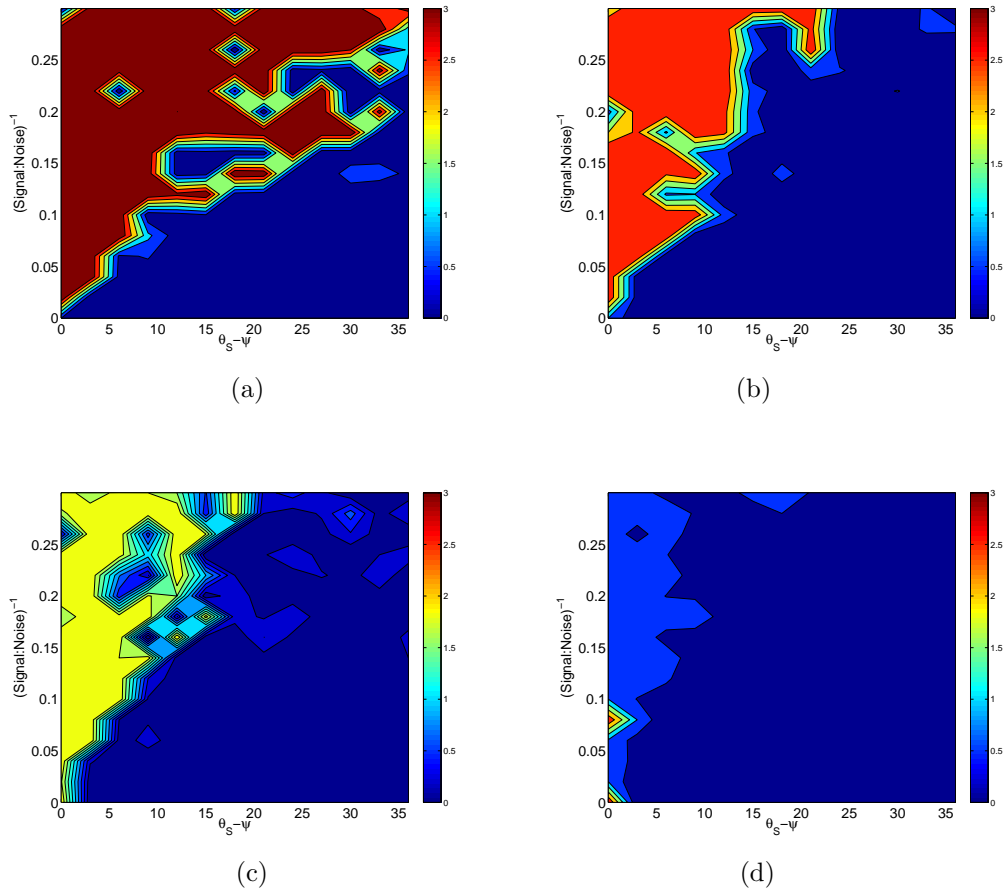


Figure 4.18: These plots show the difference between initial and measured δt from the synthetically generated seismograms (blue colours indicate that the time-lag has been accurately measured) as a function of signal-to-noise ratio and the difference between ψ and θ_S . (a) shows the accuracy when $\delta t^N = 0.075$, (b) shows $\delta t^N = 0.15$, (c) shows $\delta t^N = 0.30$, and (d) shows $\delta t^N = 0.45$.

4.6 Interpretation of shear wave splitting results

4.6.1 Synthetic tests

As in Chapter 3 I use synthetic forward modelling to determine what to expect with the range of SWS arrivals available. The source-receiver geometry for this case is limited to subhorizontal arrivals with a 70° range in azimuth (Figure 4.21a). Given such a limited range of arrivals, can we expect to image fractures, and if so, to identify their strike and density? Note that as we are dealing with subhorizontal arrivals, variation in δ does not significantly affect the inversion. Hence for the following examples I do not plot δ , plotting the misfit as a function of γ , α and ξ at the best fit value of δ . The first model I consider has no fractures, only a VTI fabric with $\gamma = 0.04$ (see Chapter 3). The results are shown in Figure 4.21; the inversion accurately identifies the lack of fractures and determines γ

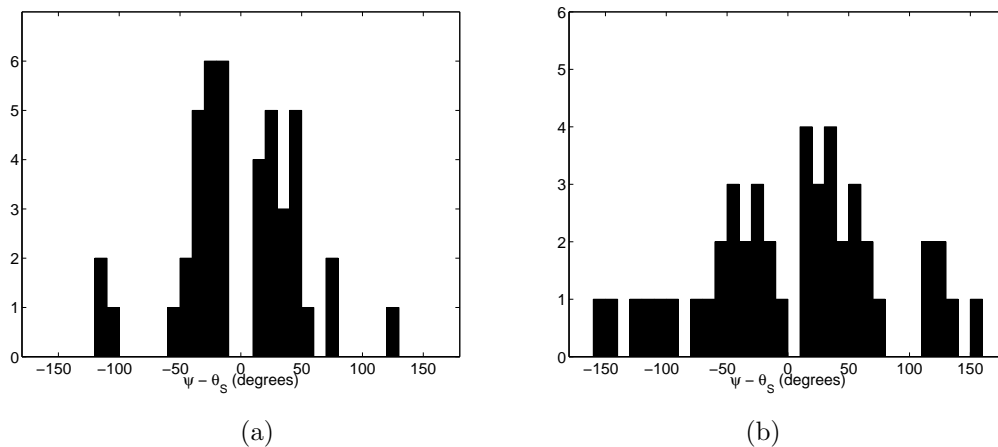


Figure 4.19: Histogram showing the differences between ψ and θ_S during water (a) and CO₂ (b) injection. Note that no successful measurements are found where they are within 10° of each other.

satisfactorily. I contrast this with a model containing fractures striking at $\alpha=120^\circ$ with a density of $\xi=0.08$. In this case, the waves propagate in directions close to the fracture normals. The results are shown in Figure 4.22. The inversion accurately identifies the fracture strike and VTI fabric strength. Fracture density is constrained to some extent, but not as accurately as for the other parameters. This is because waves travelling close to fracture normals are not split by them, making them difficult to image. A limitation exists that, for this geometry of raypaths and fractures, it is difficult to constrain fracture density. This should be remembered when we come to look at the real dataset.

To further test how well imaged the fracture strike is for this source-receiver geometry, I construct a final synthetic test, with the same range of arrivals, but fractures now striking at 90° , which is 30° away from the strike used in the previous model. The results, in Figure 4.23, show that the differences in fracture strike between this and Figure 4.22 have been correctly identified. Furthermore, the uncertainty in ξ appears to have been reduced compared to Figure 4.22. I suggest that this is because the waves have travelled at a more oblique angle to the fractures, and so are more affected by them. Again, this demonstrates the insight that can be gained by developing synthetic models. For instance, from Figure 4.22 I anticipate that our dataset will be able to constrain fracture strike but not the fracture density. Furthermore, synthetic modelling can highlight ways to improve the effectiveness of the inversion. For instance, from Figure 4.23 we suggest that had the geophones been placed such that the shear waves had travelled closer to the fracture strike (if only by a 30° difference) then it may have been easier to image the fracture density. This capacity may be of use to field engineers when selecting sites to place geophones.

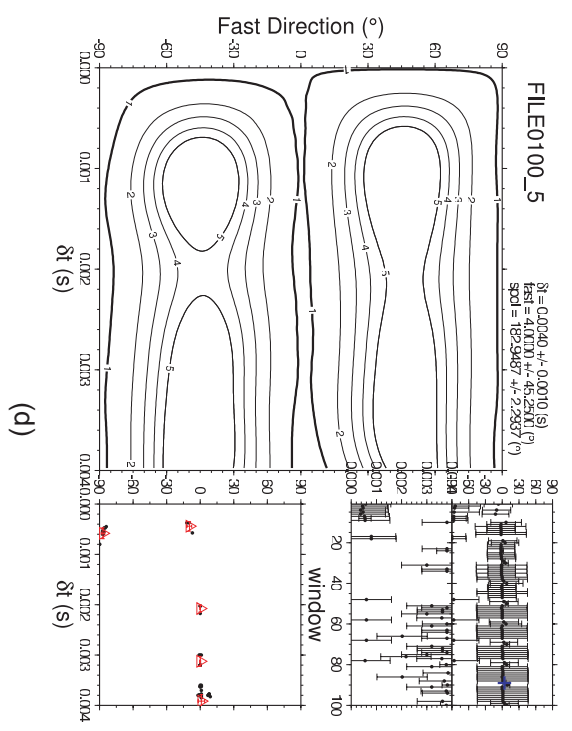
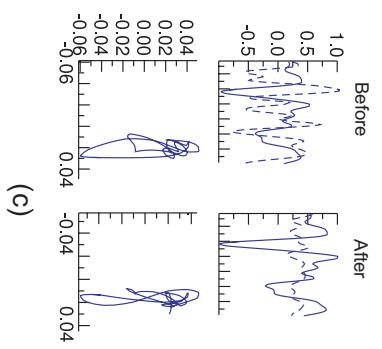
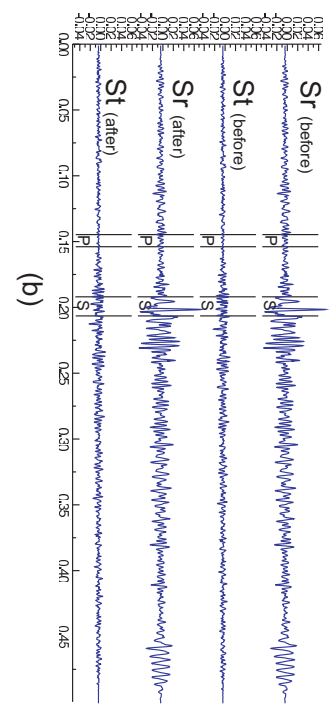
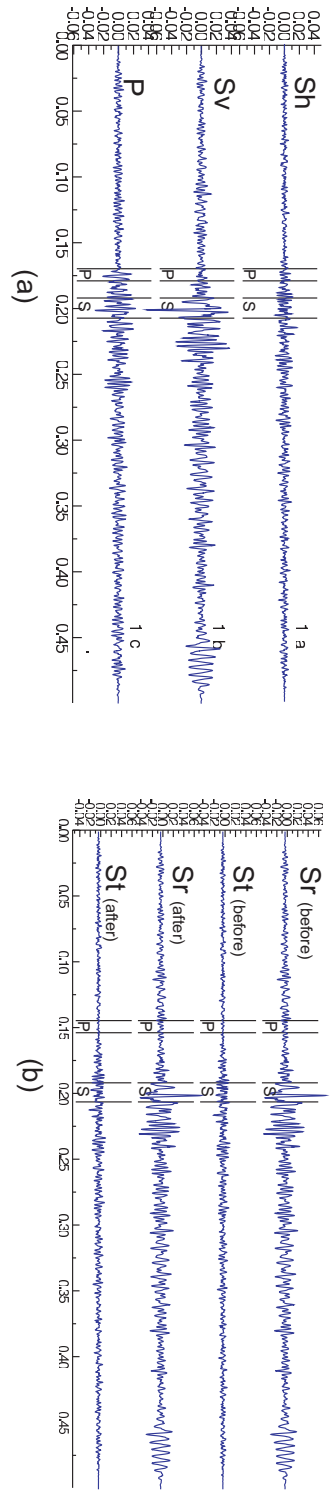


Figure 4.20: An example of a typical null splitting result. The fast direction (given by 'fast' in (d) is close to the S-wave polarisation ('spot' in (d)), so no splitting occurs. As a result, there is no energy on the initial transverse component (b), and so the inversion approach, which is based on minimising the energy on the transverse component, is not reliable.

4.6. INTERPRETATION OF SHEAR WAVE SPLITTING RESULTS

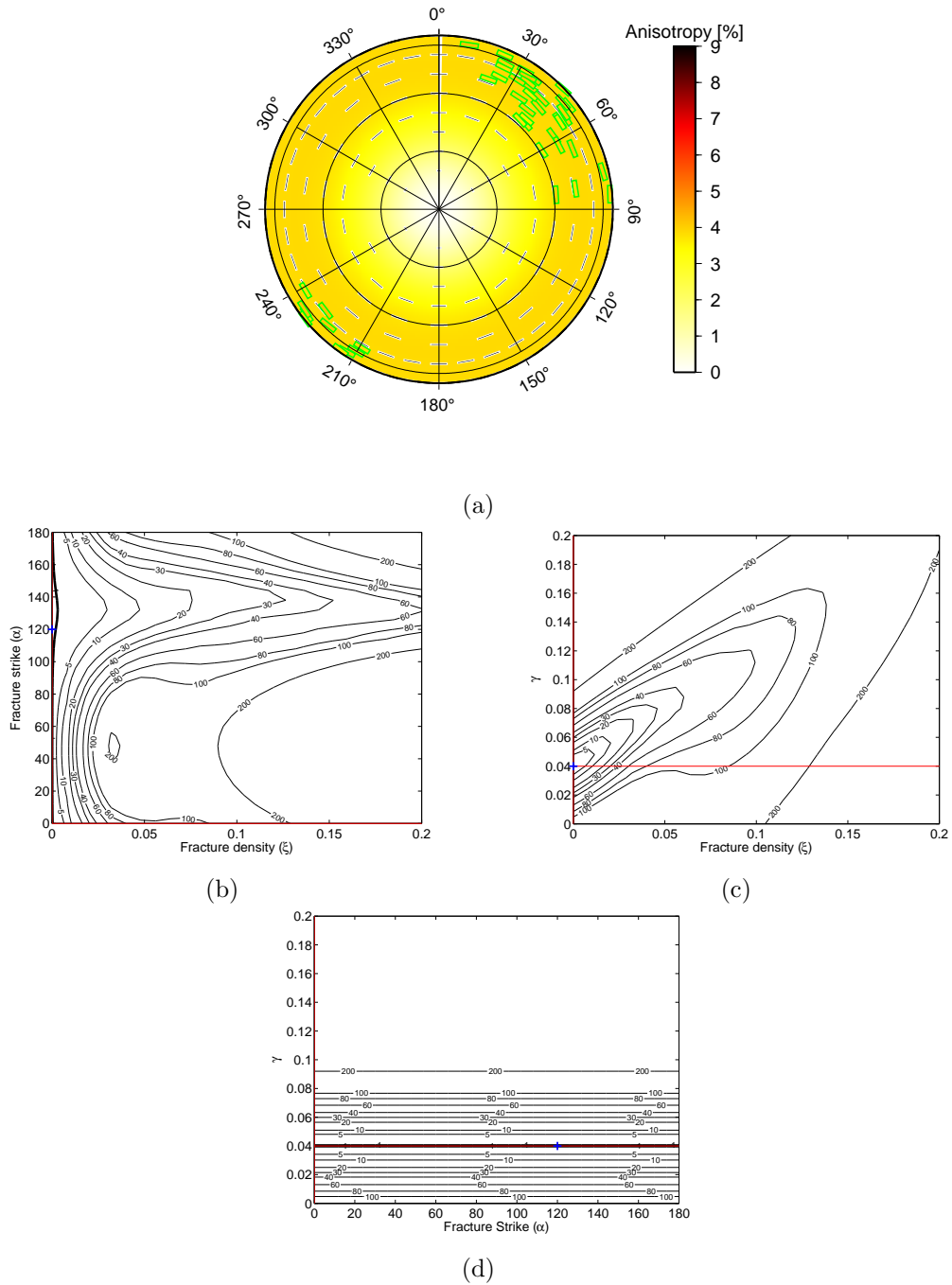


Figure 4.21: Synthetic inversion for a case with no fractures. This case uses the arrivals from the real data, which are subhorizontal. In (a) I plot an upper hemisphere projection of the synthetic data (coloured ticks) and the best fit model splitting results (thin ticks and contours) in the same format as Figure 3.5a. The initial elastic model has $\gamma=0.04$ and $\delta=0.1$, with no fractures present ($\xi=0$). As the inversion is not sensitive to δ , we plot the misfit contours as a function of γ , α and ξ . The inversion accurately identifies γ and the lack of fractures.

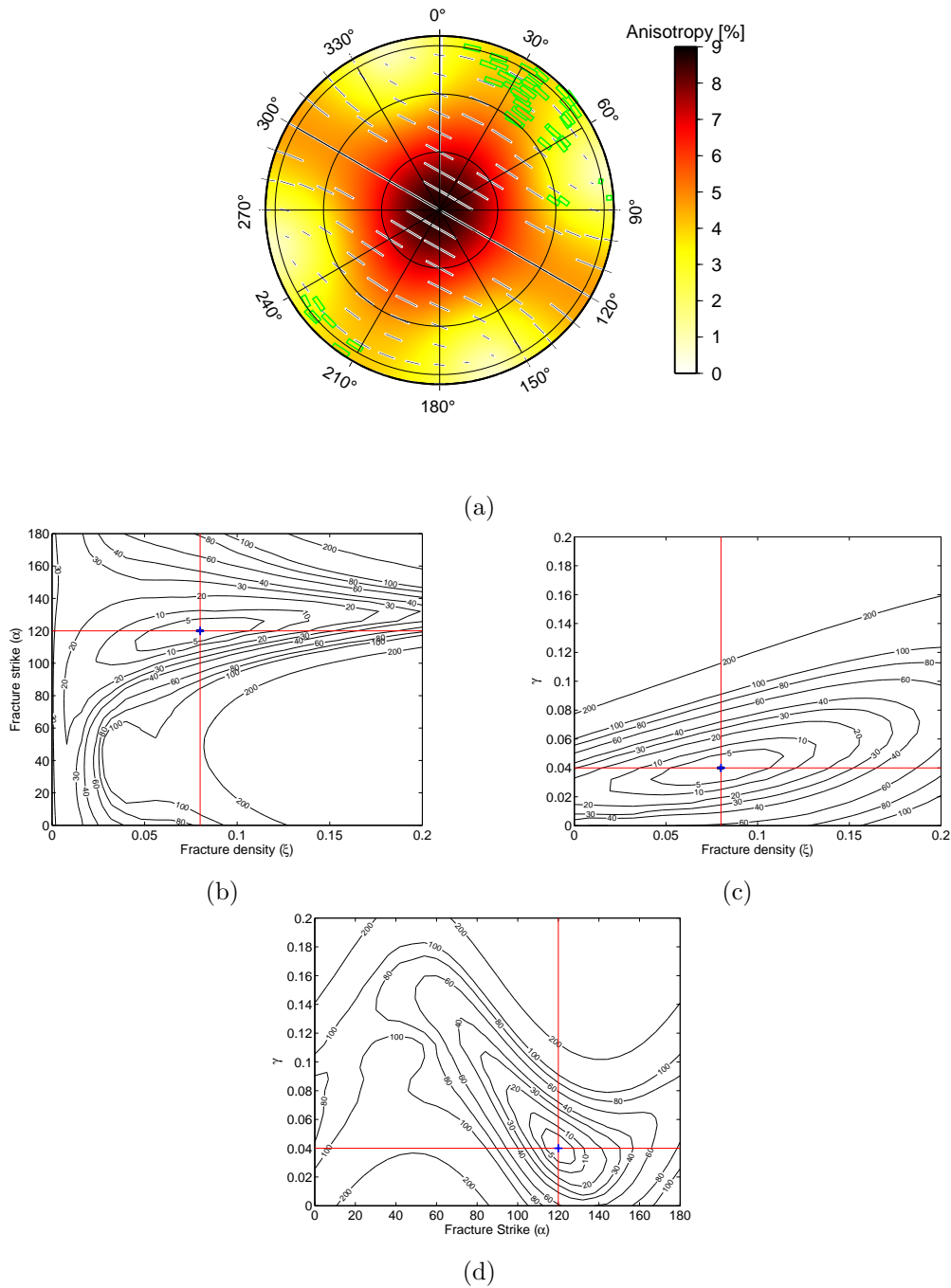


Figure 4.22: Synthetic inversion for a situation with fractures striking 120° , in the same format as Fig. 4.21. This case also has subhorizontal arrivals, but with fractures striking at 120° ($\gamma=0.04$, $\delta=0.1$, $\xi=0.08$ and $\alpha=120^\circ$). The inversion accurately identifies γ and the fracture strike, but fracture density is only poorly constrained.

4.6. INTERPRETATION OF SHEAR WAVE SPLITTING RESULTS

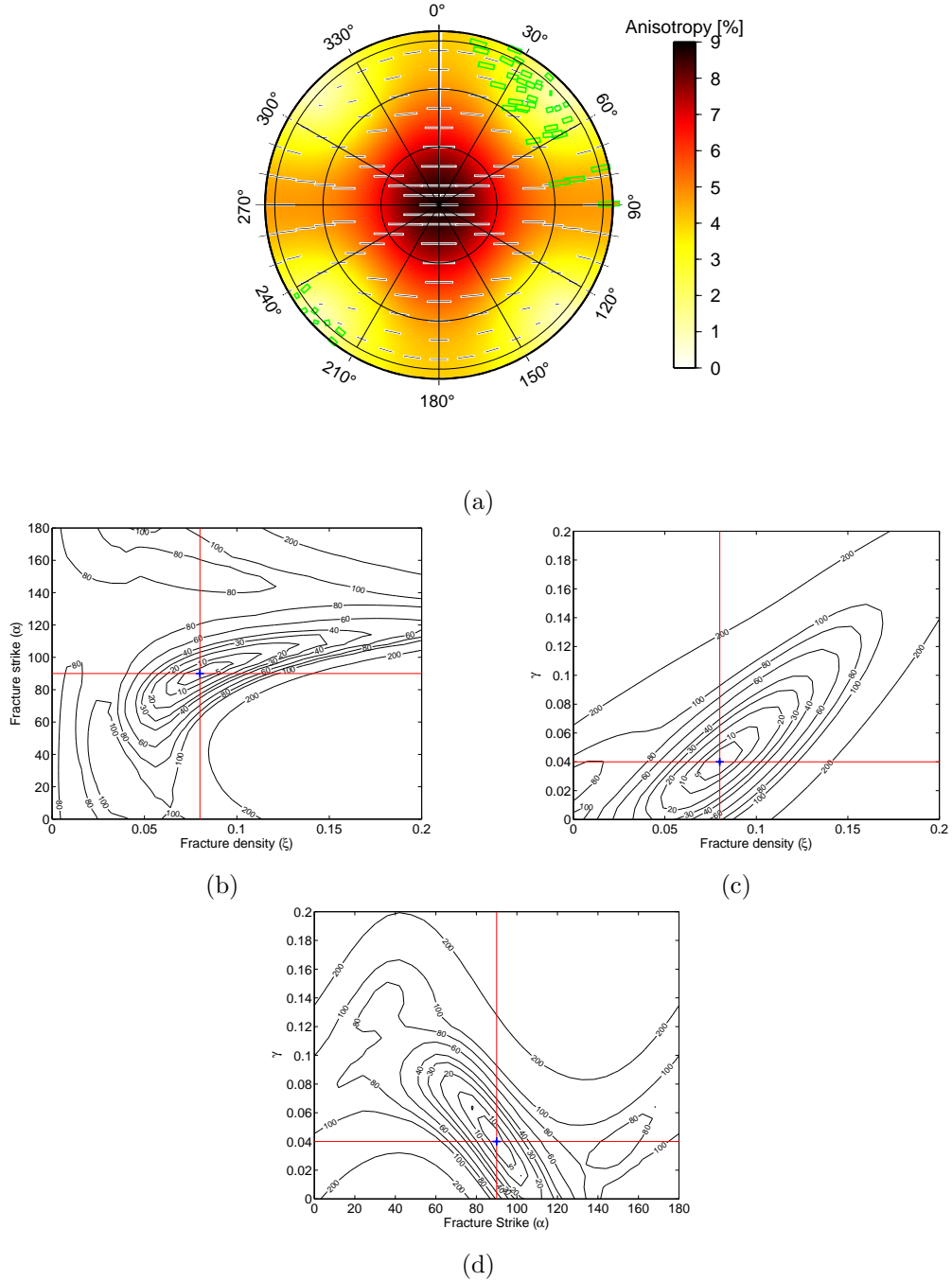


Figure 4.23: Inversion results for the final synthetic example, in the same format as Figure 4.21. This case also has subhorizontal arrivals, but with fractures striking at 90° ($\gamma=0.04$, $\delta=0.1$, $\xi=0.08$ and $\alpha=90^\circ$). As the waves have travelled more obliquely to the fractures, fracture density is better constrained than in Figure 4.22.

	ξ^1	α^1	γ	δ
Water	0.1	120°	0.04	0.1
CO ₂	0.01	141°	0.038	0.0

Table 4.3: Splitting inversion results for the events during water and CO₂ injection.

4.6.2 Interpretation of datasets

The results of the inversion for SWS during water injection are plotted in Figure 4.24 and listed in Table 4.3. I note that as anticipated from the inversions with synthetic data, the fracture strike and sedimentary fabric are well imaged (with $\alpha=120^\circ$ and $\gamma=0.04$) while the fracture density is not well constrained. As an independent measure of fracture strike, the event locations (Section 4.2) indicate the formation of fractures trending at approximately 120° from the injection well. The match between fracture strikes estimated from event locations and from SWS demonstrates the success of the SWS inversion. I plot the splitting predicted by the best fit model in Figure 4.12, and note a good match between my model and the observed splitting.

The inversion results for during CO₂ injection are shown in Figure 4.25 and listed in Table 4.3. The best fit model parameters are $\alpha=141^\circ$ and $\gamma=0.038$. The fracture strike appears to be poorly constrained. This is because, at very low values of fracture density, the fracture strike parameter becomes unimportant (if there are no fractures, it doesn't matter what direction 'no fractures' are striking). The range within the 90% confidence interval, for higher fracture densities, does match the fracture orientation imaged by the event locations during CO₂ injection. The fracture density given by the inversion for during CO₂ injection is less than that for during water injection. This might suggest that the CO₂ injection has indeed caused a smaller amount of fracturing. However, note that the 90% confidence surfaces from water and CO₂ injection overlap between $\xi \sim 0-0.06$, hence this conclusion cannot be supported given the limitations that the source-receiver geometry impose on the ability to constrain fracture density. This limitation has been identified *a priori* using synthetic forward modelling.

The match between γ for both stages is also encouraging. Kendall et al. (2007) note that the strength of VTI fabric (given by γ) often correlates with reservoir quality, as the presence of clay particles both reduces reservoir quality and introduces VTI symmetry. Although specific information about the lithologies at either depth is not available, the rocks at both depths are believed to be similar. Therefore I anticipate that γ should be similar for both depths, and this is indeed the case, a further indication of the success of this inversion method. Although I have no way to independently verify γ by any other method, the values found are well within the range expected for typical sedimentary rocks (Thomsen, 1986).

4.6. INTERPRETATION OF SHEAR WAVE SPLITTING RESULTS

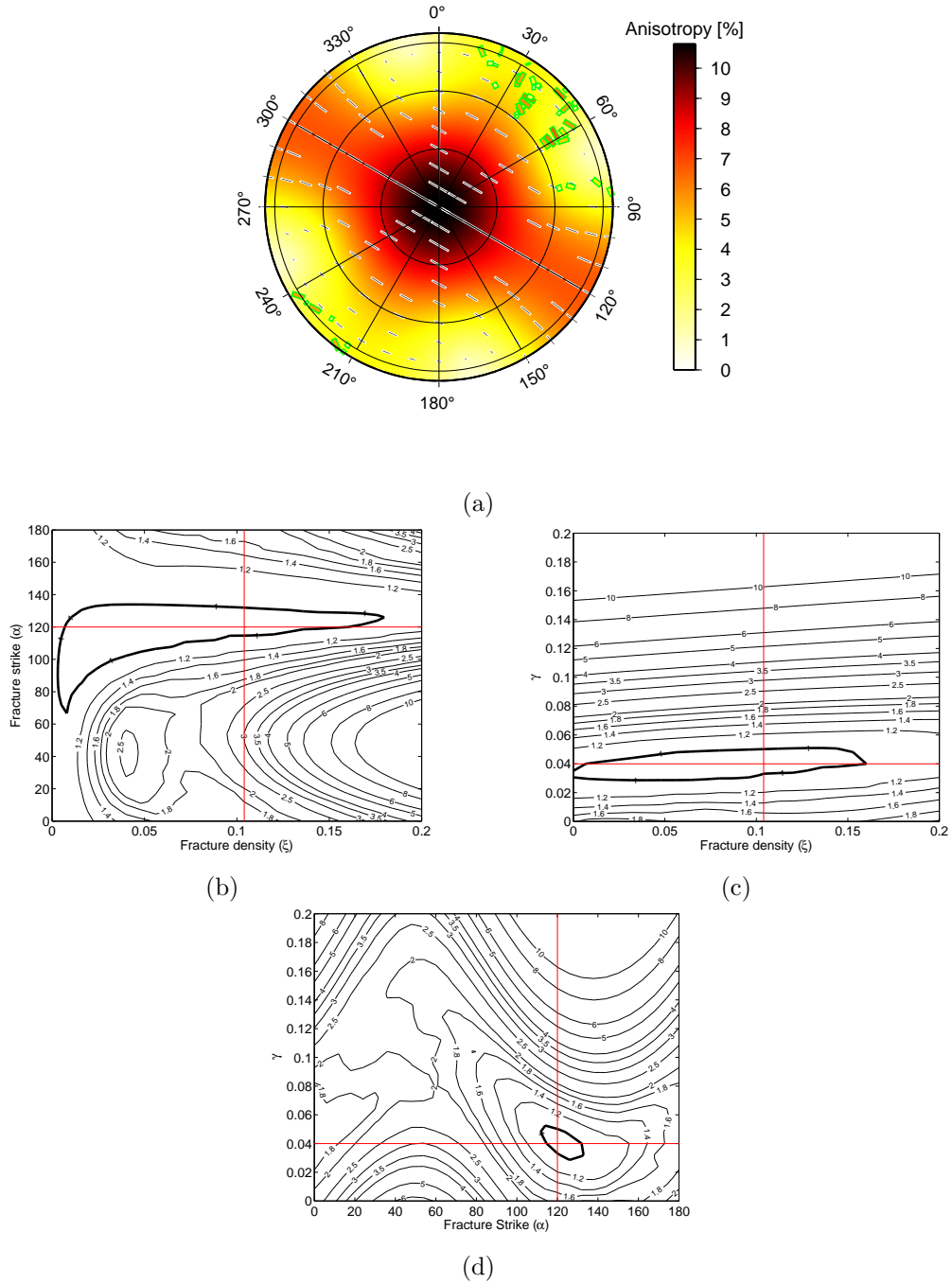


Figure 4.24: SWS inversion results for the water injection stage, in the same format as Figure 4.21. The inversion has accurately determined the fracture strike and sedimentary fabric strength. The fracture density is poorly constrained.

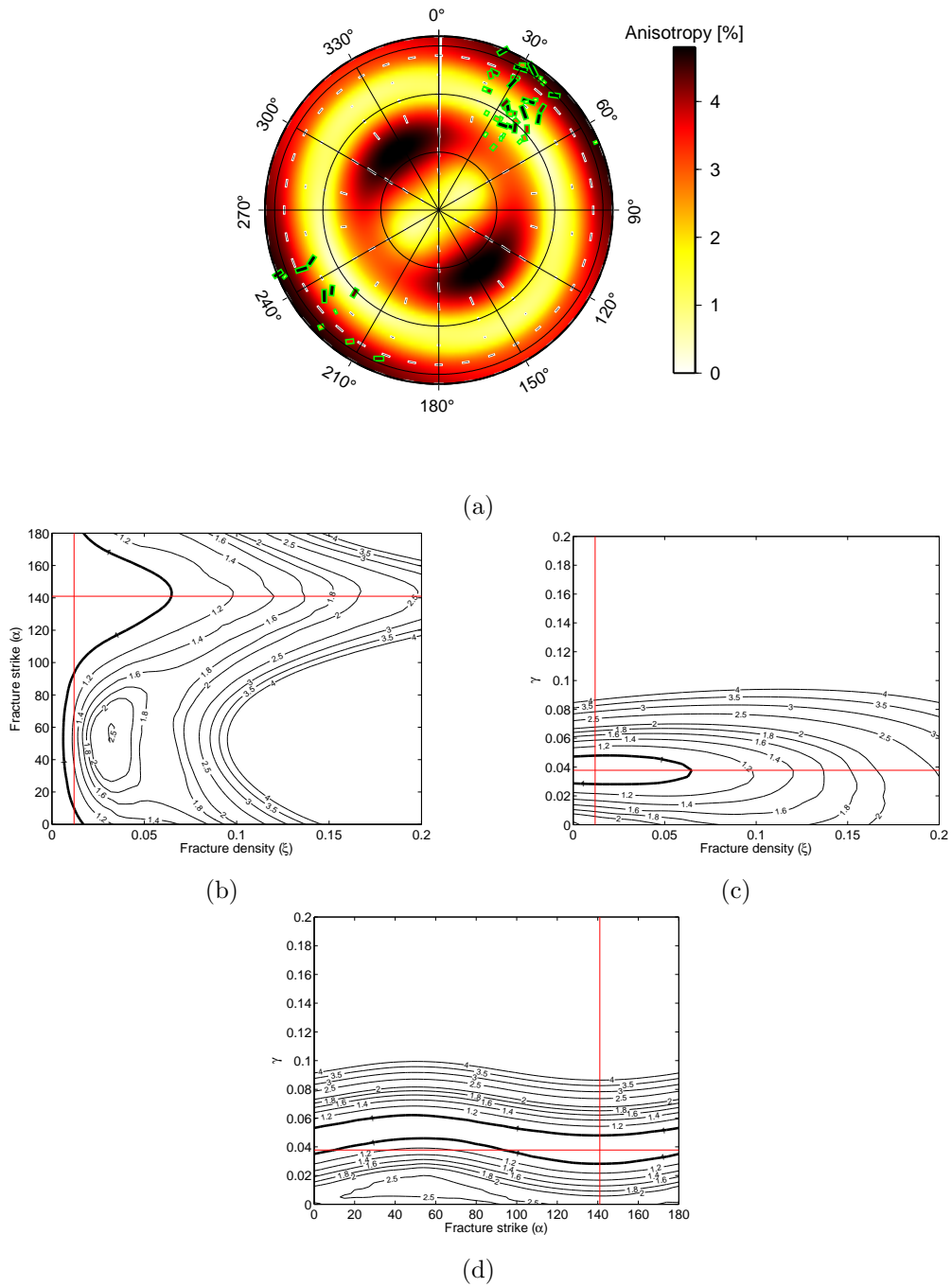


Figure 4.25: SWS inversion results for during CO₂ injection, in the same format as Figure 4.21. The best fit model is marked.

4.7 Discussion

The data presented here come from a hydraulic fracture job, where fluids have been injected at pressures greater than 40MPa with the intention of causing fracture, whereas at Weyburn injection pressures are \sim 20-25MPa, with the intention of minimising fracture. There are also differences in geology between Weyburn and the case presented here. As such, direct comparisons cannot be made. So far, little research has been conducted to compare the amount of fracturing induced by injection of different fluids with different properties. Therefore, it is of interest to compare the patterns of seismicity generated in this case. In both cases, microseismicity images vertical fractures propagating away from the injection site. There are some differences between the patterns of microseismicity - the seismogenic zone during water injection is limited to perforation depths, although it has a larger lateral extent. The seismogenic zone during CO₂ injection does not extend as far laterally, but does have microseismicity extending up to 100m above the injection point. The rates and magnitudes of seismicity generated are also similar. There is a greater temporal spread of seismicity throughout the water injection stage, while the majority of events during CO₂ injection occur at the beginning of the stage.

However, the discussion of these minor differences risks missing the wood for the trees, because overall, the patterns of seismicity induced by injection of the two fluids are remarkably similar. The primary purpose of my analysis of this data was to investigate whether the increased compressibility of CO₂ is the reason for the limited seismicity observed at Weyburn. Here, I have found that event magnitudes are loosely correlated with injection pressure, and do not appear to show a dependence on the fluid properties. The rates of seismicity are also very similar. Although at face value the SWS measurements during water injection appear to suggest a higher fracture density, the geometry of event locations and geophones has made it difficult for splitting measurements to provide good constraints, so this conclusion is not robust. I conclude that, despite the differences in compressibility, viscosity, density and relative permeability between the fluids, CO₂ and water have produced similar patterns of microseismicity. Certainly, there is no evidence to suggest that CO₂ is a ‘softer hammer’ that will be less capable of inducing microseismic events.

4.8 Summary

- A lack of seismicity observed at Weyburn has led to the suggestion that CO₂ has an inherently lower seismic deformation efficiency than water, with obvious implications for the feasibility of using microseismic events to monitor CCS sites.
- In order to test this assertion, I compared the microseismic response of CO₂ and water injection into the same reservoir - a North American oil field undergoing hydraulic fracture stimulation.
- Event locations image the formation of fractures trending away from the injection well. Events during CO₂ injection are observed well above the injection depth, possibly as a result of the increased buoyancy and mobility of CO₂.
- Event magnitudes show correlation with injection pressures for both water and CO₂. The event magnitudes and rates of seismicity for both fluids are similar. This indicates that, for this case at least, there is no difference in the amount of deformation induced by CO₂ and water injection.
- Shear-wave splitting successfully images the fractures, but within the limits imposed by the source-receiver geometry there is no evidence to suggest a lower degree of fracturing during CO₂ injection.
- A method is developed to test the sensitivity of splitting measurements to the initial S-wave polarisation. I find that SWS measurements are reliable so long as the fast direction and initial polarisation are greater than 10° apart. I also find that the selection criteria outlined by Teanby et al. (2004b) are sufficient to pick up and remove these inaccurate results.

INJECTION

Even the self-assured will raise their perceived self-efficacy if models teach them better ways of doing things.

Albert Bandura

5.1 Introduction

Microseismic monitoring provides information about the geomechanical deformation occurring in and around the reservoir. As such, the interpretation of microseismic activity can be greatly improved by geomechanical modelling. Geomechanical models commonly use finite element techniques to simulate the deformation caused by pore pressure changes in the reservoir. Injection of CO₂ will increase the pore pressure in the reservoir. This represents the loading for the geomechanical model, which computes the deformation both inside and around the reservoir. By examining the stress evolution it is possible to identify areas in and around the reservoir where fractures are likely to form or be reactivated. In this chapter I use a relatively novel technique where a geomechanical model is coupled to a fluid-flow simulator. This allows changes in pore pressure to be passed directly to the geomechanical model, and changes in porosity and permeability to be returned to update the fluid model. The modelling method has been developed by the Integrated Petroleum Engineering, Geomechanics and Geophysics (IPEGG) consortium. In this chapter I introduce the modelling technique and demonstrate it with several simple numerical simulations. I use these to examine how factors such as the reservoir geometry and material properties affect the stress evolution during CO₂ injection.

5.2 Effective stress and stress path parameters

The concept of effective stress was introduced by Terzaghi (1943). When a stress is applied to a porous material, part of the stress will be supported by the matrix material, and part will be supported by the fluid in the pores. The part of the stress supported by the matrix is termed the effective stress, given in tensorial form as σ'_{ij} . It is the effective stress that will determine the deformation of the rock frame. The effective stress is a function of the external stress applied to the rock, σ_{ij} , and the pore pressure, P_{fl}

$$\sigma'_{ij} = \sigma_{ij} - \beta_w I_{ij} P_{fl}, \quad (5.1)$$

where I_{ij} is a 3×3 identity matrix, and β_w is the Biot-Willis parameter (e.g., Mavko et al., 1992), assumed here to be 1. The magnitudes of the principle effective stresses are given by the eigenvalues of σ'_{ij} , and when referring to these I will use only one subscript, e.g., σ'_1 . The corresponding eigenvectors give the orientations of the principal effective stresses. One of the principal stresses is usually orientated

subvertically, and I shall use σ'_3 to denote this term, with σ'_1 and σ'_2 referring to the subhorizontal principal stresses.

5.2.1 Mean and differential stress

The mean stress, p , is defined as the mean of the principal stresses,

$$p = (\sigma'_1 + \sigma'_2 + \sigma'_3)/3, \quad (5.2)$$

and the differential stress, q , is defined as the difference between the maximum and minimum principal stresses,

$$q = \sigma'_3 - \sigma'_1. \quad (5.3)$$

High differential stresses will increase shear stresses and cause fractures to develop.

5.2.2 Mohr circles

During injection, a pore pressure increase will lead to an evolution of the effective stress tensor due to changes both in P_{fl} and in σ_{ij} ,

$$\Delta\sigma'_{ij} = \Delta\sigma_{ij} - \beta_w I_{ij} \Delta P_{fl}. \quad (5.4)$$

In order to visualise stress evolution, I will use Mohr circle plots, plotted in $\sigma'_n - \tau$ space. τ is the shear stress, and σ'_n is the normal stress, acting on any 2D planar surface in the rock. Each point on the circumference of the Mohr circle defines σ'_n and τ for a plane at the given angle. The shear stress, τ , is maximum when the plane is at 45° to the principal stress, is given by

$$\tau = q/2 = \frac{\sigma'_3 - \sigma'_1}{2}, \quad (5.5)$$

The Mohr circle can be defined by the maximum and minimum principal effective stresses. For any surface in the rock mass, shear failure will occur if the stresses exceed the Mohr-Coulomb envelope, given by

$$\tau = m\sigma'_n + \chi, \quad (5.6)$$

where m is the coefficient of friction and χ is the cohesion. The stress evolution in the reservoir during CO₂ injection is shown schematically in Figure 5.1 - if any point on the circle exceeds the yield envelope then shear failure can occur. m is often given in terms of an angle of friction,

$$m = \tan \phi_f \quad (5.7)$$

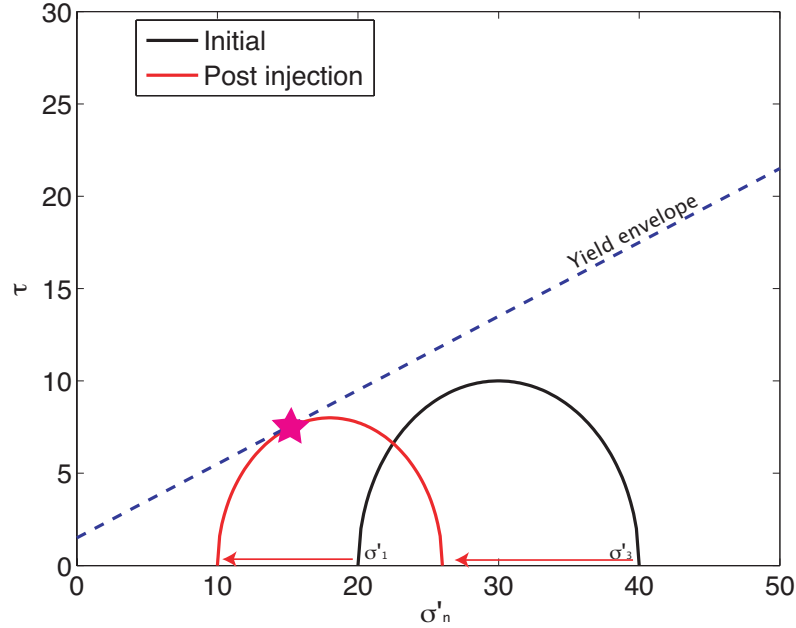


Figure 5.1: Evolution of the Mohr circle from initial to final stress state due to a pore pressure increase. The increase in pore pressure decreases the principal normal stresses, moving the Mohr circle to the left and increasing the likelihood of shear failure.

5.2.3 Stress path parameters

The changes in stress, and therefore evolution of the Mohr circle, can be defined in terms of three *stress path parameters*, K_0 , γ_1 and γ_3 :

$$K_0 = \frac{\Delta\sigma'_1}{\Delta\sigma'_3}, \quad (5.8)$$

$$\gamma_1 = \frac{\Delta\sigma_1}{\Delta P_{fl}}, \quad (5.9)$$

$$\gamma_3 = \frac{\Delta\sigma_3}{\Delta P_{fl}}. \quad (5.10)$$

In the following I assume that σ'_3 , the subvertical principal stress, is the largest. All of the stress path parameters provide specific information on the evolution of the Mohr circle during injection. The final position can be fully defined by any two of the three parameters, though at this stage I will outline all three. By considering various end-member cases one can see the effect each parameter has on the Mohr circle. This is summarised in Figure 5.2. When K_0 is small, the decrease in σ'_3 will be large compared to σ'_1 , and so the Mohr circle will reduce in size. How much so will depend on γ_1 . Where $K_0 = 1$, $\Delta\sigma'_1 = \Delta\sigma'_3$, and the circle will not change in size, only translate by an amount given by γ_1 . When $\gamma_1 = 0$, $\Delta\sigma'_1 = \Delta P_{fl}$, and the movement of the left-hand coordinate will be large, with the circle either shrinking or translating depending on the size of K_0 . Where γ_1 is large, $\Delta\sigma'_1 = 0$, and the left

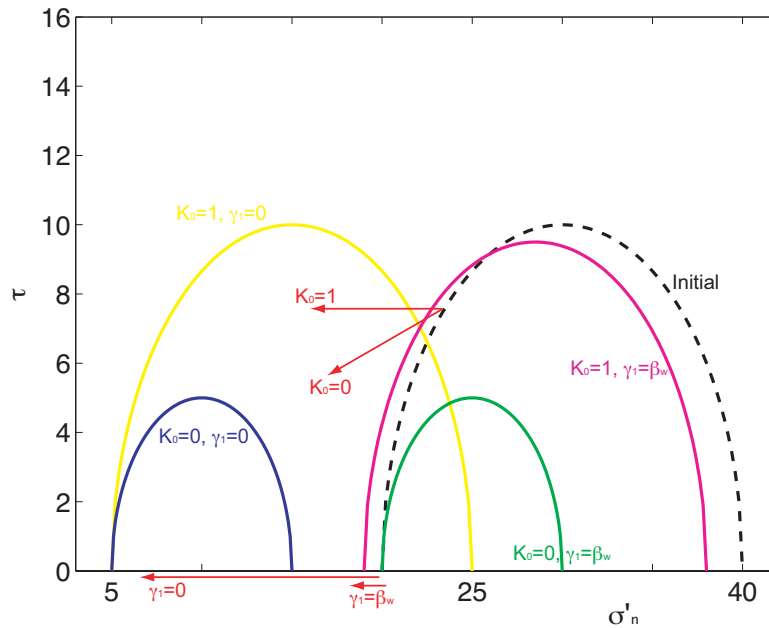


Figure 5.2: Cartoon showing how the evolution of the Mohr circle is dependent on the stress path parameters. K_0 controls the change in size of the circle, γ_1 controls how much the circle translates.

coordinate of the circle will not move, and so stress evolution is limited. When $\gamma_3 = 0$, $\Delta\sigma'_3 = \Delta P_{fl}$, and the movement of the right-hand coordinate will be maximum, with the circle either shrinking or translating dependent on the size of K_0 . When γ_3 is large, $\Delta\sigma'_3 = 0$, and the right coordinate of the circle will not move. If $K_0 = 1$ then the circle will not move, if K_0 is smaller then the circle will still shrink. The stress path parameters provide a quick way of assessing the stress evolution of a reservoir. In the following section I will compute the dependence of the stress path parameters on reservoir geometry and material properties using numerical techniques.

5.3 Numerical modelling

Most geomechanical modelling techniques use one-way coupling only, with pore pressures passed to the geomechanical model as a load. However, to increase accuracy, models should have a two-way coupling, where changes in porosity and permeability caused by deformation are returned to update the fluid flow simulation. This two-way coupling has only recently been developed in the hydrocarbon industry (e.g., Minkoff et al., 2004), and requires separate simulators to model the fluid flow and the geomechanical deformation.

5.3.1 Fluid-flow simulation

Any attempt to model geomechanical deformation of hydrocarbon reservoirs must begin by modelling the movement of fluid, the properties of the fluids, and the changes in pore pressure. Fortunately, such problems have long been of interest to the hydrocarbon industry, and so a range of commercial fluid-flow simulators are available. Most have good records of reliability for dealing with reservoir fluid flow processes. All are similar and can in theory be coupled to geomechanical simulators. Throughout this work I will be using MORE as the fluid-flow simulator, because of the ease with which it can be coupled using a bespoke Message Passing Interface (MPI) developed as part of the IPEGG project.

5.3.2 Geomechanical modelling

In order to model the geomechanical deformation, I use a finite element code, ELFEN, developed by Swansea University and Rockfield Ltd. ELFEN uses a CamClay constitutive model - this is described in detail by Crook et al. (2006) and is summarised below. In the elastic regime, the material deformation is modelled according to Hooke's law. The limits of elastic behaviour are defined by a yield surface (shown schematically in Figure 5.3) which is a smooth surface defined in $p - q$ space. The equation of the yield surface is given by

$$F(\sigma, \varepsilon_v^p) = g(\theta, p)q + (p - p_t) \tan \beta \left(\frac{p - p_c}{p_t - p_c} \right)^{1/n}, \quad (5.11)$$

where θ is the Lode angle, p_t and p_c are respectively the tensile and compressive intersects with the p axis, β is the friction angle, n is a material parameter. $g(\theta, p)$ describes a correction for the deviatoric plane,

$$g(\theta, p) = \left(\frac{1}{1 - \beta^\pi(p)} \left(1 + \beta^\pi(p) \frac{r^3}{q^3} \right) \right)^{N^\pi} \quad (5.12)$$

N^π is a material constant, and β^π is defined as a function of p as

$$\beta^\pi(p) = \beta_0^\pi \exp \left(\beta_1^\pi p \frac{p_c^0}{p_c} \right) \quad (5.13)$$

β_0^π and β_1^π are further material constants, and $r^3 = 27J_3'/2$, where J_3' is the third deviatoric stress invariant.

The evolution of the yield surface (strain hardening or softening) is computed as a function of the volumetric plastic strain, ε_v^p , following

$$p_c = p_c^0 \exp \left(\frac{v \varepsilon_v^p}{(\lambda - \kappa)} \right), \quad p_t = p_t^0 \exp \left(\frac{v (\varepsilon_v^p)_{max}}{(\lambda - \kappa)} \right), \quad (5.14)$$

where v is the specific volume, and λ and κ are the slopes of the normal compression and unloading-reloading lines (Crook et al., 2006), and $(\varepsilon_v^p)_{max}$ is the maximum volumetric plastic strain encountered by an element.

Inside the yield surface the deformation is elastic, controlled by the Young's modulus E and Poisson's ratio ν , which are given as a function of porosity, Φ and p ,

$$E = E^0 \left(\frac{p + A}{B} \right)^e (\Phi)^c, \quad \nu = \nu_{min} + (\nu_{max} - \nu_{min})(1 - \exp(-mp)). \quad (5.15)$$

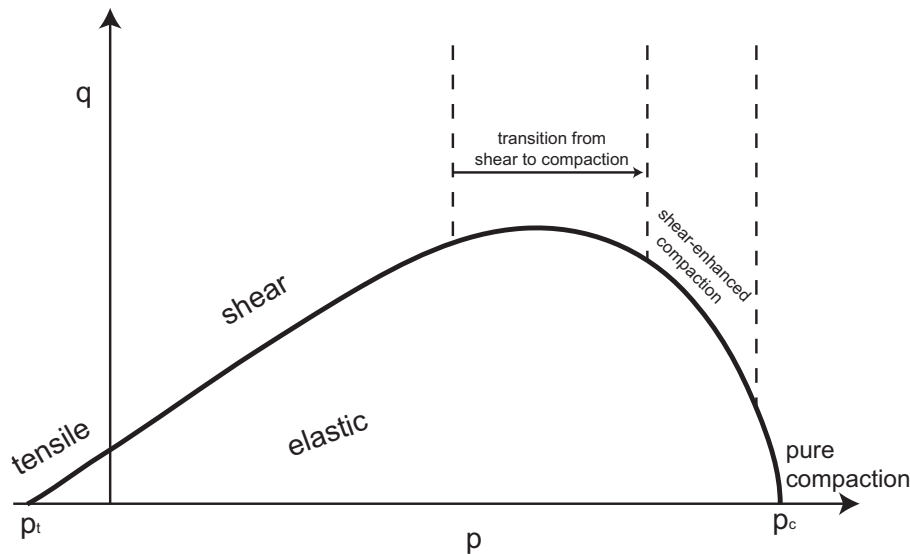


Figure 5.3: Schematic illustration of the CamClay yield surface in $p-q$ space. At low stresses the deformation is elastic. At high normal stresses compaction processes occur, while at high shear stresses brittle failure occurs. The yield surface is defined by the points p_t and p_c where it meets the p -axis.

E^0 is a reference Young's modulus, and A , B , c , e and m are constants to be determined, while ν_{min} and ν_{max} are the Poisson's ratio at high and low stresses. In the plastic regime, the plastic strain rate $\dot{\varepsilon}^p$ is given by

$$\dot{\varepsilon}^p = \dot{\lambda} \frac{d\Psi}{d\sigma} \quad (5.16)$$

where Ψ is the plastic potential, defined as

$$\Psi(\sigma, \varepsilon)_v^p = g(\theta, p)q + (p - p_t) \tan \psi \left(\frac{p - p_c}{p_t - p_c} \right)^{1/n}, \quad (5.17)$$

where ψ is the dilation angle and $\dot{\lambda}$ is a plastic multiplier.

5.3.3 Coupling of fluid-flow and geomechanical simulations

There are a number of methods that might be used to couple together fluid flow and geomechanical simulation, including full coupling, one-way coupling, explicit coupling and iterative coupling. (Dean et al., 2003). The fully coupled method involves solving the equations for fluid-flow and geomechanical deformation simultaneously in the same simulator. This method is the most numerically accurate. However, it is difficult to implement, and no commercial simulators with this facility currently exist. As a result, simplifications would have to be made in the fluid and geomechanical equations.

The other 3 methods all use separate fluid-flow and geomechanical simulators, meaning that commercial finite element fluid-flow and geomechanical deformation codes can be used. The simplest method is one-way coupling, where the pore pressure and fluid properties computed by the flow

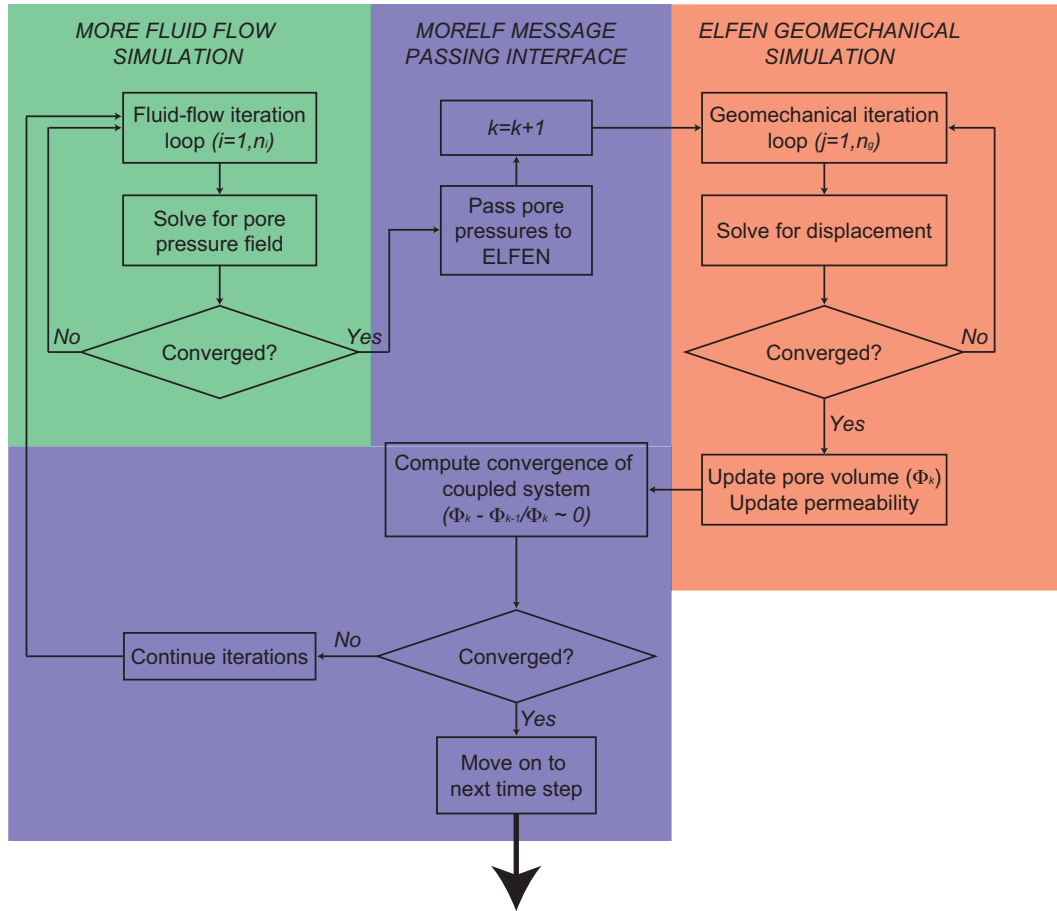


Figure 5.4: Iteration algorithm for coupled geomechanical modelling. At each timestep, MORE (green) computes the pore pressure field, which is passed via the MPI (blue) to ELFEN (red), which computes the geomechanical deformation. The MPI assesses whether the solution has converged - if it hasn't then the iteration is repeated, if it has then the MPI moves on to the next timestep.

simulator are passed to the geomechanical simulation at user-defined timesteps. The results of the geomechanical simulation are not passed back to the fluid flow simulation. As a result, this method will only be appropriate where deformation is not large enough to significantly affect porosity and permeability.

For the explicit coupling method, the fluid flow simulator is again run until a user-defined time step, where the pore pressure is passed to the geomechanical simulation. However, unlike the one-way coupling method, the changes in porosity and permeability are returned to the fluid flow simulator for use in subsequent time steps. As a result, the explicit method is more accurate than the one-way method, but as it requires the passing of data in two directions, is more computationally expensive (Dean et al., 2003). The iterative method is similar to the explicit method, except for at each time

step the fluid flow and deformation are solved in an iterative manner, with data passed back and forth between the simulations until a stable solution is found. This is illustrated in Figure 5.4. At each time step the pore pressure and fluid properties are computed by the fluid flow simulator. These are passed to the geomechanical simulator to compute deformation (using a number of sub-steps). The changes in porosity are assessed for convergence, and if not yet converging, returned to the fluid flow simulation to repeat the iteration. This method is more computationally expensive than the explicit coupling, but produces more accurate results. Comparisons suggest that this method gives the same result as fully coupled simulations (e.g., Longuemare et al., 2002), highlighting the accuracy of this approach. The combination of accuracy with the ability to link successful commercial fluid flow and geomechanical simulation packages means that the iterative coupling method is the method that I will use. The computational speed of this approach has been greatly improved by Rockfield Software through the development of a high speed message passing interface (MPI) to link between MORE and ELFEN.

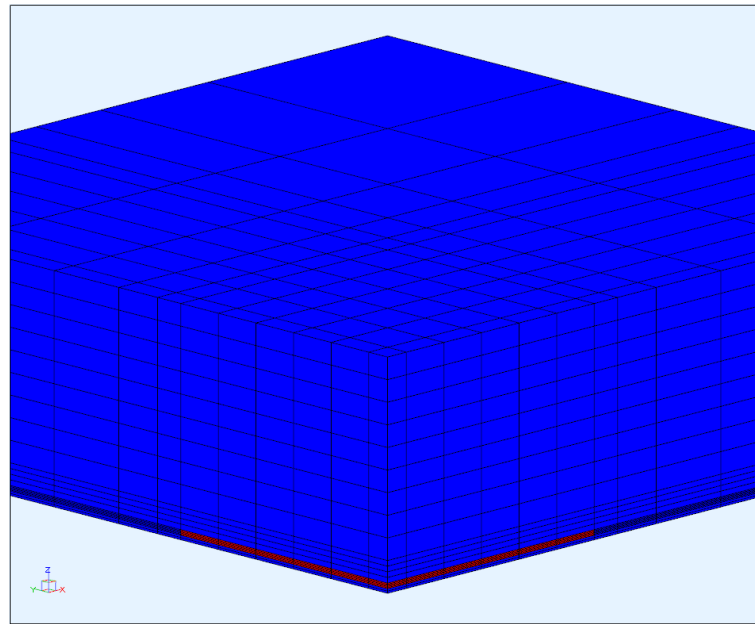
5.3.4 Workflow

Using the iteratively coupled MORE-ELFEN simulation, the workflow for developing simple geomechanical models is as follows. The geomechanical mesh is constructed using the ELFEN pre-processing GUI. The model must include both the reservoir and the over, under and side burdens, as these will also be deformed by processes occurring in the reservoir. The GUI generates the input file for geomechanical modelling. The cells are populated with mechanical properties as selected by the user based on a large database of rock physics measurements. It is the geomechanical input file that controls the simulation timesteps, convergence conditions, end times, and how often results are written to file. The MORE input file is constructed by the user. The external dimensions of the reservoir in the MORE model must match the reservoir as defined in the geomechanical input. However, they need not have the same internal mesh, as ELFEN can interpolate between them. It is the MORE file that defines the well locations and injection/production rates. Internal calculation timesteps are computed by ELFEN are of a sub-day scale. However, to produce output files for each internal timestep would lead to data overload. Therefore output files are generated by ELFEN at user-defined timesteps. In my models I produce output files at 6 evenly spaced intervals during the simulations.

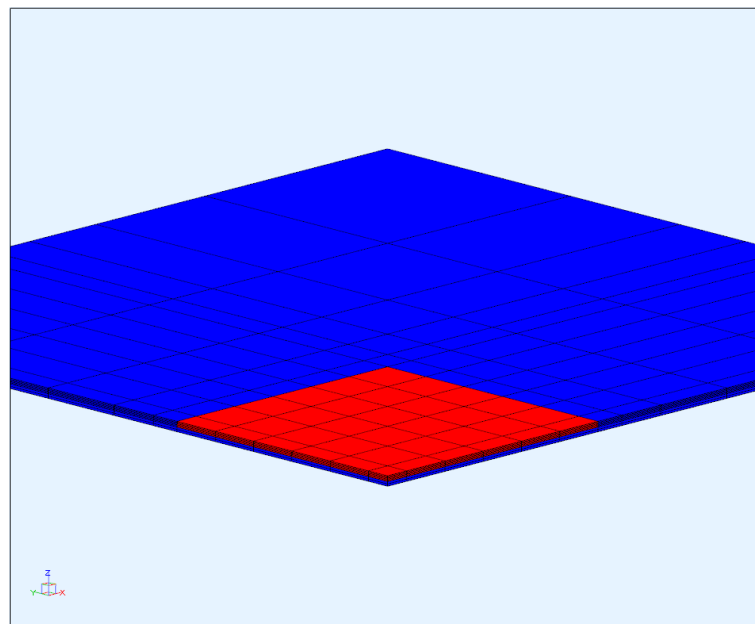
5.3.5 Simple representative models

In order to assess the sensitivity of the stress path parameters during injection to reservoir geometry and material properties, I have developed a range of simple representative models, all consisting of cuboid reservoirs contained within non-pay rocks (Figure 5.5). In order to decrease the computational requirements, I simulate only a quarter of the system, relying on symmetry arguments to complete the model.

The boundary conditions at the edges of the model are that there can be no movement perpendicular to the vertical bounding planes at the edges of the model (i.e., no movement in the x direction of the $y - z$ plane) and no vertical movement at the base of the model. I include all of the overburden up



(a)



(b)

Figure 5.5: Geomechanical grid and material regions for the simple, rectangular reservoirs. The reservoir is marked in red, the over, side and under burdens are blue. In (b) the overburden has been removed to reveal the reservoir. To save computational time, only a quarter of the model is simulated, with symmetry used to complete the model.

<i>Dimensional ratio</i>	<i>x-side length</i>	<i>y-side length</i>	<i>Thickness</i>
1z:100x:100y	7620	7620	76.2
1z:100x:5y	7620	381	76.2
1z:5x:5y	381	381	76.2

Table 5.1: Dimensions of the various cuboid reservoir models (in meters).

<i>Parameter</i>	<i>Reservoir</i>	<i>Overburden</i>
Reference Young's modulus E^0	$[7-35] \times 10^9 \text{ Pa}$	$[7-20] \times 10^9$
Poisson's ratio	0.25	0.45
Density	2700 kg/m^3	2700 kg/m^3
Porosity	$\Phi = 0.418 - 0.066z$	$\Phi = 1 - \left(\frac{z}{6.02}\right)^{1/6.35}$
Permeability	$\kappa_x = 100 \text{ mD}, \kappa_z = 10 \text{ mD}$	$\kappa_x = \kappa_z = 1 \times 10^{-6} \text{ mD}$
Biot Willis parameter	1	1
Depth to top reservoir	3048m	NA
Fluid in place	Brine	Brine
Injected fluid	Brine	NA

Table 5.2: Geomechanical and fluid-flow properties of the reservoir and overburden. The porosity is given as a function of depth, z . The permeability is anisotropic, having values in the horizontal (x) and vertical (z) directions.

to the surface, which may move freely. The base of the model is 200m below the base of the reservoir. This represents the situation where a reservoir is near to a relatively undeformable basement, which may not be applicable to some scenarios. However, the underburden boundary conditions will not have a large effect on deformation in the overburden, which forms the focus of my discussions here. I have used 3 different reservoir geometries, defined in Table 5.1, an extensive, flat reservoir with dimensional ratios of 1z:100x:100y, a long, thin reservoir with dimensional ratios of 1z:100x:5y, and a short, fat reservoir with dimensional ratios of 1z:5x:5y. Within each reservoir the simulation mesh has 6 nodes in the x and y directions, and 5 nodes in z . The mesh grid can be seen in Figure 5.5. In the over- and sideburdens the grid coarsens away from the reservoir to reduce computational expense.

The reservoir material in all cases is a sandstone, while the overburden is shale. The properties of these materials are given in Table 5.2. To create a realistic overburden, the porosity is varied as a function of depth, using a typical porosity-depth curve given in Table 5.2. The porosity as a function of depth is shown in Figure 5.6 for both the overburden and reservoir. In each of these cases, injection was simulated for 8 years, at a rate such that the pore pressure increased by 15MPa by the end of the injection period. As they have different volumes, this required a different rate of injection for each reservoir.

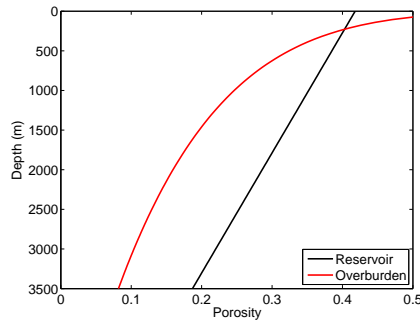


Figure 5.6: Porosity as a function of depth for the reservoir and overburden materials.

<i>Reservoir</i>	<i>Overburden</i>	<i>Ratio</i> (E_{res}^0/E_{over}^0)
7GPa	20GPa	0.35
20GPa	20GPa	1
35GPa	7GPa	5

Table 5.3: Initial Young's moduli for the range of stiff and soft reservoir models.

The Young's modulus is dependent on porosity as per equation 5.15. Assuming $e=0$ makes A and B immaterial. As a result, the Young's modulus is given by

$$E = E^0 \Phi^{-0.372} \quad (5.18)$$

in the overburden and

$$E = E^0 \Phi^{-0.4}, \quad (5.19)$$

in the reservoir. In order to test the sensitivity of the stress path to the relative stiffness of the reservoir and overburden, the reference Young's modulus is varied for both the reservoir and overburden. Segura et al. (2010) have shown that the key material property with first order control on the stress path is the ratio of Young's modulus between the reservoir and the side- and overburden. Therefore I have developed models with a stiff reservoir and soft overburden (referred to as the *stiff* model), with a soft reservoir and stiff overburden (*soft* model) and with similar stiffnesses (*medium* model). The initial Young's moduli are listed in Table 5.3, and the resulting Young's moduli, and reservoir:overburden Young's modulus ratios, as a function of depth are shown in Figure 5.7.

5.4 Results

I will show the results from the 9 models described above (3 geometries \times 3 stiffnesses). For each of these I will analyse the stress evolution in 5 locations: (1) in the centre of the reservoir; (2) at the edge of the reservoir; (3) at the corner of the reservoir; (4) in the overburden at the first node above the centre of the reservoir; and (5) in the sideburden (see Figure 5.8). For the 3 cells inside the reservoir I will consider the stress path parameters described above. Outside the reservoir there is little pore

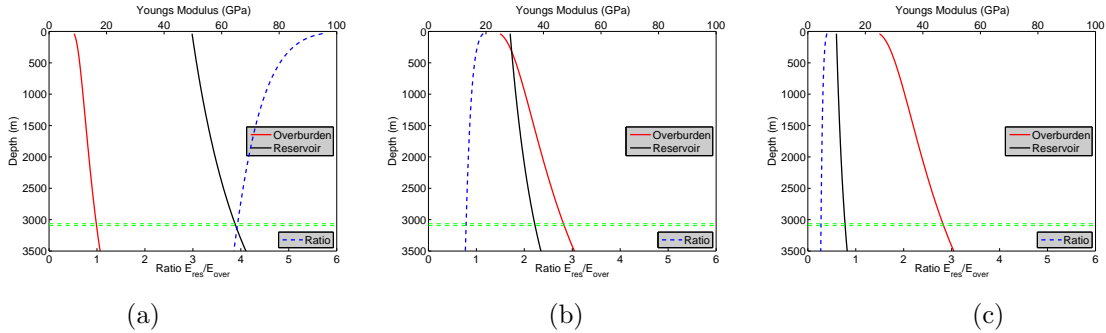


Figure 5.7: Young’s modulus as a function of depth for both the reservoir and overburden materials for (a) the stiff reservoir models, (b) the medium reservoir models and (c) the soft reservoir models. The green lines mark the reservoir interval.

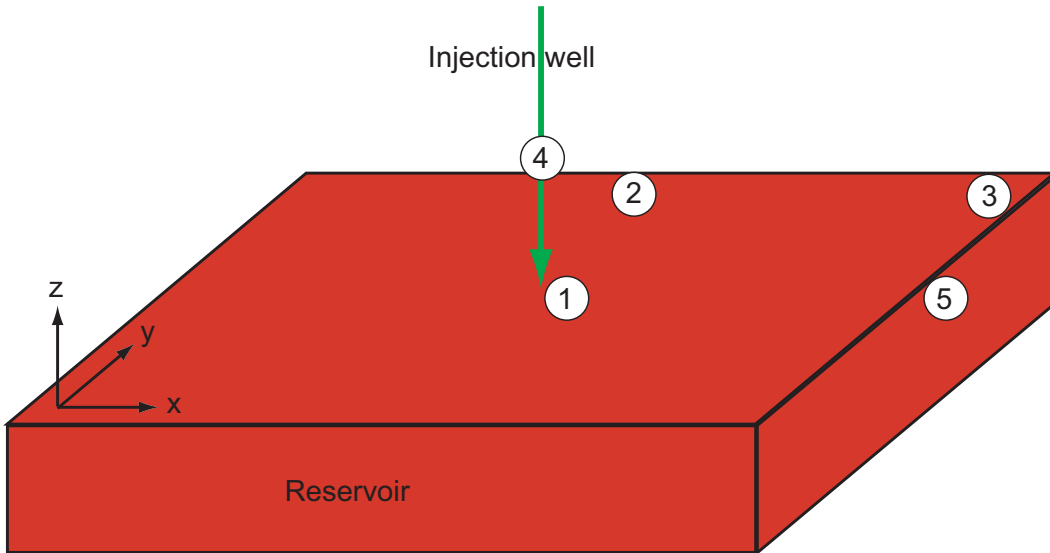


Figure 5.8: Geometry of our rectangular reservoir models showing the location of cells used to compute Mohr circles. The red box depicted here corresponds to the full reservoir (not the quarter-spot shown in Figure 5.5), which is surrounded by the over-, under- and sideburden. Injection occurs in the centre of the reservoir. Cell 1 is at the injection point, cell 2 is at the edge of the reservoir, cell 3 is in the corner of the reservoir, cell 4 is in the overburden and cell 5 is in the sideburden.

pressure change, so the stress path parameters do not have meaning. However, I will consider stress changes in these cells as a function of pore pressure change in the centre of the reservoir.

In Figure 5.9 I plot K_0 and γ_3 for each of the models. There are several things to note from this plot. Firstly, the results for the reservoirs with at least one small horizontal dimension, $1z:100x:5y$ and $1z:5x:5y$, have very similar results. This suggests that it is the smallest lateral dimension that controls the style of deformation that the reservoir will experience. The results show that K_0 is much

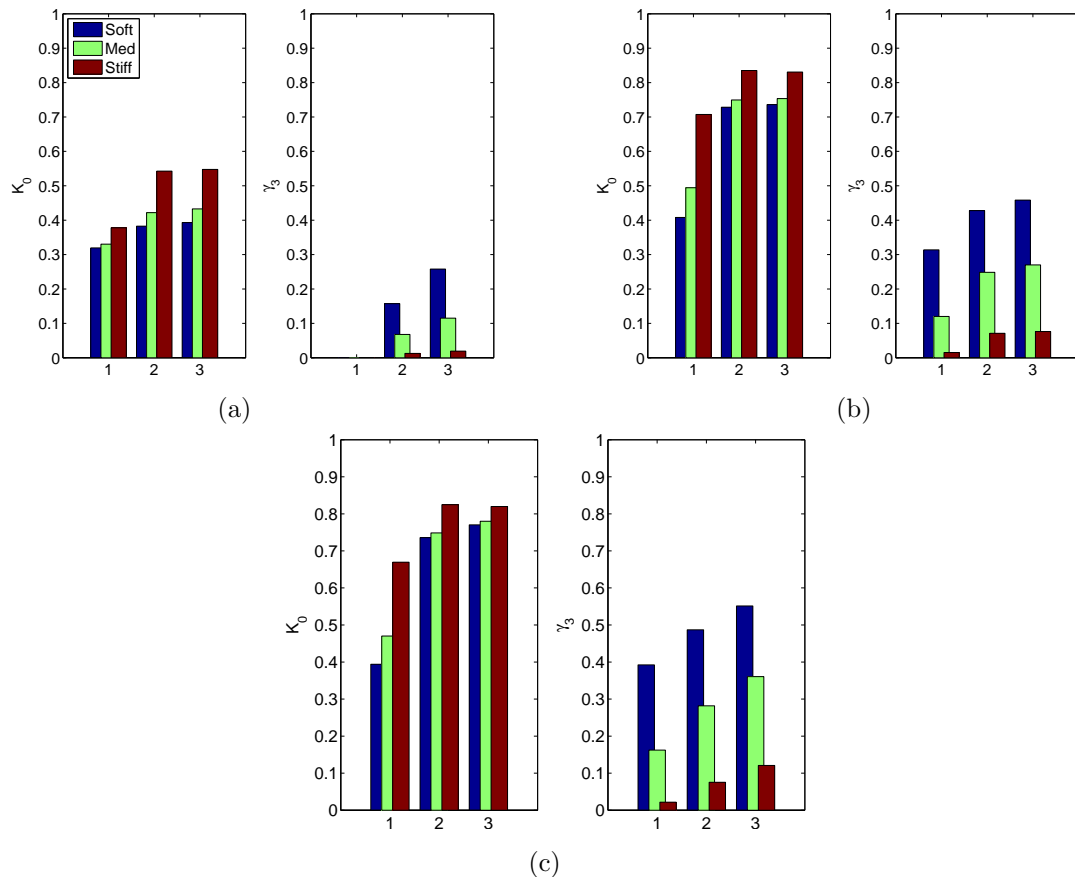


Figure 5.9: Numerical results for stress path parameters as a function of reservoir geometry and stiffness. The flat, extensive reservoir ($1z:100x:100y$) is shown in (a), the long thin reservoir ($1z:100x:5y$) is in (b) and the short, fat reservoir ($1z:5x:5y$) is in (c). There are 3 models for each geometry, with a soft, medium and stiff reservoir. I plot K_0 in the left hand panels and γ_3 in the right hand panels, for the cells at the centre (1), edge (2) and corner (3) of the reservoir.

larger for the smaller reservoirs. It is also slightly larger for elevated reservoir:overburden stiffness ratios, and for cells at the edge of the reservoir (cells 2 and 3). K_0 describes the change in size of the Mohr circle, with a low value of K_0 meaning a reduction in size. Given that a large Mohr circle is more likely to cross the failure envelope, this suggests that small, stiff reservoirs are more likely to fail, and that this effect is most significant at the edges of the reservoir. The implications that this has for rock failure and microseismic activity will be discussed below.

I find that γ_3 is largest for low reservoir:overburden stiffness ratios, and small for elevated reservoir:overburden stiffness ratios. It is larger at the edges of the reservoirs, and larger for the small reservoirs. γ_3 can be interpreted as a stress arching indicator - a small γ_3 implies that the applied stress does not change during injection, so the change in effective stress is controlled entirely by the change in pore pressure, and therefore is hydrostatic.

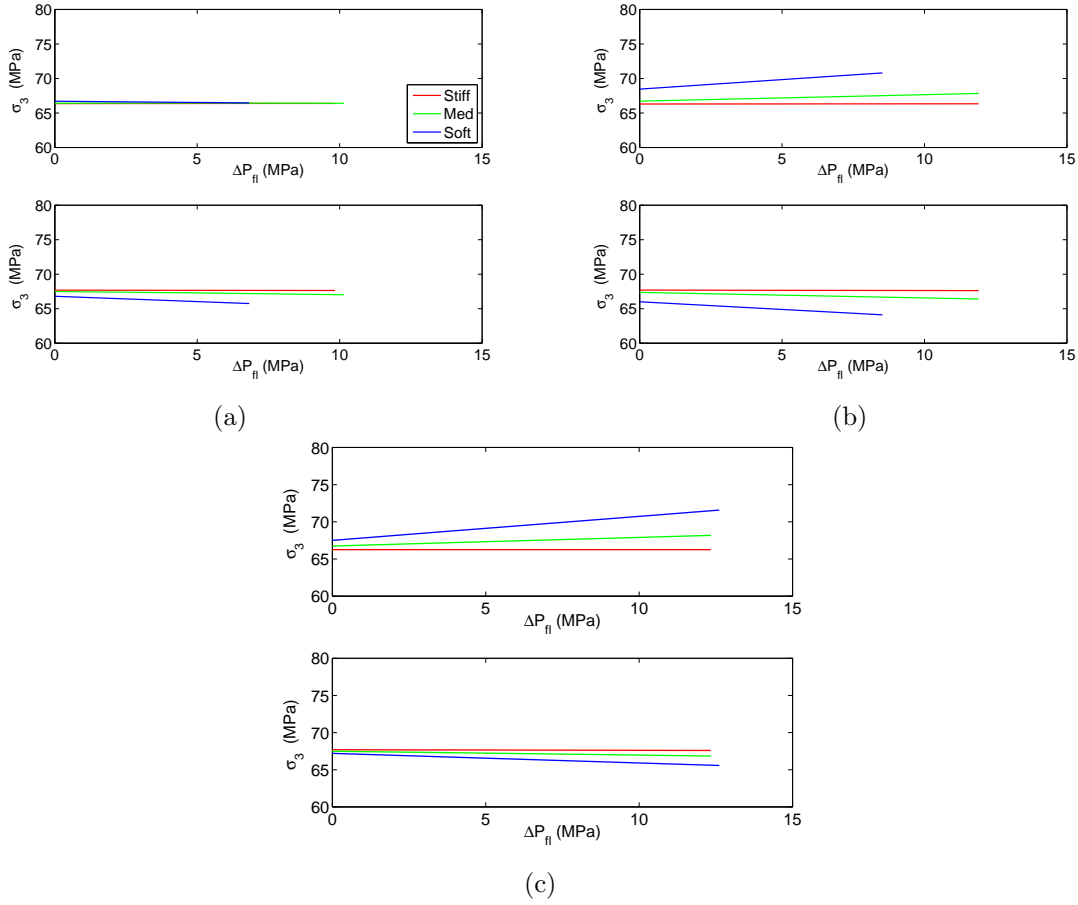


Figure 5.10: Changes in vertical stress in the overburden (upper panels) and sideburden (lower panels) with pore pressure increase in the reservoir. The flat, extensive reservoir ($1z:100x:100y$) is shown in (a), the long thin case ($1z:100x:5y$) is in (b) and the short fat case ($1z:5x:5y$) is in (c). The different coloured lines show the results for the different stiffness reservoirs.

In Figure 5.10 I plot the changes in vertical stress σ_3 in the over- and sideburden as a function of the pore pressure change at the centre of the reservoir. I note that in the overburden σ_3 increases for the smaller reservoirs, and especially so when the reservoir:overburden stiffness ratio is small. Above the extensive reservoir there is little stress change. In the sideburden of the smaller reservoirs σ_3 decreases, and again this effect is most pronounced for the softer reservoirs. There is also some stress evolution in the sideburden of the softest extensive reservoir, but this change is less than for the smaller reservoirs.

5.4.1 Stress arching

The stress evolution can be interpreted within the framework of stress arching. Stress arching is commonly observed during reservoir production (e.g., Hatchell and Bourne, 2005). As the reservoir

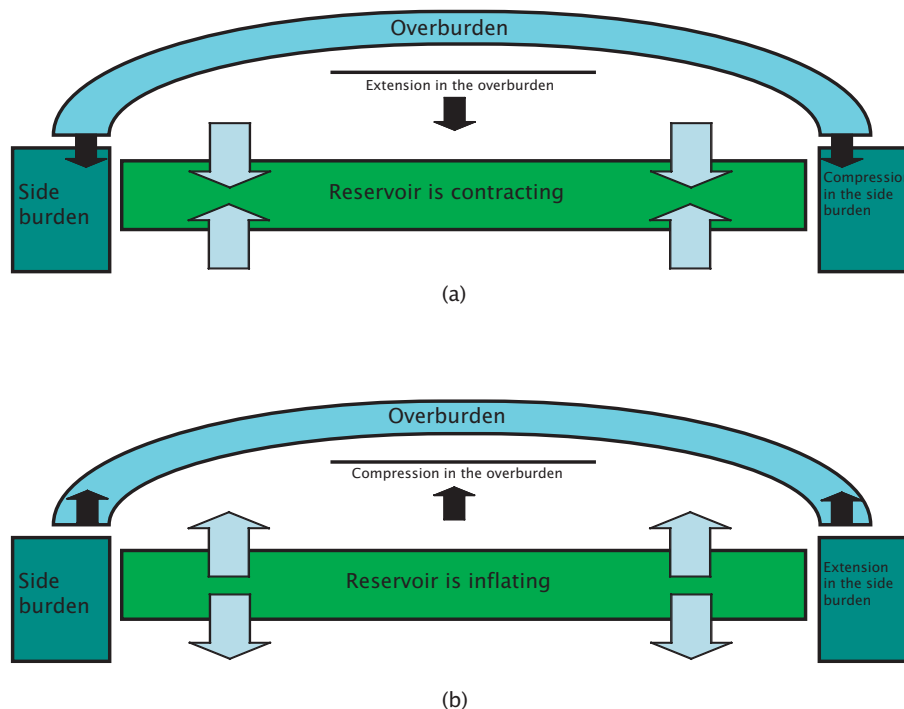


Figure 5.11: Cartoon illustrating stress arching during (a) production and (b) injection. During production, the shrinkage of the reservoir induces stretching in the overburden, and compression of the sideburden as it supports the load. The reverse happens during injection, with compression in the overburden and extension in the sideburden.

compacts with decreasing pore pressure, the overburden should subside. However, the weight of the overburden is supported by the sideburden, and so it does not subside. Instead there is extension in the overburden, while the sideburden is compacted by the extra weight that it is required to support. This process is illustrated in Figure 5.11a. With these simple injection models I have demonstrated the inverse process occurring during inflation. The increase in pressure inside the reservoir pushes the top of the reservoir upwards. However, the overburden is not lifted as it is connected mechanically to the sideburden. As a result, there is extension in the sideburden, while the overburden is compressed. This is illustrated in Figure 5.11b.

In Figure 5.12 I plot the change in vertical effective stress for the small, soft reservoir and for the stiff, extensive reservoir. For the stiff, extensive case, σ'_3 decreases due to the pore pressure increase, but there is no stress change outside the reservoir. There is no stress arching. In contrast, for the soft, short case, although the effective stress inside the reservoir decreases, it does not decrease by as much. This is because part of the load is supported by the overburden, which compacts, and by the sideburden, which extends. Stress arching has occurred.

The γ_3 parameter describes the extent to which this process is occurring. I have found that arching is likely to occur when the reservoir is soft in comparison to the over- and sideburdens. This

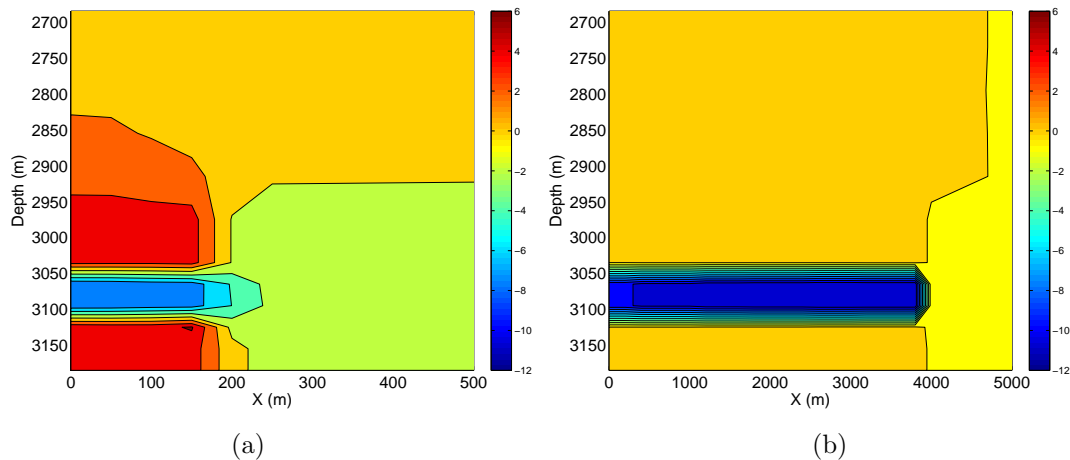


Figure 5.12: Cross sections through the centre of the reservoir showing the changes in vertical effective stress (σ'_3) at the end of injection for the short, soft reservoir case (a) and for the stiff, extensive case (b). Contours are in MPa. The short, soft case experiences stress arching as the sideburden and overburden support the load, while the stiff extensive case does not.

is because a stiffer overburden will be better able to support the loads. A soft overburden will not be able to support large loads. I have also found that arching is less likely to occur with the extensive reservoir. This is because the extensive case has a large amount of overburden to support. With smaller reservoirs, there is less overburden to be supported. I have already noted the similarity between results for the elongate and short cases. This suggests that so long as the reservoir is small in one dimension the stress arching can occur to the full extent. Finally, I have found that stress arching is more likely to occur at the edges of the reservoir. This is because the closer to the sideburden the better the mechanical connection, and so the greater load it can support. This interpretation is limited to the elastic case. The yield surface of the overburden will also control the amount of stress is can support - an overburden with low strength will fail as a response to deformation, and will be less capable of supporting stress arching.

5.4.2 Fracture potential

The likelihood of a material to experience brittle shear failure can be expressed in terms of a fracture potential, f^p . The fracture potential describes how close the stress state is to crossing the Mohr-Coulomb envelope described in equation 5.6. In the shear regime f^p is based on the ratio between the actual differential stress and the critical differential stress at failure,

$$f^p = \frac{q}{q_{crit}}. \quad (5.20)$$

The critical differential stress is given as

$$q_{crit}/2 = \chi \cos \phi_f + p \sin \phi_f, \quad (5.21)$$

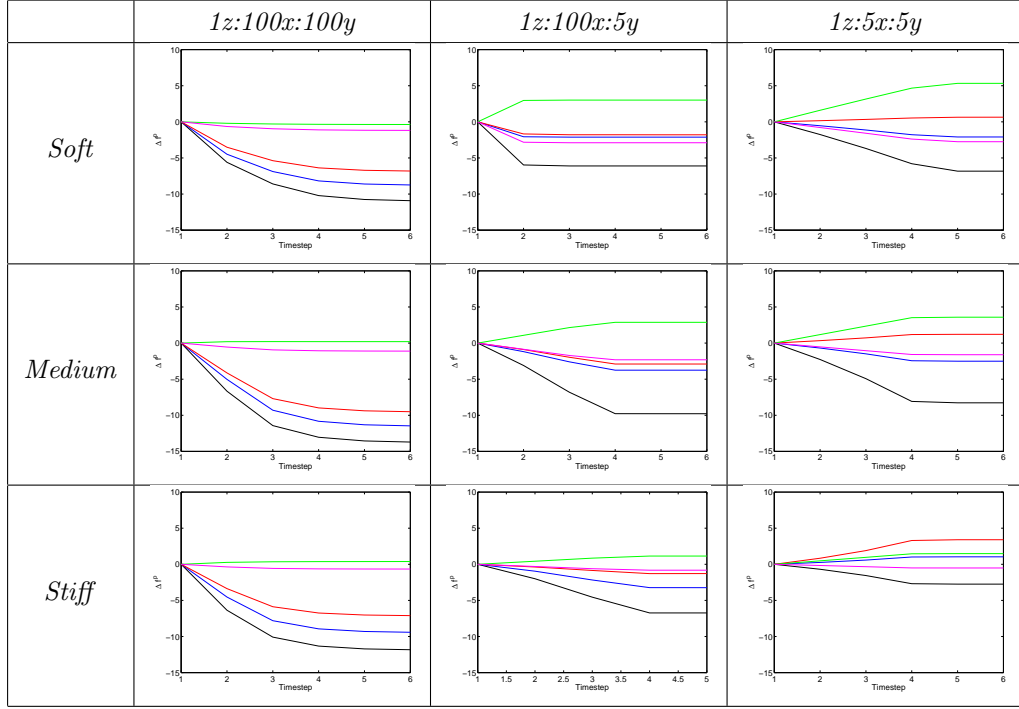


Figure 5.13: Percentage change in fracture potential during injection into the simple reservoirs. I plot the fracture potentials for all the cells examined - in the centre of the reservoir (black), at the edge of the reservoir (red), in the corner of the reservoir (blue), in the overburden (green) and in the sideburden (magenta). Increases in fracture potential are seen for the smaller reservoirs ($1z:100x:5y$ and $1z:5x:5y$). The extensive reservoir ($1z:100x:100y$) models do not see increases in fracture potential either in the reservoir or the overburden.

making the fracture potential

$$f^p = \frac{q}{2(\chi \cos \phi_f + p \sin \phi_f)}. \quad (5.22)$$

In Figure 5.13 I plot the percentage change in fracture potential through time for all of the simple reservoirs. To compute the results I use generic values for χ and ϕ_f , with $\chi=5\text{MPa}$ and $\phi_f=40^\circ$ ($m=0.84$). Cases where f^p increase represent cases where we might expect failure. I note that for the extensive reservoirs the values of f^p do not change in the overburden, because the reservoirs are too extensive for the overburden to be supported, and so stress is not transferred. The values of f^p in the reservoir decrease because, with a low value of K_0 , the Mohr circles will shrink, meaning that differential stresses are lower. Therefore I infer that the risk of shear failure for these cases is not only not increasing, but is in fact reducing.

In contrast, the smaller reservoirs show f^p values increasing during injection. For the softer reservoir it is in the overburden that the fracture potential is increasing, because stresses are transferred to the overburden, increasing the vertical stress while the horizontal stress is essentially unchanged, leading to a higher differential stress. For the stiffer reservoir it is inside the reservoir that f^p increases

because, with a higher value of K_0 , the normal stresses decrease while the differential stress does not. Therefore I infer that for these cases the injection of CO₂ is increasing the likelihood of shear failure, and therefore are more likely to generate microseismic activity.

In reality, microseismic events will generally occur on pre-existing planes of weakness such as faults or fractures. Such features are well below the element length scales used in these (and most other finite element) models, and so cannot be explicitly included. This kind of approach therefore will not be able to make exact predictions about microseismic event occurrence, either spatially or temporally. Nevertheless, by examining where fracture potential is increasing, it should still be possible to identify regions where more events are likely to occur, assuming that the planes of weakness on which events could occur are distributed evenly through the rock.

5.4.3 Shallower reservoirs

The above results have considered the effects of reservoir geometry and materials on stress evolution. They have been evaluated for a reservoir that at 3000m is quite deep. It is of interest to consider the stress evolution of reservoirs that are shallower. With this in mind I have repeated the numerical calculations, but with a reservoir at a depth of 1500m. All other modelling parameters have been kept the same, and again I consider 3 geometries, each with three sets of material properties, giving 9 models in total. In Figure 5.14 I plot the stress path parameters K^0 and γ_3 for the shallow models. I note that the stress path parameters for each reservoir are very similar to their deeper counterparts. I conclude that the depth of the reservoir does not appear to affect the stress evolution as a result of inflation.

5.5 Surface uplift

An alternative geophysical method that can and has been applied to monitoring of CCS is to use InSAR to measure ground surface uplift above a reservoir. As the reservoir inflates with CO₂ injection, the ground surface may be pushed up by an amount that is detectable using satellite-based methods. This technique has been most notably demonstrated at the In Salah site, Algeria (Onuma and Ohkawa, 2009), where uplift of a few mm has been detected. However, without a geomechanical model that simulates the reservoir and overburden it is difficult to relate surface deformation observations to reservoir processes. Such models have been developed for In Salah by Vasco et al. (2008) and Rutqvist et al. (2009). In Salah is located in the middle of a desert, a perfect environment for InSAR. As a result, measurements are very accurate, with a sub-millimetre resolution. In more challenging environments resolution may be as low as half a centimetre.

In this section I present the surface deformation above the simple reservoir models developed above. The contours of surface uplift for the 3 different geometries are plotted in Figures 5.15 to 5.17. In all cases the shape of the uplift mirrors the region of pore pressure increase above the reservoir. The extensive reservoir ($1z:100x:100y$) shows the largest uplift, while for the small reservoir ($1z:5x:5y$) the uplift is so small as to be obscured by numerical noise.

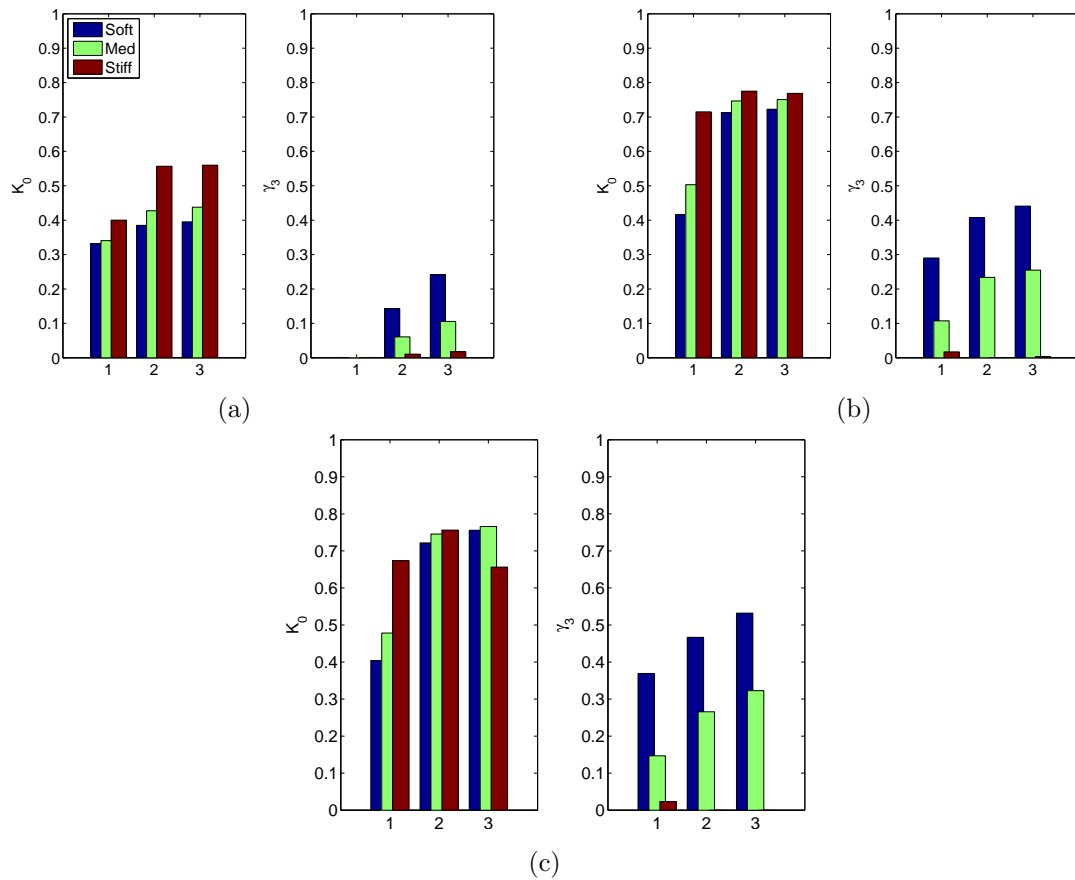


Figure 5.14: Numerical results for stress path parameters as a function of reservoir geometry and stiffness for the shallower reservoirs. This figure is in the same format as Figure 5.9.

In Table 5.4 I give the maximum amounts of uplift above each reservoir. However it is difficult to compare these results as the reservoirs have different pore pressure changes, so in Table 5.5 I give the uplift normalised by the reservoir pore pressure change for both the deep and shallow reservoirs. The centimetres of uplift above the extensive reservoirs and the millimetres of uplift above the thin reservoirs would be detectable even in more challenging environments. The sub-millimetre amounts of uplift above the small hard and medium reservoirs may be difficult to detect even in good conditions.

The normalised amounts of uplift are similar between deep and shallow cases, in some cases uplift is larger for the deep case while in some uplift is larger for the shallow case. It is not clear what causes this variation. The amount of uplift correlates with the volume of CO_2 injected, which is largest for the extensive case and lowest for the small reservoir. The overburden stiffness for the medium and soft cases are identical (Figure 5.7) yet a much larger amount of uplift is found above the soft reservoir, suggesting that the stiffness of the reservoir is a strong control on the amount of uplift expected. However, the soft overburden above the hard reservoirs leads to a greater amount of uplift than above the medium case, implying that the stiffness of the overburden is also important.

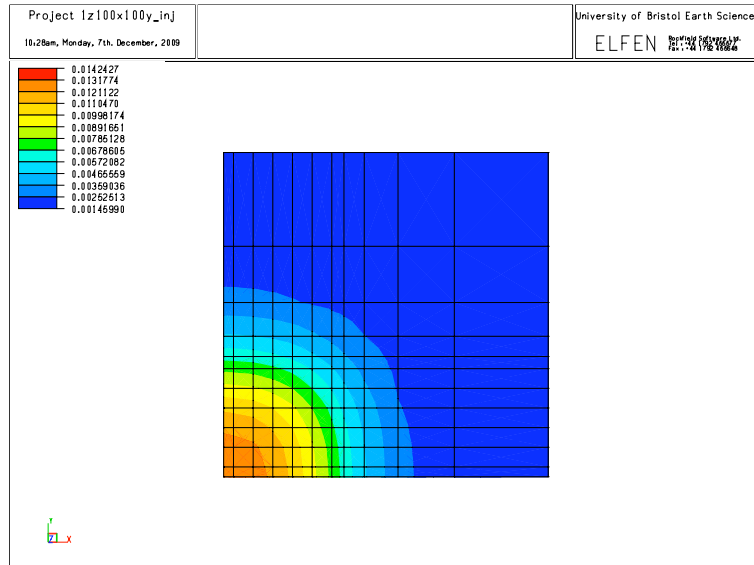


Figure 5.15: Map of surface uplift above the medium stiffness extensive model $1z:100x:100y$. Contour units are in meters. The geomechanical mesh is plotted, and the reservoir is found in the tightest mesh region. Uplift of 1.3cm is predicted above the centre of the reservoir, decaying away to the sides.

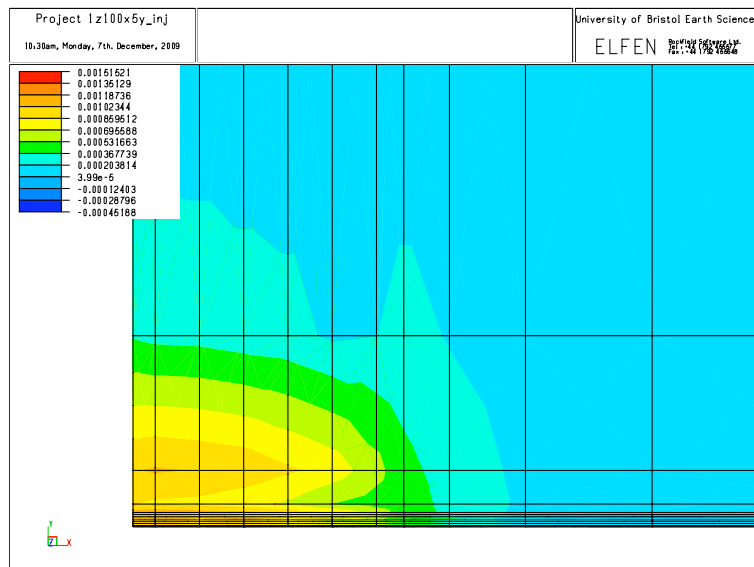


Figure 5.16: Map of surface uplift above the medium stiffness, long and thin model $1z:100x:5y$.

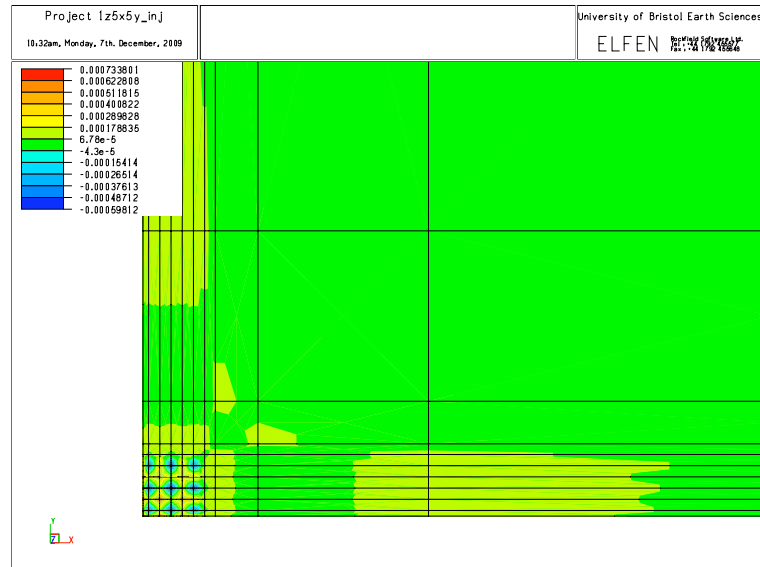


Figure 5.17: Map of surface uplift above the medium stiffness small model $1z:5x:5y$. The uplift here is so small that it is lost in numerical noise.

As important as the magnitude of uplift is the shape of the uplifted region. It is clear from Figures 5.15 to 5.17 that the uplift closely matches the shape of each reservoir, where the pressure plume has propagated even though the CO_2 has not. This may therefore be a useful tool for identification of reservoir compartmentalisation or flow in channels, provided the shape of the uplift can be constrained well enough to image reservoir features.

	$1z:100x:100y$	$1z:100x:5y$	$1z:5x:5y$
<i>Soft</i>	6.4	0.41	0.20
	4.8	0.61	0.17
<i>Medium</i>	1.3	0.11	0.06
	1.1	0.16	0.03
<i>Hard</i>	2.4	0.13	0.07
	1.4	0.16	0.04

Table 5.4: Maximum surface uplift above each of the model reservoirs (in cm). The values in blue are for the deep reservoirs, in red are for the shallow models.

	<i>1z:100x:100y</i>	<i>1z:100x:5y</i>	<i>1z:5x:5y</i>
<i>Soft</i>	9.33×10^{-3}	4.85×10^{-4}	1.60×10^{-4}
	5.98×10^{-3}	7.12×10^{-4}	2.13×10^{-4}
<i>Medium</i>	1.28×10^{-3}	9.07×10^{-5}	4.85×10^{-5}
	1.35×10^{-3}	1.84×10^{-4}	4.60×10^{-5}
<i>Hard</i>	2.40×10^{-3}	1.14×10^{-4}	5.47×10^{-5}
	1.69×10^{-3}	1.89×10^{-4}	5.18×10^{-5}

Table 5.5: Maximum surface uplift normalised by the reservoir pore pressure change (m/MPa) for each case. The values in blue are for the deep reservoirs, in red are for the shallow models.

5.6 Summary

- The use of fully coupled fluid-flow/geomechanical modelling is a recent development in the hydrocarbon industry. As part of the IPEGG project a model linking commercial fluid flow and geomechanical packages has been developed.
- I have modelled a suite of simple, cuboid reservoirs with varying geometry and material properties in order to examine the controls on stress path evolution during injection.
- I find that smaller reservoirs with a reservoir that is softer than the overburden, are prone to stress arching, where much of the load induced by injection is accommodated by the overburden. In contrast, extensive reservoirs with stiff reservoirs in comparison to the overburden do not transfer stress into the overburden.
- The potential for shear failure and microseismic activity is parameterised with a fracture potential term that describes the evolution of differential stresses. I find that failure is most likely to occur inside small, hard reservoirs, and above small soft reservoirs. Extensive reservoirs appear to have a lower risk of inducing brittle, shear failure.
- An alternative method for monitoring CO₂ injection is to observe ground deformation using satellites. I have shown how geomechanical models can be used to simulate ground deformation to link InSAR observations with reservoir processes.

GENERATING ANISOTROPIC SEISMIC MODELS BASED ON GEOMECHANICAL SIMULATION

It's not rocket science, it's rock science.

Julio Friedmann

6.1 Introduction

Seismic waves provide a means of remotely sensing the subsurface over a range of length scales. Information from time-lapse (4-D) surveys and microseismic monitoring will compliment information from bore-hole logging, flow rate measurements and pressure tests that will allow us to locate zones of CO₂ saturation, map out reservoir flow compartments and identify regions of high stress and fracturing. Commonly, it is assumed that observed time-lapse variations are simply a factor of varying fluid content. However, it is becoming increasingly clear that fluid substitution alone cannot account for all the observed temporal variations time-lapse seismic data (e.g., Hatchell and Bourne, 2005). Travel time-shifts away from the reservoir and the development of stress-induced SWS suggest that seismic properties are also sensitive to geomechanical deformation. One of the main goals of the IPEGG consortium is to quantify the sensitivity of seismic observables to geomechanical effects.

In order to relate the information given by coupled fluid-flow/geomechanical models (e.g., in situ stresses and strains, changes in porosity, and the movement and properties of fluid within the reservoir) to seismic observables, it is necessary to model the elastic stiffness of the reservoir and surrounding units. These models must be based on information provided by the coupled fluid-flow/geomechanical simulation, and must also be constrained by geologic, engineering and seismic observations. I aim to construct these models using rock physics theories that include intrinsic rock properties and incorporate the effects of changes to the applied stress field and fluid saturation. In this chapter I present and discuss a workflow to generate elastic models from the MORE-ELFEN coupled fluid-flow/geomechanical simulations.

6.2 Stress-sensitive rock physics models

The effects of stress and/or strain on rock elasticity is observed empirically to be non-linear (e.g., Nur and Simmons, 1969; Kuster and Toksoz, 1974). The stress dependence of seismic velocities is strong at low confining stresses, but weakens as confining stresses increase. The most common explanation for this observation is that at low pressures, seismic velocities are dominated by the opening and closing of discontinuities or microcracks between grain boundaries. At higher pressures, these discontinuities close and velocities increase, but become less stress dependent. A number of approaches have been used to account for the nonlinear response of velocity to stress, including empirically determined relationships (e.g., Minkoff et al., 2004), Hertz-Mindlin contact forces (e.g., Makse et al., 1999), strain-

based 3rd order elasticity tensors (e.g., Prioul et al., 2004), and continuum effective medium modelling (e.g., Sayers and Kachanov, 1995).

In seismology it is assumed that waves are elastic. As such, the relationship between stress and strain for the infinitesimal deformation caused by the passage of a seismic wave can be described via the linear generalised Hooke's law,

$$\sigma_{ij} = C_{ijkl}\varepsilon_{kl}, \quad (6.1)$$

where σ and ε are the symmetric 3×3 stress and strain tensors, and \mathbf{C} is the $3 \times 3 \times 3 \times 3$ elastic stiffness tensor. As discussed in Chapter 3, the velocity of a seismic wave propagating in any direction through an elastic media can be calculated from the 21 independent components (although the 4th order tensor has 81 elements, symmetry arguments reduce the number of independent components to 21) that describe the stiffness tensor. Hence, whether we are using ray tracing or more complex techniques such as finite element or finite difference, if we are to predict the change in seismic properties caused by stress, we must be able to determine \mathbf{C} as a function of σ (or ε). Two models that are capable of doing this are discussed below.

6.2.1 3rd-order nonlinear elasticity

Prioul et al. (2004) develop a stress-dependent rock physics model that is capable of including the effects of anisotropy and non-hydrostatic stress fields. In a simplified form this model has become immensely popular with the oil industry in the form of the R-factor of Hatchell and Bourne (2005). The formulations for nonlinear elasticity include cubic (3rd-order) terms that account for the change in stiffness with stress. By assuming that the 3rd-order terms are isotropic, the following equations can be generated for the elastic stiffness as a function of strain,

$$\begin{aligned} C_{11} &\simeq C_{11}^0 + C_{111}\varepsilon_{11} + C_{112}(\varepsilon_{22} + \varepsilon_{33}), \\ C_{22} &\simeq C_{11}^0 + C_{111}\varepsilon_{22} + C_{112}(\varepsilon_{22} + \varepsilon_{33}), \\ C_{33} &\simeq C_{33}^0 + C_{111}\varepsilon_{33} + C_{112}(\varepsilon_{22} + \varepsilon_{33}), \\ C_{12} &\simeq C_{12}^0 + C_{112}(\varepsilon_{11} + \varepsilon_{22}) + C_{123}\varepsilon_{22}, \\ C_{13} &\simeq C_{13}^0 + C_{112}(\varepsilon_{11} + \varepsilon_{33}) + C_{123}\varepsilon_{22}, \\ C_{23} &\simeq C_{13}^0 + C_{112}(\varepsilon_{22} + \varepsilon_{33}) + C_{123}\varepsilon_{22}, \\ C_{66} &\simeq C_{66}^0 + C_{144}\varepsilon_{33} + C_{155}(\varepsilon_{11} + \varepsilon_{22}), \\ C_{55} &\simeq C_{55}^0 + C_{144}\varepsilon_{22} + C_{155}(\varepsilon_{11} + \varepsilon_{33}), \\ C_{44} &\simeq C_{44}^0 + C_{144}\varepsilon_{11} + C_{155}(\varepsilon_{22} + \varepsilon_{33}), \end{aligned} \quad (6.2)$$

where

$$\begin{aligned} C_{144} &= (C_{112} - C_{123})/2, \\ C_{155} &= (C_{111} - C_{112})/4. \end{aligned} \quad (6.3)$$

The tensor \mathbf{C}^0 describes the elastic stiffness (in Voigt notation) of the rock at reference stress state (commonly, but not necessarily, zero stress). The stress dependent behaviour of the rock is then

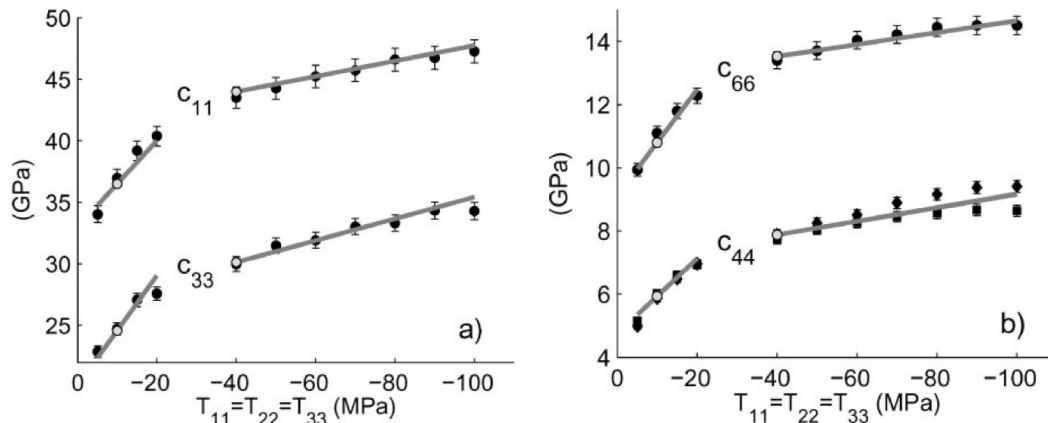


Figure 6.1: Using 3rd order elasticity to model the nonlinear elasticity of a North Sea shale. Two linear fits are given, for the low stress region (<30MPa) and high stress region (>30MPa). From Prioul et al. (2004).

Pressure (MPa)	$C_{111} \pm \Delta C_{111}$ (GPa)	$C_{112} \pm \Delta C_{112}$ (GPa)	$C_{123} \pm \Delta C_{123}$ (GPa)
5-30	-11300 ± 2900	-4800 ± 2500	5800 ± 4000
30-100	-3100 ± 600	-800 ± 500	40 ± 800

Table 6.1: Third-order terms used by Prioul et al. (2004) to empirically approximate the nonlinear elastic behaviour of a North Sea shale.

defined by the three independent non-linear coefficients C_{111} , C_{112} and C_{123} that describe the isotropic 3rd-order tensor.

The 3rd-order terms are determined empirically from lab ultrasonic measurements on core samples by minimising a least-squares misfit function between observed measurements and model predictions (see Prioul et al., 2004, for details). Equation (6.2) still requires a linear fit to the non-linear stress/stiffness curve, so linear fits are determined for high stress and low stress regions (see Figure 6.1). The values of the third-order terms for the North Sea shale shown in Figure 6.1 are given in Table 6.1.

The need to fit high and low pressure regions separately stems from trying to fit the nonlinear relationship between stress and velocity with a linear regression. The choice of where to assign the high and low pressure zones is somewhat arbitrary. Indeed, there is no conceptual reason why multiple regions could not be defined (i.e., high, medium *and* low stress regions). It has been suggested that the low pressure region, where velocities are more sensitive to stress, corresponds to stresses below the *in situ* stress from which the core was taken (e.g., Holt et al., 2000). As the core is extracted, the removal of these stresses damages the core, creating microcracks and increasing the stress sensitivity. When the core is re-stressed to *in situ* conditions in lab experiments, the microcracks are closed, and so the stress sensitivity is lowered. However, it is very difficult to test this assertion empirically.

This approach does have its strengths, in particular the reduction of a complex system to 3 empirically determined constants, which facilitates the population of any models we may wish to build. For this reason the 3rd-order approach is becoming increasingly popular in the industrial sector (Herwanger, 2007). However, in order to fully define the 3rd order tensor for isotropic samples, velocity measurements are required at non-hydrostatic stresses (Prioul et al., 2004). As a result, there is little experimental data of the sort required to determine the 3rd-order terms, and as they are empirical constructs, they tell us little about the processes that lead to the development of non-linear elasticity. For this reason I prefer an approach that considers the micro-structure of the rocks in question.

6.3 A micro-structural model for nonlinear elasticity

A number of micro-structural models exist in the literature (e.g., Zatsepin and Crampin, 1997; Shapiro and Kaselow, 2005) where variations in micro-structural parameters are defined as a function of stress and related to the overall elastic properties of the rock via an effective medium model. In this section we consider the generalised effective medium approach of Schoenberg and Sayers (1995). In this approach the elasticity of a rock is evaluated in terms of the stiffness of its mineral components and the presence of low volume displacement discontinuities, which serve to increase compliance. This model is highly generalised, where few assumptions need to be made about the discontinuities. By assuming that the discontinuities can be considered as rotationally invariant cracks, we can extend the model by using a number of methods available in the literature to describe such discontinuities (e.g., Sayers and Kachanov, 1995; Hudson et al., 1996; Hall, 2000) and how they might vary with pressure (e.g., Tod, 2002). Following the approach of Tod (2002), I develop a simple model to describe the change in elasticity of a rock as a function of the stress applied to it. This approach is capable of considering anisotropy that develops due to both intrinsic rock properties and as a result of non-hydrostatic stresses. It is also capable of providing a framework within which we might consider damage due to coring or thermal effects.

6.3.1 Theoretical background

Schoenberg and Sayers (1995) introduce an effective medium approach to describe the compliance, \mathbf{S} , of a damaged rock. This approach is defined in terms of a matrix material and a random distribution of low volume, poorly bonded discontinuities. When a stress is applied across such a discontinuity, there will be a difference in displacement between the faces - a *displacement discontinuity*, $[u_i]$ - that is proportional to the traction, $t_i = \sigma_{ij}n_j$, on the discontinuity surface s . Hence, for a discontinuity with normal \mathbf{n} , the total displacement discontinuity $[u_i]$ is given by

$$\int_s [u_i] ds \propto \sigma_{ij}n_j. \quad (6.4)$$

The total additional strain within a volume V due to the presence of a set of discontinuities x is written

$$\varepsilon_{ij} = S_{ijkl}^r \sigma_{kl} + \frac{1}{2V} \sum_x \int_s ([u_i]n_j + [u_j]n_i) ds, \quad (6.5)$$

where \mathbf{S}^r is the background compliance of the rock matrix in the absence of discontinuities. This can be estimated by calculating the Voigt average moduli based upon individual mineral elasticities and their relative modal proportions (Kendall et al., 2007) using

$$\mathbf{S}^r = (\mathbf{C}^r)^{-1} = \left(\sum_{i=1}^N f_i \mathbf{C}_i^m \right)^{-1}, \quad (6.6)$$

where \mathbf{C}^r is the effective or average stiffness, f_i is the volume fraction of mineral constituent i , and \mathbf{C}_i^m is the mineral stiffness. In the absence of mineral stiffness data, the stiffness \mathbf{C}^r can be estimated from the behaviour of the rock at high pressures (Sayers, 2002). Equation 6.5 can be rewritten as

$$\varepsilon_{ij} = (S_{ijkl}^r + \Delta S_{ijkl}) \sigma_{kl}, \quad (6.7)$$

where $\Delta \mathbf{S}$ is the additional compliance caused by the presence of the displacement discontinuities. For displacement discontinuities that are considered as planar features rotationally invariant around \mathbf{n} , $\Delta \mathbf{S}$ is given by Sayers and Kachanov (1995) as

$$\Delta S_{ijkl} = \frac{1}{4} (\delta_{ik} \alpha_{jl} + \delta_{il} \alpha_{jk} + \delta_{jk} \alpha_{il} + \delta_{jl} \alpha_{ik}) + \beta_{ijkl}, \quad (6.8)$$

where δ_{ij} is the Kronecker delta. The second and fourth order tensors α and β are given by

$$\begin{aligned} \alpha_{ij} &= \frac{1}{V} \sum_x B_T^x n_i^x n_j^x s^x \\ \beta_{ijkl} &= \frac{1}{V} \sum_x (B_N^x - B_T^x) n_i^x n_j^x n_k^x n_l^x s^x. \end{aligned} \quad (6.9)$$

B_N^x and B_T^x characterise the normal and tangential compliances across an individual discontinuity surface. For a planar, penny shaped crack with radius r , in a drained, anisotropic rock with Young's modulus E_i and Poisson's ratio ν_i (e.g., Turley and Sines, 1971), B_N and B_T in the direction i normal to the surface are given by Sayers and Kachanov (1995) as

$$B_N = \frac{16(1 - \nu_i^2)r}{3\pi E_i}, \quad B_T = \frac{32(1 - \nu_i^2)r}{3\pi E_i(2 - \nu_i)}. \quad (6.10)$$

These equations are equivalent to those provided by Hudson (1981) for penny shaped cracks in the limit that the infilling material has zero bulk modulus.

Sayers (2002) provides a set of equations describing the stiffness tensor of a rock in terms of the 6×6 compliance matrix \mathbf{S}^r (the 81 component tensor \mathbf{S}^r is condensed using Voigt notation), α and β . Hall et al. (2008) extends these terms to include the presence of an anisotropic background medium with orthorhombic symmetry, the principle axes of which are aligned with those of α , finding that

$$\begin{aligned} C_{ii} &= \left[(S_{jk}^r + \beta_{jjkk})^2 - (S_{jj}^r + \alpha_{jj} + \beta_{jjjj})(S_{kk}^r + \alpha_{kk} + \beta_{kkkk}) \right] / D \\ C_{ij} &= \left[(S_{ij}^r + \beta_{iijj})(S_{kk}^r + \alpha_{kk} + \beta_{kkkk}) - (S_{ik}^r + \beta_{iikk})(S_{jk}^r + \beta_{jjkk}) \right] / D \end{aligned} \left. \vphantom{\begin{aligned} C_{ii} \\ C_{ij} \end{aligned}} \right\} i \neq j \neq k \leq 3$$

$$C_{ii} = (S_{ii}^r + \alpha_{jj} + \alpha_{kk} + 4\beta_{jjkk})^{-1} \quad i \neq j \neq k \geq 4 \quad (6.11)$$

where

$$\begin{aligned}
D = & (S_{11}^r + \alpha_{11} + \beta_{1111})(S_{23}^r + \beta_{2233})^2 + (S_{22}^r + \alpha_{22} + \beta_{2222})(S_{13}^r + \beta_{1133})^2 \\
& + (S_{33}^r + \alpha_{33} + \beta_{3333})(S_{12}^r + \beta_{1122})^2 - 2(S_{12}^r + \beta_{1122})(S_{13}^r + \beta_{1133})(S_{23}^r + \beta_{2233}) \\
& - (S_{11}^r + \alpha_{11} + \beta_{1111})(S_{22}^r + \alpha_{22} + \beta_{2222})(S_{33}^r + \alpha_{33} + \beta_{3333}).
\end{aligned} \tag{6.12}$$

Based on previous work by Gueguen and Schubnel (2003), Hall et al. (2008) introduce an anisotropic normalising factor h_i , where

$$h_i = \frac{3E_i(2 - \nu_i)}{32(1 - \nu_i^2)}. \tag{6.13}$$

When α is multiplied by this factor, a non-dimensional discontinuity density tensor is returned, which is a function only of discontinuity number density, radius cubed, and orientation distribution,

$$\sum_{i=1}^3 h_i \alpha_{ii} = \xi_c, \tag{6.14}$$

where $\xi_c = \frac{N}{V}r^3$. N is the number of discontinuities in a volume V , and ξ_c is equivalent to the non-dimensional crack density term used in many effective medium theories, such as Hudson (1981), Hudson et al. (1996), and Thomsen (1995).

6.3.2 Inversion for scalar cracks

From equation 6.10, we can express the ratio

$$B_N/B_T = (1 - \nu_i/2). \tag{6.15}$$

Sayers and Kachanov (1995) define the scalar crack as $B_N/B_T \approx 1$ to simplify various expressions and make elasticity estimates more treatable. In making this simplification, they assume a rock with low Poisson's ratio ($\nu_o < 0.2$), where β will be at least an order of magnitude smaller than α , and so can be neglected. In this limit any crack set can be described by considering its contribution to the 3 orthogonal components of the 2nd order tensor, α_{11} , α_{22} , and α_{33} . For instance, a random isotropic distribution can be described by $\alpha_{11} = \alpha_{22} = \alpha_{33}$, and transverse symmetry by $\alpha_{11} > \alpha_{22} = \alpha_{33}$. Later in this chapter I will discuss the effects of including β in the inversion procedure.

Hall et al. (2008) develop an inversion procedure to determine α based on observed velocity measurements, assuming $\beta = 0$. Equations 6.11 and 6.12 are used to relate the observed stiffness tensor as determined from velocity measurements to the background stiffness and α . An iterative Newton-Raphson approach is used, where a Jacobian matrix describes the variation of the modelled stiffness tensor with α . It is assumed that the velocity measurements are aligned with the principle axes of α .

Figure 6.2 shows the results of this inversion procedure for several samples from the Clair reservoir, a sandstone reservoir sited on the UK continental shelf. The cores have been taken from depths of 1784, 1788, 1909, 1950, and 2194 meters. The individual samples will be referred to by their depths hereafter. The background compliances were determined using the geomathematical method described by Kendall et al. (2007). XRTG (X-Ray Texture Goniometry) and EBSD (Electron Back Scattering

Diffraction) were used to assess the preferred orientation of anisotropic minerals, or crystal preferred orientation (CPO), and mineral modal proportions were measured using QXRD (Quantitative X-Ray Diffraction). The left panels show the best fit crack density α values normalised by h_i , and the right panels compare back-calculated velocities to the observed velocities. The back-calculated velocities in general show a reasonable fit with observed velocities, especially for the P-waves (V_P). The fit for V_{P45} is poor. Hall et al. (2008) suggest that this may be a result of difficulties in cutting and analysing the core at 45° .

6.3.3 Joint inversion for α and β

For the scalar crack assumption to be appropriate, the rocks must have a low Poisson's ratio, which is generally acceptable for reservoir rocks, and the cracks must be flat, poorly bonded features. If there are significant amounts of diagenetic clay or debris within the cracks then equation 6.15 may not be valid. In order to model how cracks are influenced by pressure, I make the assumption that they are planar, penny shaped features without any fill (see next section). By analysing the contribution of β , I can assess how appropriate this assumption is.

Hall et al. (2008) provide a method for estimating β from ultrasonic velocity measurements, based on Sayers (2002); however, this method assumes that the contribution from β is small, and is responsible solely for the misfit between observed and back-calculated velocities from the inversion for α . I wish to test the assumption that β is small, and so I develop an inversion procedure where β is not required *a priori* to be small.

I assume that the cracks are disc-shaped, identical and that β is isotropic (to do otherwise introduces impractical complexity given that my principle aim is to evaluate the magnitude of β rather than its orientation distribution). I note that for such a distribution, I can rewrite equation 6.9 for α and β (Sarout et al., 2007)

$$\begin{aligned}\alpha_{ij} &= \frac{\pi N r^2}{3V} B_T \delta_{ij} \\ \beta_{ijkl} &= \frac{\pi N r^2}{15V} (B_N - B_T) (\delta_{ij} \delta_{kl} + 2(\delta_{ik} \delta_{jl} + \delta_{il} \delta_{jk})).\end{aligned}\quad (6.16)$$

The non-vanishing components of α and β are

$$\begin{aligned}\alpha_{11} &= \alpha_{22} = \alpha_{33} = \frac{1}{3} \alpha_{mm}, \\ \beta_{1111} &= \beta_{2222} = \beta_{3333}, \\ \beta_{1122} &= \beta_{1133} = \beta_{2233} = \beta_{1212} = \beta_{1313} = \beta_{2323} = \frac{1}{3} \beta_{1111},\end{aligned}\quad (6.17)$$

where

$$\alpha_{11} = \frac{\pi N r^2}{3V} B_T, \quad (6.18)$$

$$\beta_{1111} = \frac{\pi N r^2}{3V} B_T \left(\frac{B_N}{B_T} - 1 \right), \quad (6.19)$$

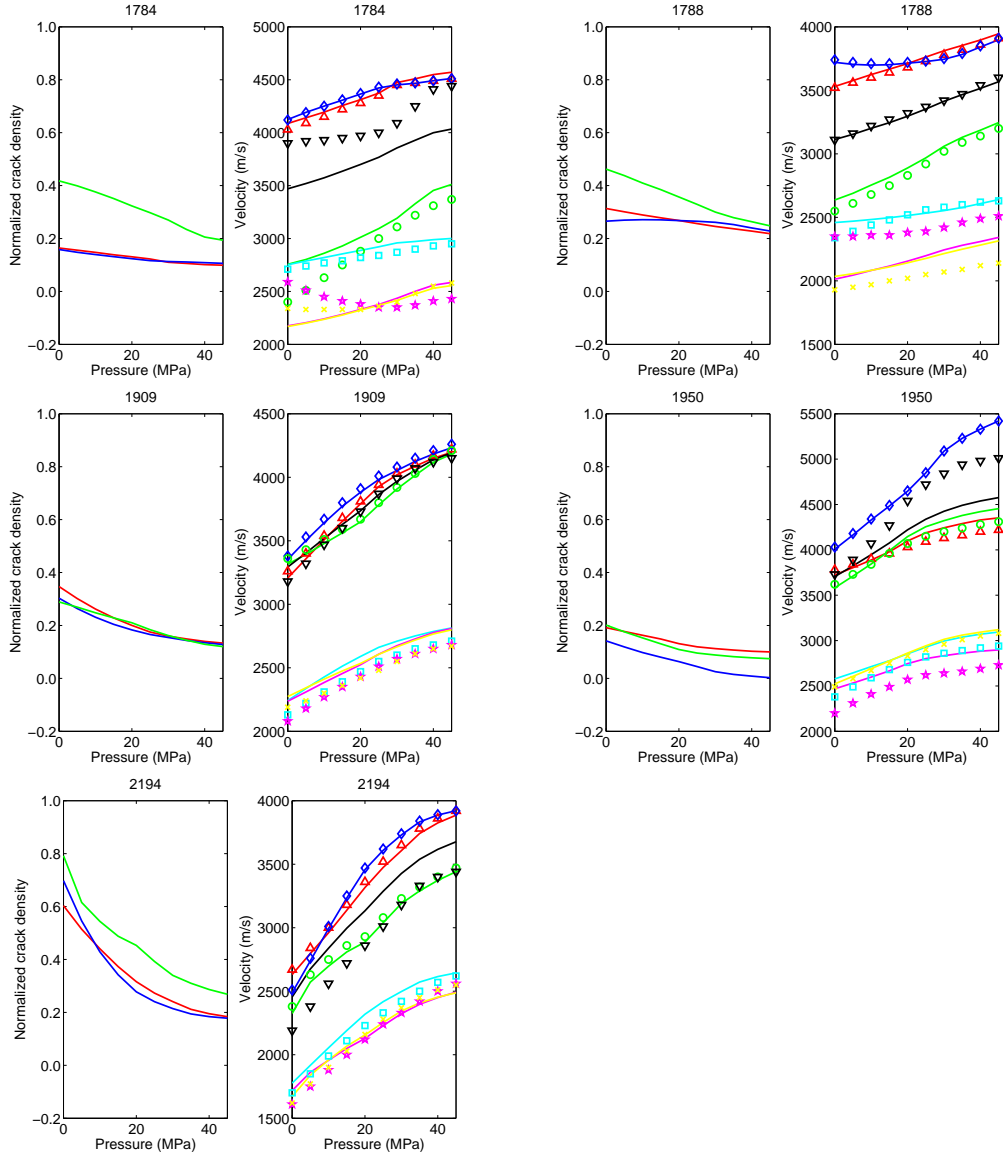


Figure 6.2: Inverted scalar crack densities and back calculated velocities for the Clair samples: Left-hand panels show α as a function of pressure (red - α_{11} , blue - α_{22} , green - α_{33}). Right-hand panels show observed velocity data (symbols) and back calculated velocities (lines) corresponding to the calculated α (red - V_{Px} , blue - V_{Py} , green - V_{Pz} , black - V_{P45} , cyan - V_{Sxy} , magenta - V_{Sxz} , yellow - V_{Syz}).

and α_{mm} is the trace of α ($\alpha_{mm} = \alpha_{11} + \alpha_{22} + \alpha_{33}$). By rearranging equations 6.18 and 6.19 I can rewrite β in terms of α and the ratio B_N/B_T , such that

$$\beta_{1111} = \frac{1}{3} \left(\frac{B_N}{B_T} - 1 \right) \alpha_{mm}. \quad (6.20)$$

Substitution of this relationship into equations 6.11 and 6.12 yields the overall stiffness as a function of both the second and fourth order crack density tensors, by way of the ratio B_N/B_T ,

$$\left. \begin{aligned} C_{ii} &= \left[(S_{jk}^r + \frac{f}{9}\alpha^m)^2 - (S_{jj}^r + \alpha_{jj} + \frac{f}{3}\alpha^m)(S_{kk}^r + \alpha_{kk} + \frac{f}{3}\alpha^m) \right] / D \\ C_{ij} &= \left[(S_{ij}^r + \frac{f}{9}\alpha^m)(S_{kk}^r + \alpha_{kk} + \frac{f}{3}\alpha^m) - (S_{ik}^r + \frac{f}{9}\alpha^m)(S_{jk}^r + \frac{f}{9}\alpha^m) \right] / D \end{aligned} \right\} i \neq j \neq k \leq 3$$

$$C_{ii} = (S_{ii}^r + \alpha_{jj} + \alpha_{kk} + \frac{4f}{9}\alpha^m)^{-1} \quad i \neq j \neq k \geq 4 \quad (6.21)$$

$$\begin{aligned} D &= (S_{11}^r + \alpha_{11} + \frac{f}{3}\alpha^m)(S_{23}^r + \frac{f}{9}\alpha^m)^2 + (S_{22}^r + \alpha_{22} + \frac{f}{3}\alpha^m)(S_{13}^r + \frac{f}{9}\alpha^m)^2 \\ &+ (S_{33}^r + \alpha_{33} + \frac{f}{3}\alpha^m)(S_{12}^r + \frac{f}{9}\alpha^m)^2 \\ &- 2(S_{12}^r + \frac{f}{9}\alpha^m)(S_{13}^r + \frac{f}{9}\alpha^m)(S_{23}^r + \frac{f}{9}\alpha^m) \\ &- (S_{11}^r + \alpha_{11} + \frac{f}{3}\alpha^m)(S_{22}^r + \alpha_{22} + \frac{f}{3}\alpha^m)(S_{33}^r + \alpha_{33} + \frac{f}{3}\alpha^m), \end{aligned} \quad (6.22)$$

where

$$f = \left(\frac{B_N}{B_T} - 1 \right). \quad (6.23)$$

Having defined a set of equations for the overall stiffness with the fourth order crack density tensor written in terms of the second order crack density tensor and B_N/B_T ratio, the inversion for crack density and B_N/B_T can then be performed using an iterative Newton-Raphson approach with model update:

$$\alpha_{ii} = \alpha_{ii} + \delta m_i, \quad i = 1, 3. \quad (6.24)$$

The vector model misfit is evaluated

$$\delta b_l = C_l^{obs} - C_l^{model} \quad l = 11, 22, 33, 44, 55, 66, 12, 13, 23, \quad (6.25)$$

where the matrix Jacobian

$$J_{il} = \frac{\partial C_l^{model}}{\partial \alpha_i} \quad (6.26)$$

is inverted to evaluate the vector model update

$$\delta m_i = J_{il}^{-1} \delta b_l. \quad (6.27)$$

The matrix Jacobian of derivatives with respect to the second order crack density tensor α_{ii} is evaluated using the following set of equations below. The partial derivatives of the denominator term

D^{-1} are

$$\begin{aligned}
 \frac{\partial D}{\partial \alpha_{ii}} &= (1 + \frac{f}{3})(S_{jk}^r + \frac{f}{9}\alpha^m)^2 + \frac{2f}{9}(S_{ii}^r + \alpha_{ii} + \frac{f}{3}\alpha^m)(S_{jk}^r + \frac{f}{9}\alpha^m) + \frac{f}{3}(S_{ik}^r + \frac{f}{9}\alpha^m)^2 \\
 &+ \frac{2f}{9}(S_{jj}^r + \alpha_{jj} + \frac{f}{3}\alpha^m)(S_{ik}^r + \frac{f}{9}\alpha^m) + \frac{f}{3}(S_{ij}^r + \frac{f}{9}\alpha^m)^2 \\
 &+ \frac{2f}{9}(S_{kk}^r + \alpha_{kk} + \frac{f}{3}\alpha^m)(S_{ij}^r + \frac{f}{9}\alpha^m) - \frac{2f}{9} \left((S_{ik}^r + \frac{f}{9}\alpha^m)(S_{jk}^r + \frac{f}{9}\alpha^m) \right. \\
 &\left. + (S_{ij}^r + \frac{f}{9}\alpha^m)(S_{jk}^r + \frac{f}{9}\alpha^m) + (S_{ij}^r + \frac{f}{9}\alpha^m)(S_{ik}^r + \frac{f}{9}\alpha^m) \right) \\
 &- (1 + \frac{f}{3})(S_{jj}^r + \alpha_{jj} + \frac{f}{3}\alpha^m)(S_{kk}^r + \alpha_{kk} + \frac{f}{3}\alpha^m) - \frac{f}{3}(S_{ii}^r + \alpha_{ii} + \frac{f}{3}\alpha^m) \\
 &(S_{kk}^r + \alpha_{kk} + \frac{f}{3}\alpha^m) - \frac{f}{3}(S_{ii}^r + \alpha_{ii} + \frac{f}{3}\alpha^m)(S_{jj}^r + \alpha_{jj} + \frac{f}{3}\alpha^m), \tag{6.28}
 \end{aligned}$$

where $i \neq j \neq k \leq 3$. The partial derivatives for $C_{ii}^\dagger = C_{ii}D$ terms are

$$\begin{aligned}
 \frac{\partial C_{ii}^\dagger}{\partial \alpha_{ii}} &= \frac{2f}{9}(S_{jk}^r + \frac{f}{9}\alpha^m) - \frac{f}{3}(S_{kk}^r + \alpha_{kk} + \frac{f}{3}\alpha^m) - \frac{f}{3}(S_{jj}^r + \alpha_{jj} + \frac{f}{3}\alpha^m), \\
 \frac{\partial C_{ii}^\dagger}{\partial \alpha_{jj}} &= \frac{2f}{9}(S_{jk}^r + \frac{f}{9}\alpha^m) - (1 + \frac{f}{3})(S_{kk}^r + \alpha_{kk} + \frac{f}{3}\alpha^m) - \frac{f}{3}(S_{jj}^r + \alpha_{jj} + \frac{f}{3}\alpha^m), \tag{6.29}
 \end{aligned}$$

where $i \neq j \neq k \leq 3$. The partial derivatives for $C_{ij}^\dagger = C_{ij}D$ (when $i \neq j$) terms are

$$\begin{aligned}
 \frac{\partial C_{ij}^\dagger}{\partial \alpha_{ii}} &= \frac{f}{9}(S_{kk}^r + \alpha_{kk} + \frac{f}{3}\alpha^m) + \frac{f}{3}(S_{ij}^r + \frac{f}{9}\alpha^m) - \frac{f}{9}(S_{jk}^r + \frac{f}{9}\alpha^m) - \frac{f}{9}(S_{ik}^r + \frac{f}{9}\alpha^m) \\
 &= \frac{\partial C_{ij}^\dagger}{\partial \alpha_{jj}}, \\
 \frac{\partial C_{ij}^\dagger}{\partial \alpha_{kk}} &= \frac{f}{9}(S_{kk}^r + \alpha_{kk} + \frac{f}{3}\alpha^m) + (1 + \frac{f}{3})(S_{ij}^r + \frac{f}{9}\alpha^m) - \frac{f}{9}(S_{jk}^r + \frac{f}{9}\alpha^m) - \\
 &\frac{f}{9}(S_{ik}^r + \frac{f}{9}\alpha^m), \tag{6.30}
 \end{aligned}$$

where $i \neq j \neq k \leq 3$.

The partial derivatives for C_{ij} ($i, j \leq 3$) are written

$$\frac{\partial C_{ij}}{\partial \alpha_{ii}} = D^{-1} \frac{\partial C_{ij}^\dagger}{\partial \alpha_{ii}} - C_{ij}^\dagger D^{-2} \frac{\partial D}{\partial \alpha_{ii}} \tag{6.31}$$

and the partial derivatives for C_{ii} ($i \geq 4$) terms are

$$\begin{aligned}
\frac{\partial C_{44}}{\partial \alpha_{11}} &= -\frac{4f}{9}(S_{44}^r + \alpha_{22} + \alpha_{33} + \frac{4f}{9}\alpha^m)^{-2} \\
\frac{\partial C_{44}}{\partial \alpha_{22}} &= -(1 + \frac{4f}{9})(S_{44}^r + \alpha_{22} + \alpha_{33} + \frac{4f}{9}\alpha^m)^{-2} \\
\frac{\partial C_{44}}{\partial \alpha_{33}} &= -(1 + \frac{4f}{9})(S_{44}^r + \alpha_{22} + \alpha_{33} + \frac{4f}{9}\alpha^m)^{-2} \\
\frac{\partial C_{55}}{\partial \alpha_{11}} &= -(1 + \frac{4f}{9})(S_{55}^r + \alpha_{11} + \alpha_{33} + \frac{4f}{9}\alpha^m)^{-2} \\
\frac{\partial C_{55}}{\partial \alpha_{22}} &= -\frac{4f}{9}(S_{55}^r + \alpha_{11} + \alpha_{33} + \frac{4f}{9}\alpha^m)^{-2} \\
\frac{\partial C_{55}}{\partial \alpha_{33}} &= -(1 + \frac{4f}{9})(S_{55}^r + \alpha_{11} + \alpha_{33} + \frac{4f}{9}\alpha^m)^{-2} \\
\frac{\partial C_{66}}{\partial \alpha_{11}} &= -(1 + \frac{4f}{9})(S_{66}^r + \alpha_{11} + \alpha_{22} + \frac{4f}{9}\alpha^m)^{-2} \\
\frac{\partial C_{66}}{\partial \alpha_{22}} &= -(1 + \frac{4f}{9})(S_{66}^r + \alpha_{11} + \alpha_{22} + \frac{4f}{9}\alpha^m)^{-2} \\
\frac{\partial C_{66}}{\partial \alpha_{33}} &= -\frac{4f}{9}(S_{66}^r + \alpha_{11} + \alpha_{22} + \frac{4f}{9}\alpha^m)^{-2}.
\end{aligned} \tag{6.32}$$

This method finds the best fitting values of α at a given B_N/B_T value. I found that when B_N/B_T was included in the Newton-Raphson scheme, it was seldom possible to find stable, convergent solutions: stationary points in the objective function were too close to the desired solution. Therefore a grid search was performed over B_N/B_T , and for each B_N/B_T value the Newton-Raphson approach was used to find α . These α values were used to back-calculate velocities, and the value of B_N/B_T that, in conjunction with the α values computed from it, minimised the misfit between back-calculated and observed velocities was selected as the most appropriate. This approach is illustrated in Figure 6.3.

The results of this inversion for the samples from the Clair reservoir are shown in Figure 6.4. Figure 6.5 shows the optimum values of B_N/B_T determined via this method. We also perform the inversion for Berea (Lo et al., 1986) and Penrith (Sayers, 2002) sandstone samples. Because EBSD and XRTG information is not available for these samples, \mathbf{S}^r is determined from the behaviour of the samples at high pressure following MacBeth (2004). The results are shown in Figure 6.6, with B_N/B_T plotted in Figure 6.7. At high pressures the observed stiffness tensors become close to \mathbf{S}^r , hence α becomes small and our inversion for B_N/B_T becomes less reliable. This problem is not encountered by the Clair samples, where the observed stiffness is always well below \mathbf{S}^r .

Figures 6.5 and 6.7 give an indication as to how appropriate the scalar crack assumption is. For a flat crack with no infill, equation 6.15 suggests that B_N/B_T should be between 0.8 and 1, depending on the Poisson's ratio of the background matrix. Although there is some spread outside these bounds, the majority of inverted B_N/B_T values are found close to this range, indicating that the scalar crack assumption is appropriate. It is also worth noting that there appears to be no systematic variation of B_N/B_T with pressure, which is implicitly predicted by the scalar crack assumption, further strengthening our confidence in making it.

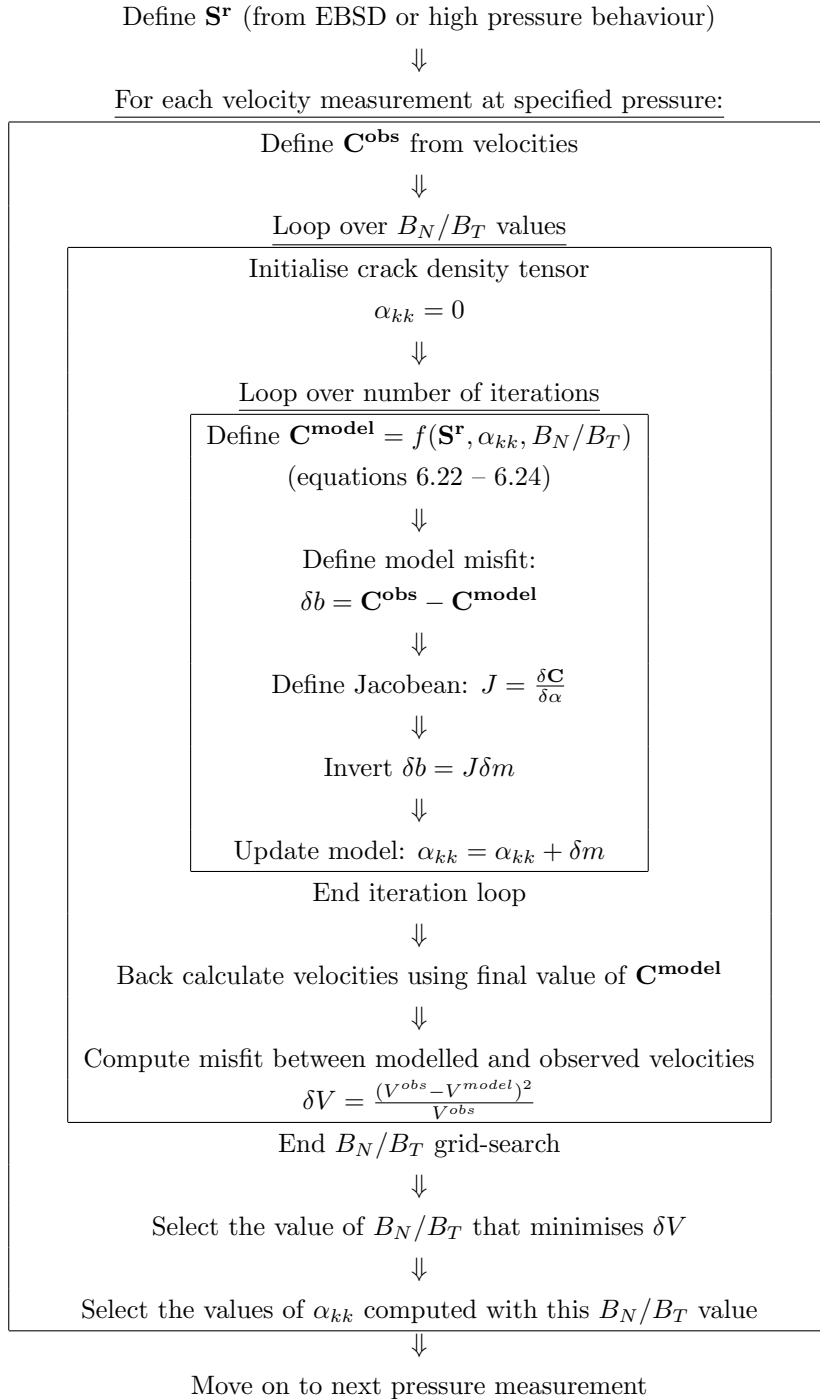


Figure 6.3: Workflow for inverting velocity measurements for B_N/B_T and the crack density tensor. Modified from Hall et al. (2008).

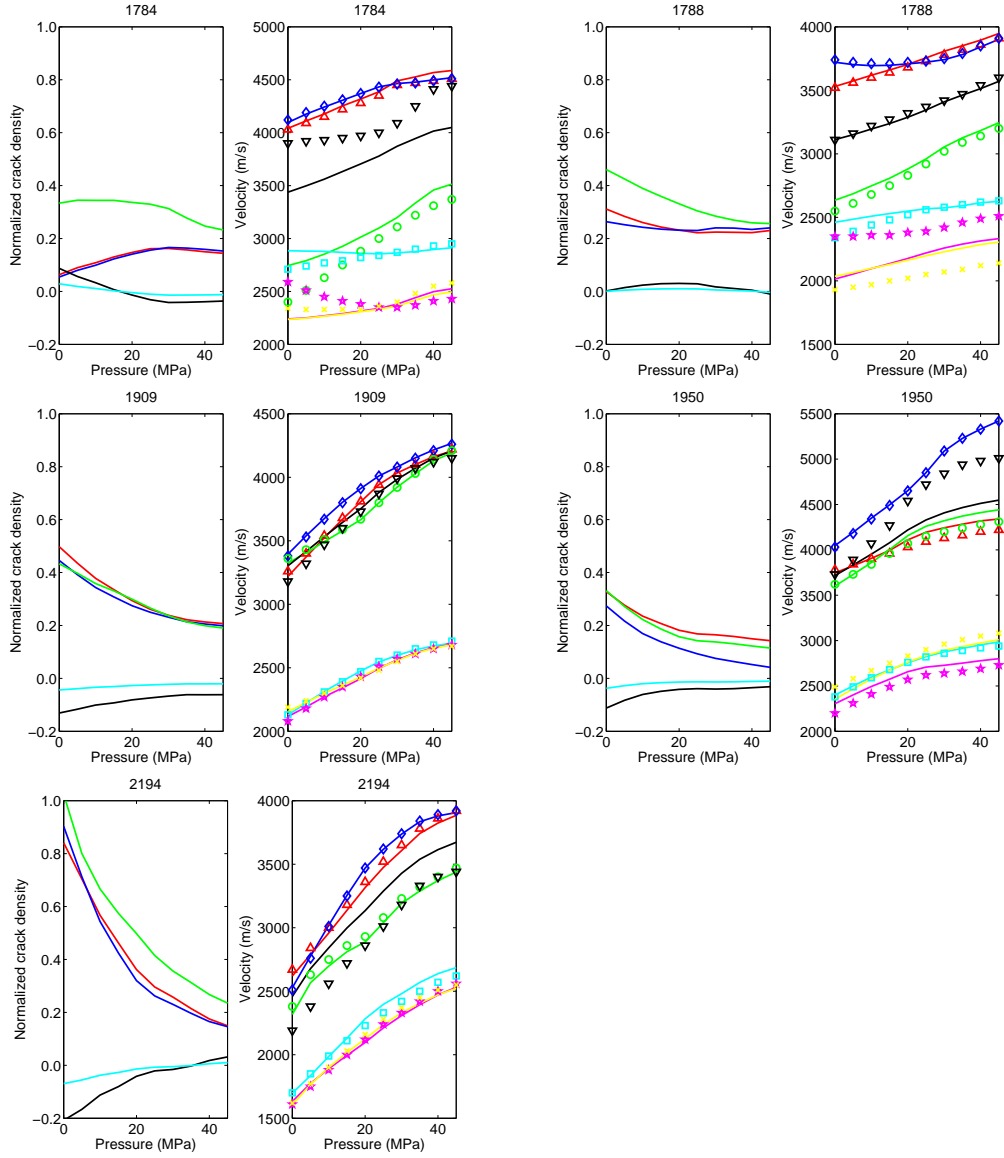


Figure 6.4: Inverted second and fourth order crack density tensor components and back-calculated velocities for the Clair samples: Left-hand panels show α and β as a function of pressure (red - α_{11} , blue - α_{22} , green - α_{33} , black - β_{iii} , cyan - β_{ijj}). Right-hand panels show velocity data (symbols) and back calculated velocities (lines) corresponding to the calculated α s and β s (red - V_{Px} , blue - V_{Py} , green - V_{Pz} , black - V_{P45} , cyan - V_{Sxy} , magenta - V_{Sxz} , yellow - V_{Syz}).

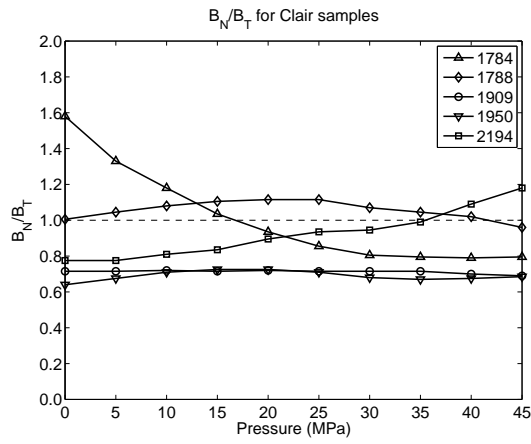


Figure 6.5: Best fit B_N/B_T as a function of pressure for the Clair samples.

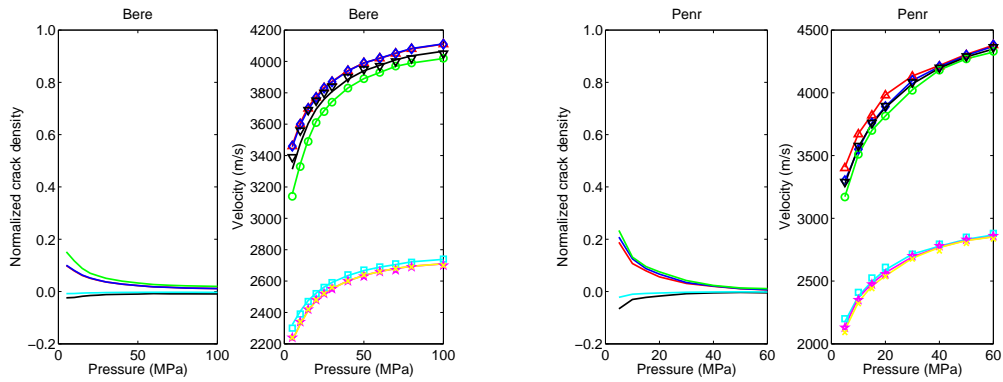


Figure 6.6: Second and fourth order crack density components and back calculated velocities for the literature samples. In the same format as Figure 6.4.

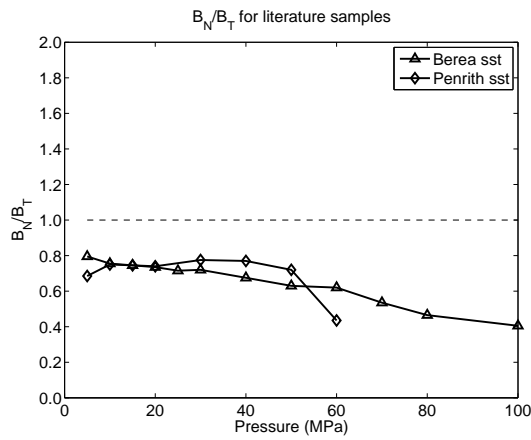


Figure 6.7: Best fit B_N/B_T as a function of pressure for the literature samples.

6.3.4 Effects of stress on crack density

We know from micro-structural analysis (e.g., Batzle et al., 1980) that cracks and discontinuities are complex features, with rough walls, nonlinear geometry, irregular intersections, and clay or diagenetic infill; however, in the previous section I have shown that by modelling them as highly simplified, rotationally invariant, smooth (penny-shaped), empty features we can still approximate the effective rock properties to a reasonable degree of accuracy. I use this observation to my advantage in order to predict how the effective properties will be influenced by an applied stress field. In effect, this model assumes that the microcracks within the rock will respond to the long duration, high strain, finite strain-rate deformation imposed by geomechanical effects in the same manner as they do to the short duration, infinitesimal strain, high strain-rate deformation imposed by the passage of a seismic wave. Therefore this assumption will only be appropriate as long as the rock doesn't undergo any plastic or brittle failure during geomechanical deformation.

Hudson (2000) and Tod (2002) present analytical models where the aspect ratio and number density of cracks is dependent upon applied stress and fluid pressure. This model considers elastic deformation only, where the permanent deformation of pores into cracks and the development of new cracks is not considered; hence, when the stress state is returned to its original magnitude, the material will relax to its reference state.

Hudson (2000) derives an expression for the change in aspect ratio, δa , of a penny-shaped crack due to a change in applied stress and/or fluid pressure,

$$\delta a = -\frac{2(1-\nu^r)}{\pi\mu^r}(\delta\sigma_{ij}n_in_j - \beta_w\delta P_{fl}) - \frac{a}{K^r}\beta_w\delta P_{fl}, \quad (6.33)$$

where $\delta\sigma$ and δP_{fl} are the change in applied stress tensor and fluid pressure, β_w is the Biot-Willis parameter, assumed here for simplicity to be unity, \mathbf{n} is the crack normal, and μ^r , ν^r and K^r are respectively the shear modulus, Poisson's ratio and bulk modulus of the matrix in the absence of compliant porosity. The right-hand term $\frac{a}{K^r}\beta_w\delta P_{fl}$ of equation 6.33 is small in comparison with the other terms and can be neglected (Hudson, 2000). Integrating equation 6.33 gives

$$a = a^0 - \frac{2(1-\nu^r)}{\pi\mu^r}\sigma^{c(\mathbf{n})}, \quad (6.34)$$

where a^0 is the aspect ratio in the absence of an applied stress (or at a pre-defined reference stress). The effects of applied stress and pore pressure combine to give the effective crack normal stress

$$\sigma^{c(\mathbf{n})} = \sigma_{ij}n_in_j - \beta_w P_{fl}. \quad (6.35)$$

For a crack with an initial aspect ratio a^0 , there will be a critical stress where

$$a^0 = \frac{2(1-\nu^r)}{\pi\mu^r}\sigma^{c(\mathbf{n})}, \quad (6.36)$$

and the crack can be considered as closed. Tod (2002) assumes an exponential distribution of initial aspect ratios. If this is the case, then crack density will decrease exponentially with pressure due to crack closure (van der Neut et al., 2007), so that

$$\xi(\sigma^c) = \xi^0 \exp(-c_r\sigma^{c(\mathbf{n})}), \quad (6.37)$$

where

$$c_r = \frac{2(1 - \nu^r)}{\pi \mu^r a^0} \quad (6.38)$$

and ξ^0 is the crack density at a defined initial pressure (usually 0 MPa).

As discussed in the previous section, by making the scalar crack assumption, we treat the overall crack distribution as three mutually orthogonal aligned sets, each contributing to one of the nonzero components of α . For each set, an initial crack density and average aspect ratio is defined; hence, for any applied stress field, α is calculated using equations 6.37 and 6.38 to give

$$\alpha_{ij} = \begin{pmatrix} \xi_1(\sigma^{c(\mathbf{n}_1)})/h_1 & 0 & 0 \\ 0 & \xi_2(\sigma^{c(\mathbf{n}_2)})/h_2 & 0 \\ 0 & 0 & \xi_3(\sigma^{c(\mathbf{n}_3)})/h_3 \end{pmatrix}. \quad (6.39)$$

6.3.5 Results

Figure 6.8 shows the results of modelling the P- and S-wave velocities using equations 6.37 to 6.39 for the samples discussed in the previous section. Table 6.2 shows the best fit initial average aspect ratios and crack densities used to produce these models.

The fit between observed and modelled velocities is reasonable. Furthermore, the initial aspect ratios range between $5 \times 10^{-4} < a^0 < 5 \times 10^{-3}$, which is a reasonable range of values expected for a distribution of flat, penny shaped cracks (Kuster and Toksoz, 1974). The results from Figure 6.8 and Table 6.2 indicate that the nonlinear elastic behaviour can be modelled based on the assumption that it is made up of stiff, non-deforming mineral grains and displacement discontinuities in the form of flat, penny shaped cracks with physically reasonable initial aspect ratio distributions.

6.3.6 Anisotropy

A benefit of my approach is the treatment of anisotropy. This model is capable of considering intrinsic anisotropy as well as stress induced anisotropy. Most rocks are intrinsically anisotropic. This intrinsic anisotropy is derived from two sources: alignment of minerals and alignment of fabrics.

The alignment of mineral grains due to depositional, deformation or diagenetic processes (crystal preferred orientations, CPO) has been well studied as a cause of anisotropy (e.g., Blackman et al., 1993; Rumpker et al., 1999; Barruol and Hoffmann, 1999; Kendall et al., 2007; Valcke et al., 2006). Elongate or platy minerals, such as micas and clays will tend to become aligned during deposition. The elasticities of these minerals can be highly anisotropic, with the principle axes of the elastic tensor aligned with the grain shape. By using the geomathematical model developed by Kendall et al. (2007) to evaluate the background compliance \mathbf{S}^r , we are able to assess the contribution of CPO to the anisotropy of a sample based on detailed petrofabric analysis. Equation 6.11 limits us to cases where the principle axes of the compliance tensor and of α are aligned. This should not pose a problem for VTI systems so long as one of the principle stress axes to be aligned vertically; however, more complicated anisotropic symmetries will still need to be dealt with carefully.

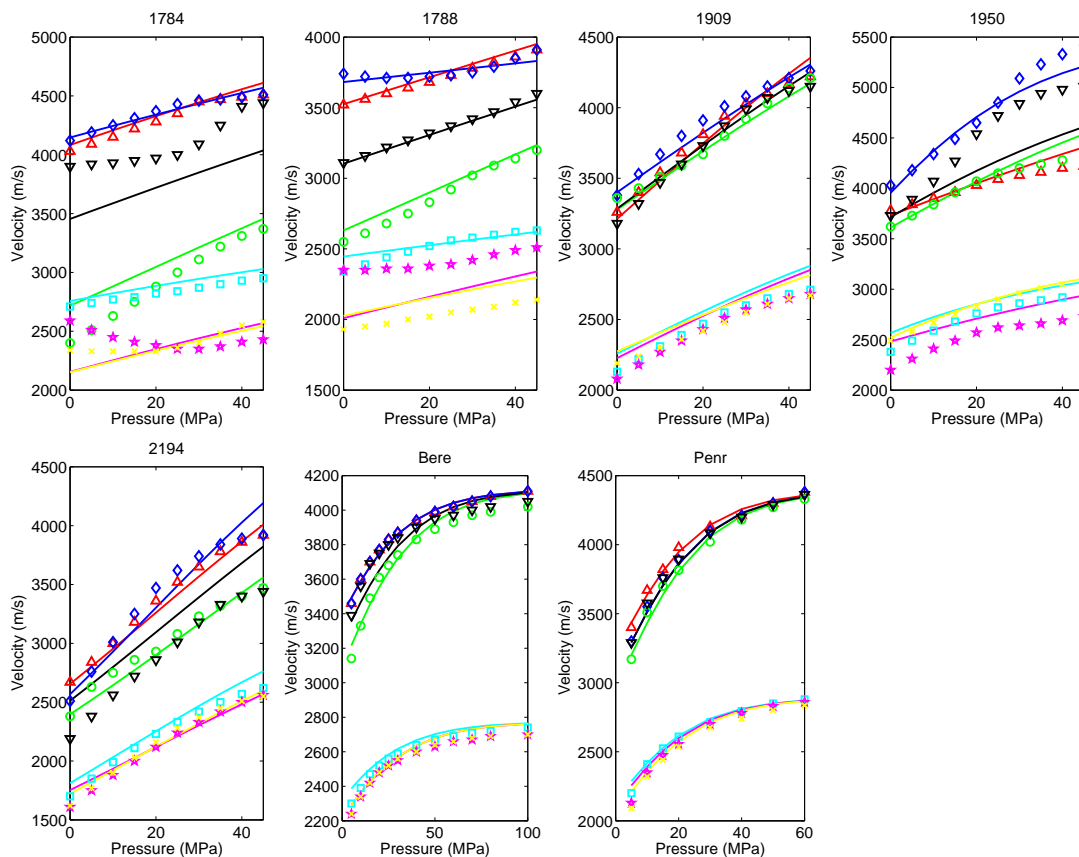


Figure 6.8: Modelled stress dependent velocities calculated using equations 6.37 - 6.39 for the Clair and literature samples (lines), shown with observed velocities (symbols). Red - V_{Px} , blue - V_{Py} , green - V_{Pz} , black - V_{P45} , cyan - V_{Sxy} , magenta - V_{Sxz} , yellow - V_{Syz} .

Shape preferred orientation (SPO) anisotropy is also related to alignment of fabric during sedimentary deposition and/or diagenesis. If platy or elongate grains are deposited in a manner such that there is a preferential alignment between grain contacts, then there will be an increase in displacement discontinuities in this direction, and hence an increased compliance. This effect is best demonstrated by the Clair samples 1784 and 1788 (Hall et al., 2008). These samples are mica rich, and these platy grains are orientated with normals parallel to the z-axis. With this the case, we expect to find that there are a greater number of grain boundaries with normals parallel to the z-axis than to the x- or y-axis. As a result, V_{Pz} is greatly reduced (Figure 6.2), and the inversion for α indicates that α_{33} is larger than α_{11} and α_{22} . Since the preferred orientation of mineralogical axes and grain boundaries will not be greatly affected by in situ reservoir stresses (unless these are of sufficient magnitude to cause deformation or failure of the mineral grains), I refer to the anisotropy that they generate as static anisotropy.

<i>Sample</i>	<i>Crack set</i>	a^0	ξ^0	<i>Sample</i>	<i>Crack set</i>	a^0	ξ^0
1784	α_{11}	0.0014	0.165	2194	α_{11}	0.0006	0.590
	α_{22}	0.0018	0.155		α_{22}	0.0005	0.635
	α_{33}	0.0012	0.440		α_{33}	0.0007	0.740
1788	α_{11}	0.0019	0.315	Bere	α_{11}	0.0009	0.085
	α_{22}	0.0044	0.280		α_{22}	0.0009	0.085
	α_{33}	0.0014	0.475		α_{33}	0.0009	0.140
1909	α_{11}	0.0007	0.345	Penr	α_{11}	0.0005	0.150
	α_{22}	0.0008	0.295		α_{22}	0.0005	0.180
	α_{33}	0.0009	0.300		α_{33}	0.0005	0.210
1950	α_{11}	0.0014	0.190				
	α_{22}	0.0004	0.150				
	α_{33}	0.0008	0.195				

Table 6.2: Best fit initial average crack aspect ratios (a^0) and densities (ξ^0) for the Clair and literature samples used to calculate the velocities as a function of stress shown in Figure 6.8.

The effects of non-hydrostatic stresses on anisotropy also are expected to be important. For example, the effects of uniaxial stresses on seismic anisotropy have been documented (e.g., Scott and Abousleiman, 2004; Sayers and Schutjens, 2007). When the applied stress is uniaxial, cracks with faces perpendicular to the principle stress axis will close, while those parallel will open or remain unaffected. As a result, velocities will be faster in the direction parallel to the maximum stress. Since the stress field within and around reservoirs is likely to be non-hydrostatic, it is important that any model used to estimate seismic velocities is capable of incorporating these effects. For example, Herwanger and Horne (2005) model seismic anisotropy due to a triaxial stress field based on 3rd order elasticity theory (Prioul et al., 2004) to explain shear wave splitting observations from the Valhall and Ekofisk fields.

Here I consider non-hydrostatic stresses by resolving the in-situ stress field in terms of stresses normal to the modelled crack faces. This is shown in Figure 6.9. In Figure 6.9a, the results of a hydrostatic compression test on a sample of Berea sandstone (Scott and Abousleiman, 2004) are shown, and best fit ξ^0 and a^0 values computed to back-calculate velocities. Scott and Abousleiman (2004) then perform a uniaxial strain test on a similar core sample. The details of the uniaxial test are shown in Figures 6.9b and 6.9c, and the results plotted in Figure 6.9d. The ξ^0 and a^0 values calculated for the hydrostatic case (given in Table 6.3) are then used to predict velocities for the uniaxial case. It can be seen that upon application of this uniaxial stress, the velocity of the P-waves along the main axis increase rapidly with pressure, while those perpendicular to the main axis increase more slowly. These effects are predicted by our model, and the fit is particularly good for the faster P-waves (V_{Px}) and fast S-waves (V_{Syz}), as well as the P-waves at 45° . The model does not accurately predict the slower P (V_{Pz}) and S (V_{Sxz}) wave velocities above a confining pressure of 20MPa. This means that the model underestimates the magnitude of shear wave splitting. Since the model predicts

	a^0	ξ^0
α_{11}	0.00031	0.250
α_{22}	0.00061	0.135
α_{33}	0.00061	0.140

Table 6.3: Best fit initial average crack aspect ratios (a^0) and densities (ξ^0) calculated from hydrostatic stress test shown in Figure 6.9a, and used to calculate the velocities for the uniaxial test shown in Figure 6.9d.

that as confining pressure increases, the crack sets orientated parallel to the main axis will gradually close and lead to increasing velocity of the slower waves. What is observed is that the anisotropy becomes ‘locked in’ (Scott and Abousleiman, 2004) and the velocities do not increase further. The reason for the locking in mechanism remains unclear and so any improvements to our analytical model will require understanding of this mechanism. It is possible that this failure arises partly due to my assumption that all deformation occurring is elastic. Scott and Abousleiman (2004) observe significant amounts of acoustic emissions when the confining stress exceeds 20MPa during the triaxial stress test, indicating that inelastic deformation is indeed occurring. It may also be possible that crack-crack interactions are affecting deformation in the manner similar to that described by Batzle et al. (1980).

Time-lapse seismic data can show an asymmetry in the P-wave velocity/effective stress (V_P/σ) relationship between stress up (compaction or pore pressure depletion) and stress down (extension or pore pressure increase) effects (e.g., Hatchell and Bourne, 2005). Observations indicate that the increase in V_P due to an increase in σ is smaller than the decrease caused by an equivalent σ decrease. The nonlinear nature of my stress-velocity model means that these effects are accounted for to an extent. However, it could be argued that the modelled asymmetry between stress up and stress down effects are not as large as those observed by Hatchell and Bourne (2005), particularly at higher stresses, where the rate of change of the velocity/stress gradient ($d^2V_P/d\sigma^2$) is lowest (Sayers, 2007). If a degree of irreversible deformation such as cement breakage occurs when the rock is moved from its initial stress state then this will increase the asymmetry, as the decrease in compliance due to a stress increase will be cancelled out by the additional compliance induced by inelastic deformation. In the following section we consider (in a qualitative sense only) how we might deal with inelastic damage within the framework outlined above.

6.3.7 Coring and damage

It is becoming increasingly clear among rock physicists that using velocities measured on cored samples may not be representative of the velocities of in situ reservoir rocks. Tests involving synthetic sandstones (e.g., Holt et al., 2000), and comparison of cored samples with well log measurements (e.g., Furre et al., 2007), indicate that in situ rocks generally have higher velocities and a lower stress sensitivity. The explanation forwarded for this is that coring of the sample causes large differential stresses that create permanent damage in the sample. While this effect is compensated to some extent

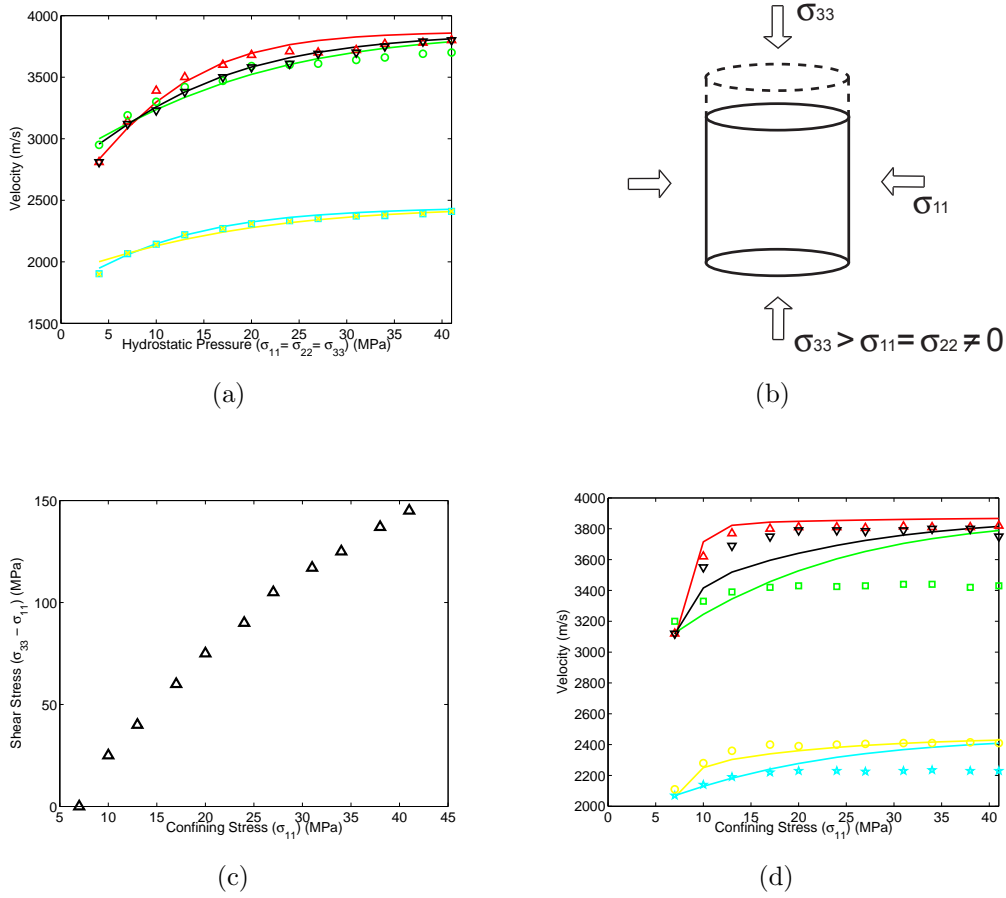


Figure 6.9: Panel (a) shows observed and back-calculated P- and S-wave velocities for hydrostatic compression of Berea sandstone. The best fit parameters (ξ^0 and a^0) for the hydrostatic case are used to model the uniaxial case (d). The details of the uniaxial experiment are shown in (b) and (c). Experimental data (symbols) from Scott and Abousleiman (2004). Red - V_{Pz} green - V_{Py} , black - V_{P45} , cyan - V_{Sxy} , yellow - V_{Syz} .

due to the fact that cores generally sample more competent zones of a reservoir, and that they may miss larger scale fractures which could increase stress sensitivity, it is of interest to consider how to account for the damage due to coring (or other mechanisms) within the framework of my model.

MacBeth and Schuett (2007) demonstrate the effect that damage can have on a sample, though in this case the damage is caused not by coring but by thermal expansion of grains during heating. Figure 6.10 shows measurements of ultrasonic P- and S-wave velocities from samples before and after they have been damaged by heating. Assuming the isotropic background compliance given by MacBeth and Schuett (2007), and an isotropic α , we use (6.37) and (6.38) to find the optimum values of ξ^0 and a^0 that minimise misfit between observed and modelled velocities.

Table 6.4 shows the values of ξ^0 and a^0 used to calculate the modelled velocities in Figure 6.10. It is clear that the differences between damaged and undamaged samples can be accounted for solely

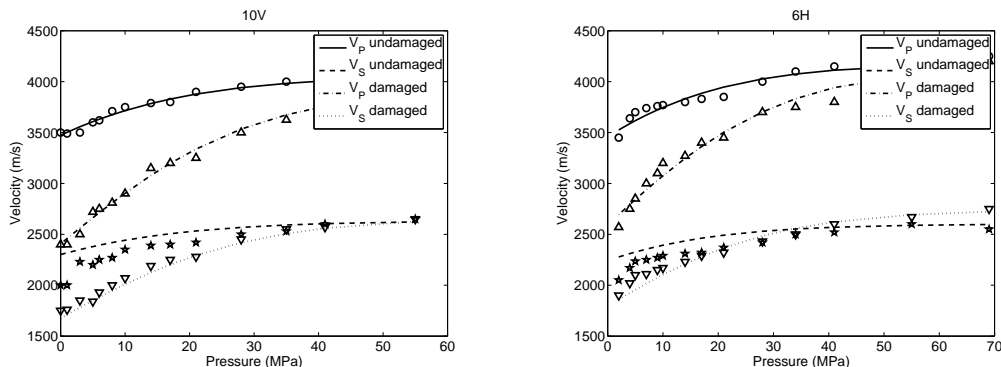


Figure 6.10: Ultrasonic P- and S-wave velocities measured before (black) and after (red) the sandstone samples 6H and 10V (from MacBeth and Schuett (2007)) have been damaged by heating. Damaged samples show a much larger stress sensitivity at low pressures. Best fit initial aspect ratio and crack densities (Table 6.4) are chosen to model the observed variation of velocity with stress.

<i>Sample</i>	a^0	ξ^0
6H undamaged	0.005	0.07
6H damaged	0.005	0.27
10V undamaged	0.005	0.065
10V damaged	0.005	0.3

Table 6.4: Best fit initial average crack aspect ratios (a^0) and densities (ξ^0) to used to generate predicted velocities in Figure 6.10. Damaged samples show similar initial aspect ratios but much larger initial crack densities.

by the increase in the initial crack density; thus the potential exists to remove the effects of coring damage from the estimates of stress dependent elasticity for in situ rocks. At present, however, I am not able to estimate how much damage the coring process will cause, and hence by how much I should decrease my estimates for ξ^0 when upscaling from lab measurements to in situ rocks.

The treatment of SPO anisotropy and core damage serve as an indication of how we might interpret the physical meaning of crack density and aspect ratio. I note at this point that these terms have been developed as theoretical parameters to model stress dependent elasticity. However, they do appear to have a correlation, if only in a qualitative sense, with physical observations such as alignment of elongate or platy grains, or the degree of damage done to a sample. This correlation strengthens my confidence in the conceptual validity of the micro-structural approach for modelling nonlinear stress dependent velocities. It is an interesting and as yet unanswered question as to whether there are any petrofabric analysis techniques might be able to develop quantitative estimates of micro-structural parameters independently from velocity observations.

6.4 Calibration with literature data

Thus far I have provided only a limited amount of stress-velocity data with which my theory can be calibrated. Many other works (e.g., Sayers, 2002; Hall et al., 2008; Prioul et al., 2004; Hornby, 1998) also only provide limited numbers of samples. What is required is a compilation of data from many samples from which trends and rules-of-thumb can be developed, as well as calibration of the typical value ranges. This information will be very useful for model population. With this in mind Doug Angus and I have used my model to invert for crack density and aspect ratio based on ultrasonic velocity measurements on over 200 samples from the literature. I am grateful to Doug Angus for compiling much of the ultrasonic velocity database upon which these calibration measurements could be made, and also for writing the shell scripts that allowed my code to work rapidly on many individual samples with minimal work input from the user. I am also grateful to Doug Schmitt for providing data compiled by many of his graduate students.

Table 6.5 list the studies in which Doug Angus found usable data, in the form of stress versus ultrasonic velocity measurements made on drained core samples. There is a large range of experimental techniques deployed across these reports. Some of these reports have measured anisotropic velocities, while some only make isotropic measurements. Some studies have used triaxial stresses to deform the samples, while some use uniaxial and some hydrostatic stresses. Where anisotropic data is available, it was inverted for, while for isotropic measurements the inversion can be collapsed into isotropic form. Similarly, when triaxial stress have been used, this is included in the inversion, while these effects can be ignored for hydrostatic cases. Where mineral data have been provided this has been used to compute the background stiffness tensor \mathbf{C}^r , and where they have not we used the behaviour at high pressures to estimate this tensor.

Figure 6.11 shows the inverted a^0 and ξ^0 values computed from 234 literature samples, coloured by lithology. Mean values for each lithology, and standard deviations, are plotted in Table 6.6. The overarching trend in Figure 6.11 is that, except for shales, the initial aspect ratios show remarkable consistency, with aspect ratios of approximately 0.0002 – 0.0006. The initial crack density estimates show greater scatter, falling between 0.0-0.5. In Table 6.6, variations between lithologies can be seen. The clearest lithology variation is that shales generally have low values for ξ^0 , and high values of a^0 . I also note that anhydrites have very low values for ξ^0 , implying a relative lack of stress sensitivity for these rocks. Carbonates also appear to be less sensitive to stress than clastic rocks. The most likely explanation is that the degree of chemical cementation found in carbonate and anhydrite rocks makes them less sensitive to stress than sandstones and conglomerates, which appear to have generally higher microcrack densities.

We also examined the dependence of initial crack density and aspect ratio on the depth from which the sample was recovered and porosity (where this information has been provided) but did not find any noticeable trends. However, most of the samples have been recovered from reservoirs. Thus, the limited depth distribution in the data may not be sufficient to extract any trends. This highlights the need to sample and measure all of the overburden when attempting to predict velocity

<i>Lithology</i>	<i>Study</i>
Sandstone	King (1966), Nur and Simmons (1969), Han (1986), King (2002) Rojas (2005), He (2006), Hemsing (2007), Grochau and Gurevich (2008) Hall et al. (2008)
Tight-gas sandstone	Han (1986), Jizba (1991)
Shale	Johnston and Christensen (1995), Hornby (1998), Bolas et al. (2005) Hemsing (2007)
Tight-gas shale	Jizba (1991)
Limestone	Simmons and Brace (1965), Nur and Simmons (1969), Brown (2002)
Dolostone	Brown (2002)
Conglomerate	He (2006)
Anhydrite	Hemsing (2007)
Clay	Hornby (1998), Bolas et al. (2005)

Table 6.5: Published core tests of stress dependent ultrasonic velocities for a variety of sedimentary lithologies.

<i>Lithology</i>	<i>No. of samples</i>	<i>Mean ξ^0</i>	<i>Mean a^0</i>	<i>St. dev. ξ^0</i>	<i>St. dev. a^0</i>
Sandstone	174	0.10	4.1×10^{-4}	0.080	1.8×10^{-4}
Carbonate	12	0.054	5.9×10^{-4}	0.087	5.4×10^{-4}
Anhydrite	2	0.01	1.6×10^{-4}	0.0024	0.7×10^{-4}
Conglomerate	10	0.19	2.5×10^{-4}	0.18	0.5×10^{-4}
Shale	26	0.026	1.18×10^{-3}	0.026	9.4×10^{-4}

Table 6.6: Mean values for ξ^0 and a^0 for each lithology, and their standard deviations.

changes through these layers. This may seem like an obvious statement to make, but rarely are such measurements made in practise.

The variation in a^0 observed in shales is worthy of further discussion. Shales are defined as siliclastic rocks with over 50% made up of grains smaller than $50\mu m$. Although, shales are usually very abundant in hydrocarbon plays, often providing impermeable seals or as an organic material enriched source rock, understanding of their mechanical properties is poor, partly due to their fine grain size, and partly due to a lack of industrial interest.

In Figure 6.12 a^0 and ξ^0 are plotted for the clay-rich samples and the Clair samples discussed earlier. Of the shale samples, the ones that fall within the global trend for a^0 of between 0.0002-0.001 are the Manville shale cores from Hemsing (2007), which contain significant amounts of quartz grains as well as clay, hence, the clay content of these rocks is on the low end of typical shales. This may explain why these samples are found close to the global trend (i.e., sandstones). The tight gas samples from Jizba (1991) are also found to have a^0 estimates that are sensitive to clay content, with elevated a^0 for samples with a high clay content.

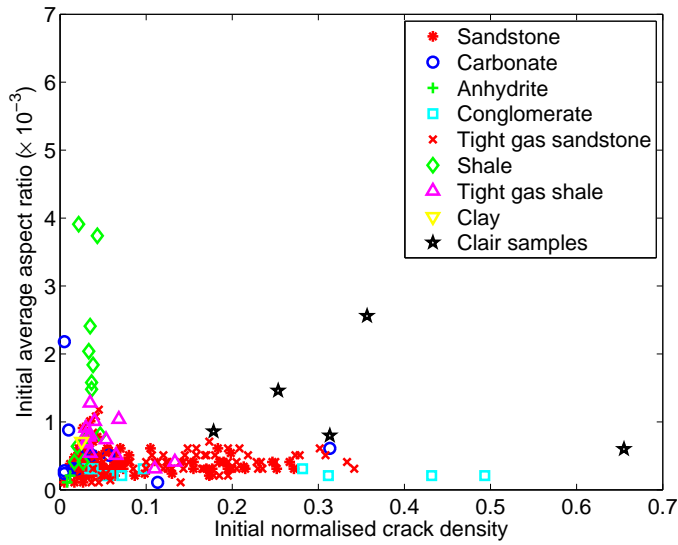


Figure 6.11: Best fit values for ξ^0 and a^0 for dry samples published in the literature for a variety of lithologies.

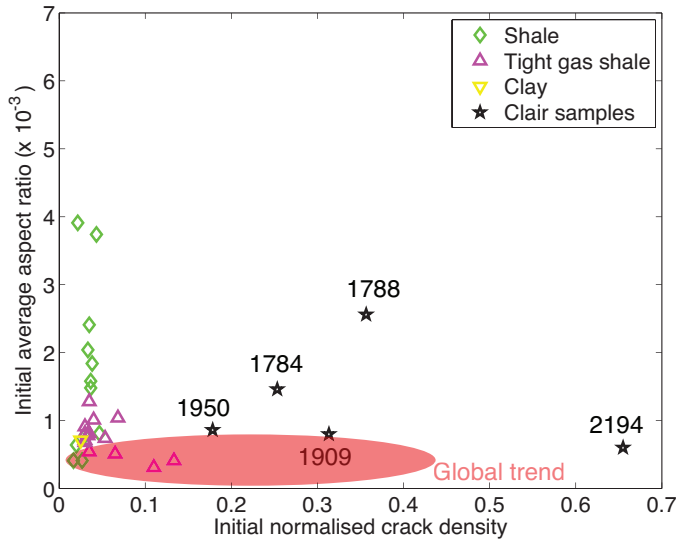


Figure 6.12: Best fit values for ξ^0 and a^0 for the clay rich samples.

When attempting to use data from literature, a problem often encountered is that the core observations provided are often limited. For example, detailed core description such as classification of sample integrity, coring damage, mineral constituents, hand samples, and back-scatter electron micrographs can all provide valuable information to complement ultrasonic measurements but may not be provided in the published work. Hence, we are limited to very broad conclusions based on global trends.

<i>Sample</i>	ϕ	κ (mD)	<i>qtz</i>	<i>fspr</i>	<i>calc</i>	<i>phyl</i>	<i>kaol</i>	ξ^0	a^0
1784	12.0	24.0	38.64	18.26	18.26	6.20	6.65	0.25	0.0015
1788	8.0	0.02	30.89	25.41	1.32	34.38	0.00	0.36	0.0026
1909	13.0	2.8	54.95	16.07	10.48	3.73	1.78	0.31	0.0008
1950	14.8	84.00	44.19	30.46	7.45	3.10	0.00	0.18	0.0009
2194	12.1	1.40	61.05	12.62	8.06	1.70	4.48	0.66	0.0006

Table 6.7: Physical properties of the Clair samples showing the % mineral constituents (qtz=quartz, fspr=feldspar, calc=calcite, phyl=phyllosilicates and kaol=kaolinite).

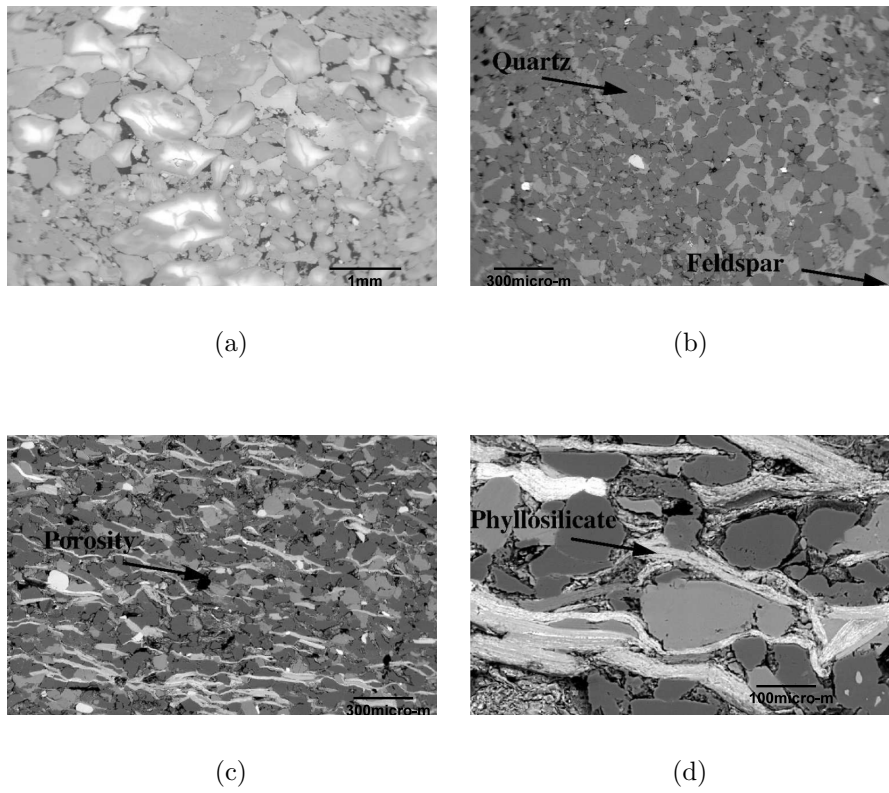


Figure 6.13: Back-scatter electron micrograph images of the Clair sandstones: clean samples 1909 (top right) and 1950, (top left), and clay-rich sample 1784 (both bottom panels). Taken from Maddock (2006).

However, this information is available for the Clair dataset discussed earlier in this section. Table 6.7 shows physical properties for the 5 Clair samples, for which a^0 and ξ^0 are also plotted in Figure 6.12. Samples 1909, 1950 and 2194 are clean sandstones, and show aspect ratios and crack densities consistent with the literature sandstone samples. Samples 1784 and 1788 have a higher clay and

mica content, and show a^0 greater than the global trend. Aspect ratio also appears to increase with increasing clay and mica content from 1784 to 1788. This would appear to confirm that increasing clay and mica content correlates with larger values of a^0 .

In order to understand this relationship, it is helpful to consider the micro-structure for clean and clay-rich samples. Figure 6.13 shows back-scatter electron micrograph (BSEM) pictures for the clean sandstones 1909 and 1950, and for the clay-rich sample 1784. The clean samples show random orientation of quartz and feldspar, with a random orientation of the diagenetic calcite (Valcke et al., 2006). The clay-rich sample shows a preferred orientation of the mica and clay grains with vertically aligned rotational symmetry due to compaction. Figure 6.13 highlights the dominance of the mica and clay, which is also noted in the ultrasonic data, where a strong VTI symmetry is observed. It is not clear whether this strong lithological anisotropy has a significant influence on aspect ratio estimates. For instance, does this initial VTI skew the inversion estimates, or does the presence of significant amounts of mica and clay lead to an inherent micro-structural bias of larger aspect ratios? It is difficult with such limited data to conclude with any certainty that it is the presence of clay particles alone that causes aspect ratios to increase. More velocity-stress data for shales and shaley (clay rich) sandstones, with accompanying petrophysical analyses, are necessary.

6.5 Comparison of rock physics models

So far I have outlined two rock physics models, the third-order elasticity approach of Prioul et al. (2004), and the approach developed in this thesis and Verdon et al. (2008). Other models available but only touched on briefly in this chapter are the R-factor (Hatchell and Bourne, 2005), and models based entirely on empirical calibration (e.g., Minkoff et al., 2004). Each model has particular advantages and issues, and each requires its own assumptions. Therefore each has its role, or niche, in the geophysicists toolbox.

The simplest method for dealing with stress sensitive velocities is to use an empirically defined relationship. Cores samples are taken from the reservoir, and velocities measured at the stresses of interest. The advantage of such an approach is that no assumptions need to be made about the physics controlling stress-sensitive seismic velocities. However, such an approach will be limited in its validity to the parameter space tested in experiments. In a real scenario, the triaxial stress tensor will vary continuously across a reservoir and overburden, and will vary through time as a result of production. Therefore it is unfeasible to conduct experiments for every stress state. Models are needed to extrapolate from experiments to the stress condition at each point in the reservoir.

One approach is to use a linear interpolation between velocities measured at hydrostatic stress conditions (e.g., Minkoff et al., 2004). Such an approach requires no assumptions about the response of seismic velocities to stress. However, such an approach is extremely limited, because in reality rocks around the reservoir are not at hydrostatic stress. An approach is needed that can map triaxial stress changes to anisotropic variations in seismic properties. Furthermore, experimental observations show

that the response of velocities to stress change is in fact nonlinear, so a linear interpolation is in fact a poor approach to take.

The approach most commonly used in industry is the R-factor model of Hatchell and Bourne (2005). This model assumes that the fractional change in vertical P-wave velocity is proportional to the vertical strain (with the R-factor being the constant of proportionality in the equation $dV_{Pz}/V_{Pz} = -R\varepsilon_{zz}$). Vertical P-wave velocities are the most commonly measured property in conventional seismic surveys, and changes in vertical stress (and strain) will be largest geomechanical effect above a compacting reservoir. The R-factor approach was developed to address this particularly relevant subset of geomechanical scenarios. Hatchell and Bourne (2005) found that R-factors were reasonable consistent across a number of sites, although R-factors for rocks experiencing compressive strain were found to be 5 times smaller than for rocks under extensional strain. However, more recent studies have shown order-of-magnitude variations in R-factors depending on lithology (e.g., Staples et al., 2007; De Genaro et al., 2008). More importantly, R-factors have been found to be dependent on the stress path (Holt et al., 2008), and on the magnitude of the applied stress (Pal-Bathija and Batzle, 2007).

The different R-factors required for extension and compaction, for different applied stress magnitudes and for different triaxial stress states, all for the same rock, means that this approach does not lend itself to model scenarios where the stress changes during production are not known in advance. This is because the R-factor model does not adequately describe the full, triaxial, anisotropic, nonlinear response of seismic velocities - it is limited to vertical strain and vertical P-wave velocities. Therefore it is not capable of dealing with the observed phenomena that fall beyond its remit. Unfortunately, these issues are very much within my remit when dealing with the geomechanical models developed in Chapter 5, so I do not use the R-factor approach. Nevertheless, because it cuts through a complicated system to leave one of the key 4D seismic parameters (vertical timeshift) correlated via one parameter (the R-factor) to one geomechanical observable (vertical strain) it remains as attractive approach within the industrial sector.

Like many rock physics models, the R-factor approach attempts to fit the observed nonlinear stress-velocity response with a linear model, which means that it is limited in its applicability. Furthermore, the model only considers the vertical P-wave velocity response to vertical strain. Observations show that vertical P-wave velocity is also modulated by horizontal deformation, although this is a second order effect (this result can be derived from equation 6.11). More importantly, even in reflection surveys, seismic waves do not travel vertically, but through a range of inclinations about the subvertical. Therefore the R-factor approach tends to break down for longer offset arrivals (Herwanger, 2007).

The third-order elasticity model developed by Prioul et al. (2004) includes the effects of triaxial stress changes on the full anisotropic stiffness tensor. This means that the effects of stress-induced anisotropy, and variations in larger offset timeshifts, can be incorporated. This model takes a mathematical approach, including the third-order terms that are usually discarded in deriving conventional linear elastic theory. Therefore, this model does not directly address the microstructural properties of the rock, although it is capable of modelling the full stiffness tensor. However, to facilitate inversion from ultrasonic data, Prioul et al. (2004) have to assume an isotropic third order tensor, which in

essence means that, although a rock might be initially anisotropic, the *change* in velocity caused by a particular stress change will be the same regardless of the axis along which this stress is applied.

The ability to deal with intrinsic and stress induced anisotropy represents a significant advantage for the Prioul et al. (2004) model. However, as with all of the models discussed above, the observed nonlinear stress-velocity relationship is fitted with a linear trend. Prioul et al. (2004) get around this issue by fitting low and high stress regions separately, an approach that significantly limits the general applicability of the model. Furthermore, the model can only be parameterised with triaxial stress velocity measurements. Such experiments are much less common in the literature, so the kind of extensive calibration that I was able to perform for the micro-structural approach is not as easily performed. Given that the Prioul et al. (2004) model is already less intuitive to grasp, the difficulties in parameterisation mean that this approach does not provide such an intuitive framework within which understand how seismic velocities respond to changes in applied stress.

The model I have outlined in this chapter attempts to describe the micro-structural response to stress changes, using this as a route to describe seismic properties via an effective medium model. Real rocks do not contain the idealised, penny-shaped discontinuities that I use as the framework for my modelling. However, it has long been recognised (e.g., Hudson, 1981; Sayers and Kachanov, 1995; Schoenberg and Sayers, 1995; Thomsen, 1995; Hall et al., 2008) that the response of compliant grain boundary discontinuities to the infinitesimal strain, high strain rate deformation induced by a seismic wave can be approximated very closely using such an approach. The additional step that I have made is to assume that the compliant grain boundary discontinuities respond in the same manner to the finite strain, low strain rate deformation induced by geomechanical stress changes as they do to the deformation during the passage of a seismic wave. This is a reasonable assumption to make so long as geomechanical deformation remains elastic. The second assumption that I make is that the size distribution of the grain boundary discontinuities can be modelled with an exponential distribution. This assumption is somewhat more arbitrary in its nature, as there is no physical reason why a power law distribution could not be used instead. However, the exponential distribution provides a good match to velocity observations, and is easily parameterised.

The advantage gained by describing stress sensitive velocities using a micro-structural model is that we can move closer to understanding the physics behind the phenomenon. By doing so, it is possible to develop a more intuitive understanding of the processes involved. The model I have developed is far more intuitive in its use than the third-order elasticity approach. For instance it is not intuitive to say how increased core damage will affect the three independent terms of Prioul's isotropic third order tensor. Furthermore, given the need to limit the third-order tensor to isotropy, this model cannot account for anisotropic rock fabrics as seen in many clay and/or mica rich rocks.

In contrast, for the micro-structural model it is intuitive to conceive that damage will increase the initial microcrack density terms, while alignment of platy minerals will increase the crack density along one axis of symmetry alone. Additionally, the improved understanding of the physical processes that a micro-structural analysis provides leads to a model that can account for observed phenomena such as intrinsic and stress-induced anisotropy, and the nonlinear response of velocities to stress (the micro-structural model has no need to fit separate linear portions of the stress-velocity curve).

Furthermore, the microstructural model can be easily parameterised and calibrated using any kind of stress-velocity data, as Doug Angus and I have performed for over 200 sample datasets found in the literature. Because it can account for many observed phenomena, including the nonlinear response to a triaxial stress tensor, and because it has been calibrated using a range of lithologies, the model is highly generalised, capable of deployment without modification for a range of scenarios. In the following chapters I will use this model to investigate the effects of geomechanical deformation on seismic observables.

6.6 Summary

- A calibrated rock physics model is required to compute the effects of stress and/or strain on seismic velocities. This model should include empirically observed effects such as nonlinear elasticity and stress induced anisotropy, but should not be unduly complex or require excessive numbers of parameters that are difficult to constrain.
- I develop a micro-structural model that fulfils these requirements, treating grain boundaries and microcracks as displacement discontinuities, the number density of which changes with the applied stress. The overall compliance of the medium can be given as the sum of its parts - the background matrix and the additional compliance introduced by the presence of the discontinuities.
- I have developed an inversion procedure that computes the 2nd and 4th order additional compliance tensors based on ultrasonic velocity measurements. Unlike previous inversion approaches, this procedure does not make any a priori assumptions about the relative magnitudes of the 2nd and 4th order tensors.
- The change in number of displacement discontinuities can be computed by treating them as penny-shaped features. The number density at a given triaxial stress is calculated using an initial crack density and crack aspect ratio at a reference stress state. These parameters can be computed from empirical observations of ultrasonic velocity changes with stress.
- I find that the model provides a good match with observation for many core samples, and does a good job of incorporating anisotropy both inherent in a sample and induced by non-hydrostatic stress changes.
- Over 200 datasets from the literature have been used to calibrate these crack density and aspect ratio parameters. I find a remarkable consistency in the aspect ratio term, while crack density appears to correspond to the degree of damage and the amount of stress sensitivity of the sample. By providing rules of thumb and typical parameter ranges, the calibration results can be used as a tool to facilitate model population.

7.1 Introduction

In Chapter 5 I generated geomechanical models to simulate the effects of pore pressure changes on the stress field in and around a reservoir. I wish to model the seismic properties of these models, and developed in Chapter 6 a rock physics model capable of mapping changes in stress into changes in seismic velocity. In this chapter I develop a workflow to generate elastic models based on the geomechanical simulations. These elastic models can then be used to make predictions about changes to seismic properties using seismic modelling tools such as ray tracing or finite difference simulation. This work was conducted as part of the IPEGG project. Doug Angus and I developed a workflow, *SeisModel*[©], specific to the IPEGG modelling tools capable of reading the output from the MORE-ELFEN simulator and computing the seismic properties on a regularised grid. I will begin this chapter by outlining this workflow.

A significant development in the linking of geomechanical simulation with seismic observation was made by Hatchell and Bourne (2005), who match changes in seismic travel times through the overburden with reservoir compaction and stress arching. I use ray tracing to compute the changes in travel time in the overburden above the models generated in Chapter 5, assessing whether travel time changes can distinguish between the different stress paths already identified. Such a tool would be very useful in determining the stress being experienced by a reservoir as CO₂ is injected, and thereby the risk of caprock failure. While undoubtedly useful, overburden travel times provide information about only one aspect of geomechanical deformation - how much the overburden is being stretched/compressed along a vertical axis. Can other seismic attributes be used to image other aspects of geomechanical deformation? One potential option is to use shear-wave splitting, which is, as we have seen, sensitive to stress changes. Therefore I also compute splitting for the simple models developed, and assess how useful such measurements would be for imaging such things as reservoir compartmentalisation.

7.2 *SeisModel*[©] workflow

7.2.1 Input of results and parameters

The first stage of the *SeisModel*[©] workflow is to import the geomechanical results from the MORE-ELFEN simulations. During the simulation a number of parameters are written to file at specified time steps. These values are then used to compute the seismic properties. The values are output on an element-by-element basis, and are given in Table 7.1. The first stage of *SeisModel*[©] is to read in these parameters from the specified geomechanical output file. A number of required inputs are not provided by the geomechanical modelling. These are read by *SeisModel*[©] from a user-defined input file. These values can be specified separately for the overburden and the reservoir, and are also given in Table 7.1.

7.2.2 Initialisation

In order to ensure that the relative velocities computed using our rock physics model match the relative stiffnesses of the materials used in the geomechanical modelling, I use an initialisation procedure such that the initial stiffness is set to be equal to that used to compute the geomechanical deformation, $\mathbf{C}^{\text{mech}} = \mathbf{C}^{\text{in}}$. These values can be increased by a specified percentage to represent the fact that dynamic stiffness (the stiffness used to calculate seismic velocities, which are low strain and high strain rate) is generally observed empirically to be larger than static stiffness (used to calculate geomechanical deformation, which has high strain at a low strain rate). By doing so I preserve the relative stiffness differences between reservoir and non-pay units, although absolute values are increased for the dynamic stiffness. I will refer to the stiffness used to compute the initial seismic velocities as \mathbf{C}^{in} , while recognising that it may be equal to, or tied to, the geomechanical stiffness \mathbf{C}^{mech} . Alternatively, where the seismic velocities of layers are known, these can be used to define \mathbf{C}^{in}

In Chapter 6 (and Angus et al., 2009) we have found that the aspect ratio rarely varies between sedimentary rocks, so I specify that the initial average aspect ratio a^0 is fixed. This means that there are two parameters that can be varied to ensure that the dynamic stiffness tensor, \mathbf{C} , at the initial

<i>Results from MORE-ELFEN</i>	
ρ_d	Density of the dry rock
ρ_{fl}	Effective density of the multiphase pore fluid
Φ	Porosity
K_{fl}	Effective bulk modulus of the multiphase pore fluid
P_{fl}	Pore fluid pressure
\mathbf{C}^{mech}	Elastic stiffness used to compute geomechanical deformation
\mathbf{C}^{in}	Elastic stiffness used to compute the initial seismic velocities
σ_{ij}	Stress tensor
<i>User-defined inputs</i>	
β_w	Biot-Willis parameter
ξ_i^0	Initial crack density tensor at zero stress
a^0	Initial crack aspect ratio
ξ^f	Number density of any user-defined fracture sets
a^f	Aspect ratio of any user-defined fracture sets
θ^f	Azimuth of normals to user-defined fracture sets
ϕ^f	Inclination of normals to user-defined fracture sets
ω	Dominant frequency of incident seismic energy, used to compute squirt-flow effects
M^g	Characteristic grain size, used to compute squirt-flow effects

Table 7.1: List of *SeisModel*[©] input parameters

time step, is equal to \mathbf{C}^{in} . These are the stiffness of the background rock \mathbf{C}^{r} (which corresponds to the idealised case of the rock mass without any compliant porosity); and the initial crack density tensor ξ_i^0 at zero stress. Hence I have two options for assigning suitable values for these parameters: to fix an initial \mathbf{C}^{r} and compute the ξ_i^0 tensor that produces a stiffness that matches \mathbf{C}^{in} ; or to fix the ξ_i^0 tensor, and compute the appropriate \mathbf{C}^{r} tensor that when combined with the assigned ξ_i^0 tensor matches \mathbf{C}^{in} .

Fixed \mathbf{C}^{r}

To initialise using a fixed background stiffness, I must first assign this stiffness. This stiffness will be greater than \mathbf{C}^{in} , but less than that of the minerals making up the rock, as the effects of stiff, spherical pores must still be accounted for. In order to approximate this stiffness I use \mathbf{C}^{in} , and increase it by multiplying by $(1 - \Phi)^{-1}$, such that

$$\mathbf{C}^{\text{r}} = \frac{\mathbf{C}^{\text{in}}}{1 - \Phi}. \quad (7.1)$$

Having approximated \mathbf{C}^{r} I compute ξ_i^0 such that the computed stiffness matches \mathbf{C}^{in} at the initial timestep. In order to do this I first compute the requisite crack density at the initial stress conditions. This will be given by the difference in compliance between \mathbf{S}^{r} and \mathbf{S}^{in} , as by rearranging equation 6.7 we have

$$\Delta \mathbf{S} = \mathbf{S}^{\text{in}} - \mathbf{S}^{\text{r}}. \quad (7.2)$$

In order to compute the unnormalised crack density terms I use the inversion procedure outlined in Chapter 6 to compute the crack density based on an observed stiffness and a background compliance using a Newton-Raphson approach, having first rotated both into a coordinate system defined by the principle stress directions. In this case the ‘observed stiffness’ is \mathbf{C}^{in} . The computed crack densities are then normalised using the h_i parameter given in equation 6.13. Having computed the normalised crack density at the initial stress conditions, I rearrange equation 6.37, so that the crack density at zero stress, ξ_i^0 , is given by

$$\xi_i^0 = \frac{\xi(\sigma_i)}{\exp(-c_r \sigma_i)}. \quad (7.3)$$

The initial crack density tensor is then rotated back into global (ENZ) coordinates to be used in predicting stress dependent stiffnesses at future timesteps.

Fixed ξ_i^0

To initialise using a fixed initial crack density, I must compute the crack density at the initial stress conditions, and then remove this additional compliance from \mathbf{S}^{in} to give \mathbf{S}^{r} . The unnormalised crack density at the initial stress conditions is given by

$$\alpha = \begin{pmatrix} \xi_1^0 \exp(-c_r \sigma_1)/h_1 & 0 & 0 \\ 0 & \xi_2^0 \exp(-c_r \sigma_2)/h_2 & 0 \\ 0 & 0 & \xi_3^0 \exp(-c_r \sigma_3)/h_3 \end{pmatrix}, \quad (7.4)$$

assuming that the initial crack density tensor has been rotated into the coordinate system of the initial principle stress directions. The second and fourth order crack density tensors are used to

compute the additional compliance caused by the presence of the discontinuities, using equation 6.8. By rearranging equation 6.7, I can compute the background stiffness from $\Delta\mathbf{S}$ and the actual stiffness \mathbf{C}^{in} . In compliance terms

$$\mathbf{S}^{\text{r}} = \mathbf{S}^{\text{in}} - \Delta\mathbf{S}. \quad (7.5)$$

The background compliance is then rotated into the global coordinate system and inverted to give the background stiffness \mathbf{C}^{r} to be used in the stress dependent calculations.

The sensitivity of a rock to stress in this model is controlled primarily by the initial crack density tensor. Doug Angus and I have performed extensive analysis of literature data in order to calibrate this parameter (Angus et al., 2009), and have found reasonable consistency. We find that ξ^0 is between 0.05 for stress insensitive rocks and 0.3-0.5 for very stress sensitive rocks (Chapter 6). In contrast, the selection criteria for the background stiffness tensor \mathbf{C}^{r} , defined by the behaviour at high stress or petrophysical analysis, is not as well constrained. Therefore I prefer the second initialisation approach described, assigning a fixed initial crack density and then computing the appropriate background stiffness.

7.2.3 Stress dependence

Having computed the background stiffness \mathbf{C}^{r} , the effects of stress changes on the dynamic stiffness can be computed for subsequent ELFEN timesteps. The initial crack density tensor ξ_i^0 and the background stiffness tensor \mathbf{C}^{r} are rotated into the coordinate frame defined by the principal stress directions. The updated crack density tensor is computed using equations 6.37 - 6.39, and this additional compliance is added to the rotated background stiffness using equation 6.11. The updated stiffness is then rotated back into the global coordinate system. This provides the full, dynamic, stress dependent, anisotropic stiffness tensor, \mathbf{C} , at each timestep. It is assumed that, because the compliant pore space has negligible volume, stress changes have no effect on the rock density.

7.2.4 Fractures

Throughout this thesis I have differentiated between cracks, which are small, pervasive features of a similar size to the grains, and fractures, which are larger scale features. As well as the stress dependent cracks, *SeisModel*[©] can include sets of aligned fractures superimposed on top of the stress dependent fabric already calculated above. *SeisModel*[©] uses the method outlined in Chapter 3, adding the additional compliance introduced by the fractures to the inverse of the stress dependent stiffness computed above. The compliance of the fractures can be computed using either the low frequency, high frequency or frequency dependent models (Chapter 3). Any number of aligned fracture sets can be added in this manner. I assume that the fractures are of insignificant volume, so there is no alteration to the rock density.

7.2.5 Fluid substitution

SeisModel[©] also computes the changes in seismic velocity induced by changes in fluid saturation. *SeisModel*[©] provides two options for doing this - using the low frequency anisotropic Gassmann equation (Brown and Korranga, 1975) given in equation 3.9, or the frequency dependent Chapman (2003) model which includes squirt flow and global flow effects. Because the focus of my work is on the effects of stress and not fluid substitution, I will use the low frequency Gassmann approach. The fluid bulk modulus and porosity are provided by the MORE-ELFEN results, but the mineral stiffness is also required to compute the saturated stiffness. In order to estimate this, *SeisModel* extrapolates from the background stiffness tensor computed in the initialisation step to the limit of zero porosity, using

$$\mathbf{C}^m = \frac{\mathbf{C}^r}{1 - \Phi}. \quad (7.6)$$

The fluid saturated density is computed using the porosity and the densities of the fluid and rock, all of which are provided by MORE-ELFEN, using

$$\rho = \rho_d + \Phi\rho_{fl}. \quad (7.7)$$

SeisModel[©] also provides the option to skip any of these steps if we wish to ignore the contribution from fractures, stress dependence or fluid substitution.

7.2.6 *SeisModel*[©] Output

SeisModel[©] generates an output file at each timestep. The header of this file contains information about the grid geometry making up the seismic model, and the elevations of any surfaces (such as the top of the reservoir) which can be used by ray-tracing algorithms. For each node, the E, N and Z coordinates of the node are provided, along with the final stiffness tensor computed by the *SeisModel*[©] workflow in 6×6 Voigt notation. These files can then be used to compute seismic observables such as travel-time to the top of the reservoir, reflection coefficients, and shear wave splitting at each timestep. I will now show the seismic results for the geomechanical models constructed in Chapter 5.

7.3 Results from simple geomechanical models

7.3.1 Overburden travel time-shifts

The normal incidence travel time for a reflection from the top of the reservoir can quickly and easily be computed by ray-tracing through the elastic model developed, and it is also easily observed on 4-D seismic surveys. This change to this observable has been the most commonly deployed technique used to link geomechanical deformation with geophysical observations (e.g., Hatchell and Bourne, 2005). I use the Christoffel equation (Chapter 3) to compute the changes in velocity of a vertically propagating P-wave through the centre of the 9 simple reservoir models developed in Chapter 5. The user-defined parameters that I use are listed in Table 7.2. Having computed the velocities, I compute the change

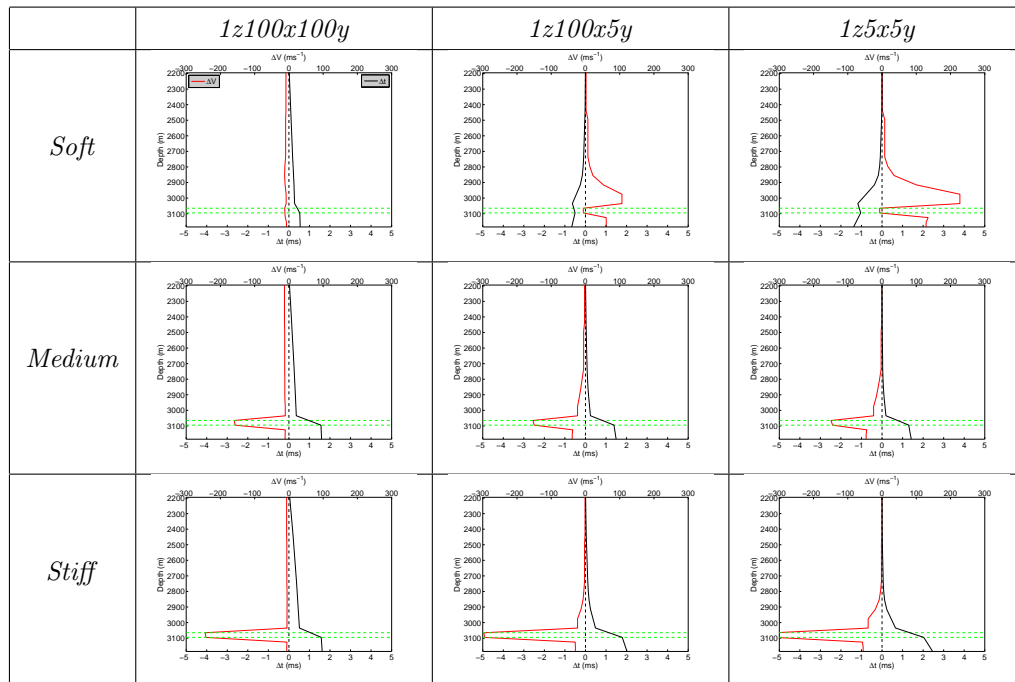


Figure 7.1: Changes in the normal incidence P-wave velocity (red) and travel time (black) through the centre of the geomechanical models developed in Chapter 5. The reservoir interval is marked by the green dotted lines.

to the two-way travel time (TWTT) for reflections coming from the overburden and reservoir. These are plotted in Figure 7.1.

<i>Parameter</i>	<i>Value</i>	<i>Parameter</i>	<i>Value</i>
β_w	1.0	a^0	0.0005
$\xi_{reservoir}^0$	0.1	ξ^f	0.0
$\xi_{overburden}^0$	0.05		

Table 7.2: User-defined input parameters to compute changes in seismic velocities for the simple reservoir models.

For all cases in Figure 7.1 there is a decrease in velocity in the reservoir. No fluid saturation changes have been included in this model, so this decrease is caused solely by stress and pore fluid pressure changes. The presence of CO₂ would cause further velocity decreases, and so disentangling the contributions to velocity slowdown from pressure and saturation changes will be difficult without some form of rock physics and geomechanical model. If the slowdown is assumed to be caused by saturation changes alone (as is often the case) then CO₂ saturation could be overestimated.

In Chapter 5 I noted that the small, soft reservoirs were most prone to stress arching and compression in the overburden. This overburden compression leads to increases in vertical P-wave velocity.

This can be seen for the soft $1z100x5y$ and $1z5x5y$ models (Figure 7.1). The accumulated TWTT change is at most 1ms, a small but detectable shift. At present no CCS project has looked for overburden travel time-shifts, so we cannot know whether such shifts really do occur above CCS reservoirs, but I noted in Chapter 5 that reservoirs where stress arching develops are at a greater risk of failure in the overburden. TWTT shifts in the overburden might provide a tool to image whether or not this is happening. However, the pore pressure changes simulated in the geomechanical model were large, as were the contrasts between material properties in the reservoir and overburden, and yet the TWTT shift is at the lower end of what is detectable. Therefore it is conceivable that stress arching can occur without generating detectable overburden TWTT shifts. That said, more complicated and realistic models may produce larger time-shifts. Further work is needed both in terms of better measurements of overburden material properties for modelling, and in looking more diligently at changes in TWTT from overburden reflections from real datasets.

7.3.2 Shear wave splitting

As we have seen in earlier chapters, shear wave splitting can be a useful tool for identifying non-hydrostatic stress changes. Yet SWS has rarely been used to link seismic observations with geomechanical deformation. This is in part because splitting is rarely measured in or above reservoirs as part of industry standard practise, and partly because few rock physics models, such as Prioul et al. (2004) and Verdon et al. (2008), exist that translate triaxial stress changes into variations in anisotropy. At Valhall, a producing reservoir in the North Sea that is experiencing significant subsidence, Olofsson et al. (2003) noted a characteristic ‘ring’ of SWS in the overburden marking the extent of the region of depletion in the reservoir. Herwanger (2007) generated a geomechanical model of the Valhall reservoir, and used the Prioul et al. (2004) model to predict the anisotropy, and thereby the SWS, in the reservoir and overburden, finding that it is subsidence over the depleting reservoir that has generated the SWS pattern. The good match between SWS observations and geomechanical modelling found by Herwanger (2007) is promising, yet attempts to link seismic observation with geomechanical modelling are still generally limited to overburden P-wave travel times. In this section I will generate predictions about splitting generated by my simple models.

In Figure 7.2 I plot the fast directions and splitting magnitudes for a shear wave travelling vertically through the 3 different shaped medium stiffness reservoirs (flat and extensive, long and thin, and small). The resulting pattern is that at the centres of the reservoirs there is no anisotropy. SWS is generated at the edges of the reservoir. Inside the reservoir, the fast direction is orientated parallel to the edge of the reservoir, while outside the reservoir the fast direction is orientated perpendicular to the edge. The explanation for this, in terms of stress redistribution around an expanding reservoir, is illustrated in Figure 7.3. At its centre, the reservoir expands uniaxially, so no splitting develops. However, moving towards the edges, the reservoir can expand preferentially into the sideburden, where no pore pressure changes occur, meaning that the stresses perpendicular to the edge can be released in comparison to the stresses parallel. Therefore, with larger horizontal stresses parallel to the reservoir edge, the fast splitting direction becomes orientated in this direction. The sideburden is compressed

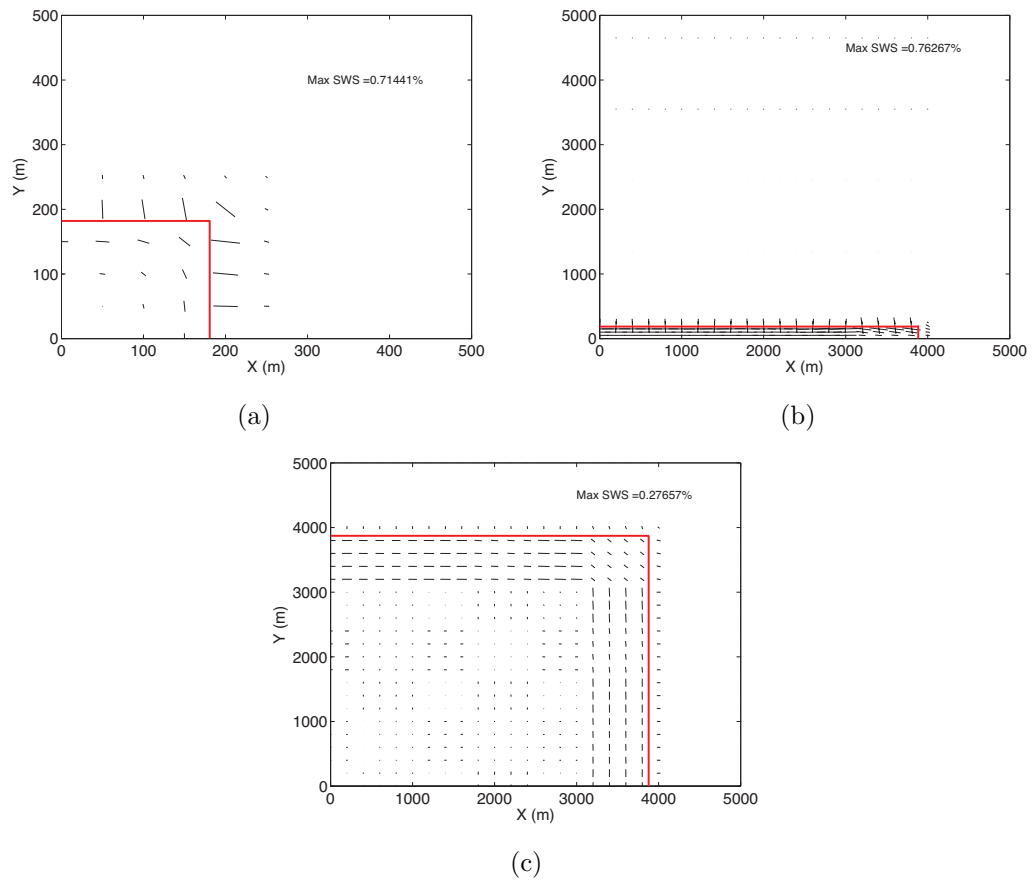


Figure 7.2: Shear wave fast direction and splitting magnitude for a vertically propagating wave through the simple, medium stiffness reservoir models. The edges of the reservoirs are marked in red, and the maximum splitting amounts are given.

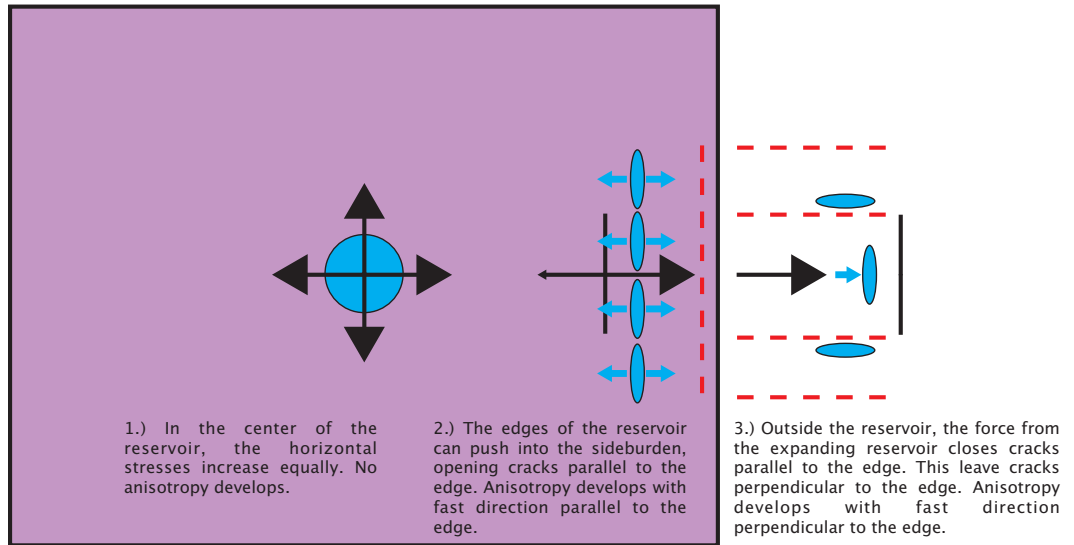


Figure 7.3: Cartoon depicting the horizontal stress redistribution around an expanding reservoir, demonstrating the SWS patterns seen in Figure 7.2. The red dashes indicate the resulting SWS pattern.

by the expansion of the reservoir, increasing the horizontal stress perpendicular to the reservoir edge. As a result, the fast direction is orientated perpendicular to the reservoir.

The maximum splitting magnitude modelled here is below 1%. Even a splitting magnitude of 1% may be hard to detect given that the maximum raypath length for a vertical wave through the anisotropic region is 75m. Therefore the splitting modelled here is at the limits of detectability. Additionally, in Chapters 3 and 4 I found that when inverting for anisotropy using splitting from microseismic events it is difficult to resolve more than one anisotropic fabric. Therefore detecting different regions of anisotropy with orthogonally polarised fast direction will be very challenging.

Nevertheless, in Chapter 6 (Figure 6.9) I noted that the rock physics model does tend to underestimate splitting. Furthermore, the presence of fractures could serve to amplify the amount of splitting induced by stress changes. Additionally, while splitting of microseismic events might not be able to resolve adjacent anisotropic fabrics, splitting of 9C controlled source seismic data, or Amplitude Variation with Offset and Azimuth (AVOA), may be able to image such fabrics.

This SWS pattern has been generated because there is a discontinuous edge between where pressure is increasing and where it is not. Therefore, these prediction have a limited applicability, because in reality reservoirs are often not bounded in this manner. Nevertheless, a sealing vertical fault would generate the kind of edge around which the modelled splitting pattern could develop. Such a feature would be of great importance for storage security, as an undetected sealing fault would prevent the dispersion of both the injected CO_2 and also the pressure wave through the target reservoir. We have seen that small reservoirs (or the equivalent, such as a compartmentalised large reservoir) are prone

to stress arching and at higher risk of failure. Therefore compartmentalisation by undetected sealing faults could lead to potentially drastic changes in geomechanical deformation. SWS, though difficult to observe, could be used as a tool to image these effects.

7.4 Summary

- I have developed a workflow to map changes in stress computed by geomechanical simulation into changes in the dynamic elastic stiffness tensor of the reservoir and overburden rocks. The models can be initialised such that the dynamic stiffness match the geomechanical stiffnesses (or a multiple thereof).
- The workflow can also model the effects of fractures and of fluid substitution.
- I have computed the changes in overburden two-way travel time above the simple reservoirs. I find that where stress arching occurs an increase in vertical P-wave velocity leads to a detectable travel time decrease.
- I have also made predictions about anisotropy induced by stress changes. The amount of splitting predicted may be difficult to observe, but does indicate how anisotropy could provide a useful indicator of reservoir compartmentalisation.

LINKING GEOMECHANICAL MODELLING AND MICROSEISMIC OBSERVATIONS AT WEYBURN

The minimum conditions for site closure and transfer of responsibility includes [...] the conformity of the actual behaviour of the injected CO₂ with the modelled behaviour.

*Directive 2009/31/EC of the European Parliament
on the geological storage of carbon dioxide*

8.1 Introduction

The above segment from the EU Parliament's directive on CO₂ storage highlights the need to develop models that are validated by observation. For reservoir fluid-flow models this involves history matching with injection and production rates, downhole pressure changes and CO₂ plume geometry as imaged by controlled source seismics. However, can we also apply this to geomechanical models? Can we find ways to validate geomechanical models of sites like Weyburn with observables from the field?

In the previous chapters I have outlined an approach to model the geomechanical deformation produced by CO₂ injection, and to predict seismic observations based on the geomechanical model. In this chapter I will demonstrate the workflow by applying it in its entirety to Weyburn. By doing so I hope to constrain the geomechanical model by making comparisons with the observed seismic results, and to improve the understanding of why the microseismic events are located as they are.

The workflow that I will use is outlined in Figure 8.1. I use the approach outlined in Chapter 5 to generate a representative geomechanical model of the Weyburn reservoir, simulating both the field depletion and the recent CO₂ injection. By considering the induced stress changes I will compute the changes to the fracture potential for various points around the reservoir, and thereby the likelihood of microseismic activity, and I will compare these inferences with the observations made in Chapter 2. I use the method described in Chapter 6 to invert ultrasonic measurements made on Weyburn reservoir cores for initial crack density and aspect ratio, and use these values as input to the workflow in Chapter 7 to compute seismic properties. I will model shear wave splitting induced by non-hydrostatic stress changes, and compare these results with the splitting observations made in Chapter 3. Such comparisons with observation can be used to calibrate the models, and changes can be made to various model parameters to improve the fit between model predictions and observations. This will improve the confidence in the models when they are used to assess the security of CO₂ storage in the reservoir.

8.2 Model description

A general description of the Weyburn field is provided in Chapter 2. The reservoir has a thickness of 30-40m, and is laterally extensive over many kilometres with little vertical relief. The top and base of

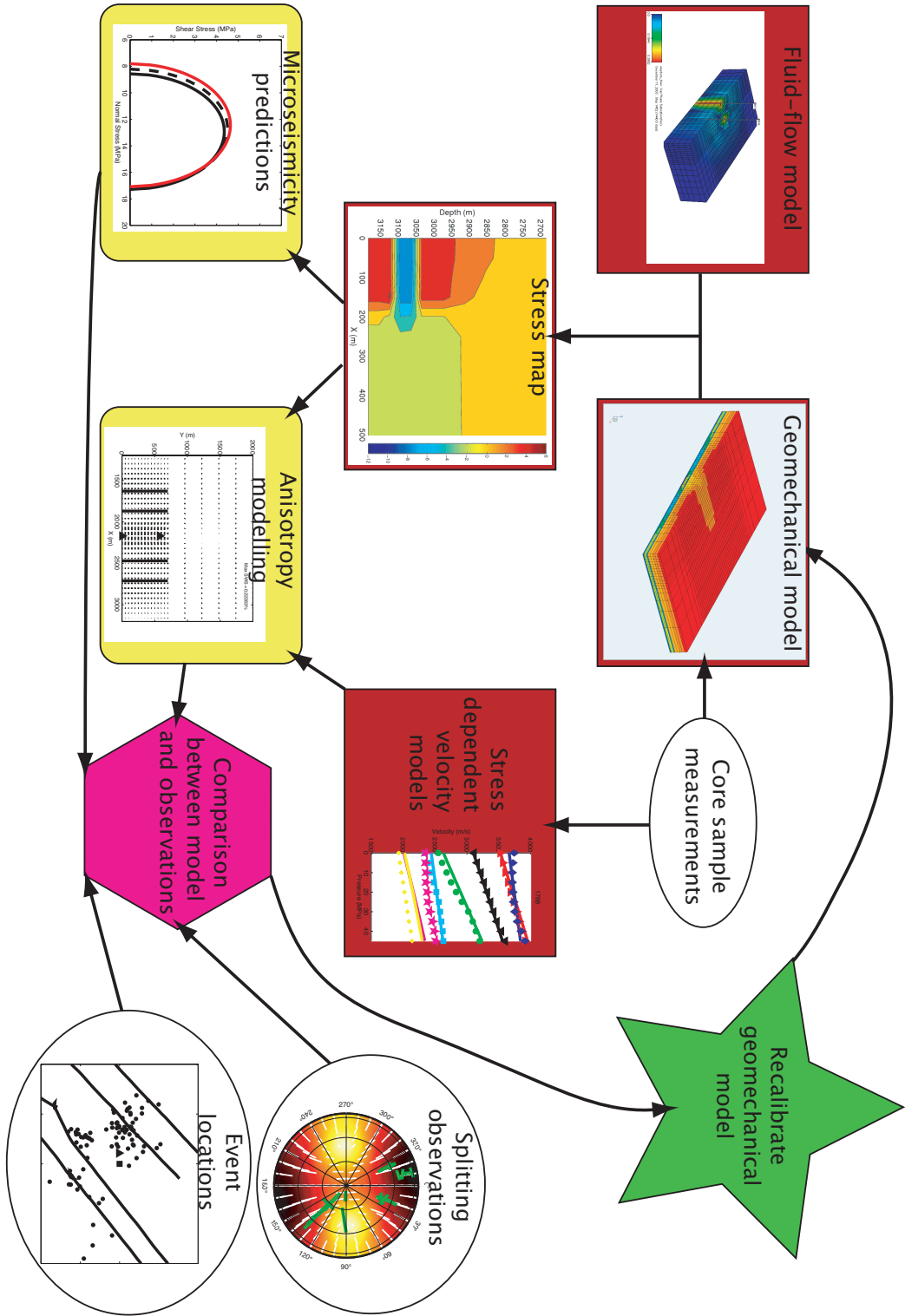


Figure 8.1: Workflow demonstrating how the predictions from coupled geomechanical models can be compared with microseismic observations in order to calibrate and refine the models.

<i>Layer</i>	<i>Thickness</i>	Φ	κ_x	κ_z
Marly	13m	0.25	5mD	4mD
Vuggy	27m	0.15	10mD	7mD

Table 8.1: Flow properties used to simulate the Weyburn reservoir.

the reservoir are bounded by impermeable and stiff evaporites (the Midale and Frobisher evaporites, respectively), and overlying the Midale evaporite is a secondary seal of Mesozoic shale (the Watrous). Above these layers are further overburden rocks that will not be modelled directly in this work.

8.2.1 Fluid flow simulation

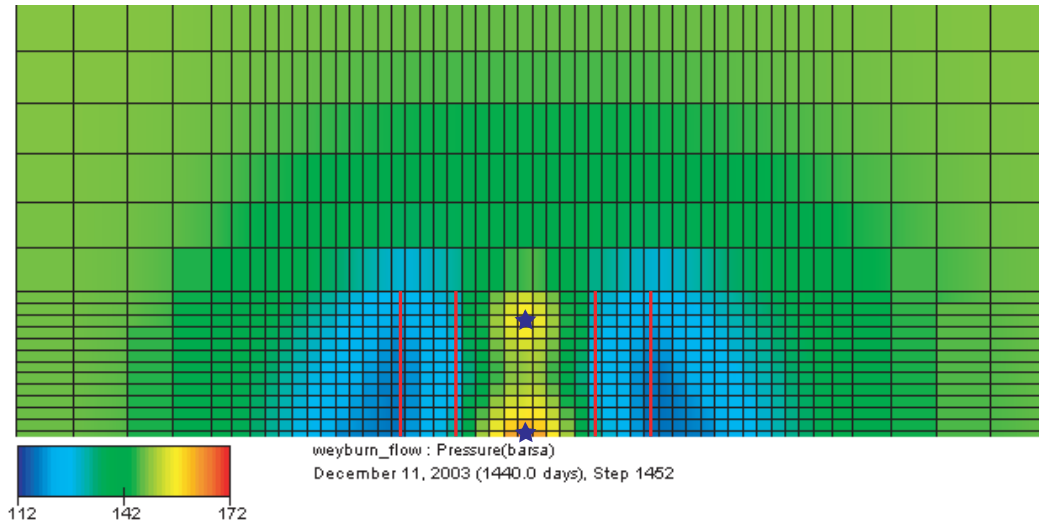
The fluid flow simulation only has to simulate the reservoir. Because the reservoir is laterally extensive with little topography, it is appropriate to model it as a flat layer with a structured mesh. I set up the injection and production wells to approximate the pattern at Weyburn where microseismic monitoring has been deployed. 4 horizontal wells are modelled, trending parallel to the y axis. In between the production wells are 3 vertical injection wells with a spacing in the y direction of 500m. The horizontal wells are completed over a length of 1400m in the reservoir. To reduce computational requirements I model only half of the reservoir, and complete the simulation by assuming that the model is symmetrical about the x axis. Therefore the figures in this chapter show only the half of the model that has been simulated.

The region enclosed by the wells is approximately 1.5×1.5 km. However, I extend the model to 4.4km in the x direction and 4km in the y direction in order to reduce the influence of edge effects. The reservoir is 40m thick, and for the purpose of fluid flow simulation is split into upper Marly and lower Vuggy layers, whose flow properties are given in Table 8.1. Although these properties differ slightly from the values given in Chapter 2, discussion with the field operators (*D. Cooper, pers. comm., 2009*) suggests that these values provide the best match with observed pressures and gas saturation.

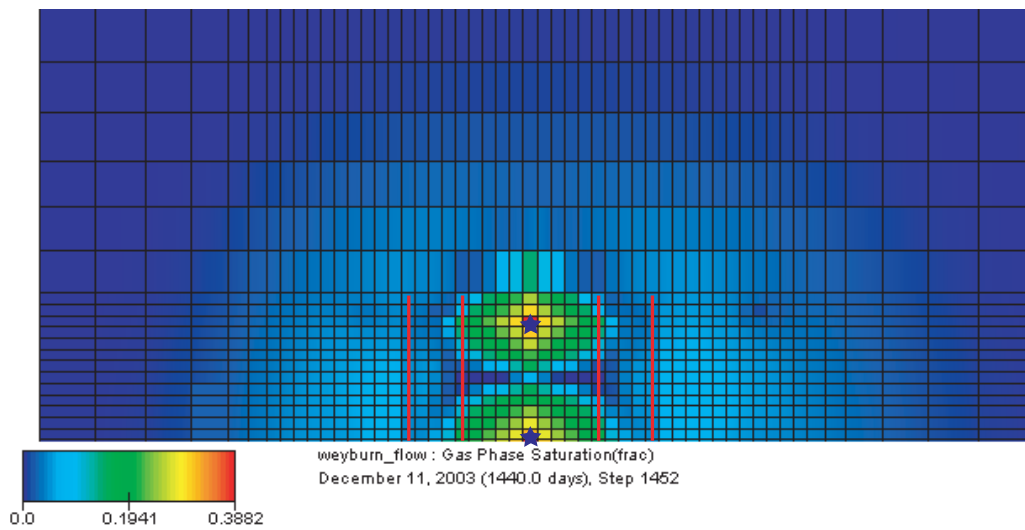
The mesh through the well region has a minimum spacing of $60 \times 50 \times 4$ m ($x \times y \times z$), with an increasingly coarse mesh used laterally away from the wells (up to 240×275 m). The flow simulation mesh is depicted in Figure 8.2. The flow regime is as follows: For one year there is no injection in order to ensure that the model has stabilised; after this the field is produced for two years through all the wells, drawing the pressure down from 15 to 10MPa; then the three vertical wells are switched to inject CO_2 for 1 year, increasing the pressure to ~ 18 MPa, while the pressure is still below 15MPa at the producers. This provides an approximation of the state of the field after 1 year of injection (i.e., by the end of 2004, the end of Phase IB). The gas injection rate at each well is 100MSCM/day. The pore pressures and gas saturations at the end of the simulation are plotted in Figure 8.2.

8.2.2 Geomechanical model

The geometry of the reservoir in the geomechanical model must be the same as for the fluid flow modelling. For the geomechanics I use a mesh spacing of $60 \times 50 \times 20$ m ($x \times y \times z$) in the reservoir,



(a)



(b)

Figure 8.2: Map views of (a) pressure (in bar) and (b) gas saturation at the top of the reservoir after one year of injection computed by the fluid flow simulation of Weyburn. The vertical injection wells are marked by the blue stars, the horizontal producing wells by red lines. Reflective symmetry along the x axis means that I can model only half the reservoir, and use symmetry arguments to complete the model.

<i>Unit</i>	<i>E (GPa)</i>	ν	ρ (kg/m ³)	Φ	<i>Layer top (m)</i>	<i>Layer base (m)</i>
Overburden	5.0	0.25	2000	0.2	0	1210
Watrous	14.0	0.23	2000	0.1	1210	1410
Marly Evaporite	24.0	0.34	2700	0.05	1410	1430
Reservoir	14.5	0.31	2200	NA	1430	1470
Frobisher Evaporite	24.0	0.34	2700	0.05	1470	1490
Underburden	20.0	0.25	2500	0.1	1490	2490

Table 8.2: Material parameters for the units of the Weyburn geomechanical model. All layers are saturated with water with $K=2.2\text{GPa}$ and $\rho=1100\text{kg/m}^3$, except the reservoir, whose porosity and saturation are determined by the fluid-flow simulation.

coarsening away from the wells. The different reservoir units are too thin to model separately, because as the aspect ratios of the elements become too high, so the solutions become unstable. One solution would be to reduce the mesh spacing in the x and y directions, allowing for a reduction in mesh spacing in the z direction. However, this would significantly add to the computation time of the models. Average material values across the reservoir are used instead. The top of the reservoir is at 1430m. The overburden is modelled to the surface, the underburden is modelled to a depth of 2480m. The non pay rocks are divided into 4 units: the evaporite units bounding the reservoir, the overlying Watrous shale, while the remainder of the overburden above the Watrous, and the underburden below the Frobisher evaporite are modelled with uniform representative properties.

8.2.3 Material properties

The material properties for each unit are given in Table 8.2, based on core sample work by Jimenez Gomez (2006) and Chalaturnyk (*pers. comm. 2007*). The boundary conditions are set as for all the models in Chapter 5, where the top of the model is a free surface. The planes at the sides and base of the model are prevented from moving in a direction normal to the boundary, although they are free to move within the plane of the boundary (i.e. at the $x - z$ boundary, nodes can move vertically and horizontally in the x direction, but not in the y direction).

8.2.4 Rock physics properties

To predict the changes in seismic properties as outlined in Chapters 6 and 7 the crack density and aspect ratio parameters must be calculated using ultrasonic velocity measurements. The data that I use are taken from Brown (2002), who performed ultrasonic velocity measurements on Vuggy and Marly core samples with variations in the applied hydrostatic stress (Figure 8.3). Brown (2002) only makes measurements along one axis, so it is only possible to invert for an isotropic rock. I use the method outlined in Chapter 6 to invert these measurements for the rock physics parameters, given in Table 8.3. The values fit comfortably within the global trends identified during calibration with literature samples given in Chapter 6. A comparison between modelled and observed velocities is

<i>Unit</i>	a_0	ξ^0	B_N/B_T
Marly	0.0006	0.125	0.51
Vuggy	0.0006	0.02	1.0

Table 8.3: Inverted rock physics properties for the Marly and Vuggy samples described in Brown (2002).

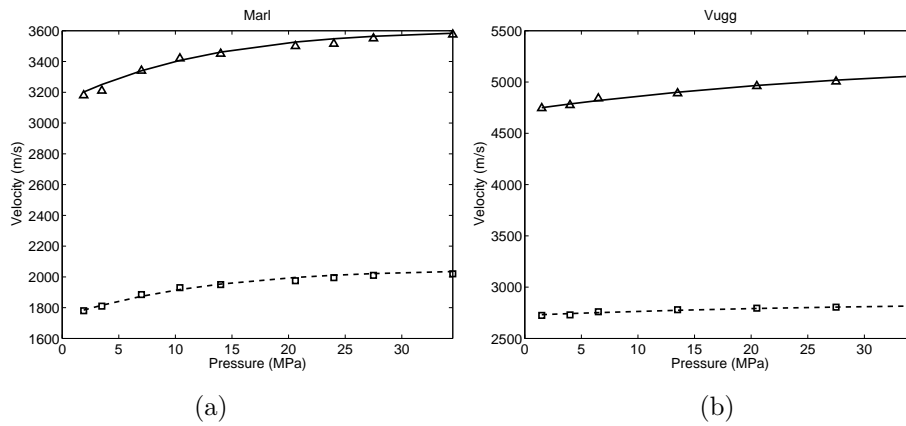


Figure 8.3: Observed ultrasonic P (solid lines) and S (dashed lines) velocities (symbols) and back calculated values (lines) as a function of stress for the Marly (a) and Vuggy (b) units.

shown in Figure 8.3, and I note an excellent match. The average mismatch between modelled and observed velocities is 0.5% - equal to the experimental errors in measurement (Brown, 2002). The crack density tensors as a function of the applied stresses are plotted in Figure 8.4. These inverted values are used in the subsequent section to model changes to P-wave velocity and shear wave splitting. No ultrasonic measurements on overburden materials are available, so generic values are used.

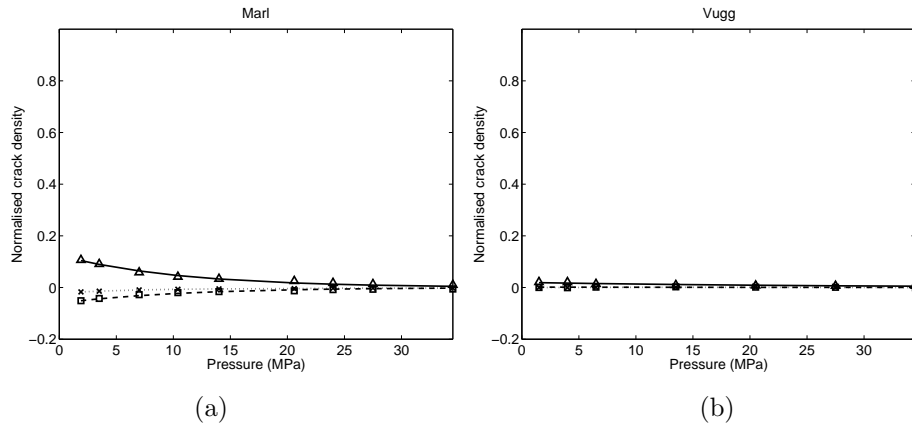


Figure 8.4: Crack densities of the Weyburn Marly (a) and Vuggy (b) rocks inverted from velocity observations (symbols) and using stress-sensitive modelling (lines). The 2nd order tensor components (solid lines) and 4th order tensor diagonal (dashed lines) and off-diagonal (dotted lines) components are shown.

8.3 Results

8.3.1 Stress evolution and failure

The total simulation run lasts 4 years - one year pre-production, two years of production, one year of injection. As in Chapter 5, the results I will now discuss are output by ELFEN at equally spaced, user defined timesteps. In Figure 8.5 I plot the vertical effective stress in the reservoir and overburden after injection. Around the injection wells there is a lower effective stress due to pore pressure increase, while there is a higher effective stress around the producing wells. In the overburden there is increase in effective stress above the injection wells, as the expanding reservoir pushes into the overburden, while the compaction of the reservoir reduces the effective stress above the production wells in the overburden. However, these stress effects in the overburden are small.

To compute the fracture potential I use equation 5.22 and the values for cohesion and angle of friction measured from core samples by Jimenez Gomez (2006). These are given in Table 8.4. Of course, these values represent the strength of intact rock, and not the planes of weakness which would be the first places to experience shear failure. Therefore, the high value for cohesion found by Jimenez Gomez for the evaporite is probably unrealistic, so I use an arbitrarily reduced value. I am most interested in the change in f^p , whether it increases or reduces, which is relatively insensitive to the values of χ and ϕ_f , rather than absolute magnitudes of f^p . Therefore the choice of these values is not particularly important.

In Figure 8.6 I plot the evolution of fracture potential through time in the reservoir and overburden at the injection and production wells, while in Figures 8.7 and 8.8 I plot snapshots of the fracture potential before production begins (ELFEN output timestep 3), during production (timestep 8), after

<i>Unit</i>	χ	ϕ_f
Caprock	5 (18.5) MPa	45°
Reservoir	3.5 MPa	40°

Table 8.4: Yield envelope parameters for the Weyburn model. A lower value than that measured on core samples is used for the cohesion of the caprock, which is given in brackets.

3 months of injection (timestep 12) and after 1 year of injection (timestep 16), both in the reservoir (Figure 8.7) and in the overburden (Figure 8.8). From these figures I note that fracture potential increases in the reservoir during production, while it is relatively unchanged in the overburden. Once injection begins, there is a sharp increase in fracture potential in the overburden above the injection wells, while there is a drop in fracture potential in the reservoir at the injection well. The fracture potentials at the producing wells are relatively unchanged during injection.

In general, there are some qualitative comparisons that can be made between this model and the observations made at Weyburn. For instance, the fact that across most of the reservoir fracture potential is not increased by injection matches with the lack of seismicity recorded. Also, this model suggests that fracture potential should be higher at the production wells than at the injection wells, which matches the observations that the majority of events occur close to the producers. However, this model can not explain why so many events are located in the overburden above the producing wells, while the models predict that there should be microseismicity above the injection well, where none is observed. The suitability of this model can also be assessed through a comparison of the seismic anisotropy that it predicts.

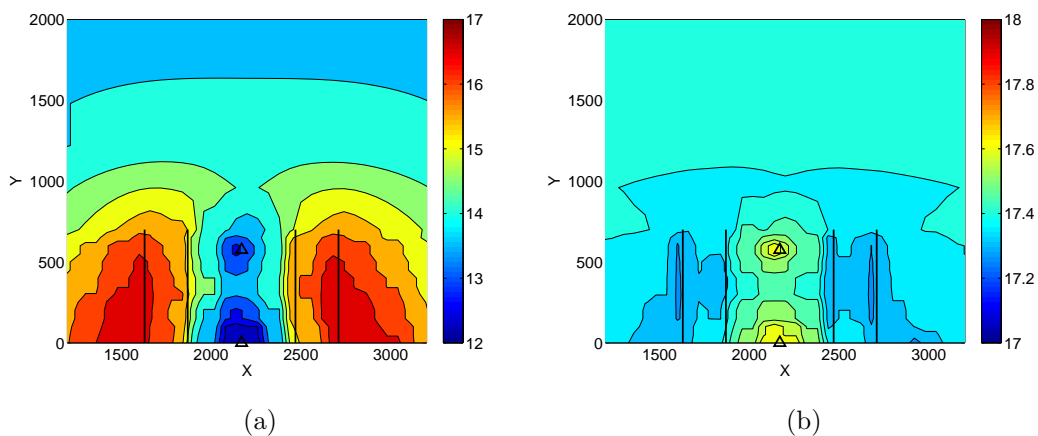


Figure 8.5: Map view of vertical effective stress in (a) the reservoir and (b) the overburden of the Weyburn model at the end of 1 year of CO₂ injection. The horizontal producers and vertical injectors are marked by lines and triangles respectively. Contours are in MPa.

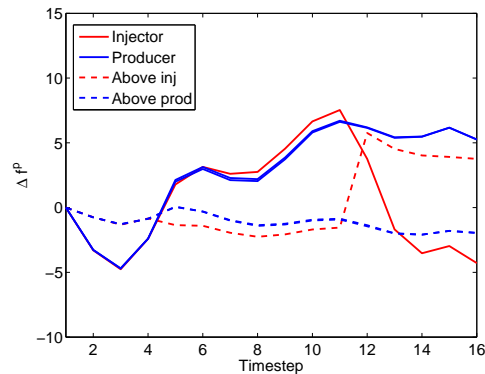


Figure 8.6: Percentage change in fracture potential in the Weyburn reservoir (solid lines) and overburden (dotted lines). f^P near the injection well is marked in red, near the producers in blue. Fracture potential does not increase anywhere after injection begins (timestep 11) except in the overburden near the injection wells (dotted red line). Therefore this region should be most prone to microseismic activity.

8.3.2 Seismic Properties

To compute the seismic properties based on the stress changes I use the method outlined in Chapter 7. The shear-wave splitting patterns predicted by this model are plotted in Figure 8.9a for the reservoir and 8.9b for the overburden. No significant splitting patterns develop either in the reservoir or overburden. This does not match with the observations made in Chapter 3, where a strong HTI fabric was observed striking to the NW, perpendicular to the horizontal well trajectories.

I conclude that this initial model, whose input parameters were based on core measurements from the field, does not provide a good match with my observations of microseismic activity and seismic anisotropy in the field. The question to ask, then, is why this should be? One potential answer lies in the fact that measurements on cores represent the intact rock, whereas the reservoir is dominated by fractures, which provide key fluid-flow pathways in the reservoir, and, as the name of the lower formation suggests, vugs. Core scale measurements can only account for microscale properties - features that are much smaller than the core size. The effects of meso and macro scale features, such as vugs or fractures, that are a similar size as, or larger than, the cores will not be included in core analysis. The presence of fractures and vugs will significantly soften the elastic stiffness of the reservoir. Because the overburden has far fewer fractures, and no vugs, I will keep their properties the same while reducing the stiffness of the reservoir.

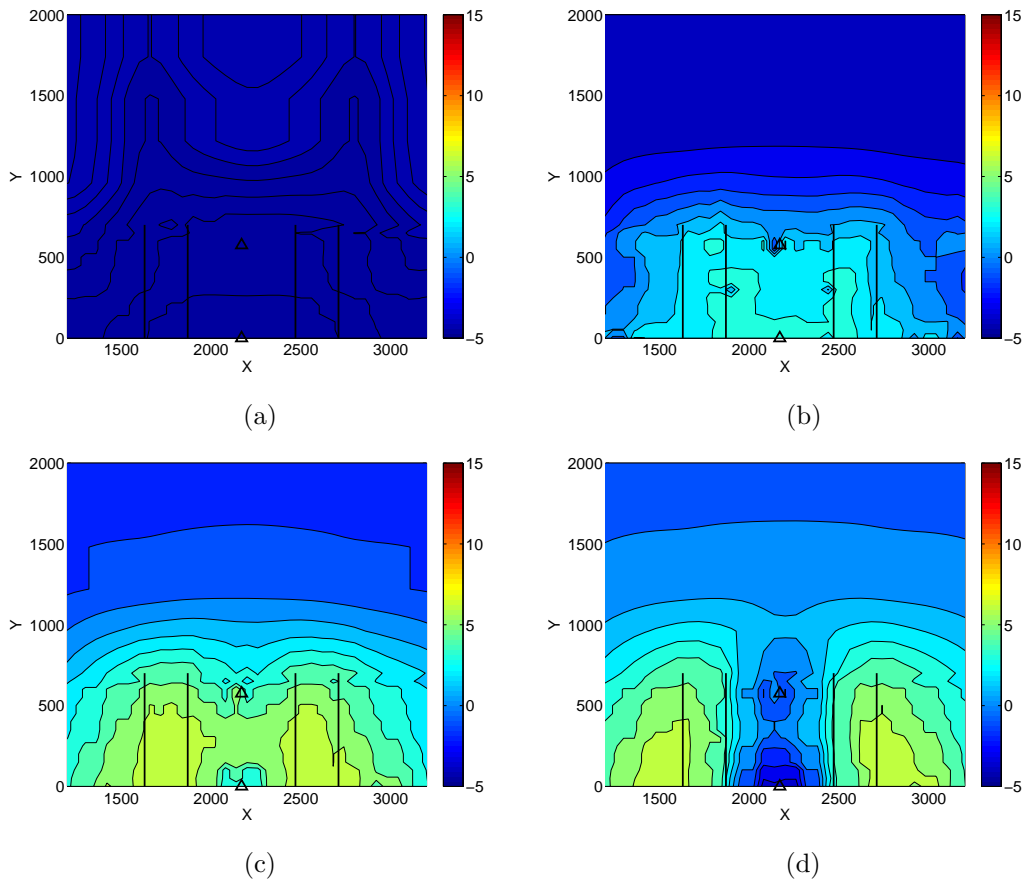


Figure 8.7: Percentage change in fracture potential in the Weyburn reservoir (a) before production, (b) during production, (c) just after the onset of CO₂ injection, and (d) after 1 year of injection.

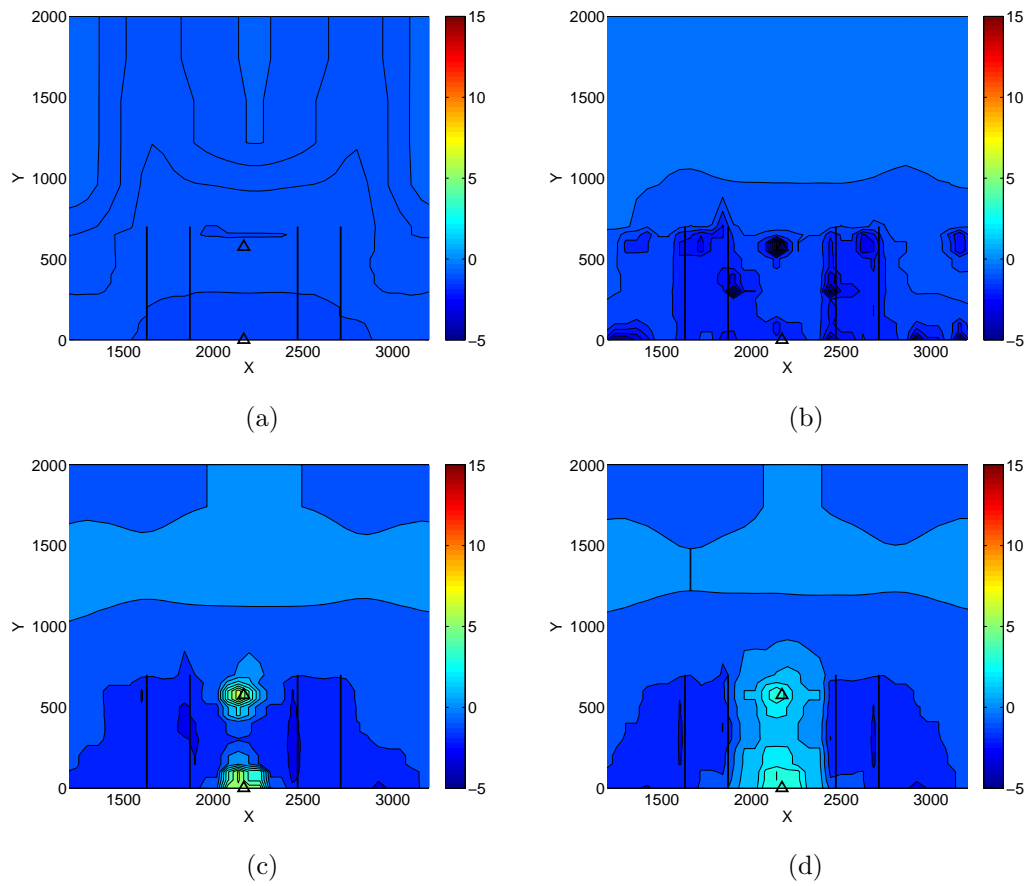
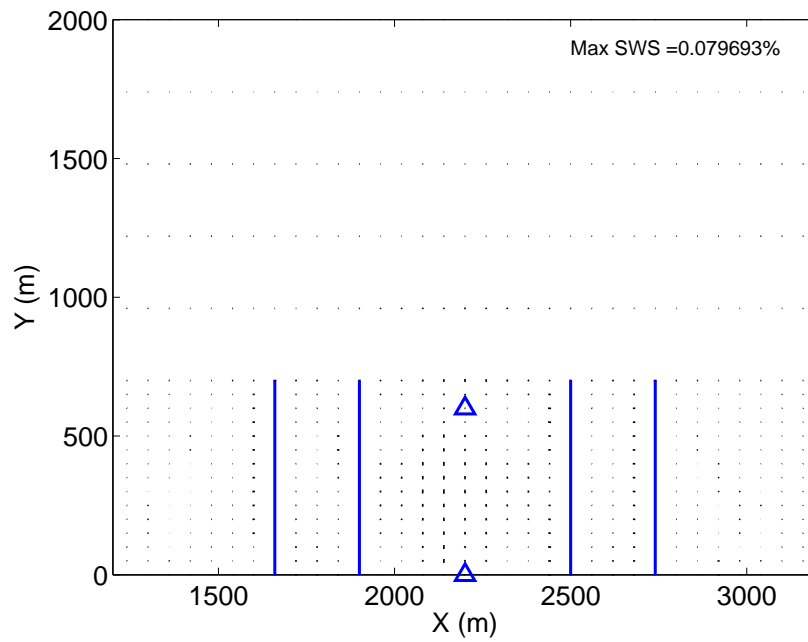
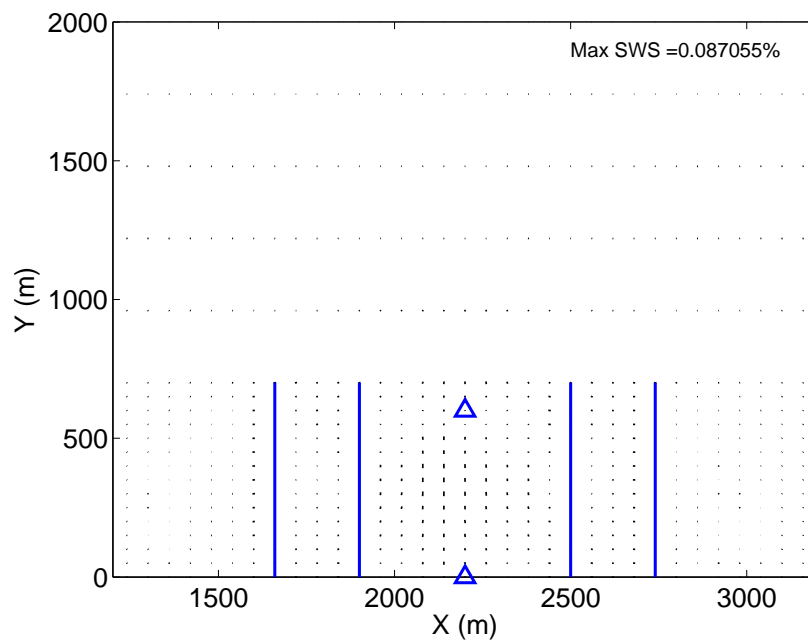


Figure 8.8: Percentage change in fracture potential in the overburden of the Weyburn reservoir (a) before production, (b) during production, (c) just after the onset of CO_2 injection, and (d) after 1 year of injection.



(a)



(b)

Figure 8.9: Modelled shear wave splitting in the Weyburn reservoir (a) and in the evaporite caprock (b) after 1 year of injection. Tick orientations mark the fast direction, tick lengths mark the splitting magnitude, and the maximum splitting values are given.

8.4 A softer reservoir?

For the updated model, I reduce the Young's modulus of the reservoir to 0.5GPa, while keeping all the other properties the same as for the first model. Therefore this model has a reduced reservoir:overburden stiffness ratio. The stress evolution for this model is plotted in Figure 8.10. The trends are the same as for the stiffer model (Figure 8.5). However, because in this case the reservoir is softer in comparison to the overburden, more stress can be transferred from the reservoir to the overburden (as demonstrated in Chapter 5). As a result, the changes in effective stress in the reservoir are reduced, while the changes in stress in the overburden are increased.

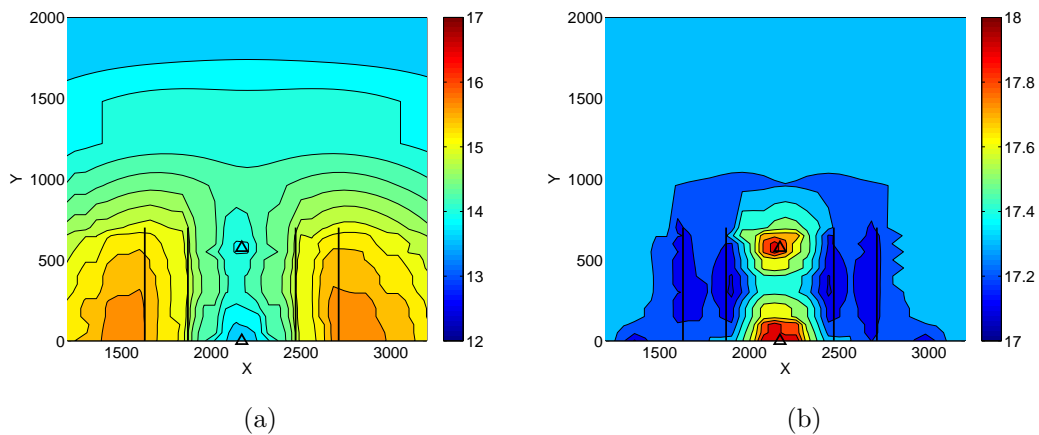


Figure 8.10: Vertical effective stress in (a) the reservoir and (b) the overburden of the softer Weyburn model after injection. The locations of the vertical injection wells (triangles) and horizontal producers (lines) are marked.

The fracture potentials for the softer model are computed as for the first model, using the values in Table 8.4. The results are shown evolving through time in Figure 8.11, with snapshots across the reservoir and overburden in Figures 8.12 and 8.13 respectively. As with the stiffer reservoir, the fracture potential increases during production. However, the behaviour in the overburden is different once injection begins. The fracture potential at the producing wells is relatively unchanged. However, the onset of injection leads to a sharp increase in f^p in the overburden above the producing wells. After an initial increase in f^p in the overburden, the rocks around and above the injection well experience a decrease in fracture potential, returning to values similar to what they were before production had begun. This provides a much better match with observations made in Chapter 2, where events occur in the reservoir and overburden near the horizontal production wells, but few if any events are found near the injection well. In particular, this model shows how stress transfer into the overburden, which is promoted by a reservoir that is softer in comparison to the overburden (as noted in Chapter 5), can generate increases in shear stress, and therefore a greater likelihood of microseismicity, above the horizontal production wells.

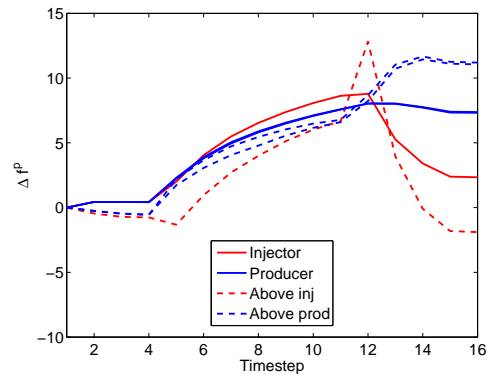


Figure 8.11: Percentage change in fracture potential in the softer Weyburn reservoir (solid lines) and overburden (dotted lines). f^p near the injector is marked in red, near the producers in blue.

The shear wave splitting predictions are plotted in Figure 8.14. As with the stiffer case, little splitting develops in the reservoir. However, in the overburden some significant and coherent splitting patterns develop. Above the production wells the fast directions are orientated parallel to the well trajectories (the y axis), while above the injection wells the fast directions are orientated perpendicular to this (parallel to the x axis). This represents the development of significant stress anisotropy from the initial isotropic state.

In Chapter 3 I observed an HTI fabric with a fast direction to the NW, perpendicular to the NE well trajectories. This splitting was measured on waves travelling to geophones sited above the injection well, from microseismic events located in or above the reservoir. Therefore, most of the raypath is in the overburden. Therefore, the splitting they experience will be caused by anisotropy in rocks above the injection well. As such, the predictions from the model, with fast directions orientated perpendicular to the well trajectories above the injection well, do provide a good match with observations made at Weyburn.

It appears, therefore, that the model with a softer reservoir in comparison to the overburden produces event location and shear wave splitting predictions that match well with observations, while the original model does not. This demonstrates the need to link geomechanical models with observations, by doing so discrepancies can be identified and corrected for, leading to the development of improved models.

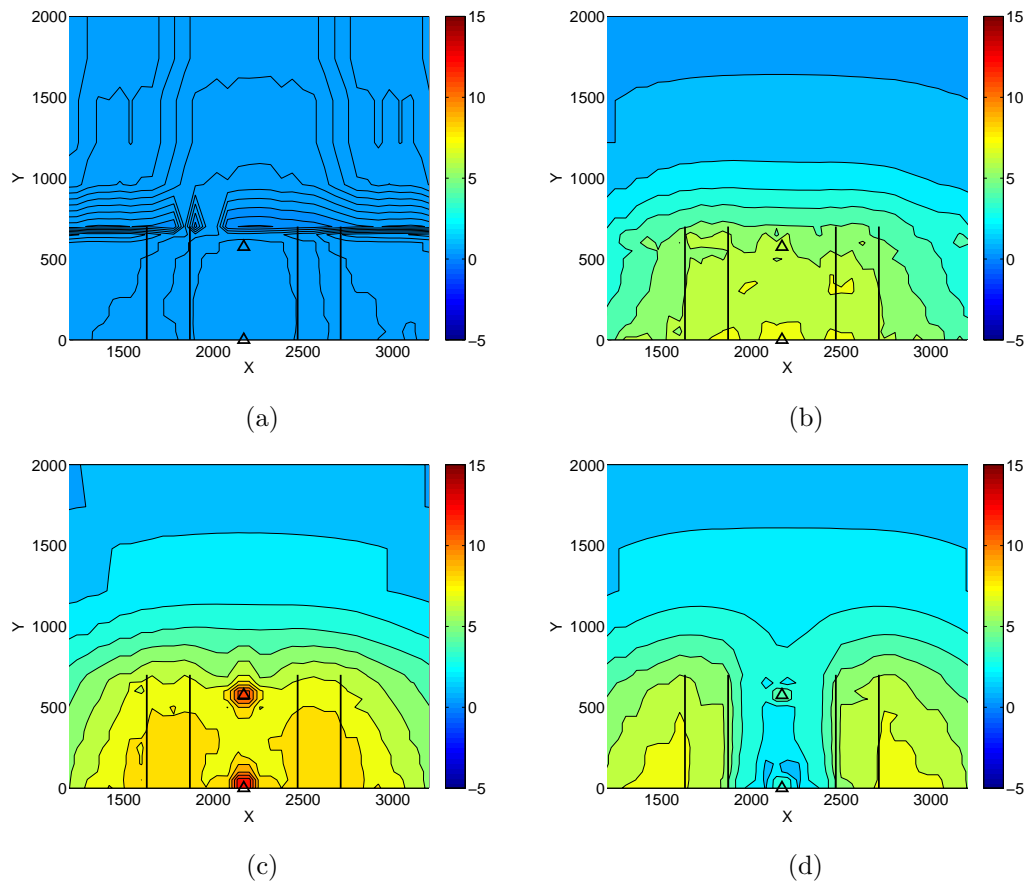


Figure 8.12: Percentage change in fracture potential in the softer Weyburn reservoir (a) before production, (b) during production, (c) just after the onset of CO_2 injection, and (d) after 1 year of injection.

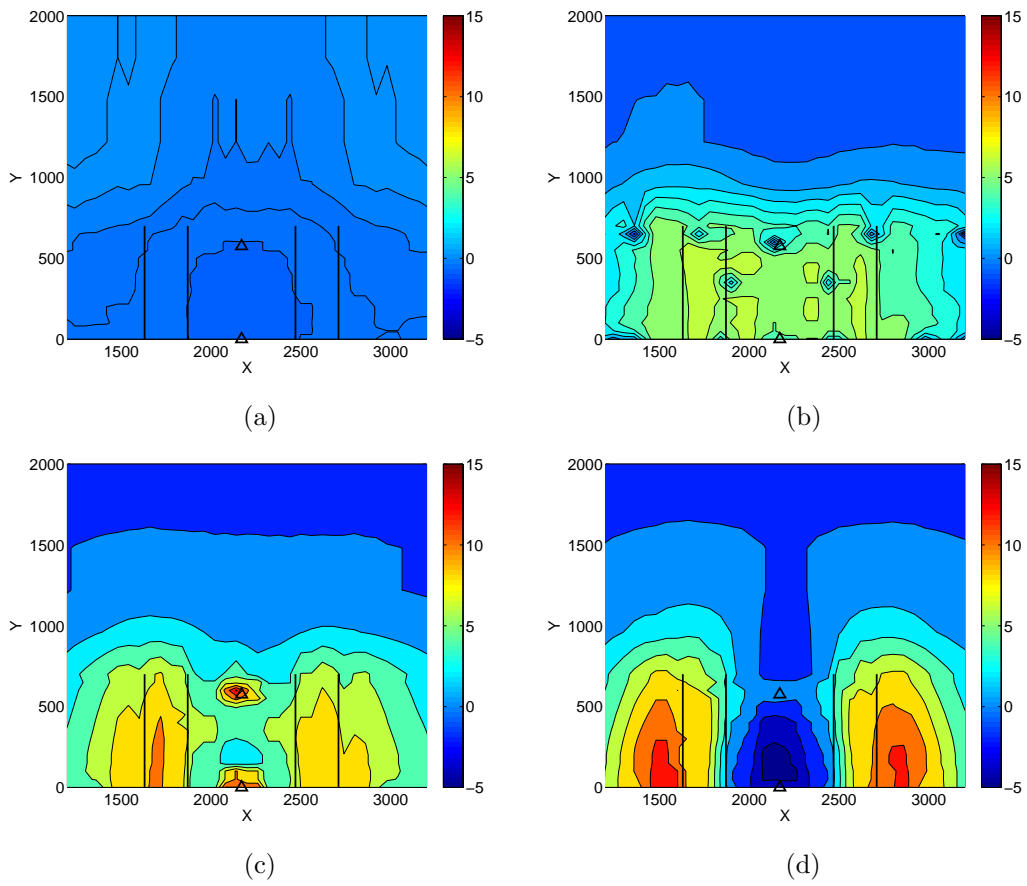
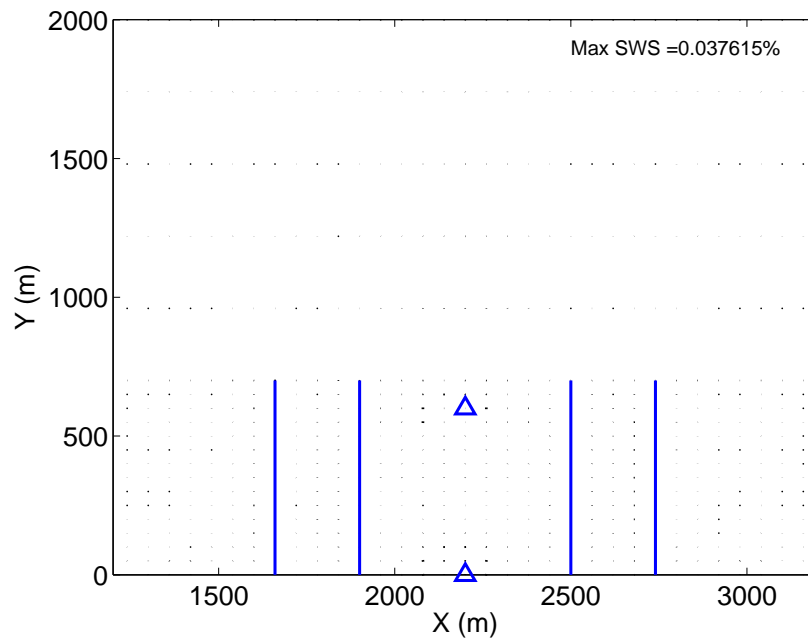
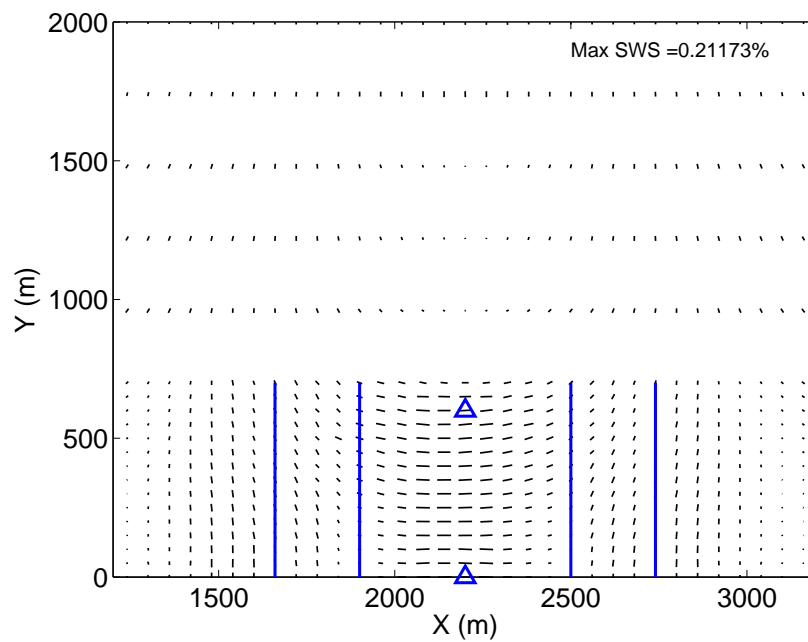


Figure 8.13: Percentage change in fracture potential in the overburden of the softer Weyburn reservoir (a) before production, (b) during production, (c) just after the onset of CO_2 injection, and (d) after 1 year of injection.



(a)



(b)

Figure 8.14: Modelled shear wave splitting in the softer Weyburn reservoir (a) and in the evaporite caprock (b) after 1 year of injection. There is little splitting in the reservoir, but splitting orientated perpendicular to the injection wells, and parallel to production wells, in the caprock.

8.4.1 Heterogeneity

The models I have presented here do not deal with reservoir heterogeneity. Values for porosity, permeability and mechanical properties are constant for each layer in the model. In reality, carbonate reservoirs such as Weyburn are renowned for their heterogeneity, across many length scales. That there is heterogeneity at Weyburn is clear from the range in porosity and permeability seen in Table 2.1. The match between 4-D seismic imaging of the CO₂ plume at Weyburn and fluid-flow modelling suggests that such heterogeneity is not having a particularly strong effect on CO₂ distribution at the scale of each pattern. However, where there is variation in flow properties (especially porosity) it is likely that there are also variations in mechanical properties as well.

Differences in porosity through a carbonate reservoir imply differences in rock fabrics, as well as possible differences in diagenesis. As I have demonstrated in Chapter 6, differences in grain-scale architecture can exert significant influence on elastic stiffness. Furthermore, differing degrees of carbonate cementation will produce different elastic stiffnesses as well. I have not investigated the effects of these variations, so it is difficult to comment with certainty on what their effects might be. Nevertheless, this issue is worthy of discussion. The role of heterogeneity - regions of the reservoir that are stiffer or softer than the mode - is probably dependent on the length-scale of the heterogeneities in question. Small heterogeneities (reservoir thickness seems a suitable length to which to scale these relative terms) will probably not lead to changes in the shape of stress loops around the reservoir. Small scale features such as this are best incorporated using an effective medium approach where the stiffness of the reservoir is scaled according to the fraction of the rock that is made up of these stiffer regions. This is, in essence the approach taken for any finite element modelling approach, where each node is assigned properties representative of the rock surrounding that point.

However, larger scale heterogeneous zones may act to change the nature of the geomechanical response of a reservoir. For instance, it is possible to envisage stiff zones within a reservoir that, if of a sufficient scale, could act as ‘pillars’ on which to support stress arches that would otherwise not be capable of supporting the overburden of an extensive reservoir. As I have shown in Chapter 5, whether or not a stress arch can develop has a significant effect on the evolution of stresses in and around an inflating reservoir. Scope for further study exists to investigate this issue. Such a study would involve using a geostatistical model which varies the difference in mechanical properties between the heterogeneous zones and the ‘background’ reservoir material, the proportion of the reservoir made up of the ‘heterogeneous’ material, and, importantly, the characteristic length scale of the heterogeneous zones. By using this geostatistical model as an input for the geomechanical modelling, it should be possible to determine at what length-scales and proportions heterogeneities with a reservoir begin to influence the stress path during production and injection.

8.5 Discussion

Event locations at Weyburn indicate that there is microseismicity in the overburden. This observation was a cause for concern, as it was inferred that the events represented either CO₂ leakage, or at least

pore-pressure being transferred into the overburden. Either would imply that pathways exist for CO₂ to migrate out of the reservoir. Nevertheless, within the resolution available, controlled source 4-D seismic monitoring surveys do not indicate any leakage. However, without geomechanical modelling, there is no alternative explanation for why the events are found where they are.

A representative geomechanical model shows that, if the reservoir is softer than measured in core samples, deviatoric stress will increase in the overburden, increasing the chances of shear failure and thereby of microseismic activity, especially above the producing wells. In contrast, if there were pore-pressure connections, or buoyant fluid leaking into the overburden, I anticipate that microseismicity would be located above the injection well, where pore pressures are highest and buoyant CO₂ is situated. This is what I observed during the hydraulic fracture described in Chapter 4.

At Weyburn events are located above the producing wells, suggesting that the former is the case - a softer than anticipated reservoir is transferring stress into the overburden, inducing microseismicity. The anisotropy generated by such stress transfer also matches the observations of anisotropy made at Weyburn. Angus et al. (2010) show that it is changes to the stress state that have the strongest control on the distribution of microseismic events. Fluid migration plays only a secondary role. The microseismicity in the overburden at Weyburn is not an indication that fluids are leaking into the overburden.

It is therefore worth asking whether we are putting the hydraulic integrity of the caprock at risk with this microseismicity? Unfortunately this question is difficult to answer, as even active faults and fractures do not necessarily act as conduits for fluid flow, and there is no way of knowing how well connected any fractures in the caprock may be. The fact that there are few events, most of which are of low magnitude, suggests that there are not many large-scale fractures in the overburden. Most importantly, the integrated geophysical and geochemical monitoring systems at Weyburn do not indicate any leakage, so it would appear that any fracturing generated by microseismicity in the overburden is not currently providing a pathway for leakage. By continuing to monitor the field it will be possible to ensure that this remains the case.

The reduction in stiffness I show to produce the match with observations is large - from 14 to 0.5GPa. This is done to show the changes that a softer reservoir can produce *in extremis*. In this case the changes to fracture potential and shear wave splitting introduced by a softer reservoir are clear for the reader to see. As the stiffness is reduced from 14GPa, the trends that I have highlighted gradually establish themselves. It is well known that the presence of fractures and vugs will make core sample measurements overestimate the true values. However, an order of magnitude overestimate is perhaps too much to attribute entirely to the presence of fractures and vugs. It is at this point that we should remind ourselves that what we are dealing with here is a simplified representative model, useful for determining the principal controls on reservoir stress changes, and the directionality of stress changes introduced by variations material parameters. In this case, we suspect that the Young's modulus is overestimated by an unknown amount, and we know that reducing it will produce a stress path closer to that inferred from microseismic observations. However, to determine more exactly how much the Young's modulus needs to be reduced to get a good match with observation will probably require a more detailed model that provides a better match with the details of the reservoir geology, and a

more precise way of determining how much of an increase in fracture potential is needed to generate microseismicity.

8.6 Summary

- I apply the workflow developed in Chapters 5 - 7 to the Weyburn reservoir.
- I develop a simple coupled fluid-flow/geomechanical model representing a typical pattern from the field, including the stiff evaporite layers lying above and below the reservoir. This model simulates the depletion during production through horizontal wells, and the subsequent injection of CO₂ into the reservoir through a vertical wells.
- I use the inversion method developed in Chapter 6 to compute initial crack densities and aspect ratios for the Weyburn rocks, enabling me to use the workflow developed in Chapter 7 to compute changes in seismic observables.
- The first model I develop uses mechanical properties based on core sample measurements. The regions where there is an increased likelihood of microseismic activity, and the stress-induced anisotropy, do not provide a good match with the observations made in Chapters 2 and 3.
- I develop an alternative model with a reservoir unit that is softer than the overburden. The motivation for doing so is that the presence of fractures and vugs in the reservoir, which are not accounted for in core sample measurements, will make it considerably softer than rock physics tests would suggest.
- This softer model does a much better job of matching both microseismic event patterns and shear wave splitting predictions with the observations made in Chapters 2 and 3. This demonstrates the importance of linking geomechanical models with observable indicators of deformation in the field in order to groundtruth and calibrate the models.
- The geomechanical model demonstrates that the occurrence of microseismicity in the overburden does not represent fluid migration through the caprock, but merely the transfer of stress.

Geological storage will be safe, and more permanent than any human activity since Stonehenge.

Ron Masters, 2009

This thesis has investigated the use of microseismic techniques to monitor CO₂ injection and storage, as well as using geomechanical models to guide the interpretation of these observations. A summary of the findings has been provided at the end of each chapter, but in this section I will review the key findings, highlighting novel contributions to the field and areas for future research.

The first part of this thesis has concerned itself with observations of microseismic events induced by CO₂ injection. A concern is that the pressure changes caused by injection will generate fracturing in the overburden, providing a leakage pathway for buoyant supercritical CO₂. Microseismic monitoring can image this process directly. Microseismic activity can also be used to image fluids moving through the overburden. The aims of microseismic monitoring for CCS are, then, slightly paradoxical in that geophones are placed in the ground with the hope that they will not record anything. They are there to provide a warning if things go wrong. This is not the only CCS monitoring technique that aims to detect nothing: for example if no change is detected during shallow aquifer fluid sampling and soil gas flux measurement, then the storage site will be deemed successful. Microseismic monitoring should provide a much earlier warning of leakage than soil gas fluxes and shallow aquifer sampling. In contrast, some techniques such as 4-D controlled source seismic monitoring aim to find a detectable change after injection, so long as it is limited to the target reservoir zone.

I have presented the results of over 5 years of microseismic monitoring at Weyburn. There have been less than 100 events over this period, indicating that the reservoir is undergoing little deformation, and that the CO₂ is generally moving through the reservoir aseismically. This is encouraging with regard to security of storage. The few events that are observed are generally located near to the production wells to the NW and SE, and many could be located in the overburden, though event depths are not well constrained. Although it may at first glance be worrying if microseismicity is identified in the overburden, this does not mean that the events are caused by CO₂ moving into the caprock. Indeed, inasmuch as that the events are located near the producers, while the CO₂ plumes centre on the injectors, it is very unlikely that the events recorded represent leakage. This matches 4-D seismic observations that do not show any fluid migration above the injection wells.

This of course begs the question: what would microseismic monitoring detect if CO₂ injection was causing fracturing and creating leakage pathways in the rock. I have attempted to answer this question by comparing hydraulic fracture data from CO₂ and water injection. This example is not directly equivalent to CCS scenarios, as the injection pressures used are much higher. Nevertheless, this can be considered to be a worst case scenario, exactly what microseismic monitoring will be deployed to detect for CCS projects, and so lessons can be learnt. During injection, the event locations image the growth of fractures from the injection site, both laterally and above the injection point. If such observations were made at a storage site, and in particular if events are detected moving well above the injection depth, then the injection regime would have to be reconsidered, and possibly remediation

work would be required as well. This example proves that if CO₂ is injected at pressures that are too large for a particular formation to contain, events with a detectable magnitude will occur, which can be imaged using a downhole passive seismic array.

Shear wave splitting measurements made on microseismic data are useful as an indicator of fracture-induced anisotropy. This technique was first developed using teleseismic waves with subvertical arrival angles. The splitting from such waves is relatively easy to interpret, with fast direction corresponding to fracture strike, and splitting magnitude giving the number density of fractures. However, microseismic data has arrival angles which are often subhorizontal, making the splitting harder to interpret. Nevertheless, I have developed a technique to invert for fracture properties using rock physics theory, and shown that it is possible to identify fracture orientations using SWS despite a highly unfavourable source-receiver geometry.

Splitting analysis on the Weyburn events reveals the presence of a principal fracture set striking to the NW, and a weaker, poorly imaged set striking to the NE. Previous work on core samples do confirm the presence of conjugate fractures with these orientations. However, there is a discrepancy in that core analysis indicates that the set striking to the NE should be the dominant set. To understand this discrepancy, and to improve the interpretation of what the microseismic event locations mean for storage security, I have constructed geomechanical models to represent the Weyburn reservoir.

The state of the art in geomechanical modelling of reservoirs is to couple together fluid-flow and finite element geomechanical models. Such models can be used to predict the stress evolution during injection, and hence the likelihood of brittle failure and microseismic events. I have defined several stress path parameters, and have used these to study the controls that reservoir geometry and material properties have on stress evolution. I find that small reservoirs are more prone to stress arching effects, so long as the overburden is sufficiently stiff. In contrast, flat, extensive reservoirs do not tend to transfer stress into the overburden. I have found that the extent to which this can happen is controlled by the smaller of a reservoir's horizontal dimensions. The smaller reservoirs that transfer more stress into the overburden are more likely to generate fracturing, both inside and above the reservoir. This finding may be an important criterion when selecting potential sites for their carbon storage potential.

I have also modelled the effects of reservoir geometry and material properties on the amount of surface uplift. The results demonstrate that the amount of uplift can differ by orders of magnitude depending on the reservoir geometry and material properties. The modelled uplift for the simple examples ranges from several centimetres, which would be easily detectable, to sub millimetre-scale, which would not be detectable even in very favourable conditions. This demonstrates the need to use accurate geomechanical models both when considering the use of InSAR as a monitoring tool, and also when inverting measured surface deformation for pore pressure change.

To be confident that geomechanical models are providing accurate predictions, it is necessary to groundtruth and calibrate them with observations. There are a number of methods that can be used to do this, one of which will be changes to seismic properties. It is known from empirical observation that stress changes alter seismic properties, and that non-hydrostatic stress changes create anisotropy. I have developed a model that can account for these effects, while being simple to use and easy to

calibrate. This model has been calibrated with over 200 different core measurements, and has been found to be remarkably consistent.

I have applied this model to simple geomechanical models in order to determine the sensitivity of seismic properties to stress path effects. The results have demonstrated the potential to diagnose what stress path a reservoir is following using 4-D seismic techniques. By diagnosing the stress path, geomechanical models can be calibrated, allowing the risk of fracturing to be determined. I have also demonstrated how anisotropy could potentially be used as an indicator of reservoir compartmentalisation.

Having developed and demonstrated the workflow to move from geomechanical modelling to seismic predictions, I apply the concept to the real example of the Weyburn field. I have generated a simple model that represents the major features of the reservoir. The initial material parameters used to populate the model were derived from core sample measurements. However, the predictions from this model do not provide a good match with either microseismicity or anisotropy observations. It is a well known (and yet often ignored) fact that mechanical tests on core samples do not, for obvious reasons, include the effects of large scale fractures on the overall properties of a material. Upscaling commonly finds that the rock mass is softer than determined by core tests, and this is particularly true for heavily fractured rocks, such as the Weyburn reservoir. When the Weyburn model is recomputed with a smaller Young's modulus for the reservoir, a much closer match is found between model predictions and observations.

There are many free parameters that can be varied in a geomechanical model, all of which can influence the result. We generally do our best to constrain the information put into such a model using many sources to aid model population, from 3-D controlled source seismics, borehole logs and core work. However, this information does not directly correspond to the information that is needed - i.e. the poroelastic and plastic response of the rock mass, as a whole (not a limited, core-sized sample), to the relatively large and long-term stresses applied during CO₂ injection (as opposed to the low-magnitude, short duration stress applied by an acoustic or seismic wave). These measurements provide proxy information for what we really need. As such, each parameter in the model has a degree of uncertainty to it.

The question then must be: how should we deal with this uncertainty in order to have any kind of confidence in model predictions? One option is to use a stochastic method, where a probability function is assigned to each parameter, and the resulting probabilities for the results are computed. However, even such a method must first assign probabilities to the input parameters, which does not get away from the original problem, in that the probability function will be based on proxy measurements and will not directly represent the required parameter. Therefore we must have a method for determining which models provide the most appropriate results, a decision which must be based on comparison with observations in the field. A number of observations might be made with which to groundtruth geomechanical models, such as surface deformation or borehole tiltmeters. In this thesis I have used observations of induced seismicity and anisotropy to constrain my models, and have demonstrated that some of the information used to construct the original model, in this case the Young's modulus provided by core sample measurements, does not actually do a good job of

modelling the deformation. This is because the effects of fractures in the reservoir are not accounted for in upscaling from core to reservoir scale. When this effect is accounted for, the model provides a much better match with observation.

CCS regulators have not yet made clear what legal requirements will be for a CCS site to be deemed acceptable throughout its period of operation. It has been suggested that for transfer of site responsibility from operator to government at the end of operations, it must be demonstrated that the actual behaviour of the site matches modelled behaviour, allowing accurate long-term predictions to be made. This suggestion is intended for fluid-flow models, where the oil industry has had far more experience in developing full-field simulations with history-matching to well activity and the CO₂ plume as imaged by 4-D seismic surveys. The question remains whether geomechanical models can be developed with the accuracy required to fulfil a legal obligation such as this? Geomechanical modelling is a less mature technique than fluid-flow modelling, and the parameter space available in a geomechanical model is far broader than a fluid-flow simulation.

At present, it does not seem likely that geomechanical models will be a legal requirement for CCS, where an inability to develop an accurate model would represent a failing of the site. Indeed, given the current state of maturity of the technique, it seems that such a requirement would be difficult to meet. However, there may be certain circumstances, for example a site that appears to have a large amount of geomechanical activity, or where fracturing is a particular risk, where it may be especially important to develop a good mechanical model to ensure safe storage. Perhaps microseismic monitoring and/or surface deformation measurements can be used to indicate sites where accurate geomechanical modelling is necessary.

Furthermore, even without a legal requirement for it, geomechanical modelling can still be a useful tool, as demonstrated in this thesis. Geomechanical modelling in the forward sense can be used to make predictions about observable effects should a reservoir behave in a certain manner (i.e., a perfectly sealed case, a worst case, etc.). By linking forward geomechanical models with observables such as microseismic events, it is possible to identify which models most accurately represent reality. In essence, these models provide us with a tool with which to test hypotheses about how the reservoir is responding geomechanically, allowing us to reject those that do not provide a close match with reality. By doing so, we can improve our understanding of the risk to secure storage posed by geomechanical deformation at a particular site.

It is still not clear whether microseismic monitoring should always, sometimes or never be used for CCS. An important first step in such a monitoring project would be to establish the pre-injection level of seismicity, and also to develop a good geomechanical model of the reservoir. This would aid in the decision making process, providing information about the likelihood of generating observable seismic events, for both the desired and worst case scenario. However, at present, because Weyburn is the only storage site to deploy microseismic monitoring, it is difficult to draw more definitive conclusions. Given the state of CCS with respect to political uncertainties and public acceptance, the most appropriate approach must be to deploy monitoring overkill on early projects, thereby proving to the public that CCS is safe, and providing the research community with the opportunities to determine which

techniques are best for each particular circumstance. For this reason I anticipate that microseismic monitoring will be deployed in many future CCS projects.

9.1 Novel Contributions

This thesis contributes several novel ideas to the fields of microseismic monitoring, rock physics and geomechanical modelling, demonstrated using previously unpublished datasets. In particular, the direct inversion of splitting measurements for fracture properties outlined in Chapter 3 represents an important development on the standard practise of assuming that shear wave fast direction corresponds directly to fracture strike. Instead, the inversion procedure allows the effects of sedimentary fabrics and/or dual fracture sets to be imaged, while the use of synthetic tests allows the error limits imposed by event distributions to be computed.

The amount of microseismic activity to be expected during CO₂ injection is not only poorly known, but the issue is rarely raised in CCS literature. Though not directly applicable to Weyburn, the comparison of hydraulic fractures using CO₂ and water shown in Chapter 4 provides a useful contribution in this area, and will hopefully stimulate further research regarding this issue.

Rock physics models do exist to map geomechanical deformation to changes in seismic properties (e.g., Hatchell and Bourne, 2005; Prioul et al., 2004; Zatsepin and Crampin, 1997). However, these models are sometimes limited in their application (Hatchell and Bourne, 2005), and do not explain what is happening at microscale levels (Hatchell and Bourne, 2005; Prioul et al., 2004), or are rarely used because of difficulties in calibrating the models (Prioul et al., 2004; Zatsepin and Crampin, 1997), or because they are difficult to apply (Zatsepin and Crampin, 1997). The rock physics model developed in Chapter 6 is simple in its application, and yet it models observed nonlinear effects and stress-induced anisotropy. Furthermore, the model has its basis in observable microscale features of the rock matrix. The model is easy to calibrate, and I have done so with over 200 core samples of varying lithology. These advantages have already lead to considerable interest from within the hydrocarbon industry.

In Chapter 8 I apply a workflow to go from geomechanical modelling to making predictions about seismic properties (microseismic activity in this case), and comparing these predictions with observations made at Weyburn, using these comparisons to inform and update the geomechanical model. Although geomechanical models have previously been used in combination with rock physics to predict seismic properties (generally using the models cited above, e.g., Minkoff et al., 2004; Hatchell and Bourne, 2005; Herwanger and Horne, 2005), I am unaware of any models that make comparisons with microseismic data. This is significant in that microseismic data is an important and easily monitored indicator of geomechanical deformation. Furthermore, none of the papers cited above have used the seismic observations to inform the geomechanical models. By identifying the discrepancies between initial models and observation, I am able to construct geomechanical models that provide a better match with seismic observations. This process represents an important step in demonstrating the

accuracy of a particular model, which will be useful for any reservoir activity but particularly for proving the integrity of a CCS site to the satisfaction of any regulator.

9.2 Future Work

If CCS is to be used a tool for reducing anthropogenic CO₂ emissions by a significant amount then the current pilot scale projects must be scaled up both in terms of the size of each project and the number of projects. As such, the lessons learnt during this scale-up will inevitably add a huge amount of understanding to what we have gained from the pilot projects. Therefore it is likely that there will be a huge amount of development moving forward some of the ideas presented in this thesis.

This thesis presents a workflow to match geomechanical modelling predictions with microseismic activity in order to improve our understanding of deformation in reservoirs. This workflow consists of a number of separate steps, bringing together a number of different disciplines, and improvements in all of them are likely to be developed in the near future.

The event locations presented in this thesis have been computed by ray-tracing through 1-D velocity models blocked from borehole logs. Already, new techniques are being developed where the velocity model is inverted for in combination with the event locations, providing more accurate event locations and improved velocity models. Additionally, velocity models used for event location are usually isotropic, yet shear wave splitting observations show that anisotropic models would often be more appropriate. Multiplet analysis and/or reverse time migration have also shown potential to reduce the error in event location. With improved event locations, our interpretations of microseismic activity will be improved.

Although semi-automated, the shear wave splitting measurements that I make have been picked manually, and the quality control is also done manually. This is possible because there is only a small amount of data. With larger datasets, these steps must be automated, and techniques are currently being developed that can do so (e.g., Wüstefeld et al., 2010a). This technique also identifies null results automatically, which can be important in determining the orientation of anisotropic symmetry axes.

The geomechanical models developed are simple and representative in nature. I anticipate that, with greater computing power, full models will be developed with increasing regularity that will allow the reservoir to be modelled in more detail. However, this greater detail must be accompanied by more accurate model population. The elastic stiffness across a reservoir unit will not be uniform, but variable throughout, and this variation could potentially be included if the information could be inverted for based on high quality 3-D seismic observations or based on geostatistical models that describe characteristic scales and distributions of heterogeneity. Additionally, it is known that CO₂ will react with the minerals of reservoir rocks, with dissolution of calcite being the principal effect. With improvements in experimental measurement and reactive transport modelling, the effects of dissolution on rock mechanical properties might also be included.

Finally, the comparison that I have made between microseismic observation and model predictions is, in this case, purely a qualitative comparison. It should be possible to develop ways of comparing model prediction with observation in a quantitative fashion. This would allow the fit between many models and a range of observations to be computed numerically, allowing inversion processes to be used that, from an initial starting model, can run through a large range of models, perturbing the input parameters and moving towards the model that provides the best match with the range of geophysical observations that can be made on a CCS site.

BIBLIOGRAPHY

- Abt, D. L., Fischer, K. M., 2008. Resolving three-dimensional anisotropic structure with shear wave splitting tomography. *Geophysical Journal International* 173 (3), 859–886.
- Al-Anboori, A. S. S., 2006. Anisotropy, focal mechanisms, and state of stress in an oilfield: Passive seismic monitoring in Oman. Ph.D. thesis, University of Leeds.
- Al-Harrasi, O., Al-Anboori, A., Wüstefeld, A., Kendall, J.-M., 2010. Seismic anisotropy in a hydrocarbon field estimated from microseismic data. : *in press*, *Geophysical Prospecting*.
- Angus, D. A., Kendall, J.-M., Fisher, Q. J., Segura, J. M., Skachkov, S., Crook, A. J. L., Dutko, M., 2010. Modelling microseismicity of a producing reservoir from coupled fluid-flow and geomechanical simulation. *Geophysical Prospecting* 58 (5), 901–914.
- Angus, D. A., Verdon, J. P., Fisher, Q. J., Kendall, J.-M., 2009. Exploring trends in microcrack properties of sedimentary rocks: An audit of dry core velocity-stress measurements. *Geophysics* 74 (5), E193–E203.
- Backus, G. E., 1962. Long-wave elastic anisotropy produced by horizontal layering. *Journal of Geophysical Research* 66, 4427–4440.
- Bakulin, A., Grechka, V., Tsvankin, I., 2002. Seismic inversion for the parameters of two orthogonal fracture sets in a VTI background medium. *Geophysics* 67 (1), 292–299.
- Balmforth, N. J., Craster, R. V., Rust, A. C., 2005. Instability in flow through elastic conduits and volcanic tremor. *Journal of Fluid Mechanics* 527, 353–377.
- Barruol, G., Hoffmann, R., 1999. Upper mantle anisotropy beneath the Geoscope stations. *Journal of Geophysical Research* 104, 10757–10774.
- Batzle, M. L., Simmon, G., Siegfried, R. W., 1980. Microcrack closure in rocks under stress: Direct observation. *Journal of Geophysical Research* 85 (B12), 7072–7090.
- Blackman, D. K., Kendall, J.-M., 1997. Sensitivity of teleseismic body waves to mineral texture and melt in the mantle beneath a mid-ocean ridge. *Philosophical Transactions of the Royal Society of London, A* 355, 217–231.
- Blackman, D. K., Orcutt, J. A., Forsyth, D. W., Kendall, J.-M., 1993. Seismic anisotropy in the mantle beneath an oceanic spreading center. *Nature* 366, 675–677.
- Bolas, H. M. N., Hermanrud, C., Teige, G. M. G., 2005. Seal capacity estimation from subsurface pore pressures. *Basin Research* 17, 583–599.
- Boness, N. L., Zoback, M. D., 2006. Mapping stress and structurally controlled crustal shear velocity anisotropy in California. *Geology* 34, 825–828.

BIBLIOGRAPHY

- Brown, L. T., 2002. Integration of rock physics and reservoir simulation for the interpretation of time-lapse seismic data at Weyburn field, Saskatchewan. Master's thesis, Colorado School of Mines, Golden, Colorado.
- Brown, R. J. S., Korrinda, J., 1975. On the dependence of the elastic properties of a porous rock on the compressibility of the pore fluid. *Geophysics* 40 (4), 608–616.
- Bunge, R. J., 2000. Midale reservoir fracture characterization using integrated well and seismic data, Weyburn field, Saskatchewan. Master's thesis, Colorado School of Mines, Golden, Colorado.
- Chapman, M., 2003. Frequency-dependent anisotropy due to meso-scale fractures in the presence of equant porosity. *Geophysical Prospecting* 51, 369–379.
- Crampin, S., 1991. A decade of shear-wave splitting in the Earth's crust: what does it mean? what use can we make of it? and what should we do next? *Geophysical Journal International* 107, 387–407.
- Crampin, S., Gao, Y., Peacock, S., 2008. Stress-forecasting (not predicting) earthquakes: A paradigm shift? *Geology* 36, 427–430.
- Crampin, S., Peacock, S., 2008. A review of the current understanding of seismic shear-wave splitting in the earth's crust and common fallacies in interpretation. *Wave Motion* 45, 675–722.
- Crook, A. J. L., Willson, S. M., Yu, J. G., Owen, D. R. J., 2006. Predictive modelling of structure evolution in sandbox experiments. *Journal of Structural Geology* 28 (5), 729–744.
- De Gennaro, S., Onaisi, A., Grandi, A., Ben-Brahim, L., Neillo, V., 2008. 4D reservoir geomethanics: A case study from the HP/HT reservoirs of the Elgin and Franklin fields. *First Break* 26, 53–59.
- De Meersman, K., van der Baan, M., Kendall, J.-M., 2006. Signal extraction and automated polarization analysis of multicomponent array data. *Bulletin of the Seismological Society of America* 96 (6), 2415–2430.
- Dean, R. H., Gai, X., Stone, C. M., Minkoff, S. E., 2003. A comparison of techniques for coupling porous flow and geomechanics. *Proceedings of the 17th SPE reservoir simulation symposium, SPE* 79709.
- Dyer, B. C., Cowles, R. H. J. J. F., Barkved, O., Folstad, P. G., 1999. Microseismic survey of a North Sea reservoir. *World Oil* 220, 74–78.
- Eisner, L., Duncan, P. M., Heigl, W. M., Keller, W. R., 2009. Uncertainties in passive seismic monitoring. *The Leading Edge* 28, 648–655.
- Furre, A. K., Andersen, M., Moen, A. S., Tonnessen, R. K., 2007. Sonic log derived pressure depletion predictions and application to time-lapse seismic interpretation. 69th EAGE Annual Meeting, Expanded Abstracts.

- Gassmann, F., 1951. Uber die elastizitat poroser medien. *Vierteljahresschrift der Naturforschenden Gesellschaft in Zurich* 96, 1–23.
- Grechka, V., 2007. Multiple cracks in VTI rocks: Effective properties and fracture characterisation. *Geophysics* 72 (5), D81–D91.
- Grechka, V., Tsvankin, I., 2003. Feasibility of seismic characterisation of multiple fracture sets. *Geophysics* 68 (4), 1399–1407.
- Grochau, M. H., Gurevich, B., 2008. Investigation of core data reliability to support time-lapse interpretation in Campos Basin, Brazil. *Geophysics* 73 (2), E59–E65.
- Gueguen, Y., Schubnel, A., 2003. Elastic wave velocities and permeability of cracked rocks. *Tectonophysics* 370, 163–176.
- Hall, S. A., 2000. Rock fracture characterisation and seismic anisotropy: Application to ocean bottom seismic data. Ph.D. thesis, University of Leeds.
- Hall, S. A., Kendall, J.-M., 2000. Constraining the interpretation of AVOA for fracture characterisation. In: Ikelle, L., Gangi, A. (Eds.), *Anisotropy 2000: Fractures, Converted Waves, and Case Studies*. Society of Exploration Geophysics, pp. 107–144.
- Hall, S. A., Kendall, J.-M., Maddock, J., Fisher, Q., 2008. Crack density tensor inversion for analysis of changes in rock frame architecture. *Geophysical Journal International* 173, 577–592.
- Han, D.-H., 1986. Effects of porosity and clay content on acoustic properties of sandstones and unconsolidated sediments. Ph.D. thesis, Stanford University.
- Hatchell, P., Bourne, S., 2005. Rocks under strain: Strain-induced time-lapse time shifts are observed for depleting reservoirs. *The Leading Edge* 24, 1222–1225.
- He, T., 2006. P- and S-wave velocity measurement and pressure sensitivity analysis of AVA response. Master's thesis, University of Alberta.
- Hemsing, D. B., 2007. Laboratory determination of seismic anisotropy in sedimentary rock from the Western Canadian Sedimentary Basin. Master's thesis, University of Alberta.
- Herwanger, J., 2007. Linking Geomechanics and Seismics: Stress Effects on Time-Lapse Seismic Data. *EAGE Distinguished Lecturer Program*, London.
- Herwanger, J., Horne, S., 2005. Predicting time-lapse stress effects in seismic data. *The Leading Edge* 24, 1234–1242.
- Holloway, S., 2001. Storage of fossil fuel-derived carbon dioxide beneath the surface of the earth. *Annual Reviews of Energy and the Environment* 26, 145–166.
- Holt, R. M., Brignoli, M., Kenter, C. J., 2000. Core quality: Quantification of coring-induced rock alteration. *International Journal of Rock Mechanics and Mining Science* 37, 889–907.

BIBLIOGRAPHY

- Holt, R. M., Fjaer, E., Nes, O. M., Stenebråten, J. F., 2008. Strain sensitivity of wave velocities in sediments and sedimentary rocks. 42nd U.S. Rock Mechanics Symposium.
- Hornby, B. E., 1998. Experimental laboratory determination of the dynamic elastic properties of wet, drained shales. *Journal of Geophysical Research* 103 (B12), 29945–29964.
- Horne, S., MacBeth, C., 1994. Inversion for seismic anisotropy using genetic algorithms. *Geophysical Prospecting* 42, 953–974.
- Hudson, J. A., 1981. Wave speeds and attenuation of elastic waves in material containing cracks. *Geophysical Journal of the Royal Astronomical Society* 64, 133–150.
- Hudson, J. A., 2000. The effect of fluid pressure on wave speeds in a cracked solid. *Geophysical Journal International* 143, 302–310.
- Hudson, J. A., Liu, E., Crampin, S., 1996. The mechanical properties of materials with interconnected cracks and pores. *Geophysical Journal International* 124, 105–112.
- Hudson, J. A., Pointer, T., Liu, E., 2001. Effective medium theories for fluid saturated materials with aligned cracks. *Geophysical Prospecting* 49, 509–522.
- Jimenez Gomez, J. A., 2006. Geomechanical performance assessment of CO₂ - EOR geological storage projects. Ph.D. thesis, University of Alberta.
- Jizba, D. L., 1991. Mechanical and acoustical properties of sandstones and shales. Ph.D. thesis, Stanford University.
- Johnson, J. W., Nitao, J. J., Steefel, C. I., Knauss, K. G., 2001. Reactive transport modelling of geologic CO₂ sequestration in saline aquifers: The influence of intraaquifer shales and the relative effectiveness of structural, solubility, and mineral trapping during prograde and retrograde sequestration. NETL Proceedings, First National Conference on Carbon Sequestration.
- Johnston, J. E., Christensen, N. I., 1995. Seismic anisotropy of shales. *Journal of Geophysical Research* 100 (B4), 5991–6003.
- Jones, G. A., Raymer, D., Chambers, K., Kendall, J. M., 2010. Improved microseismic event location by inclusion of a priori dip particle motion: a case study from Ekofisk. *Geophysical Prospecting* 58, 727–737.
- Jones, R. H., Stewart, R. C., 1997. A method for determining significant structures in a cloud of earthquakes. *Journal of Geophysical Research* 102, 8245–8254.
- Kendall, J.-M., Fisher, Q. J., Covey Crump, S., Maddock, J., Carter, A., Hall, S. A., Wookey, J., Valcke, S., Casey, M., Lloyd, G., Ben Ismail, W., 2007. Seismic anisotropy as an indicator of reservoir quality of siliclastic rocks. In: Jolley, S., Barr, D., Walsh, J., Knipe, R. (Eds.), *Structurally complex reservoirs*. Vol. 292. Geological Society of London Special Publication, pp. 123–136.

- Kendall, J.-M., Pilidou, S., Keir, D., Bastow, I. D., Stuart, G. W., Ayele, A., 2006. Mantle upwellings, melt migration and magma assisted rifting in Africa: Insights from seismic anisotropy. In: Yirgu, G., Ebinger, C. J., Maguire, P. K. H. (Eds.), *Structure and evolution of the rift systems within the Afar volcanic province, Northeast Africa*. Vol. 259. Geological Society of London Special Publication, pp. 57–74.
- Kendall, J.-M., Stuart, G. W., Ebinger, C. J., Bastow, I. D., Keir, D., 2005. Magma assisted rifting in Ethiopia. *Nature* 433, 146–148.
- King, M. S., 1966. Wave velocities in rocks as a function of changes in overburden pressure and pore fluid saturants. *Geophysics* 31, 50–73.
- King, M. S., 2002. Elastic wave propagation in and permeability for rocks with multiple parallel fractures. *International Journal of Rock Mechanics and Mining Science* 39, 1033–1043.
- Kuster, G. T., Toksoz, M. N., 1974. Velocity and attenuation of seismic waves in two-phase media: Part I. Theoretical formulations. *Geophysics* 39 (5), 587–606.
- Liu, E., Crampin, S., Booth, D. C., 1989. Shear-wave splitting in cross-hole surveys: Modeling. *Geophysics* 54 (1), 57–65.
- Lo, T.-W., Coyner, K. B., Toksoz, M. N., 1986. Experimental determination of elastic anisotropy of Berea sandstone, Chicopee shale, and Chelmsford granite. *Geophysics* 51 (1), 164–171.
- Longuemare, P., Mainguy, M., Lemonnier, P., Onaisi, A., Gerard, C., Koutsabeloulis, N., 2002. Geomechanics in reservoir simulation: Overview of coupling methods and field case study. *Oil and Gas Science and Technology* 57 (5), 471–483.
- MacBeth, C., 2004. A classification for the pressure-sensitivity properties of a sandstone rock frame. *Geophysics* 69 (2), 497–510.
- MacBeth, C., Schuett, H., 2007. The stress dependent elastic properties of thermally induced microfractures in aeolian Rotliegend Sandstone. *Geophysical Prospecting* 55, 323–332.
- Maddock, J., 2006. Missing title. Ph.D. thesis, University of Leeds.
- Makse, H. A., Gland, N., Johnson, D. L., Schwartz, L. M., 1999. Why effective medium theory fails in granular materials. *Physical Review Letters* 83 (24), 5070–5073.
- Mavko, G., Mukerji, T., Dvorkin, J., 1992. *The Rock Physics Handbook*. Cambridge University Press.
- Maxwell, S. C., Shemeta, J., Campbell, E., Quirk, D., 2008. Microseismic deformation rate monitoring, SPE 116596. Presented at the SPE Annual Technical Conference.
- Minkoff, S. E., Stone, C. M., Bryant, S., Peszynska, M., 2004. Coupled geomechanics and flow simulation for time-lapse seismic modeling. *Geophysics* 61 (1), 200–211.

BIBLIOGRAPHY

- Nur, A. M., Simmons, G., 1969. The effect of saturation on velocity in low porosity rocks. *Earth and Planetary Science Letters* 7, 183–193.
- Olofsson, B., Probert, T., Kommedal, J. H., Barkved, O., 2003. Azimuthal anisotropy from the Valhall 4C 3D survey. *The Leading Edge* 22, 1228–1235.
- Onuma, T., Ohkawa, S., 2009. Detection of surface deformation related with CO₂ injection by DInSAR at In Salah, Algeria. *Energy Procedia* 1, 2177–2184.
- Pal-Bathija, A., Batzle, M., 2007. An experimental study of the dilation factor in sandstones under anisotropic stress conditions. *SEG Expanded Abstracts* 26, 1545–1549.
- Pendrigh, N. M., 2004. Core analysis and correlation to seismic attributes, Weyburn Midale Pool, Southeastern Saskatchewan. *in* Summary of investigations Volume 1, Saskatchewan Geological Survey, Sask. Industry Resources, Misc. Rep. 2004-4.1.
- Pointer, T., Liu, E., Hudson, J. A., 2000. Seismic wave propagation in cracked porous media. *Geophysical Journal International* 142, 199–231.
- Prioul, R., Bakulin, A., Bakulin, V., 2004. Non-linear rock physics model for estimation of 3D subsurface stress in anisotropic formations: Theory and laboratory verification. *Geophysics* 69, 415–425.
- Rathore, J. S., Fjaer, E., Holt, R. M., Renlie, L., 1994. P- and S-wave anisotropy of a synthetic sandstone with controlled crack geometry. *Geophysical Prospecting* 43, 711–728.
- Rial, J. A., Elkibbi, M., Yang, M., 2005. Shear-wave splitting as a tool for the characterization of geothermal fractured reservoirs: lessons learned. *Geothermics* 34, 365–385.
- Rojas, M. S., 2005. Elastic rock properties of tight gas sandstones for reservoir characterization at Rulison Field, Colorado. Master's thesis, Colorado School of Mines, Golden, Colorado.
- Rümpker, G., Tommasi, A., Kendall, J.-M., 1999. Numerical simulations of depth-dependent anisotropy and frequency-dependent wave propagation effects. *Journal of Geophysical Research* 104, 23141–23153.
- Rutledge, J. T., Phillips, W. S., Mayerhofer, M. J., 2004. Faulting induced by forced fluid injection and fluid flow forced by faulting: An interpretation of hydraulic fracture microseismicity, Carthage Cotton Valley Gas Field, Texas. *Bulletin of the Seismological Society of America* 94 (5), 1817–1830.
- Rutqvist, J., Vasco, D. W., Myer, L., 2009. Coupled reservoir-geomechanical analysis of CO₂ injection at In Salah, Algeria. *Energy Procedia* 1, 1847–1854.
- Sarout, J., Molez, L., Gueguen, Y., Hoteit, N., 2007. Shale dynamic properties and anisotropy under triaxial loading: Experimental and theoretical investigations. *Physics and Chemistry of the Earth* 32, 896–906.

- Sayers, C. M., 2002. Stress-dependent elastic anisotropy of sandstones. *Geophysical Prospecting* 50, 85–95.
- Sayers, C. M., 2007. Asymmetry in the time-lapse seismic response to injection and depletion. *Geophysical Prospecting* 55, 1–7.
- Sayers, C. M., Kachanov, M., 1995. Microcrack induced elastic wave anisotropy of brittle rocks. *Journal of Geophysical Research* 100, 4149–4156.
- Sayers, C. M., Schutjens, P. T. M., 2007. An introduction to reservoir geomechanics. *The Leading Edge* 26, 597–601.
- Schoenberg, M., Sayers, C. M., 1995. Seismic anisotropy of fractured rock. *Geophysics* 60 (1), 204–211.
- Scott, T. E., Abousleiman, Y., 2004. Acoustical imaging and mechanical properties of soft rock and marine sediments. Tech. Rep. 15302, Dept of Energy, <http://www.osti.gov/energycitations/purl.cover.jsp?purl=/828441-uiLUfO/native/>.
- Segura, J. M., Fisher, Q. J., Crook, A. J. L., Dutko, M., Yu, J., Skachkov, S., Angus, D. A., Verdon, J. P., Kendall, J.-M., 2010. Reservoir stress path characterization and its implications for fluid-flow production simulations. *sub judice*, Petroleum Geosciences.
- Shapiro, S. A., Kaselow, A., 2005. Porosity and elastic anisotropy of rocks under tectonic stress and pore-pressure changes. *Geophysics* 70 (5), N27–N38.
- Silver, P. G., Chan, W. W. J., 1991. Shear-wave splitting and subcontinental mantle deformation. *Journal of Geophysical Research* 96, 16429–16454.
- Simmons, G., Brace, W. F., 1965. Comparison of static and dynamic measurements of compressibility of rocks. *Journal of Geophysical Research* 70 (22), 5649–5656.
- Sminchak, J., Gupta, N., Byrer, C., Bergman, P., 2002. Issues related to seismic activity induced by the injection of CO₂ in deep saline aquifers. *Journal of Energy & Environmental Research* 2, 32–46.
- Staples, R., Ita, J., Burrell, R., Nash, R., 2007. Monitoring pressure depletion and improving geomechanical models of the Shearwater field using 4D seismic. *The Leading Edge* 26, 636–642.
- Tandon, G. P., Weng, G. J., 1984. The effect of aspect ratio of inclusions on the elastic properties of unidirectionally aligned composites. *Polymer Composites* 5 (4), 327–333.
- Teaby, N. A., Kendall, J.-M., Jones, R. H., Barkved, O., 2004a. Stress-induced temporal variations in seismic anisotropy observed in microseismic data. *Geophysical Journal International* 156, 459–466.
- Teaby, N. A., Kendall, J.-M., van der Baan, M., 2004b. Automation of shear-wave splitting measurements using cluster analysis. *Bulletin of the Seismological Society of America* 94 (2), 453–463.
- Terzaghi, K., 1943. *Theoretical Soil Mechanics*. Wiley, New York.

BIBLIOGRAPHY

- Thomsen, L., 1986. Weak elastic anisotropy. *Geophysics* 51 (10), 1954–1966.
- Thomsen, L., 1995. Elastic anisotropy due to aligned cracks in porous rock. *Geophysical Prospecting* 43, 805–829.
- Tod, S. R., 2002. The effects of stress and fluid pressure on the anisotropy of interconnected cracks. *Geophysical Journal International* 149, 149–156.
- Torvanger, A., Kallbekken, S., Rypdal, K., 2004. Prerequisites for geological carbon storage as a climate policy option. *CICERO Report* 2004:04.
- Turley, J., Sines, G., 1971. The anisotropy of Young's modulus, shear modulus and Poisson's ratio in cubic materials. *Journal of Physics D: Applied Physics* 4, 264–271.
- Valcke, S. L. A., Casey, M., Lloyd, G. E., Kendall, J.-M., Fisher, Q. J., 2006. Lattice preferred orientation and seismic anisotropy in sedimentary rocks. *Geophysical Journal International* 166, 652–666.
- van der Neut, J. R., Sen, M. K., Wapenaar, K., 2007. Monitoring effective stress changes in fault zones from time-lapse seismic reflection data - a model study. 69th EAGE Annual Meeting, Expanded Abstracts.
- Vasco, D. W., Ferretti, A., Novali, F., 2008. Reservoir monitoring and characterization using satellite geodetic data: Interferometric synthetic aperture radar observations from the Krechba field, Algeria. *Geophysics* 73 (6), WA113–WA122.
- Verdon, J. P., Angus, D. A., Kendall, J.-M., Hall, S. A., 2008. The effects of microstructure and nonlinear stress on anisotropic seismic velocities. *Geophysics* 73 (4), D41–D51.
- Verdon, J. P., Kendall, J.-M., 2010. Detection of multiple fracture sets using observations of shear-wave splitting in microseismic data. *accepted*, *Geophysical Prospecting*.
- Verdon, J. P., Kendall, J.-M., Maxwell, S. C., 2010a. A comparison of passive seismic monitoring of fracture stimulation due to water versus CO₂ injection. *Geophysics* 75 (3), MA1–MA7.
- Verdon, J. P., Kendall, J.-M., White, D. J., Angus, D. A., 2010b. Linking microseismic event locations with geomechanical models to minimise the risks of storing CO₂ in geological formations. *sub judice*, *Earth and Planetary Science Letters*.
- Verdon, J. P., Kendall, J.-M., Wüstefeld, A., 2009. Imaging fractures and sedimentary fabrics using shear wave splitting measurements made on passive seismic data. *Geophysical Journal International* 179 (2), 1245–1254.
- Verdon, J. P., White, D. J., Kendall, J.-M., Angus, D. A., Fisher, Q., Urbancic, T., 2010c. Passive seismic monitoring of carbon dioxide storage at Weyburn. *The Leading Edge* 29 (2), 200–206.

- White, D., 2009. Monitoring CO₂ storage during EOR at the Weyburn-Midale field. *The Leading Edge* 28, 838–842.
- White, D. J., 2008. Geophysical monitoring in the IEA GHG Weyburn-Midale CO₂ monitoring and storage project. *SEG Expanded Abstracts* 27, 2846–2849.
- Wilson, M., Monea, M., Whittaker, S., White, D., Law, D., Chalaturnyk, R., 2004. IEA GHG Weyburn CO₂ Monitoring & Storage Project Summary Report 2000-2004. PTRC.
- Wookey, J., 2010. Direct probabilistic inversion of shear-wave data for anisotropy. *Bulletin of the Seismological Society of America*, *sub judice*.
- Wookey, J., Helffrich, G. R., 2008. Inferences on inner-core shear-wave anisotropy and texture from an observation of PKJKP waves. *Nature* 454, 873–876.
- Wüstefeld, A., Al-Harrasi, O., Verdon, J. P., Wookey, J., Kendall, J.-M., 2010a. A strategy for automated analysis of passive microseismic data to study seismic anisotropy and fracture characteristics. *Geophysical Prospecting* 58 (5), 755–773.
- Wüstefeld, A., Bokelmann, G., 2007. Null detection in shear-wave splitting measurements. *Bulletin of the Seismological Society of America* 97 (4), 1204–1211.
- Wüstefeld, A., Kendall, J.-M., Verdon, J. P., van Aas, A., 2010b. Monitoring of rock fracture beyond lab experiments: An example of shear-wave splitting in mining operations. *sub judice*, *Earth and Planetary Science Letters*.
- Zatsepin, S., Crampin, S., 1997. Modelling the compliance of crustal rock-I. Response of shear-wave splitting to differential stress. *Geophysical Journal International* 129, 477–494.
- Zimmer, U., Maxwell, S., Waltman, C., Warpinski, N., 2007. Microseismic monitoring quality-control (QC) reports as an interpretative tool for nonspecialists, SPE 110517. Presented at the SPE Annual Technical Conference.

BIBLIOGRAPHY

A

LIST OF SYMBOLS

The table below lists the mathematical symbols that are used throughout this thesis. Other symbols used less extensively are defined in the text.

<i>Symbol</i>	<i>Definition</i>	<i>Symbol</i>	<i>Definition</i>
ψ	Fast S-wave polarisation	δV_S	% Difference in S-wave velocities
δt	Time lag between fast and slow S-waves	δt^N	Normalised time lag between fast and slow S-waves
θ_S	Initial S-wave polarisation	ω	Seismic wave frequency
θ	Arrival azimuth	ϕ	Arrival inclination
ξ	Fracture or microcrack density	γ	Thomsen's parameter
δ	Thomsen's parameter	α	Fracture strike
μ	Lamé parameter	λ	Lamé parameter
ν	Poisson's ratio	ρ	Rock density
C	Stiffness tensor	S	Compliance tensor
B_N	Normal compliance of a fracture set	B_T	Tangential compliance of a fracture set
$\Delta \mathbf{S}$	Additional compliance	a	Fracture aspect ratio
c	Fracture aperture	r	Fracture radius
κ	Rock permeability	Φ	Rock porosity
η	Viscosity	K	Bulk modulus
E	Young's modulus	β_{ijkl}	4th order crack density
α_{ij}	2nd order crack density	β_w	Biot-Willis parameter
P_{fl}	Pore pressure	σ_{ij}	Stress tensor
ε	Strain tensor	σ'_{ij}	Effective stress tensor
p	Mean effective stress	q	Differential effective stress
τ	Shear stress	σ'_n	Normal effective stress
K_0	Stress path parameter	γ_1	Stress path parameter
γ_3	Stress path parameter	χ	Cohesion
m	Coefficient of friction	ϕ_f	Angle of friction
q_{crit}	Fracture critical shear stress	f^p	Fracture potential

APPENDIX A. LIST OF SYMBOLS

B

IN SUPPORT OF CARBON CAPTURE AND STORAGE

The following essay was submitted to (and did not win) the Institute of Environmental Management and Assessment's Student Essay Award, and I have taken the liberty of reproducing it here. It outlines in more detail the need for CCS to help solve the world's CO₂ emissions problems.

In Support of Carbon Capture and Storage

James P. Verdon

Ph.D Student

Centre for the Experimental and Theoretical Study of the Earth's Interior,

University of Bristol, U.K.

May 20th, 2009

The need to generate electricity with minimal CO₂ emissions to reduce the impact of climate change is almost universally accepted. However, arguments still rage over the best way to achieve this. Possible options include demand reduction and improved efficiency, nuclear power, renewable energy and carbon capture and storage (CCS). It is on this last option, capturing of CO₂ at power stations and storage in deep geologic strata, that this essay will focus. This technique has been brought into public consciousness with the recent decision by the U.K. government to commission up to 4 large-scale CCS demonstration projects. CCS is not a magic bullet that can provide the solution alone, and nor should it be used as an excuse to continue burning fossil fuels at our current rates. However, I am convinced that, when the energy needs of the world's developing economies are taken into account, CCS must have a role to play if we are serious about minimising the amount of CO₂ we emit. Nevertheless, public awareness of this technique is limited, and public opinion of CCS is mixed, principally as a result of criticism by environmental groups¹. I will discuss the issues raised, and outline why CCS is not quite the immature and unsafe technology that it is often made out to be.

The advantages of renewable energy sources are well documented, and so an important question to ask is why shouldn't the U.K. aim for an electricity generation mix centred on renewable energy? The U.K. is in a particularly good position to take advantage of renewable energy - we have abundant wind and wave energy arriving on our west coast, while the Severn estuary has one of the largest tidal ranges in the world. However, even if the U.K. were to wean itself off its dependency on fossil fuels for electricity generation, the world's climate change problems would not be solved. If global CO₂ emissions are to be controlled, then the key battlegrounds must be China and India.

Estimates of future energy demand² suggest that, of all the increases between now and 2030, almost half will come from China and India. China is already the world's largest emitter of CO₂, while India will be the third largest by 2015. At present, over 70% of the electricity generated in these countries comes from coal. As these countries expand their economies to develop a Western standard of living, so their energy demands will increase - in the case of India possibly by up to 4 times the current demand. By 2030, China will have added more generation capacity than exists currently in the USA. Given that there remains over 400 million Indians without electricity, and that CO₂ emissions per person for both nations are still far lower than the west, 'there can be no moral grounds for expecting China and India selectively to curb their economic growth simply because world energy demand is rising unacceptably'².

¹e.g., Rochon *et al.*, 2008, Flannery, 2005, pp 249-257 and Bjureby *et al.*, 2009

²IEA World Energy Outlook, 2007, p3

Both China and India are aggressively pursuing alternative energy strategies, principally encouraging efficiency and renewable energy - hydropower³ and wind in China, and solar and wind in India. However, even the best case scenarios, assuming maximum penetration of renewable energy technologies and maximum efficiency, predict that Chinese energy demand will still increase by 90%⁴, and that 65% of electricity generation will still come from coal⁵. In short, as they seek to provide improved living standards for their people, the energy demands of these two nations will by far outstrip what can be supplied by renewable sources, and fossil fuels will continue to be burned in large quantities. If the resulting CO₂ emissions are to be avoided, adopting CCS on a large scale is left as the only option. It is for this reason that the majority of analyses agree that CCS must be used to abate between 15-50% of the world's CO₂ emissions⁶.

Many environmental groups dislike the CCS paradigm. It is seen as tainted by the mistrusted fingers of big corporations, and an excuse for those who don't care about climate change to continue 'business-as-usual' while paying lip-service to environmental issues. They are also concerned that CCS will be used as an excuse to abandon renewable energy development. The numbers show why CCS cannot be viewed as such, by either side. This is not a choice of either renewables or CCS. If we are serious about controlling global CO₂ emissions then we must do both! Harvest renewable energy wherever possible, and capture and store the CO₂ that is emitted from the fossil fuel power stations that remain.

Opponents of CCS often argue that the technique has never been demonstrated on a commercial scale, and therefore that we don't know how to do it, and that it can't be relied on. The short answer is that there must be a first time for everything! Even so, CCS is not the unknown quantity that it is often made out to be. Since the 1970s the oil industry has injected CO₂ into many oil fields, as this can increase oil production. Hence, much of the infrastructure needed to transport and inject CO₂ is already well developed. Furthermore, the soft drinks industry brings huge experience of transporting and dealing with CO₂. In fact, the principal reason why CCS has not been taken up on a commercial scale is the lack of financial incentives for doing so. There is abundant funding available for research on CCS. However, if companies are to make the large investments necessary for the deployment of CCS there needs to be certainty over how much they will be recompensed for doing so. It is this lack of economic certainty, derived from a lack of political will-power, that has stalled the development of CCS⁷.

Even so, there are sites where CO₂ is being stored on a large scale. In order to avoid the Norwegian offshore CO₂ tax, Statoil have been injecting CO₂ into the Utsira formation at Sleipner since 1996 at a rate of ~1 million tonnes per year. Many different geophysical and geochemical monitoring techniques have shown conclusively that the CO₂ is moving through the target reservoir with no

³The 3 Gorges Dam being the most famous (and controversial) example

⁴IEA World Energy Outlook, 2007, p361

⁵IEA World Energy Outlook, 2007, p373

⁶e.g., IEA Energy Technology Perspectives, 2008, Metz *et al.*, 2005, p13, James *et al.*, 2007, p10, Kuuskraa, 2007,

p7

⁷Pew Center Congressional Policy Brief, 2008, p7

leakage⁸. At a second site in North America, CO₂ removed from the waste stream of a gasification plant in North Dakota is piped to Weyburn, Canada, and stored in a mature oil field. CO₂ has been injected since 2000, and now over 3 million tonnes are being stored every year. It is anticipated that the field will store over 50 million tonnes of CO₂ - this is equivalent to the emissions of half a million (gas-guzzling American) cars per year. Again the comprehensive monitoring program, using both the latest geophysical techniques as well as geochemical tracers, gives no indication of any leakage⁹. BP have been storing CO₂ at their In Salah gas field since 2004 at a rate of ~1 million tonnes per year, while smaller scale projects that demonstrate the entire chain of CCS operations - from capture at a power plant to storage underground - are now operational at Schwarze Pumpe in Germany, and at Lacq in France.

The majority of the public are barely aware of the existence of these successful CCS operations. Environmental groups are more trusted than politicians and power companies, and some of these groups (especially Greenpeace, the largest) prefer to highlight scare stories that have only the smallest relation to CCS operations. Perhaps the most widely circulated centres on the release of CO₂ from a volcanic lake in Cameroon, Lake Nyos¹⁰. The lower layers of the lake became saturated with CO₂ emitted from volcanic vents on its bottom, and when the lake overturned approximately 2 million tonnes were released during the night of 21st August, 1986. The cloud of CO₂ enveloped nearby villages, and 2000 people were suffocated. This story is used to highlight in the public mind the dangers of large scale leakage near to urbanised areas.

However, could a Lake Nyos style event ever occur above a CCS operation? The CO₂ at Nyos was volcanic in origin, but it was the overturning of the lake that allowed the CO₂ to escape so rapidly. A common public misconception is that oil is found underground in vast caverns or 'lakes', and that CO₂ would be stored in a similar manner. In fact oil, and CO₂, are trapped in the microscopic pores between the grains that make up a sedimentary rock. The low permeability of such systems prevents the rapid movement of fluids. Simple physical calculations show that the pressure gradients needed to move CO₂ trapped in sedimentary rock at rates comparable to the release at Lake Nyos are unfeasibly large. In short, not possible. Furthermore, the instruments deployed to detect CO₂ leaks above storage sites are so sensitive that they pick up seasonal variations in plant growth rate!¹¹ and so are capable of detecting the tiniest CO₂ leak. A Lake Nyos style CO₂ release from a CCS operation is not a possibility.

A second issue raised recently relates to a water leak from the Utsira formation above the Tordis Field in the North Sea¹². Statoil are currently storing polluted water from the Tordis Field in the Utsira formation, and in 2008 it was found that injection had created fractures allowing leakage to the sea-floor. As discussed above, the Utsira formation is also being used for CCS at Sleipner. The problem, according to Greenpeace, is that as the Utsira has fractured at Tordis, it must therefore be unstable at Sleipner as well. In fact, Tordis and Sleipner are over 300km apart from each other. The

⁸Torp and Gale, 2004

⁹Wilson *et al.*, 2004

¹⁰Rochon *et al.*, 2008, p7 & p30

¹¹Wilson *et al.*, 2004, p88

¹²Bjureby *et al.* 2009 and Greenpeace Briefing, 2009

Utsira rock properties vary significantly between the two locations - and at Tordis it is the high mud volumes in the rock that have lead to the instabilities. In short, Tordis was a poor site for Statoil to choose for injection, selected with, as both Greenpeace and Statoil agree, ‘insufficient geological understanding and weak modelling analyses’¹³.

In contrast, the Utsira at Sleipner has almost zero mud, and so makes an excellent site for injection. At Sleipner these properties were rigorously tested prior to CO₂ injection (as they are, and will be, at all potential CCS sites), and this is why storage has continued successfully for over 12 years, with 12 million tonnes safely secured in the target reservoir. The Greenpeace report goes on to misrepresent a peer-reviewed scientific paper about Sleipner¹⁴ claiming that ‘A more disturbing possibility is that much less CO₂ is being stored in the formation than estimated, meaning that CO₂ is leaking at an unknown rate’¹⁵, when the article in question makes no claim of this kind. It would appear that some environmental groups are choosing not only to ignore the numerous analyses that show how renewable energy alone cannot solve our climate issues, but also choosing to ignore or misrepresent the scientific research that is demonstrating the safety of geological carbon storage.

Environmental groups such as Greenpeace will continue to play an important role in the 21st Century as mankind attempts to deal with anthropogenic climate change. Their track record in mobilising support, challenging those who would put self-interest before the environment, and inspiring the wider public is second to none. However, when the economic development of India and China is considered, CCS becomes a necessity. Furthermore, ongoing CCS operations and scientific research continue to demonstrate the viability of this technique. The environmental opposition to CCS is derived from a gut mistrust of power generation and oil companies. As Carl Sagan once said:

I try not to think with my gut. If I’m serious about understanding the world, thinking with anything besides my brain, as tempting as that might be, is likely to get me into trouble.

Now is no time, and climate change is no problem, to be left to our guts to solve. CCS must be deployed, not instead of, but alongside renewable energy if mankind is to generate electricity without generating CO₂.

¹³Bjureby *et al.* 2009, p5

¹⁴Bickle *et al.*, 2007

¹⁵Greenpeace Briefing, 2009, p4

Word Count: 1979 words

References

- Bickle, M., A. Chadwick, H.E. Huppert, M. Hallworth & S. Lyle, 2007.** Modelling carbon dioxide accumulation at Sleipner: Implications for underground carbon storage: *EPSL*, vol 255, pp 164-176.
- Bjureby, E., E. Rochon, T. Gulowsen, 2009.** Reality check on carbon storage: *Greenpeace International*, 8 pages.
- Congressional Policy Brief, 2008.** Addressing emissions from coal use in power generation: *Pew Center for Global Climate Change*, 16 pages.
- Flannery, T., 2005.** *The Weather Makers: Penguin Group*, 315 pages, ISBN 0-713-99930-6.
- IEA World Energy Outlook 2007.** India and China Insights. 600 pages, ISBN 978-92-64-02730-5.
- IEA Energy Technology Perspectives 2008.** 650 pages, ISBN 978-92-64-04142-4.
- James, R., R. Richels, G. Blanford & S. Gehl, 2007.** The power to reduce CO₂ emissions: *EPRI Energy Technology Assessment Center*, 45 pages.
- Greenpeace Briefing, 2009.** Leakages in the Utsira formation and their consequences for CCS policy: *Greenpeace International*, 5 pages.
- Kuuskraa, V.A., 2007.** A program to accelerate the deployment of CO₂ capture and storage (CCS): Rational, objectives, and costs: *Pew Center for Global Climate Change*, 54 pages.
- Metz, B., O. Davidson, H. de Coninck, M. Loos & L. Meyer, 2005.** Carbon Dioxide Capture and Storage: IPCC Special Report: *Cambridge University Press*, 431 pages, ISBN 13-978-0-521-86643-9.
- Rochon, E., J. Kuper, E. Bjureby, P. Johnston, R. Oakley, D. Santillo, N. Schulz & G. von Goerne, 2008.** False Hope: Why carbon capture and storage won't save the climate: *Greenpeace International*, 42 pages.
- Torp, T.A. & J. Gale, 2004.** Demonstrating storage of CO₂ in geological reservoirs: The Sleipner and SACS projects: *Energy*, vol 29, pp 1361-1369.
- Wilson, M., M. Monea, S. Whittaker, D. White, D. Law & R. Chalaturnyk, 2004.** IEA GHG Weyburn CO₂ monitoring & storage project summary report 2000-2004: *Petroleum Technology Research Center*, 273 pages, ISBN 0-9736290-0-2.